Signatures of a 4pi periodic Andreev bound state in topological Josephson junctions

Kévin Le Calvez

Communauté
UNIVERSITÉ Grenoble Alpes

THÈSE

Pour obtenir le grade de

DOCTEUR DE la Communauté UNIVERSITÉ GRENOBLE ALPES

Spécialité : **Nanophysique** / **Nanoscience**

Arrêté ministériel : 7 Août 2006

Présentée par

Le Calvez Kévin

Thèse dirigée par **Hervé Courtois**
et codirigée par **Benjamin Sacépé**

préparée au sein **Institut Néel, CNRS**
et de **École Doctorale de Physique**

Signatures of a 4π periodic Andreev bound state in topological Josephson junctions

Thèse soutenue publiquement le **12/04/2017**,
devant le jury composé de :

Teun M. Klapwijk
Directeur de recherche, Delft University of Technology, Président
Marco Aprili
Directeur de recherche, Laboratoire de Physique des Solides - Orsay, Rapporteur
Tristan Cren
Directeur de recherche,CNRS, Institut des NanoSciences de Paris, Rapporteur
François Lefloch
Ingénieur de recherche, Institut Nanosciences et Cryogénies CEA - Grenoble, Examinateur

Acknowledgement

Ce travail de thèse n'aurait pas pu être réalisé sans ses multiples soutiens ainsi que son financement initial par le groupement de laboratoire Lanef. C'est pour cette raison que ce chapitre de remerciement est nécessaire.

I would like to start these acknowledgement by thanking the member of the jury : Teun Klapwijk for having accepted to be its president, Marco Aprili and Tristan Cren who accepted to read and correct this manuscript and finally Franҫis Lefloch who represented Universite Grenoble Alpes.

J'adresse ensuite mes remerciements à Hervé Courtois, Clemens Winkelmann et Benjamin Sacépé qui m'ont accueilli dans leur groupe de recherche. Hervé a accepté d'être mon directeur de thèse. Il a su apporter un soutien de qualité et son expertise scientifique pendant les discussions scientifiques.

D'une manière générale, je voudrais remercier tous les membres de l'équipe Champ proche et/ou QNES de l'institut Néel.

Merci Benjamin pour tes conseils avisés et ton encadrement de qualité. Grâce à toi, cette thèse a été une très belle aventure dans le monde de la topologie et de la matière condensée. Tu m'as accompagné tout au long des multiples étapes de ce projet. Lors de notre première rencontre dans les couloirs de l'INAC, je n'aurais pas pu imaginer que le simple projet de STM Besoke de Claude puisse m'amener aussi loin ! J'espère que tu trouveras le temps de te reposer entre ton nouvel arrivant et tes nouveaux étudiants !

Merci Claude pour nous avoir donné accès à ton STM. Les mesures étaient très belles, je regrette que l'on n'ai pas pu voir d'effet de proximité. Les Majoranas étaient quand même bien jolis dans nos systèmes !

Manuel Houzet et Julia Meyer de l'INAC se sont largement impliqués dans la partie théorique de cette thèse. Le modèle développé dans ce manuscrit d'empoisonnement thermiquement activé n'aurait pas pu voir le jour sans leur soutien. Je tiens à les remercier pour leur aide et leurs explications éclairées sur la physique des Majorana.

Toute la caractérisation des échantillons massifs et mésoscopiques s'est faite dans le pôle automatisation. Ainsi, je voudrais remercier Frederic, Philippe, Jacques et Florent qui ont eu la patience de me former sur les équipement et les techniques de caractérisation. Malgré ma maladresse récursive, ils ont su me faire confiance.

Mes connaissances en chimie et croissance de cristaux étaient plus que basiques au début

de ce projet. C'est grâce au soutien de Philippe Plaindoux, Jacques Marcus et Marine Liotaud que j'ai pu combler ces lacunes et produire des cristaux de bonne qualité. Je tiens également à remercier Richard Haettel pour son aide lors des nombreux recuits de divers échantillons. In a tight collaboration with Yusuke Suzuki we developped together the growth of the BSTS material. I hope you enjoyed your stay at Grenoble and the climbing we did together.

Une campagne de mesure sous fort champ magnétique a été réalisée au LNCMI de Toulouse. Dans ce cadre, je souhaite remercie Walter Escoffier pour son soutien avant, pendant et après ces mesures. Merci Florian de m'avoir fait découvrir cette ville bien agréable après une semaine de travail intensif.

Ce projet a été également accompagné par Christophe Hoarau qui nous a bien aidé pour comprendre ces fameuses résonances RF. Il a, entre autre, simulé les modes théoriques de résonance ce qui nous a permis de finalement comprendre en profondeur le fonctionnement de notre système.

Les non-permanents de l'institut Néel ont mis en place un système de parrainage pour les doctorants. Bertrand Menaert a été mon parrain pendant ces 3 années. je te remercie pour ton oreille attentive et tes divers conseils.

Bien plus que des collègues, les étudiants de l'équipe QNES ont su créer une ambiance chaleureuse et conviviale. Je remercie en particulier Alessandro, Alvaro, Aurélien, Anna, Bivas, David, Johanna, Katrin, Louis et Sayanti pour le soutien que vous avez pu amener à toute heure du jour et de la nuit (Hé oui la salle blanche tourne aussi tard dans la nuit). Pour les soirées jeux improvisées pour célébrer la mort des nombreux échantillons ! Pour les gâteaux cuits à des heures tardives, motivés par des raisons burlesques. Ou simplement pour décompresser :).

Arrive enfin les nombreuses personnes qui ne se sont pas professionnellement impliquées dans ce projet. Malgré tout, elles m'ont soutenu et ont participé de près ou de loin à ma santé mentale pendant ces trois (presque quatre) années malgré le rythme élevé de cette aventure. Je pense en désordre à Alexis, Aurele, David, Marine, Aurore, Pierre, Charlotte, Laurent, Emilie, Candice, Marc, François.

Viennent maintenant mes parents et Anne-Gaël qui m'ont accompagné pendant ces longues années d'études. Ils ont toujours cru en mes capacités et m'ont réconforté dans les moments opportuns. Ils étaient là pour les moments charnières de mon éducation. C'est grâce à eux que je suis ici à présent.

Enfin je ne remercierai jamais assez Sophie qui a été à mes cotés pendant maintenant six années. Tu m'as encouragé quand je perdais confiance, tu étais présente lors des bons mais aussi des moments plus difficiles. Sans toi je n'aurai pas tenu.

Pour ceux qui sont arrivés jusque là, je vous souhaite une bonne lecture. En espérant qu'elle vous apporte un point de vue original sur le couplage des isolants topologiques avec la supraconductivité.

Contents

Introduction

MICROELECTRONICS is based on three possible states of condensed matter: metallic, insulating and semiconducting states. On top of these, there exists some materials for which the bulk has a different state than the edge. They are called topological insulators and have an electrically insulating bulk with conducting edges. One of the most common system presenting such behavior is a two dimensional electron gas (2DEG) under a strong perpendicular magnetic field [97]. While the bulk of the 2DEG is insulating, one-dimensional conducting edge channels propagate at the border of the sample. This type of state is called the quantum Hall effect. To fully grasp the physics describing this type of system, the branch of mathematics named topology is adapted to condensed matter physics.

Topology studies the invariance of certain quantities under smooth deformation of systems. For example, a doughnut and a coffee cup have both one hole. Therefore, according to topology, they belong to the same class of materials as the first one can be smoothly deformed into the other and vice-versa. However, a sphere and a doughnut are inequivalent and to transform one into the other, a hole needs to be drilled. This idea of classifying systems into different topological classes has been adapted to condensed matter physics. This classification has led to the distinction between different energy gaps in electronic band structures. Two energy gaps may not be equivalent with respect to topology. At the interface between two topologically inequivalent gaps, the band structure must close leading to gapless (conducting) surface states.

In 2007, the idea that the 2D quantum Hall effect could have an equivalent in three dimensions has been developed by L. Fu, C.L. Kane and E.J. Mele. They have predicted the existence of a new type of insulator : the three dimensional topological insulator (3D TI)[65], which is a band insulator in the volume but is covered by metallic surface states. These surfaces host electronic states with a linear energy dispersion relation, similarly to the Dirac cone in graphene. Figure 1 displays the energy dispersion relation of these surface states. The spin of the electron being always perpendicular to the momentum of the electron which results in a peculiar spin-momentum locking. Such a spin polarization is key as it brings a protection for the electrons against backscattering.

The linear energy dispersion relation and the spin momentum locking of the surface states on a 3D TI have led to an abundance of theoretical predictions. One of the most

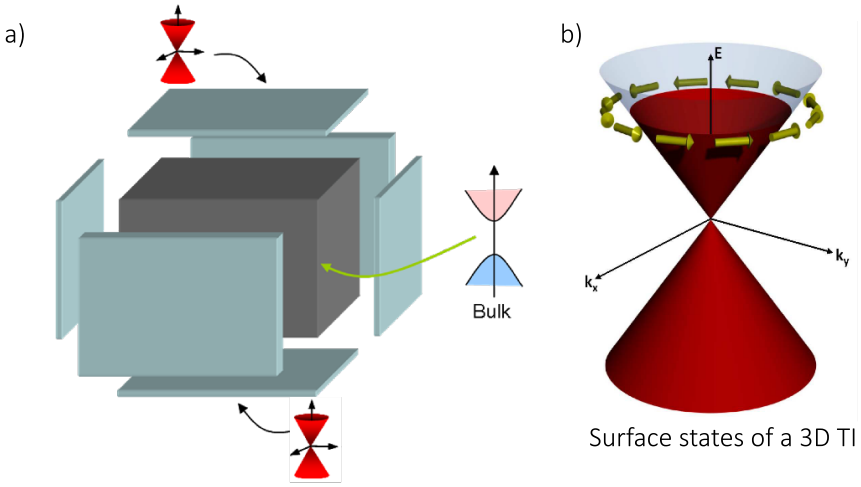

Figure 1. – a) Schematic description of a three dimensional topological insulator (3D TI). b) Band structure of the surface states on a 3D TI. The arrows represent the spin of the electrons and are always perpendicular to its momentum. Adapted from [164].

exciting prediction is the emergence of new electronic excitations with peculiar topological properties when a 3D TI is coupled to a superconductor [63]. These excitations would behave exactly like the Majorana Fermion particle in high energy physics forecast by E. Majorana in 1937 [118].

This excitation called in condensed matter physics the Majorana bound state is governed by non-Abelian statistics and is thus expected to be the building block of the prospective topological quantum computing. For this reason, Majorana physics has dragged major attention recently from the condensed matter physics community. The Majorana bound state could live in a region with non-conventional superconductivity that is induced at the surface of a 3D TI in contact to a conventional superconductor.

In this thesis, we have fabricated Josephson junctions on topological insulators to unveil possible signatures of this unconventional superconductivity and the associated Majorana bound state. We first focus on the material growth and characterization. Then we investigate the theoretical and experimental signatures of Majorana bound states in topological Josephson junctions.

Chapter 1: We present a short introduction on topology in condensed matter physics. We introduce a simple model of topological insulator in one dimension and then extend it to two and three dimensions.

Chapter 2: We show in this chapter how Bi_2Se_3 has been the easy to grow and most appealing material to study the physics of topological insulators. However, this compound is intrinsically doped in the bulk leading to a bulk parallel conduction. Such a short-circuit through the bulk parallel conduction precludes to properly study the physics of the surface

states. That is why we develop in parallel another compound $BiSbTeSe_2$ which was recently identified as a truly bulk insulating topological insulator.

We first introduce the family of 3D TI based on bismuth to motivate our efforts. We then present the method we have used to grow the quaternary compound. We show how electronic transport in our compound is dominated by the surface states and thus is appropriate to be used for topological Josephson junctions.

Chapter 3: This chapter presents the method we used to fabricate topological Josephson junctions on bismuth based TI.

Chapter 4 : Placing two superconductors at the extremities of a normal metal can lead to a non-dissipative current inside the metal. This geometry called Josephson junction is introduced in this chapter. We present the associated physics, mainly the Andreev bound states (ABS). We focus on the different regimes defining the transport properties.

Then we change the normal metal of the Josephson junction to a topological insulator. We present the various and unexpected physics associated to such a topological Josephson junction. The main new property is the change of periodicity from 2π to 4π of a peculiar Andreev bound state (the previously mentioned Majorana bound state).

Probing this modification of periodicity is possible by performing Shapiro measurement, in which radio frequency wave is shined on the junction while recording the voltage-current characteristics. In conventional Josephson junctions, plateaus are formed at equidistant voltages V_n. The 4π periodic ABS is expected to change the Shapiro map by presenting only the even plateaus V_{2n}.

We finish by reviewing the recent experiments reporting signatures of this new periodicity.

Chapter 5: We simulate the VI characteristics of a topological Josephson junction using a simple phenomenological model, the so-called resistively shunted junction model. We observed two signatures of the 4π periodic ABS, one of which had never been reported in literature. The frequency dependence observation of these signatures enables us to estimate the amount of supercurrent carried by the 4π periodic ABS.

To improve this model, we include Joule heating effects. We start by developing this model on conventional Josephson junctions. Finally we extend it to the case of the topological Josephson junctions and give a possible explanation of the experimental observation of all Shapiro steps despite the presence of a 4π periodic ABS.

Chapter 6: We report in this chapter on the main experimental results of this thesis. We present Shapiro measurements performed on topological Josephson junctions based on Bi_2Se_3. We show two signatures of a 4π periodic ABS. The comparison between the experimental observations and the simulations of previous chapter supports the presence of such an unconventional ABS.

Abbrevations

ABS	:	Andreev bound state
4π-tABS	:	Topologically protected 4π periodic Andreev bound state
BdG	:	Bogoliubov de-Gennes
CPR	:	Current–phase relation
DOS	:	Density of states
IV	:	Current–Voltage
JJ	:	Josephson junction
LZ	:	Landau–Zener
MBS	:	Majorana bound state
MF	:	Majorana Fermion
RF	:	Radio frequency
TI	:	Topological insulator
TJJ	:	Topological Josephson junction

Chapter 1

Introduction on topological insulators

This chapter is an introduction to topological insulators (TIs). We review the history of TIs starting from the quantum Hall effect (QHE) to the zero-field TI in two and three dimensions. This chapter is mainly based ref. [73, 171].

1 Context

The band theory of solids first developed by Bloch in 1929 [23] successfully described the electronic conduction in metals, insulators and semi-conductors. It consists in calculating the energy dispersion of electrons in a periodic lattice. Its synthetic representation in the first Brillouin zone gives information on the type of conducting material. The schematic in figure 1.1 summarizes the three main types of band structure.

If the Fermi level lies inside a band gap, no electrons can conduct making the material an insulator. For a small band gap in comparison to the thermal energy ($k_B T$), the material is classified as a semi-conductor. If on the contrary, the Fermi level crosses the conduction or the valence band, electrons can then respond to an external electrical field, giving rise to a current. The material is a conductor.

Despite its powerful description of electrical conduction in condensed matter, the band theory failed to explain the physics of disordered materials and the observation of Quantum

Hall effect emerging in two dimensional electron gas (2DEG).

In the presence of a strong magnetic field perpendicular to a 2DEG, the electronic energy dispersion splits into equidistant levels called Landau levels (see figure 1.2a). If the Fermi energy is placed in-between two Landau levels, band theory predicts the 2DEG to be insulating. However, in 1980 von Klitzing et al observed conducting behavior characterized by a quantized Hall resistance in this type of system [97].

This observation is understood by the upward bending of the Landau levels close to the edge of the sample as described in figure 1.2b-c. As the Landau levels gain energy on the edges of the sample, the low index levels cross the Fermi energy enabling the existence of conducting states at the border of the sample. These edge channels are unidimensional states that are protected against local disorder. Indeed, an electron propagating in this state cannot backscatter as the counter propagating channel is on the other side of the sample.

It has been first understood by D.J. Thouless that this new state of matter, the quantum Hall state, is related to an anomalous topology of the Fermi surface. Topology studies the invariance of physical quantities under a smooth deformation of systems. The power of topology was used recently by physicists to understand and predict the appearance of new phases in condensed matter physics. The associated theory called the topological band theory aims at studying the topology of the band structure.

2 The use of topology in condensed matter

In 2016 the Nobel prize was dedicated to Thouless, Duncan, Haldane and Kosterlitz for use of topology in condensed matter physics[169]. The main purpose of this Nobel prize was the prediction and understanding of the BKT transition. It is a phase transition from one type of topological phase to another type of topology. This type of transition does not originate from the breaking of a symmetry as usually described by the Landau theory. Therefore, using topology in condensed matter opens new ways to study and understand

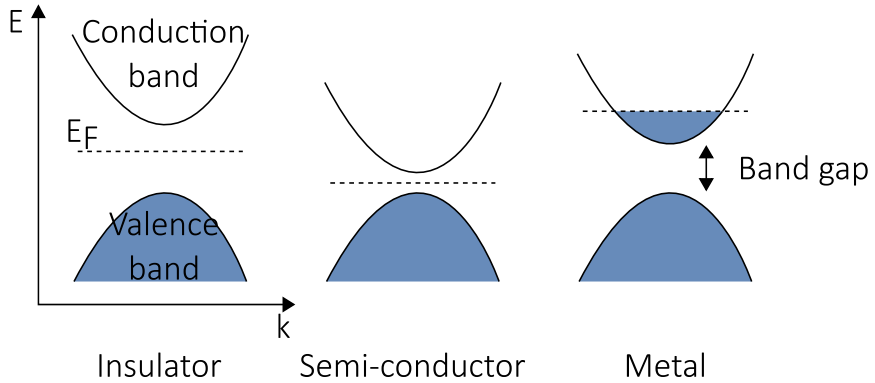

Figure 1.1. – The three main types electronic band structure in solids. The maximum energy of the electrons is the Fermi energy E_F. If E_F lies inside the electronic band gap, then the material is an insulator (large gap : $E_g > k_B T$) or a semi-conductor (small gap $E_g \leq k_B T$). If E_F crosses an energy band, then the material is a metal.

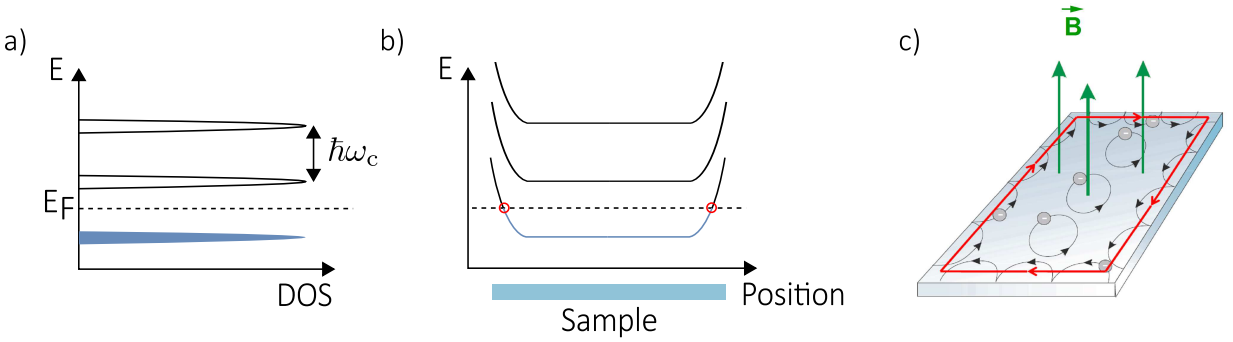

Figure 1.2. – Limitation of the Band theory in the case of Quantum Hall regime. a) Energy of the Landau levels in the bulk of the quantum Hall regime, with $\omega_c = \frac{eB}{m}$ the cyclotron orbit. The material is supposed to be insulating in this configuration. b) Spatial dependence of the Landau levels. At the border of the sample, due to the edge potential, the energy levels cross the Fermi energy (red circle). c) Sketch of the edge channel circulating at the border of a sample from [73].

phenomena that have never been predicted before.

2.1 Classification of topological matter

The topological matters have been classified depending on the symmetries the Hamiltonian breaks or verifies [5, 94, 143, 154, 155]. Three symmetries were used: the Time-Reversal symmetry Θ, the Particle-Hole symmetry Ξ and the Chiral symmetry $\Pi = \Theta\Xi$. In total, there are ten topological classes that classifies the types of topology.

For a given topological class, depending on the dimension of the material (1D, 2D or 3D), the topology of the band structure can be trivial (weak TI) or non-trivial (strong TI). In the case of a non-trivial topology, the material has protected edge states. In the case of a trivial topology these edge states are not protected.

For example, the quantum Hall state (2D) does not verify any of the three symmetries whereas, the quantum spin Hall state that will be described in section 3.2 verifies Time-Reversal symmetry but breaks the two others. Therefore, those two states do not correspond to the same topological class. However both systems host one dimensional edge states that are protected from disorder. On the contrary, vacuum verifies all symmetries and therefore is classified as a trivial insulator.

The protection from backscattering is lost if there exists a counter propagating channel close (in position, spin and energy) to the initial forward channel. Such system would allow the elastic backscattering of electrons. This is the case for weak topological insulators that have an even number edge states.

A different point of view is to associate some integer numbers for each topological classes. They are called topological invariants and define the topology of the band structure. A simple schematic presenting the topology of a material band structure and its associated topological invariant is given in figure 1.3a. A doughnut has an integer number of holes (one) representing the topological invariant. One can observe the continuous deformation from a doughnut to a cup. Therefore, both objects belong to the same topological class with the topological invariant 'number of hole = 1'.

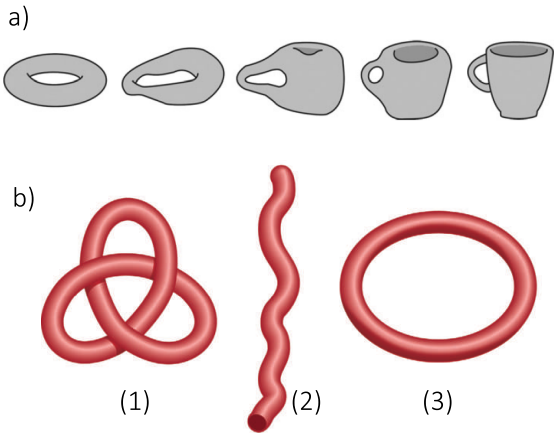

Figure 1.3. – a) Continuous deformation of a doughnut into a cup. They have the same number of holes, hence belong to the same topological class. From [117]. b) Example of strings that do not have the same topology. The trefoil knot (1) cannot be transformed into a ring (3) without cutting the string and thus passing by a string with open ends (2). From [124].

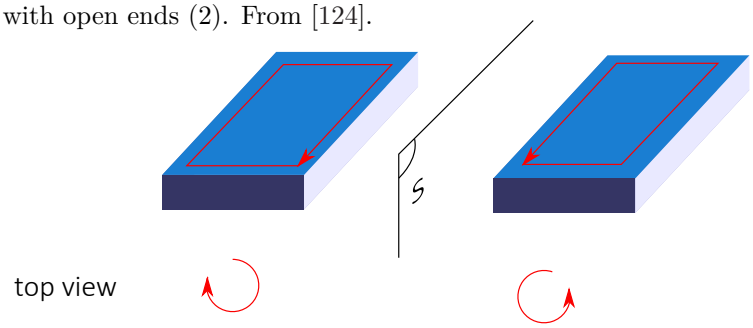

Figure 1.4. – Schematic of the chiral property of the quantum Hall edge state. The initial system (left) has an edge state rotating clockwise. The symmetric with respect to a vertical plane changes the rotation direction of the edge state. The right system is not identical to the left one.

In figure 1.3b are represented different material that do not belong to the same topological classes. The trefoil knot belongs to a different class than the ring. From this analogy, we understand that bringing in contact two systems that do not have the same topological band structure results in the 'cutting' of the band structure at the interface of the two systems. This corresponds to edge states at zero energy. Each time the string in figure 1.3 needs to be cut to be transformed into a ring corresponds to the number of edge channels. An even number of edge channel defines a weak topological insulator without protection from back scattering whereas an odd number corresponds to a strong TI.

2.2 What is chirality ?

Edge states will exist at the interface between a topologically non-trivial phase and a topologically trivial phase (as, for instance, vacuum). Because the two topological phases do not break or verify the same symmetries, these states will be chiral [1].

The notion of symmetry is intrinsic to the Hamiltonian describing the system that is invariant or not under quantum transformation. Therefore, the presence of chiral edge states

1. Sometimes called helical. An helical state is simply a state with a chirality along an axis.

at the border of a system is included in its microscopic description [10, 75]. However, we choose here to introduce the notion of chiral edge states by the observation of the resulting edge states of topological systems. This approach may be not rigorous nor complete but aims at being accessible to non specialist readers.

Chirality is the general property of a system to change when mirrored by an axis or plane of symmetry. For instance, the state in a quantum Hall regime is chiral. Indeed, as described by figure 1.4, the left system has a state propagating clockwise. The symmetric of this system with respect to a plane changes the direction of propagation. As the initial system and its symmetric do not correspond, the edge state is chiral. This notion of chirality always remains when talking about edge states of topological regions.

3 From one to three dimensions TI

In this section we present examples of strong topological insulators in one, two and three dimensions. Each of them host edge states of zero, one and respectively two dimensions that are protected from disorder.

3.1 One dimensional TI: the SSH model

To best understand the nature of a topological insulator, we present the simplest model of one dimension that historically has been the first observed topological insulator. The molecule of polyacetylene is a one dimensional chain that can host soliton states theoretically studied by Su, Schrieffer and Heeger [164]. This molecule presented in figure 1.5 consists in a chain of carbon atoms linked by either single or double bonds. The remaining covalent bond of the carbon atoms is linked to an atom of hydrogen.

The SSH model is described by a tight binding Hamiltonian of $2N$ sites with spinless fermions. Only two parameters describe the hopping of electrons by their probability t_1 and t_2 depending if the bond is simple or double. The two limit cases are $t_1 = 1, t_2 = 0$ and $t_2 = 1, t_1 = 0$ that correspond to electrons that can hope only to a single side. The left case of figure 1.5 is associated to intra-cell hopping of electrons whereas the right case corresponds to inter-cells hopping.

The associated Hamiltonian is given by :

$$H = \sum_{n=1}^{2N} t_{\mathrm{n}} c_{\mathrm{n}}^{\dagger} c_{\mathrm{n+1}} + H.c. \tag{1.1}$$

with $c_{\mathrm{n}}^{\dagger}$ being the creation operator of an electron on the site n and $H.c.$ the Hermitian conjugate of the first term in the sum.

The simplest model corresponds to $t_{\mathrm{n}} = t_1$ and $t_{\mathrm{n+1}} = t_2$. Its energy dispersion is presented in figure 1.6 for two different configurations. The red line corresponding to $t_1 \neq t_2$ describes a gapped band structure, whereas the blue dotted line for $t_1 = t_2$ is not

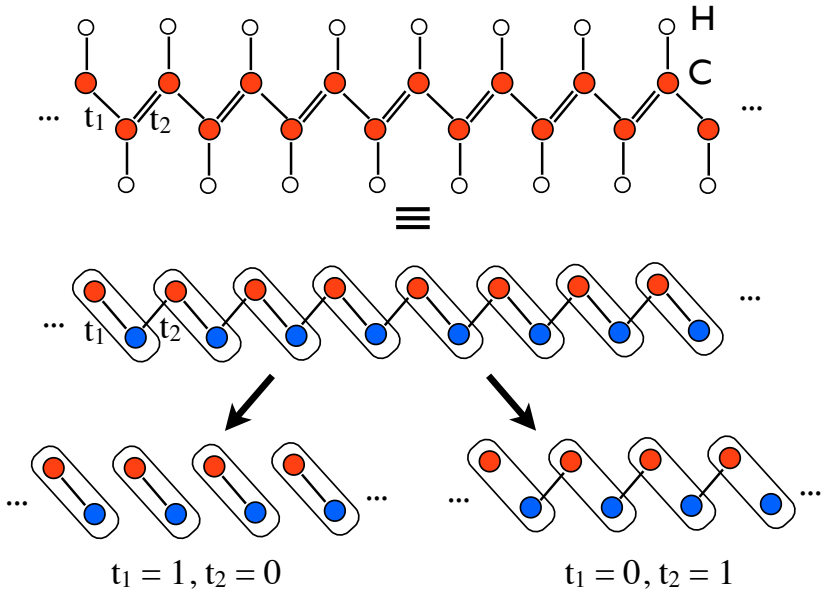

Figure 1.5. – Schematic representation of a molecule of polyacetylene extracted from [171]. Atoms of carbon are bond by either single or double bonds. The hopping term of electrons from one carbon to its left (right) neighbour is t_1 (t_2). The two limit cases $t_1 = 1$ and $t_1 = 0$ are sketched in the lower schematic.

gapped. If we suppose a system with N conducting electrons, the Fermi levels is then placed at zero energy. For this Fermi level, as long as $t_1 \neq t_2$ the system is insulating.

Let us now focus on the topological nature of this system. We will see that the limit cases of intra and inter-cell hopping are in-fact not topologically equivalent. We can first notice that the case $t_1 > t_2$ is equivalent to $t_1 = 1, t_2 = 0$ and so is $t_1 < t_2$ equivalent to $t_1 = 0, t_2 = 1$. Indeed, we can change continuously the Hamiltonian from $t_1 = 1, t_2 = 0$ to any value of $t_1 > t_2$ without closing the band gap. The same procedure can be done between $t_1 = 0, t_2 = 1$ and any value of $t_1 < t_2$. However, to change the system from $t_1 < t_2$ to $t_1 > t_2$, the gap closes and the chain becomes conducting. This gap closure reveals the different affiliation of the two cases to two different topological classes. The case of intra-cell hopping ($t_1 = 1, t_2 = 0$) is arbitrary called the trivial case whereas the case of inter-cell hopping ($t_1 = 0, t_2 = 1$) is topologically non-trivial. Therefore, the gaps of the two cases are not equivalent.

Now we consider a chain that is composed of intra-cell hopping on the left side of $n = 3$ and on the right side of $n = 7$ but contains a region of *inter*-cell hopping in-between $n = 3$ and $n = 7$ as described in figure 1.7. Away from the two interfaces ($n = 3, 7$), the region can be denoted as the bulk of the chain. It has a gapped band structure and hence is insulating. However, at the two interfaces, we observe that the electron sitting on the site A3 does not bond to any neighbour whereas the two sites 6B and 7B share a single electron from A7 representing a hole on a B site.

The energy of the two charges is zero for the electron sitting on A3 because it is isolated from its neighbours, whereas the hole on site 6B and 7B also has zero energy from symmetry argument. In addition, these charges are chiral because they do not share the same sublattice (A and B).

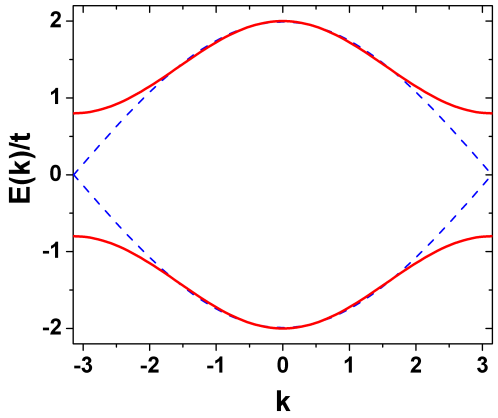

Figure 1.6. – Energy dispersion of the states of the SSH model. The red curve corresponds to the case $t_1 \neq t_2$ whereas the dotted blue line to $t_1 = t_2$. Adapted from [164].

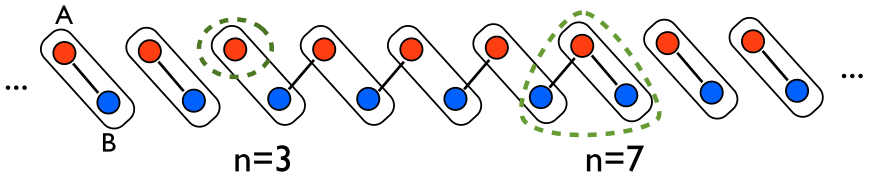

Figure 1.7. – Example of charge soliton in the SSH model. The system is composed of inter-cell hopping in-between $n = 3$ and $n = 7$ and outside of this region the system has intra-cell hopping. Extracted from [171].

To conclude on this model, the presence of a topologically non-trivial region leads to an even number of interfaces hosting chiral edge states. Each interface contains zero energy charges of one dimension lower (here 0D) than the one of the system (here 1D).

From the band structure point of view, the two band gaps of the intra-cell and the inter-cell hopping are not equivalent. Therefore, the gap closes at the interface leading to available conducting states at zero energy.

The effect observed in this simple 1D model remain for 2D and 3D topological insulators. In the next section we describe the general idea of those types of systems and give experimental example.

3.2 2D topological insulator: quantum spin Hall state

The quantum spin Hall (QSH) regime predicted by Kane & Mele in 2005 is the famous example of two dimensional non-trivial topological phase, commonly named as the 2D topological insulator [93].

The QSH regime has similarities to the quantum Hall regime. Indeed, both have an insulating bulk and conducting edge channels as described by the figure 1.8a. However, in comparison to the QH regime that does not differentiate the spin of the electrons, the QSH does. The edge channels in the QSH regime are spin polarized and counter propagate depending on their spin. Thus we can see the QSH as the superposition of two counter propagating edge channels originating from spin polarized QH edge states of opposite

magnetic field.

The band structure of such phase is presented in figure 1.8b. The structure is composed of two linear branches that crosses at zero energy and zero wave vector which resembles the Dirac cone of graphene. However, these branches are spin polarized. Hence at positive energy, the spin up electrons (red line) propagate in a positive k direction whereas the spin down electrons propagate to the opposite direction.

Similar to the protection of the edge states of the QH regime, these states are protected from backscattering of non-magnetic impurities [2]. Indeed, for a spin up electron to elastically backscatter, the only available state at the same energy is the one at opposite momentum and opposite spin. Therefore, in the absence of magnetic interaction, the spin cannot flip and hence the electron cannot switch to the branch of opposite momentum.

The band structure of the QSH is chiral in the sense that the symmetric with respect to the $k = 0$ plane of the red branch in figure 1.8b is a spin up branch at the same position of the blue branch. As the spin is not symmetric, these states are chiral.

In 2006 Bernevig et al proposed a quantum well structure of HgTe encapsulated by CdTe to observe the quantum spin Hall regime[20]. Mercury telluride has an inverted gap structure with respect to the one of cadmium telluride as presented in figure 1.9a. To be continuous, the Γ_6 and Γ_8 bands have to cross each other at the interface between HgTe and CdTe.

The band structure of the three regions interact and form subbands in the quantum well. The most important ones, E1 and H1, are represented in figure 1.9b for two different well thicknesses d. In the case of small quantum well ($d < d_c$), the CdTe band structure dominates and the sample is insulating. However, for a large sample ($d > d_c$), the subbands in the quantum well invert each other. In this configuration, the upper band H1 needs to connect to the Γ_8 band of CdTe. This connection leads to the crossing of the Fermi level by the H1 subband. The same procedure happens for the E1 subband. Therefore, the crossing of those bands leads to spin polarized edge channels. This is the previously described quantum spin Hall effect.

To prove the proposed model of Bernevig et al, the group of L. W. Molenkamp measured

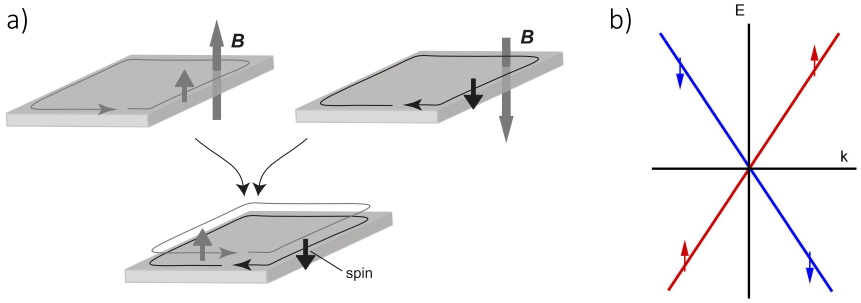

Figure 1.8. – Quantum Spin Hall state seen as the superposition of two spin polarized Quantum Hall states. The edge states are counter propagating with opposite spins. from [126]. b) Energy dispersion of the edge states.

2. Note that in the QH regime, the edge states are protected from all types of impurities including the magnetic ones.

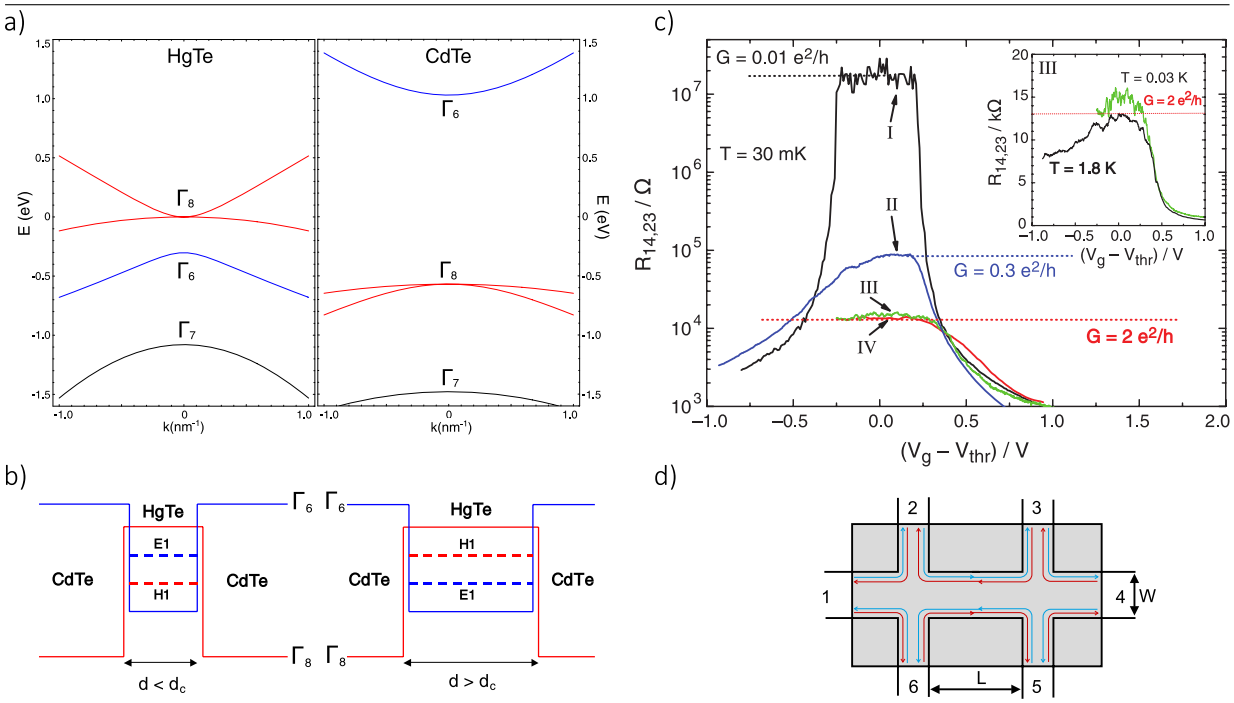

Figure 1.9. – Band structure of HgTe and CdTe close to the Fermi energy. The Γ_8 band contains an heavy and a light band. b) Band structure of a quantum well composed of CdTe-HgTe-CdTe. In continuous lines are represented the position of Γ_6 and Γ_8 bands of the isolated materials. In dotted lines are presented the subbands E1 and H1. For a small (large) well $d < d_c$ ($d > d_c$), the two subbands are dominated by the initial band structure of CdTe (HgTe). c) Longitudinal resistance of Hall bars fabricated on different quantum wells of CdTe-HgTe-CdTe. The samples III and IV have a thickness larger than the critical thickness d_c whereas the other samples are smaller. The former samples display a quantized conductance corresponding to two channels of conduction. d) Schematic representation of the sample measured in c). Adapted from [20, 98, 99].

the conductance of such structure. Their main results is presented in figure 1.9c-d. They observed the conduction of only two channels for a geometry of a large quantum well, as expected by the proposed model.

3.3 3D topological insulator

In 2007 Fu, Kane and Mele discovered the three dimensional equivalence of the quantum spin Hall regime [65]. As for 2D TIs, three dimensional topological insulators (3D TIs) possess an insulating bulk with conducting edges. However, the edges of a 3D crystal are its surfaces. Therefore, the 3D bulk of a 3D TI is insulating and only its surfaces are conducting.

As described in figure 1.10a, the band structure of the bulk of a 3D TI is gapped whereas its surfaces are gap-less which allows the formation of a metallic 2DEG. In addition, these metallic surfaces have a linear dispersion relation, as the one of graphene, with a spin polarization. This spin polarization is similar to the one of the QSH but here in 2D, the dispersion relation in figure 1.10b presents a cone with a spin perpendicular to the

momentum which rotates with it. This spin texture of the Dirac cone is called spin helicity and describes chiral edge states.

For the same reason as for the QSH regime, these surface states are protected against backscattering as long as no magnetic impurities are involved. Therefore, the main difference between these surface states and a simple 2D electron gas in semiconductors is that it is not subject to localization due to disorder and thus remains metallic even at zero temperature.

The first material identified as being a 3D TI was Bi_xSb_{1-x} in 2007 by Fu and Kane [64]. In 2009, the three compounds Bi_2Se_3,Bi_2Te_3 and Sb_2Te_3 that have the same crystallographic structure are identified to be 3D TI [181, 190]. Latter strained HgTe was also classified as a 3D TI [30].

The bismuth based compound (Bi_2Se_3,Bi_2Te_3,Sb_2Te_3,...) materials have the same rhombohedral crystal structure with the space group $R\bar{3}m$. The crystal structure of Bi_2Se_3 is presented in figure 1.11a. The unit cell is composed of five atoms forming quintuple layers. Each quintuple layer is bond by Van-der-Waals interaction whereas the inner bonds are covalent.

This layered crystal structure enables the exfoliation perpendicular to the c axis of such material into thin flakes. This technique developed for graphene exfoliation is already mature in research labs and has been quickly adapted to these types of materials.

The band structure of Bi_2Se_3 is presented in figure 1.11b-d. The computation and ARPES measurement of its band structure shows a large gap of 0.3 eV that is 10 times larger than the thermal energy at ambient temperature. The surface states are visible in the band structure. They form a single Dirac cone at the Γ point inside the bulk band gap.

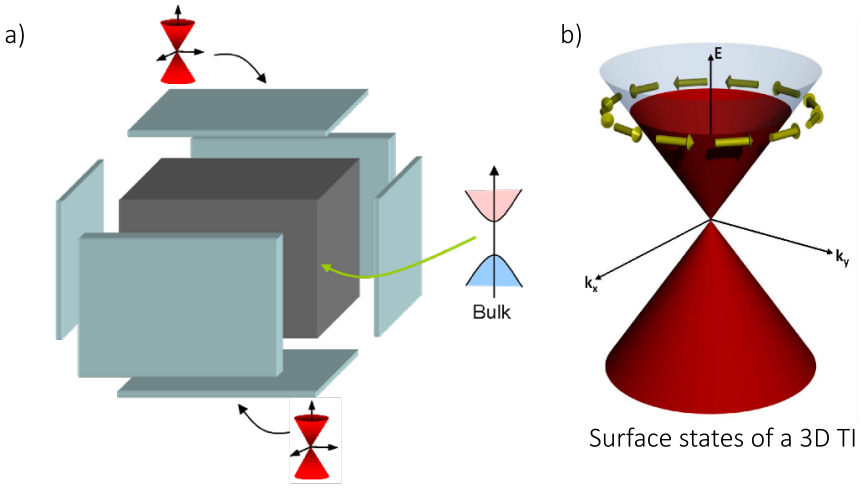

Figure 1.10. – a) Schematic description of a three dimensional topological insulator (3D TI). b) Band structure of the surface states on a 3D TI. The arrows represent the spin of the electrons and are always perpendicular to its momentum. Adapted from [164].

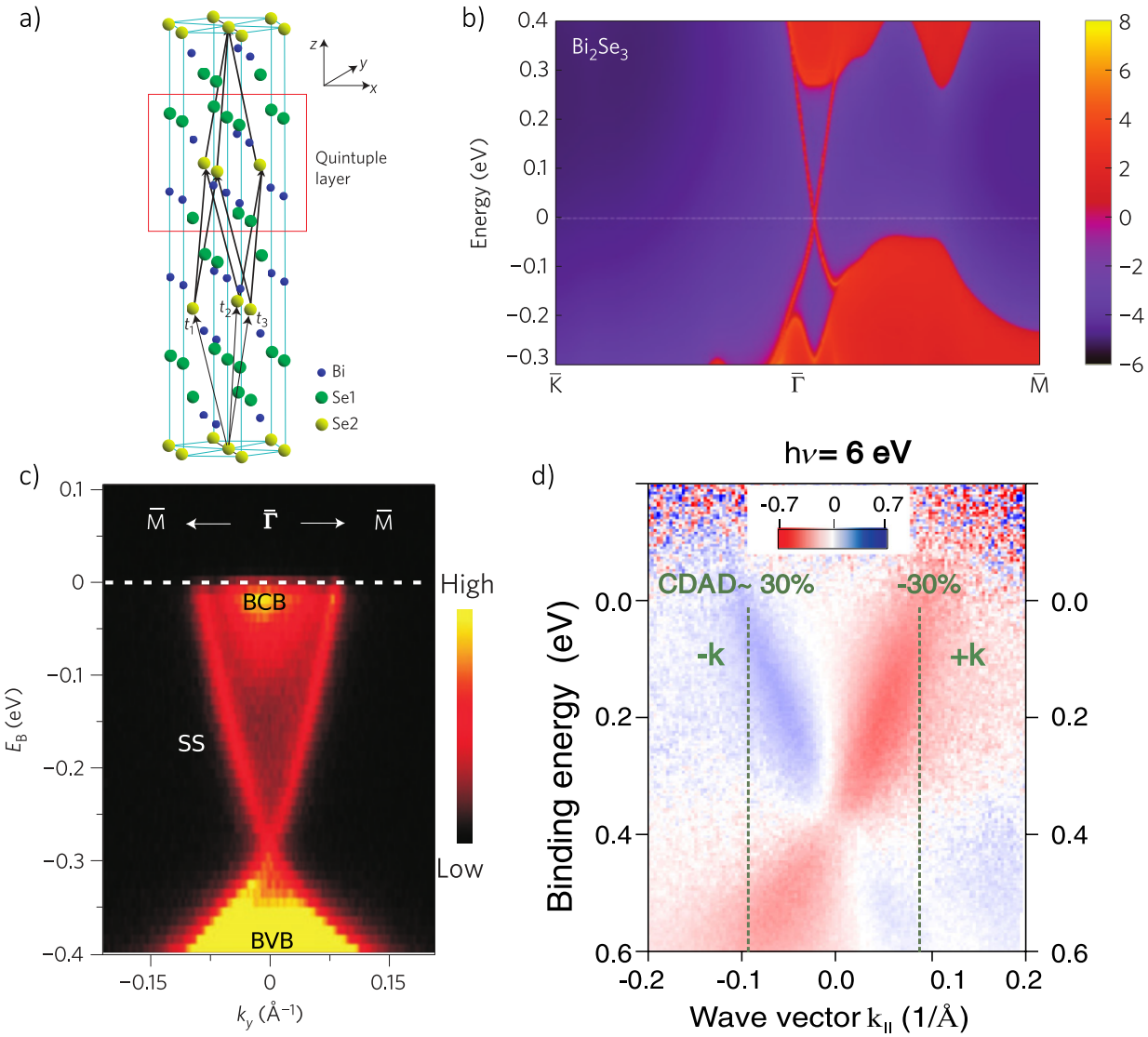

Figure 1.11. – Simulation and experiment on Bi_2Se_3. a) Crystal structure of the material. The red rectangle points at the unit cell. b) Band structure calculated by ref [190]. c) Angle resolved photo emission spectroscopy (ARPES) probing the band structure of Bi_2Se_3. BC(V)B: Bulk conduction (valence) band, SS: Surface states. Extracted from [181]. d) Polarized ARPES measurement showing the helicity of the Dirac cone at the surface of Bi_2Se_3. Extracted from [147]

Despite their very promising aspects, Bi-based 3D TI compounds have a major drawback that is the residual doping of their bulk. Experimentally, none of the three compounds has a Fermi level inside the band gap, which makes their bulk effectively metallic. That is why we investigate in this thesis the growth of a bulk insulating TI based on the same crystallographic structure : the quaternary compound $BiSbTeSe_2$.

4 Conclusion & outlook

After their discovery, 3D TIs were foreseen for the great purpose of being part of the key element of topological quantum computers. Indeed, in 2008, Fu & Kane predicted that a Josephson junction in which the weak link is the surface state of a 3D topological insulator hosts a particular excitation at zero energy [63]. This excitation called in condensed matter physics the Majorana bound state exhibits a non-Abelian statistics which would allow one to perform topological quantum computing [3].

We therefore study in this work Josephson junctions fabricated on bismuth-based 3D TI to investigate the Majorana bound state.

Chapter 2

Growth and characterization of bismuth based topological insulators

Since 2009, Bi_2Se_3 appears as a very promising topological insulator due to its large bulk band gap and the presence of a single Dirac cone for surface states. However, bismuth selenide has a metallic bulk which makes difficult to disentangle in transport measurements the signal of the surface from that of the bulk.

This chapter presents the crystal growth we have performed to fabricate crystals that have vanishing bulk conduction: $BiSbTeSe_2$ (BSTS). We start by presenting shortly the bismuth based three dimensional (3D) topological insulators (TIs) then we describe the procedure we followed for the growth of all compounds studied in this thesis. Finally we describe the growth of the various crystals of BSTS that we made.

1 Introduction to Bi_2Se_3 and its family

After their theoretical prediction in 2007, lots of efforts have been made to obtain topological insulator crystals [64, 65]. In 2009, Bi_2Se_3, Bi_2Te_3 and Sb_2Te_3 were predicted to be 3D TIs. Bismuth selenide has the largest energy gap with 0.3 eV and a Dirac point located inside the gap, which made it the most appealing material to study topological properties [190].

In this section we introduce the state of the art of the bismuth-based topological insulators from the crystallographic structures and electronic properties point of view.

1.1 Crystallographic properties

Bismuth based 3D TIs are layered materials sharing the same rhombohedral crystallographic structure with the space group $R\bar{3}m$. The latter is described in figure 2.1a-c with the example of Bi_2Se_3. The stacking order of a quintuple-layer is Se_1 - Bi_1 - Se_2 - Bi_1' - Se_1', with Se_1 and Se_1' respectively Bi_1 and Bi_1' being equivalent sites in the lattice, whereas Se_1 and Se_2 are two inequivalent sites.

The same year of the prediction of the topological nature of Bi_2Se_3 (BS), the group of Hasan performed angle resolved photo-emission spectroscopy (ARPES) on a BS crystal [181], see Figure 2.1d. One can notice the bulk band gap (between the yellow upper and lower bands) and the surface states forming a Dirac cone in-between the band gap. A similar measurement proved the spin polarization of those surface states [147].

The Fermi level of BS is in the conduction band, the bulk is thus n-doped. Therefore BS has a metallic bulk with conducting surface states. To be able to probe only the surface states, enormous efforts have been made to reduce the bulk conductivity.

1.2 Bismuth based topological insulators

The n-doping of Bi_2Se_3 originates from the selenium vacancies that act as electron donors [78, 128]. On the other hand, Bi_2Te_3 is a p-doped material due to the anti-site defects of tellurium: An atom of bismuth sitting on a tellurium site produces a negative charge

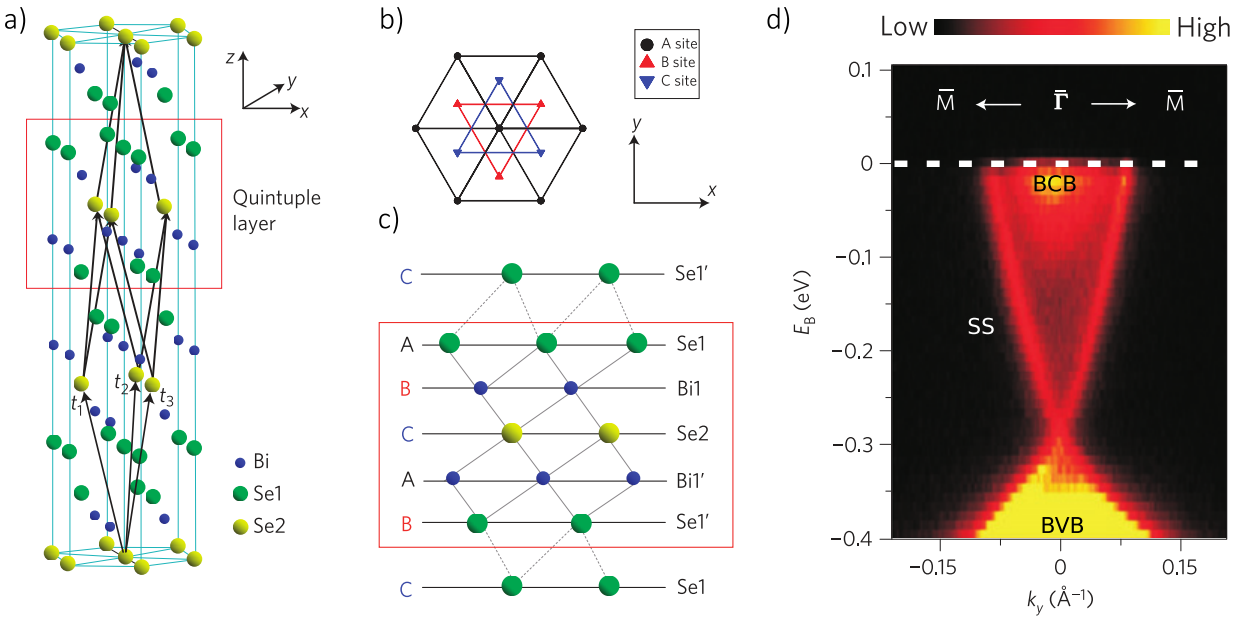

Figure 2.1. – Extracted from [181, 190]. a) Crystal structure of Bi_2Se_3 with primitives lattices vectors $t_{1,2,3}$. The red square designates one unit cell of a quintuple layer of Bi_2Se_3. b) Top view of the lattice. The triangular lattice has three different positions noted as A,B & C. c) Zoom on one quintuple layer. The bond in-between two atoms inside the quintuple layer is a covalent bond, whereas two quintuple layers are linked by Van der Waals bonds. d) Angle resolved photo-emission spectroscopy of Bi_2Se_3. One can distinguish (from bottom to top) the bulk valence band (BVB), the surface states (SS) forming a Dirac cone and the bulk conduction band (BCB).

which is compensated by a hole in the valence band [34, 149]. In order to reduce their bulk conduction, both materials have been thoroughly studied by chemical doping (Bi_2Se_3 : [6, 31, 55, 80], Bi_2Te_3 : [34, 88, 137, 189]), ionic liquid gating [185], molecular beam epitaxy deposition [76] or photon exposure [59]. However, none of these studies reported on the sole observation of surface transport.

A different approach was carried out in parallel. It consists in producing a crystal where the n and the p-doping compensate. For this reason, Bi_2Te_2Se, Bi_2Se_2Te and $BiSbTeSe_2$ (BSTS) compounds were proposed as alternative [14, 131, 140, 141]. The exact ratios of those materials have been tuned to shift the Dirac point and Fermi level location [9, 59, 132, 140, 168, 176, 180].

However, the only material based on bismuth that showed a clear signature of the surface states in transport measurement was the stoichiometric BSTS [182] [1]. Since this publication in 2014, we investigated the growth of this quaternary compound. In this thesis we present the procedure we followed to optimize the growth of the sole material BSTS.

1. For a short time, Bi_2Te_2Se was seen as a promising compound, that is why we put efforts in growing it.

2 Growth methods of stoichiometric crystals

In this thesis, we have grown several topological insulator crystals. We have followed the same procedure for all the growth : First we study the existing phase diagrams of the ternary or quaternary material we want to grow. Second we perform a thermal differential analysis (TDA) on the compound to know its melting temperature and which ratio of the raw elements one should put in the quartz tube/crucible. Finally, we perform a melting growth method to produce the final crystal in a larger quantity and to optimize the quality.

2.1 Estimation of the possible reactions

We perform a thermal differential analysis (TDA) using the commercial set-up DSC 404S from Netzsch presented in figure 2.2. It consists in a crucible in which we place a small quantity of raw elements (500 mg). The crucible is heated up inside the oven of the set-up while recording precisely its temperature T_{sample} and the temperature of the oven T_{oven}. When a reaction occurs in the crucible (fusion / crystallization), T_{sample} will differ from T_{oven}. $DT = T_{\text{sample}} - T_{\text{oven}}$ is then positive (negative) for an exothermic (endothermic) reaction. During the experiment, the pressure is kept ambient with an argon flow of 150 mL/min.

Performing a TDA informs on the temperatures at which the reactions occur during a growth. We also need to make sure that the observed reactions produce the desired compound (BSTS). For that, we characterize the grown material with energy dispersive X-ray spectroscopy (EDX) and powder X-ray diffraction (XRD). If needed, we can change the stoichiometry of the raw elements to adjust the final composition.

To remove the oxide on the raw elements, we clean them within the day of growth

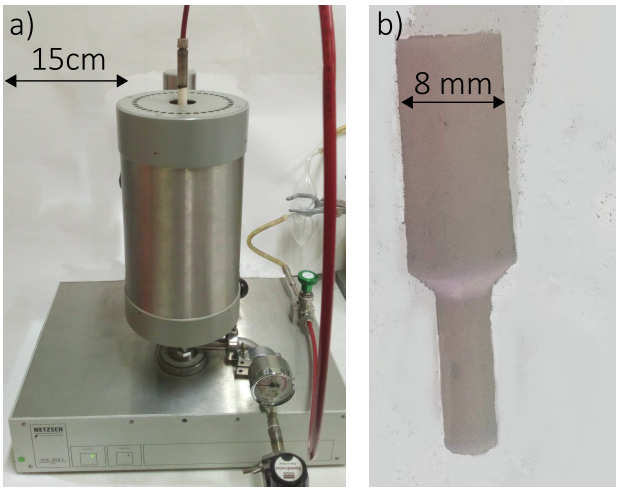

Figure 2.2. – Commercial set-up used to perform the thermal differential analysis. a) Picture of the Netsch 404S. The furnace is 15 cm diameter. Inside the furnace is disposed a crucible (b) wherein the growth elements are put.

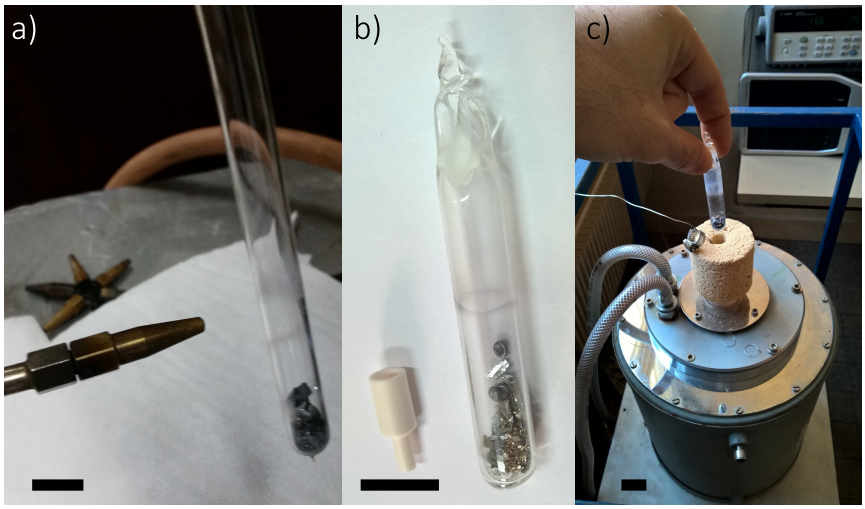

Figure 2.3. – Homemade set-up used to grow topological insulator crystals. a) Closure of a quartz tube with a torch. b) Closed quartz tube. On the left, the crucible of the TDA is shown for comparison. c) Quartz tube put in the adapted oven in which we have grown the crystals. In all pictures, the horizontal black line is 1 cm for scale.

by diluting each element in the appropriate solution (cf table 2.1), then rinsing them in distilled water and ultrasounds. Once dried, the elements are weighed with a precision of 0.01 mg and placed in a crucible (for the TDA) or in a quartz tube for crystal growth.

Element	Bi	Sb	Te	Se
Cleaning solution	KOH	H_2O	HCl	Ethanol

Table 2.1. – Cleaning solution to remove the possible oxides on the raw elements.

2.2 Melting growth in quartz tube

Once we know the melting temperature and the initial composition to obtain a stoichiometric crystal, we can grow the desired compound in a larger amount (~ 3 g). For that we put the raw elements in an air-evacuated quartz ampoule. The procedure is shown in figure 2.3.

3 Growth of $BiSbTeSe_2$

Now that the general procedure to grow a new material has been presented, we discuss the exact approach we followed for the growth of BSTS.

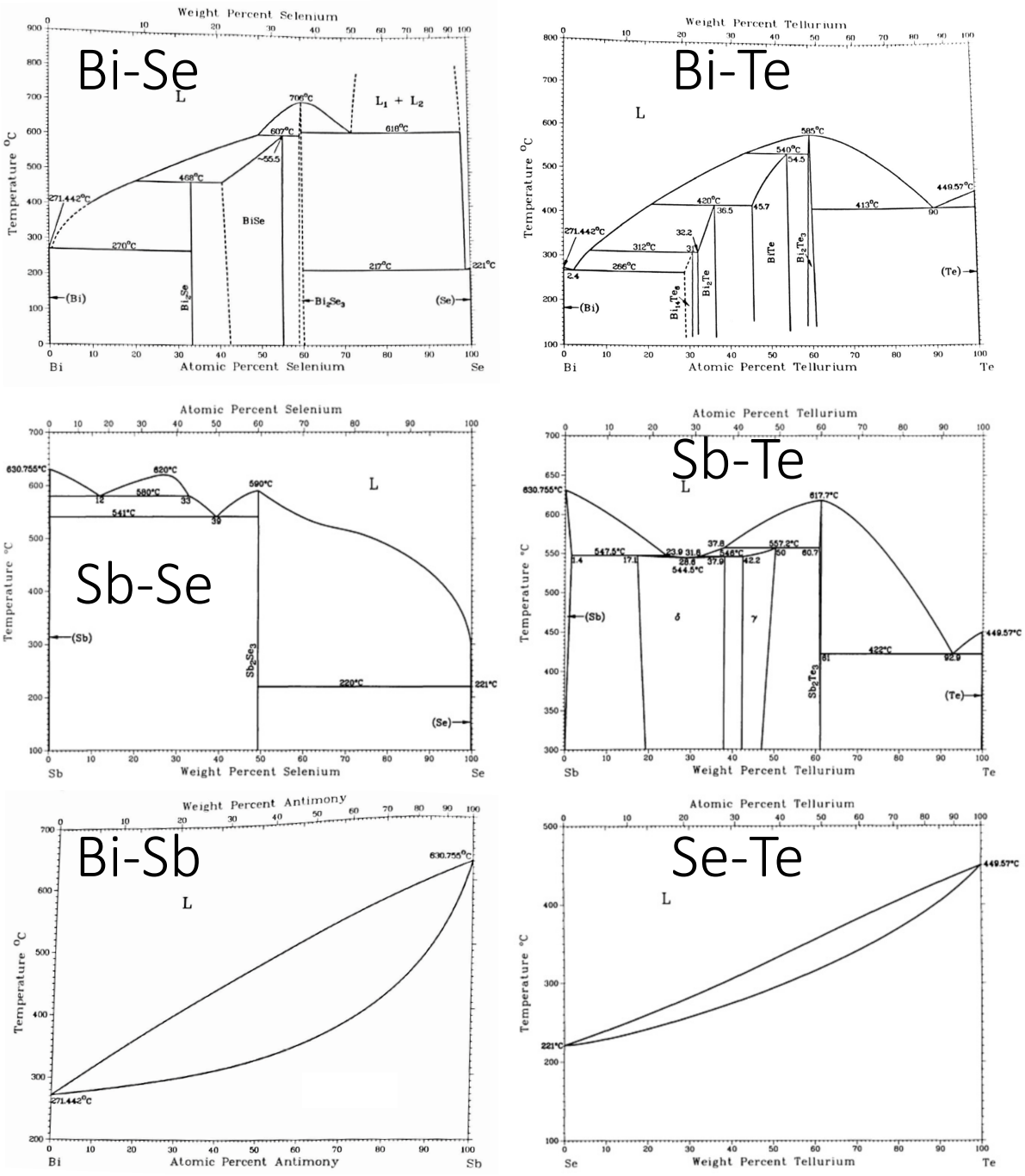

Figure 2.4. – Binary phase diagrams between the four components of the material $BiSbTeSe_2$. These graphs are extracted from Massalski & Okamoto [119]. L represents the liquid phase and the other compounds are labelled with their melting temperatures. We should recall that only the binary compounds Bi_2Se_3, Bi_2Te_3 and Sb_2Te_3 are topological insulators with the rhombohedral crystallographic structure.

3.1 Binary phase diagrams for $BiSbTeSe_2$

Before growing a material, its phase diagram needs first to be studied. As BSTS is a quaternary compound, there exists no phase diagram displaying the temperature dependence of the different possible compounds between the four components. However, we can still observe the 6 binary phase diagrams displayed in figure 2.4. In these diagrams, we note that it is always possible to form the compound A_2B_3 with A=(Bi,Sb), B = (Se,Te) that has a melting point between 585 °C and 706 °C. In addition to these main compounds, bismuth reacts with tellurium and selenium to produce other compounds with a different crystal structure : Bi_2Se, BiSe, BiTe, Bi_2Te and Bi_4Te_6. No defined compound is formed between Se and Te or between Bi and Sb.

From these diagrams, one anticipates that the melting point of BSTS should be below 706 °C [2]. The possible compounds that will be formed during the growth are the one listed above as well as the ternary and quaternary compounds based on the structure of A_2B_3.

3.2 Thermal differential analysis on $BiSbTeSe_2$

To determine the exact melting point of BSTS and which proportion we must use to have a stoichiometric $BiSbTeSe_2$, we performed TDA on the stoichiometric proportion of elements :

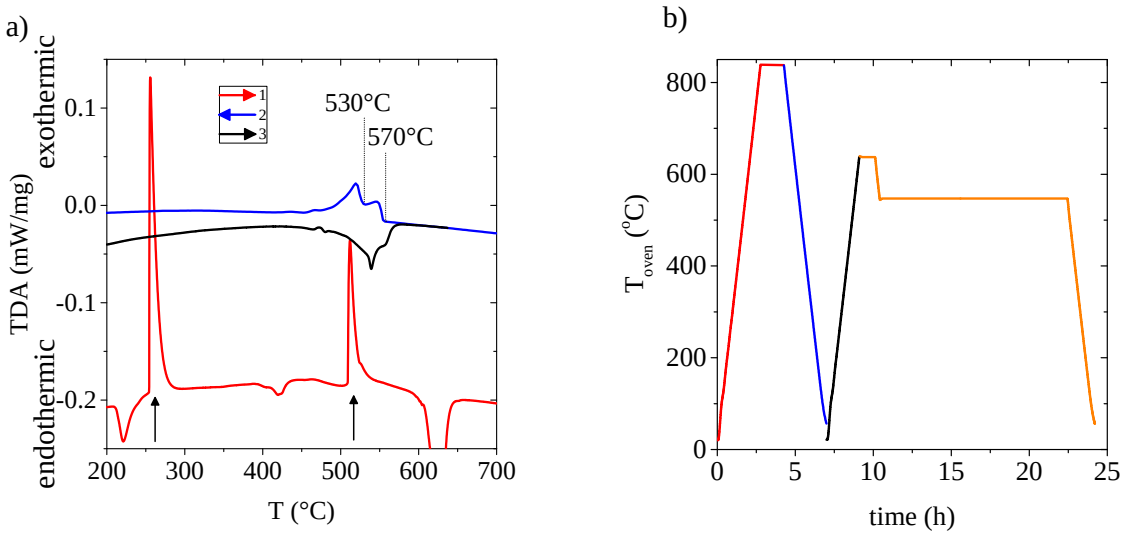

Figure 2.5. – a) Thermal differential analysis on the sample $BSTS_a$. Each positive (negative) spike corresponds to an exothermic (endothermic) reaction. All heatings and cooldowns were done at a speed of 300 °C/h. The red curve has been shifted down for clarity. b) Temperature evolution of the oven during the TDA of a).

2. A binary compound is more stable than its quaternary equivalent. Hence Bi_2Se_3 is more stable than $BiSbTeSe_2$.

$$1\ \mathrm{Bi} + 1\ \mathrm{Sb} + 1\ \mathrm{Te} + 2\ \mathrm{Se} = \mathrm{BSTS_a}$$

with index 'a' denoting the first sample of BSTS.

The results of the TDA are shown in figure 2.5. The first heating cycle (red curve), displays a minimum (endothermic reaction) which is the melting of selenium at $\approx 220\,^{\circ}\mathrm{C}$. The two exothermic reactions (vertical black arrows) are most probably the production an alloy between bismuth and tellurium at 253 °C and of Bi_2Se at 508 °C. A last reaction of fusion appears at 630 °C that is most probably the fusion of a compound based on Bi_2Se_3. Once the sample is liquid, its composition is homogeneous and the growth of BSTS can start by cooling down the sample. The temperatures are not exactly the same as the one referenced in the binary phase diagram because all temperatures are shifted in the presence of the four elements.

The first cooling cycle (blue curve in figure 2.5) displays only two maxima corresponding to two unknown reactions.

Once the crystal is formed, the second heating (black curve) displays the same two reactions at 530 °C and 570 °C that are reproducible. Above the upper temperature, no reaction occurs anymore. Hence the solution is presumably liquid above 570 °C. We do not know a priori which one of the two reactions produces the desired BSTS. To discriminate between the two, we have reproduced a TDA with the *same* sample. During the cooldown, we have waited 12h between the two reactions at 560 °C before quickly cooling down to room temperature at 300 °C/h.

After EDX analysis, we concluded that the grown material is not homogeneous with at least three phases. From XRD, we know that there are two types of crystallographic structures. In addition, its global average composition is given in the table 2.2. In this table the concentration are normalized relative to the composition of A_2B_3:

Element	Bi /(Bi+Sb)	Sb/ (Bi+Sb)	Te(Te+Se)	Se/(Te+Se)
Relative composition	1.24	0.76	0.81	2.19

Table 2.2. – Relative composition of sample $\mathrm{BSTS_a}$ determined by EDX.

We observe the low ratio of antimony and tellurium with respect to the expected composition of $BiSbTeSe_2$. Those elements have either evaporated or migrated to the border of the crucible during the growth and therefore their concentration have decreased when growing the main crystal.

From the TDA of $\mathrm{BSTS_a}$, we conclude that (1) there are two reactions occurring during its growth, (2) starting with a stoichiometric proportion of $BiSbTeSe_2$ does not produce a stoichiometric crystal.

To compensate this shift in composition, we change the initial composition and perform a second TDA:

$$1\ \mathrm{Bi} + 1.1\ \mathrm{Sb} + 1.1\ \mathrm{Te} + 2\ \mathrm{Se} = \mathrm{BSTS_b}$$

During this TDA, we followed the temperature evolution by first heating the whole material above its melting temperature (620 °C), then in a second cycle, we stay below the two

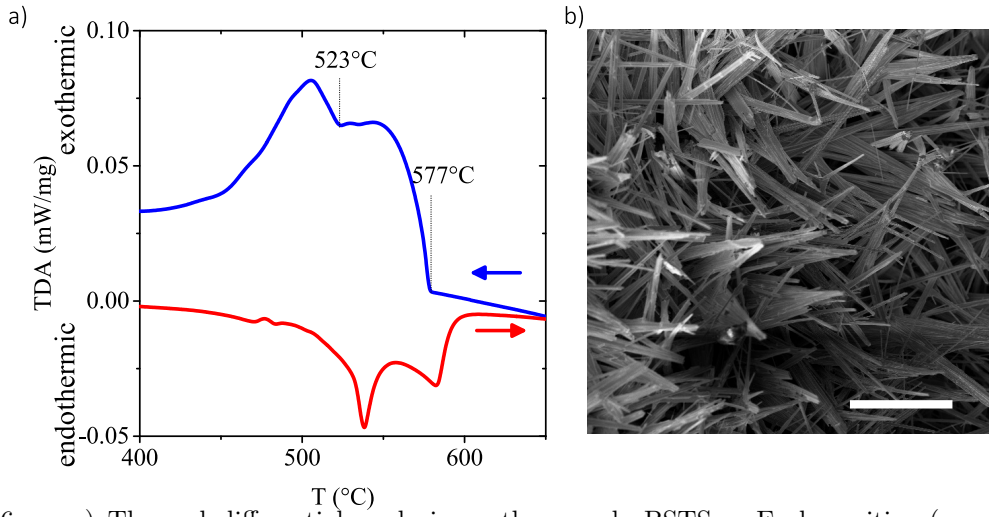

Figure 2.6. – a) Thermal differential analysis on the sample $BSTS_b$. Each positive (negative) spike corresponds to an exothermic (endothermic) reaction. The heating was at 300 °C/h and the cooling at 1200 °C/h. b) Scanning electron microscopy image of the surface of the sample $BSTS_b$. The horizontal white line is 50 µm for scale.

reactions previously identified, that is, a plateau at 520 °C, to promote the compound stable below 530 °C :

$$30\,^\circ\mathrm{C} \xrightarrow{300\,^\circ\mathrm{C/h}} 850\,^\circ\mathrm{C}\ (1\,\mathrm{h}30\,\mathrm{min}) \xrightarrow{-1200\,^\circ\mathrm{C/h}} 30\,^\circ\mathrm{C}$$
$$\xrightarrow{300\,^\circ\mathrm{C/h}} 850\,^\circ\mathrm{C}\ (30\,\mathrm{min}) \xrightarrow{-6000\,^\circ\mathrm{C/h}} 520\,^\circ\mathrm{C}\ (12\,\mathrm{h}) \xrightarrow{-6000\,^\circ\mathrm{C/h}} 30\,^\circ\mathrm{C}$$

The time in brackets represents the waiting time at the given temperature, whereas the speed between two temperatures is written on top of the arrows.

The TDA results are shown in figure 2.6a for the first cooldown (−1200 °C/h) and the second heating (300 °C/h), as highlighted by the colors above. We observe the same two reactions as in figure 2.5 at $T = 523\,^\circ\mathrm{C}$ and $T = 577\,^\circ\mathrm{C}$. The difference between the heating and cooling speeds explains the shift in the reaction temperatures between the blue and the red line.

In this growth, some whiskers of Bi_2Se_3 appeared at the surface of the material (see figure 2.6b). They have grown during the landing at 520 °C.

From the EDX and XRD analysis, two phases are present with a similar composition and the same crystallographic structure A_2B_3:

Element	Bi /(Bi+Sb)	Sb/ (Bi+Sb)	Te(Te+Se)	Se/(Te+Se)
Composition Phase 1	1.02	0.98	1.11	1.89
Composition Phase 2	0.90	1.10	1.07	1.93

We observe an almost equal composition of bismuth and antimony but now the composition of selenium is less than expected. This lack of selenium originates presumably from the growth of the Bi_2Se_3 whiskers that drain the selenium out of the main crystal.

From the TDA on $BSTS_b$, we conclude that (1) the reaction at $\approx 530\,^\circ\mathrm{C}$ corresponds to the growth of Bi_2Se_3 hence the reaction at $\approx 570\,^\circ\mathrm{C}$ probably produces BSTS, (2) the

final composition is still not the expected one but the deviation is easily understood by the formation of Bi_2Se_3 whiskers.

To conclude on those two thermal differential analyses, we know that the reaction temperature of BSTS is $\approx 570\,°C$ and that we need to change the initial composition by putting more tellurium (stoichiometry 1.1) and more antimony (stoichiometry 1.1) to obtain a stoichiometric BSTS.

3.3 Growth of nearly stoichiometric $BiSbTeSe_2$

We use an evacuated quartz tube to grow a crystal with a mass of 3 g and a more stable oven to follow landing steps of several hours. The next sample has the composition concluded in the previous subsection :

$$1\ \mathrm{Bi} + 1.1\ \mathrm{Sb} + 1.1\ \mathrm{Te} + 2\ \mathrm{Se} = \mathrm{BSTS_c}$$

During the melting growth method, we follow the time–temperature superposition principle : to grow a crystal with a solidification temperature T_{sol}, either we wait a short time just above T_{sol} or we stay a long time way above T_{sol}. The probability to obtain a seed is large close to T_{sol}, hence the waiting does not need to be long at this temperature. The probability decreases at higher temperature, therefore in that case we need to increase the landing time to start the growth with a seed. In our case, $T_{\mathrm{sol}}^{BSTS} = 577\,°C$.

The temperature evolution we choose is:

$$30\,°C \xrightarrow{300\,°C/h} 655\,°C(2\,h) \xrightarrow{-100\,°C/h} 620\,°C(24\,h) \xrightarrow{-50\,°C/h} 30\,°C$$

We expect the reaction measured at 577 °C to occur during the waiting at 620 °C.

The temperature of the quartz tube is also recorded to know the exact temperature of the sample [4]. It is displayed in figure 2.7a-b where we observe a reaction occurring at 625 °C. This means that during the landing of 24 h, the whole solution did not solidify. The reaction at 625 °C produced a second unintended phase that is visible in scanning electron microscopy image : in figure 2.7d, two phases with a different chemical composition are visible. We present the chemical compositions of these two phases in table 2.3.

The reaction that occurs at 625 °C produces most probably the dark phase with a lower density of heavy elements. This phase does not have the expected stoichiometric concentration, therefore the reaction at 625 °C is unwelcome.

3. There is a shift between the setpoint (620 °C) and T_{sample} (628 °C) due to the non perfect home-made set-up. We put efforts in having repeatable growth conditions. For that we tried two different ovens. $\mathrm{BSTS_c}$ and $\mathrm{BSTS_d}$ are grown in two different ovens.

4. The attentive reader may wonder why we do not call this experiment a TDA as we record T_{sample} and T_{oven}. In fact, the only difference is the precision of the measurement. In the commercial TDA set-up, T_{sample} is measured directly inside the crucible, whereas in this home-made set-up, T_{sample} is poorly estimated by a thermometer placed near the quartz tube.

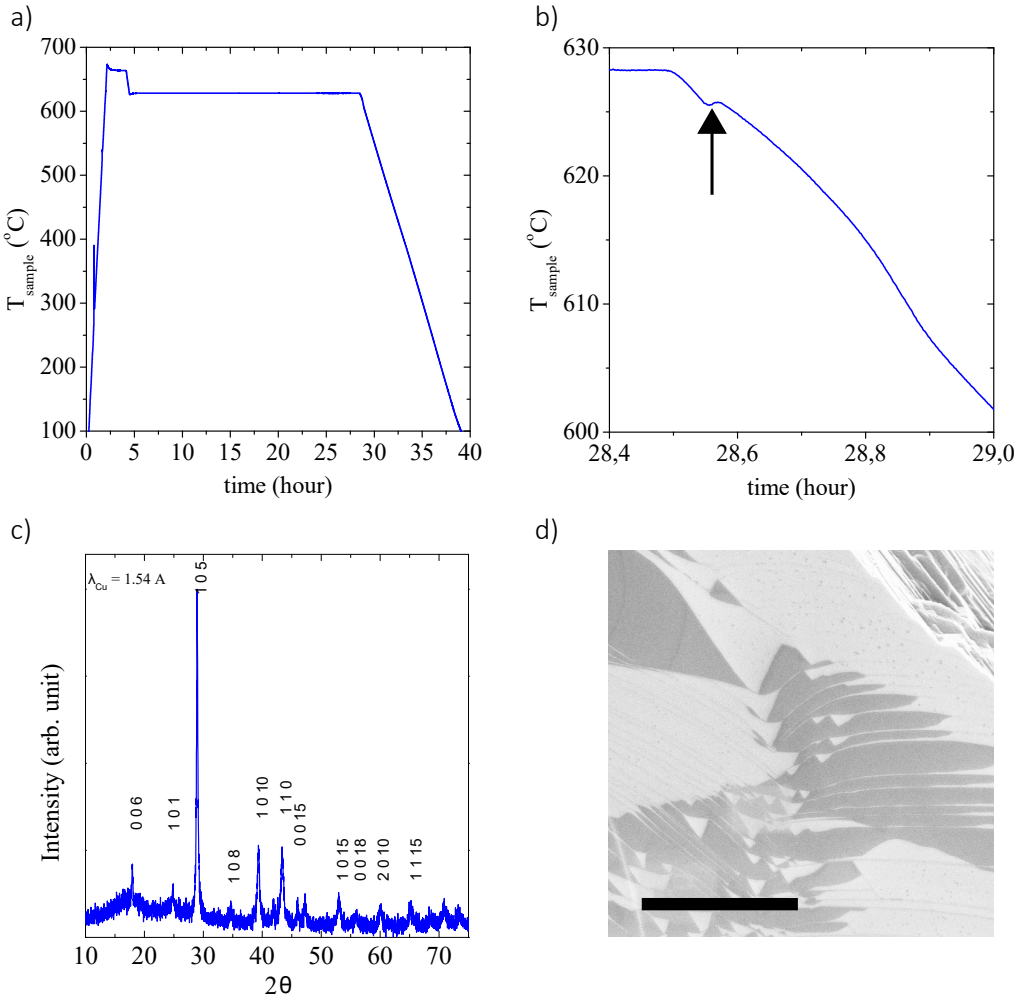

Figure 2.7. – Details on $BSTS_c$: a) Temperature of the quartz tube during the growth. b) Zoom of a) during the cooldown. Highlighted by the black arrow, a reaction occurs at 625 °C after the landing at [3] 628 °C. c) Powder X–ray diffraction of $BSTS_c$. The expected hkl plane indexes are labeled. d) Scanning electron microscopy image of $BSTS_c$ with an in-lens detector. Two phases are visible. The horizontal black line is 50 µm for scale.

We characterized this sample by XRD presented in figure 2.7c. The index of the diffraction peaks expected for a rhombohedral structure are labelled. No extra peak is present, therefore, in this growth, we managed to produce a crystal with only rhombohedral crystallographic structures.

To avoid the second reaction at 625 °C, we choose to slightly change the ratio of selenium and tellurium so that the reaction will be less favorable and second we stay longer at the landing of 628 °C. This last growth has the following composition :

$$1\ \mathrm{Bi} + 1.1\ \mathrm{Sb} + 1\ \mathrm{Te} + 2.1\ \mathrm{Se} = \mathrm{BSTS_d}$$

The temperature evolution of the growth of $BSTS_d$ is the following :

$$30\,^\circ\mathrm{C} \xrightarrow{300\,^\circ\mathrm{C/h}} 655\,^\circ\mathrm{C}(2\,\mathrm{h}) \xrightarrow{-100\,^\circ\mathrm{C/h}} 620\,^\circ\mathrm{C}(\mathbf{48\,h}) \xrightarrow{-50\,^\circ\mathrm{C/h}} 30\,^\circ\mathrm{C}$$

Element	Bi /(Bi+Sb)	Sb/ (Bi+Sb)	Te(Te+Se)	Se/(Te+Se)
Composition Phase dark grey	0.84	1.16	1.12	1.88
Composition Phase light grey	1.04	0.96	1.04	1.96

Table 2.3. – Chemical composition of $BSTS_c$.

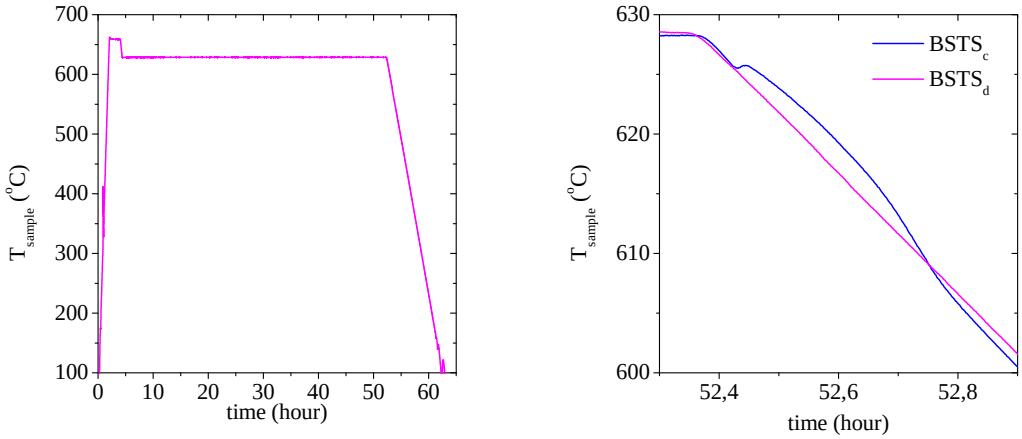

Figure 2.8. – Growth of $BSTS_d$: a) Temperature of the quartz tube during the growth. b) Zoom of a) during the cooldown. We add the temperature evolution of $BSTS_c$ shifted in time to compare the two cooldowns.

Figure 2.8 displays the recorded temperature of the sample $BSTS_d$ (purple curve) and compares with the one of $BSTS_c$ (blue curve). We observe no reaction during the cooldown of $BSTS_d$. Therefore, all material have reacted during the landing at 628 °C and we expect the crystal to have a single phase.

We used this last crystal we have grown to produce topological Josephson junctions detailed in chapter 7.

3.4 Characterization of the final crystal

We present in this section the full characterization of our crystal denoted $BSTS_d$. We first display its crystal structure with XRD measurement, its chemical composition with EDX and neutron scattering and finally we report on its magneto-transport properties.

X-ray diffraction The XRD measurement is presented in figure 2.9. We observe spikes at the expected diffraction angle. No extra phase is seen. Therefore, the material contains only the rhombohedral crystal structure of A_2B_3, with the estimated lattice parameters $a = 0.416\,\text{nm}$ and $c = 2.94\,\text{nm}$.

Laue diffraction We performed a Laue diffraction measurement on an extracted sample to know along which crystal surface the sample cleaves. The diffraction pattern is presented

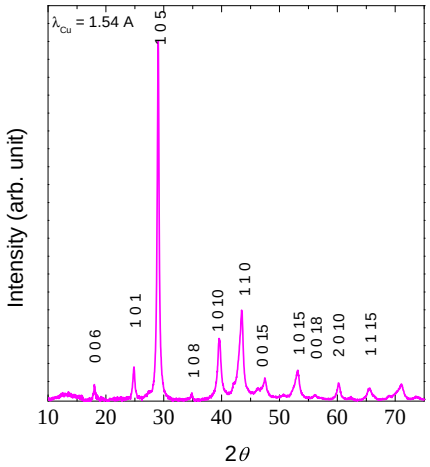

Figure 2.9. – Powder X-ray diffraction of $BSTS_d$. The expected peaks are labeled by their hkl index.

in figure 2.10. By comparing the observed pattern with a calculated one for a surface perpendicular to the 001 axis, we conclude that the crystal easily cleaves perpendicular to the c-axis. This observation is compatible with the rhombohedral crystal structure that has quintuple layers linked by Van-der-Waals bonds.

Energy Dispersive X-ray spectroscopy The scanning electron microscopy observation displayed clean cleaved surfaces presented in figure 2.11. The EDX measurements at different positions on the sample informs on the homogeneity of the concentration of elements. The average composition measured with standards at different locations is presented in the following table:

Element	Bi /(Bi+Sb)	Sb/ (Bi+Sb)	Te(Te+Se)	Se/(Te+Se)
Average composition	1.00	1.00	0.89	2.11

We estimate a perfect ratio between bismuth and antimony. However, there is a slight over-concentration of selenium with respect to tellurium. We could reduce this shift by

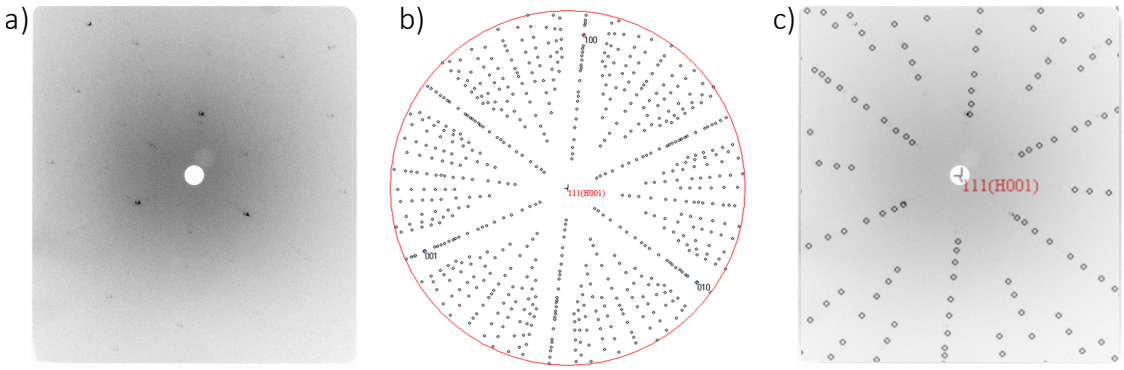

Figure 2.10. – Laue diffraction of BSTS. a) measurement of our BSTS. b) Prediction of the diffraction pattern for a rhombohedral crystal structure cleaved orthogonal to the c axis. c) Superposition of a) and b).

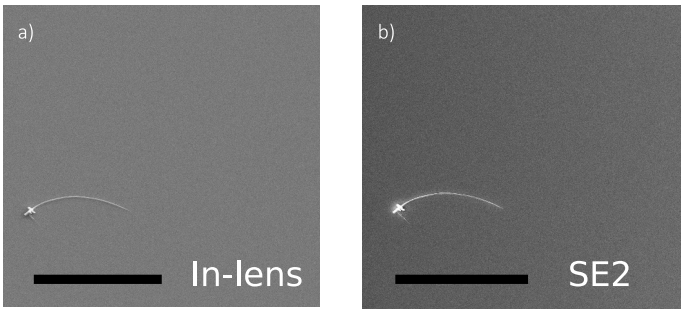

Figure 2.11. – In-lens (a) and secondary electron (b) image of a scanning electron microscopy of a cleaved sample from $BSTS_d$. We observe a large flat area (a) that has a homogeneous composition (b). The black line is 10 µm for scale.

slightly decreasing the amount of raw selenium placed in the quartz tube. This further work should be done to improve the crystal quality.

Neutron scattering Thanks to a collaboration with Y. Suzuki and Prof. K. Kadowaki at the University of Tsukuba, a neutron scattering experiment has been performed at Ibaraki Materials Design Diffractometer on our BSTS to estimate the site occupancy of the crystal structure. The results are presented in figure 2.12. This measurement concluded on the following site occupancy of the crystal structure.

Site / Occupancy	Bi	Sb	Te	Se
Bi,Sb	50%	50%	0	0
Se(1)	0	0	0	100%
Se(2)	0	0	50%	50%

Table 2.4. – Site occupancy of $BiSbTeSe_2$ determined by neutron scattering.

The occupancy of site Se(2) is a mix of selenium and tellurium. This mix could induce defects at the surface of BSTS and be the reason why the transport properties of our BSTS are not as good as the one reported by Xu et al [182]. However, as nobody in the literature ever reported on this site occupancy, we cannot compare our results. However, this estimation of the site occupancy is compatible with the one proposed for Bi_2TeSe_2 [87].

We also give a second estimation of the lattice parameters : $a = 0.416\,789$ nm and $c = 2.950\,04$ nm.

Transport measurement Finally, the last characterization has been done by performing magneto-transport measurement on cleaved crystals of different geometries (thickness t, width W, length L). The results are shown in figure 2.13 where we plot the resistivity, sheet resistance, carrier density and mobility of the samples versus temperature. The resistivity and sheet resistance are calculated by estimating the crystal geometry with an optical microscope. The carrier density and mobility are estimated by Hall measurements

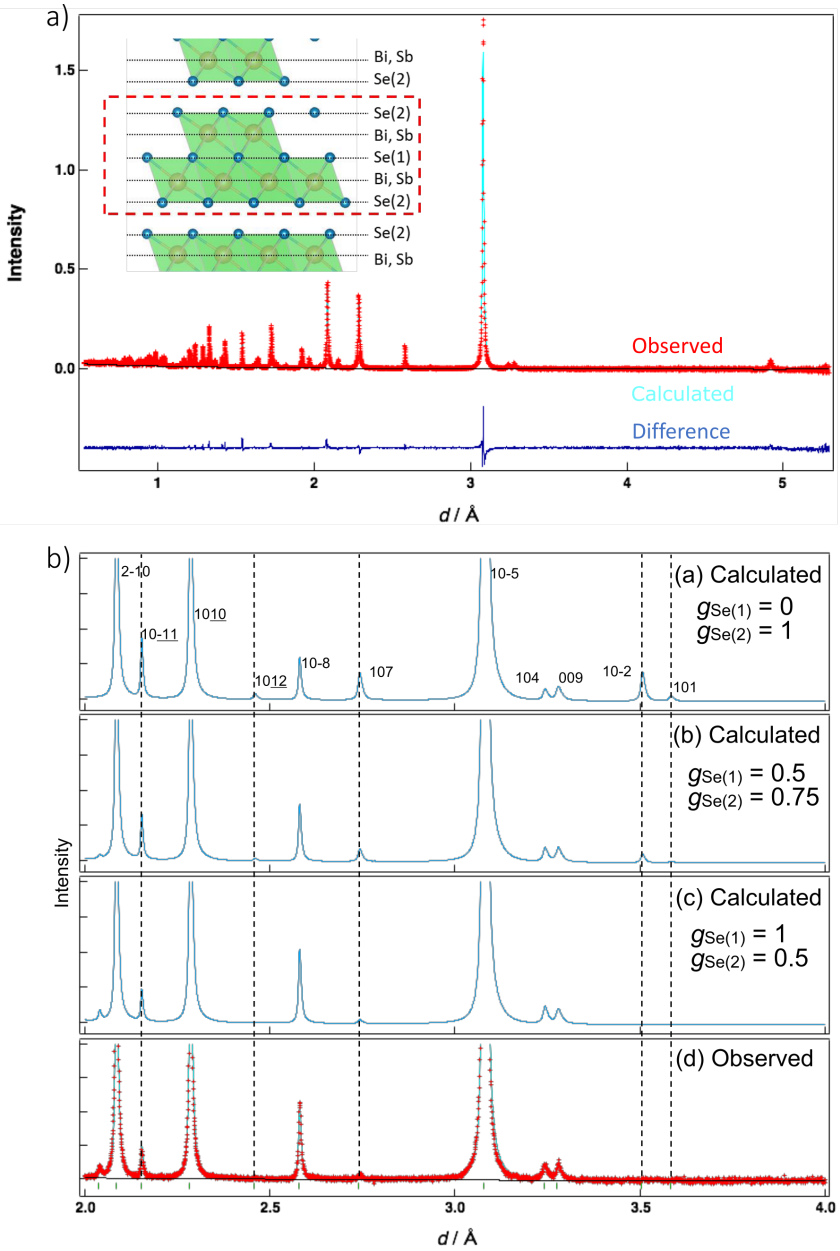

Figure 2.12. – Neutron scattering experiment on $BiSbTeSe_2$.a) Measured (red cross) intensity of the diffraction profile. The position of the expected peaks has been calculated (light blue) by Rietveld refinement analysis. The difference between simulation and measurement is displayed in dark blue. (inset) Schematic of the crystal structure of BSTS. b) Calculated pattern for different site occupancy for various selenium and tellurium ratios of the two sites Se(1) and Se(2). The closest match corresponds to the following occupation. Bi site : 50% Bi, 50% Sb; Se(1) site (inside) : 100% Se ; Se(2) site (outside) : 50% Se, 50% Te. Extracted from Suzuki et al [165].

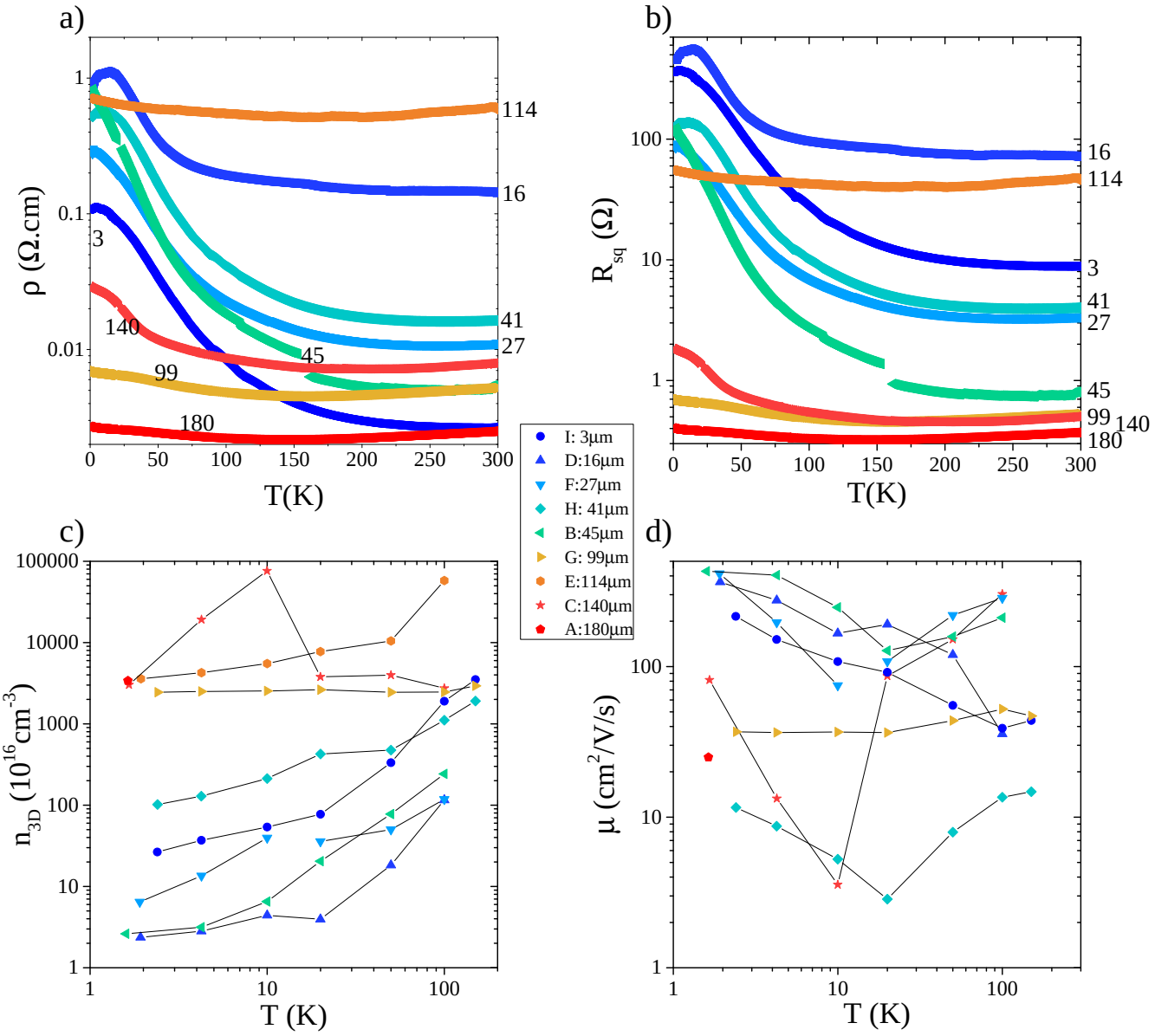

Figure 2.13. – Transport properties of samples extracted from $BSTS_d$. All samples are manually cleaved in the shape of a rectangle. The contact in silver paste are placed in the geometry of a Hall bar. Their thicknesses are estimated with optical microscopy. The resistivity (a) and sheet resistance (b) are measured versus temperature. At several temperatures, we perform Hall measurements to estimate the carrier density (c) and electron mobility (d).

using the crystal geometry : $n_{3D} = \frac{1}{teR_H}$, with e the electron charge and R_H the Hall resistance.

We observe an increase and saturation of resistivity and sheet resistance for decreasing temperature. This behavior is typical of a truly bulk insulating topological insulator. The insulating bulk contributes mostly to transport at room temperature. This contribution evolves like a semiconducting material with diverging resistance at lower temperature, thus reducing its contribution to transport. Below a threshold temperature, the resistance saturates because the metallic surface states of the TI short-circuit the insulating bulk. The resistivity saturates up to $1\,\Omega\,\mathrm{cm}$ for thin samples. The thinner the sample, the higher the resistivity and sheet resistance at low temperature. It is more appropriate to display the sheet resistance when the resistance is dominated by surface transport. In this case, the sheet resistance is supposed to be constant whatever the thickness. It is exactly what we observe in figure 2.13b where the thin samples have a sheet resistance saturating around $500\,\Omega$.

Sample BSTSd-E (orange curve) does not behaves like the other ones, which shows that our crystal is not perfectly homogeneous.

We estimate the Hall carrier density at several temperatures presented in figure 2.13c-d. We observe a decrease of the carrier density for thinner samples up to few $1 \times 10^{16}\,\mathrm{cm}^{-3}$. This small density is consistent with a large contribution from the surface transport at low temperature. However, the carrier mobility is lower than $500\,\mathrm{cm}^2/\mathrm{Vs}$, which is too small to observe any Shubnikov-de-Haas oscillation from the surface states.

From this magneto-transport measurement we confirm the topological insulator character of the material we have grown. We have observed the low contribution from bulk transport at low temperature.

4 Conclusion on the growth

In this chapter we have presented the process to grow $BiSbTeSe_2$ TI. We used two separated steps to optimize the growth. First we performed a thermal differential analysis to obtain the important reaction temperatures and second we grew in quartz tubes a larger amount of material with larger monocrystals.

Thanks to thermal differential analysis and systematic characterization of the grown materials, we have produced a homogeneous compound $BiSbTeSe_2$.

Finally, we have obtained and characterized a 3D topological insulator that has an electronic transport dominated by its surface states at low temperatures.

This material has been used to fabricate topological Josephson junctions that are presented in chapter 7.

Chapter 3

Fabrication of Josephson junctions on bismuth based topological insulators

We present in this chapter the optimized fabrication process for topological Josephson junctions with exfoliated Bi-based compounds.

We begin with a short description of the state-of-the-art on previous realization of topological junctions on bismuth based topological insulator crystals (Bi_2Se_3 and $BiSbTeSe_2$). Afterwards, we turn to our techniques of exfoliation of topological insulator crystals. In the last part we emphasis our process to improve the contact between the flake and the superconducting material.

1 State of the art of bismuth based Josephson junctions

The topological nature of bismuth chalcogenides compounds with the rhombohedral crystal structure has been predicted in 2009 by Zhang et al [190] in Bi_2Se_3,Bi_2Te_3 and Sb_2Te_3. In these materials, the heavy elements have a large spin-orbit coupling that induces in the bulk of the crystal a band inversion between the conduction and valence

band. Due to band continuity, this inversion in the bulk has to be canceled at the borders of the material which therefore produces some conducting surface states.

Since then, various other compounds with the same crystal structure and composed of bismuth, antimony, selenium or tellurium have been proposed to have an electrically insulating bulk and topological protected metallic surface states [115, 131, 175]. For a long time, it was not possible, in these materials, to only probe the surface states in transport measurement. This is due to the remaining conductance of the bulk in parallel to the metallic surface states.

Only recently quantum Hall effect has been observed in the topological insulator $BiSbTeSe_2$, which makes it a very promising candidate to explore the Majorana physics in transport measurements [182].

In the following section, we review the state of the art of Josephson junctions produced on these bismuth based compounds and in particular two materials of which the cleaved surface of the crystal is a layer of selenium [1]: Bi_2Se_3 and $BiSbTeSe_2$.

1.1 Josephson Junctions on Bi_2Se_3

Bi_2Se_3 has been widely used to produced Josephson junctions. In 2011, the first junctions are produced with aluminum leads and a contact layer of titanium [145]. In their study, the authors have been able to tune the Fermi level through the Dirac point while recording the normal resistance and the critical current of the device. The $R_N I_c$ product does not vary much : $R_N I_c \approx 15\,\mu eV$ and remains around 5% of the superconducting gap of the electrodes.

Later, different superconducting electrodes were used to successfully induce superconductivity by proximity effect in Bi_2Se_3: Pb: [184], Nb: [105, 106] Al: [66, 67, 161, 179], W: [188], Sn: [183].

Most of these contacts are improved by using an argon etching before depositing the superconductor and depositing an intermediate layer of platinum or titanium between the superconductor and the crystal [36, 66, 105, 112, 179].

It is also possible to have a superconducting proximity effect by depositing the leads with sputtering deposition [105, 183] or with the focus ion beam [188] rather than the usual metal vapor deposition.

Up to now, no clear hint of the topological nature of the induced superconductivity in Bi_2Se_3 has been probed by AC transport measurement (neither Shapiro measurement nor measurement of the AC Josephson effect by emission). This absence of signature may come from the large contribution of the bulk conduction of this material that hides the transport signal of the surface states. Indeed, in this material, the Fermi level often lies in the conduction band making the bulk metallic. Therefore the bulk produces a very large contribution in transport measurement that may hide the topological nature of the surface transport.

1. According to the neutron diffraction of the previous chapter, the external layer of $BiSbTeSe_2$ is in fact a mix of selenium and tellurium atoms.

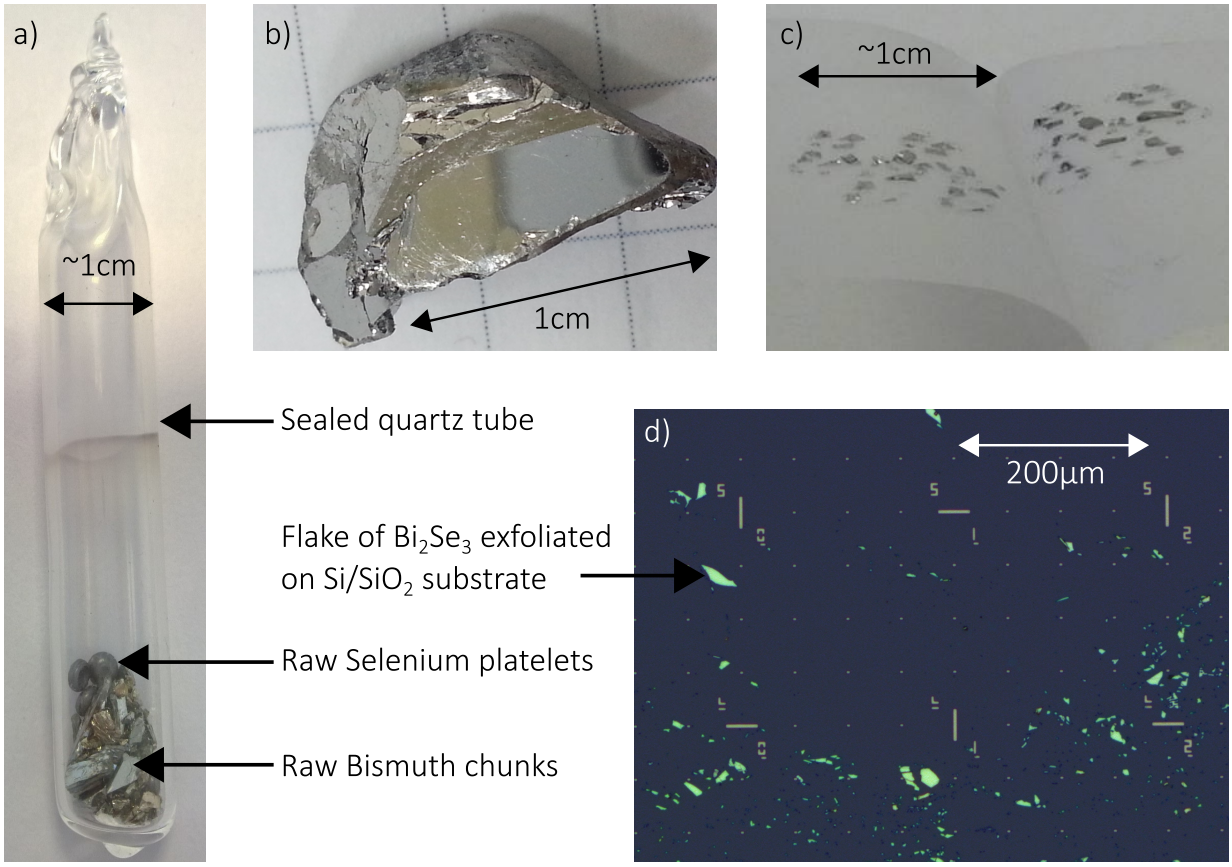

Figure 3.1. – Pictures of the different steps in order to exfoliate a crystal. a) We grow the crystal by placing the raw elements inside an evacuated quartz tube. b) Once grown, the crystal of Bi_2Se_3 is easily cleavable and presents large shiny areas. c) We use the scotch tape technique to exfoliate the chunk of crystal and bring in contact the scotch tape with a substrate of Silicon. d) Optical image of the substrate after exfoliation. The substrate was prepared by depositing a marker-field: orange lines and dots.

1.2 Josephson Junctions on $BiSbTeSe_2$

Only recently, the quantum Hall effect has been observed in the quaternary compound $BiSbTeSe_2$ [182] (named BSTS). This first observation of such clear signature from the surface states of a bismuth-based topological insulator material is promising.

The associated Josephson junctions have been realized with aluminum [112] and niobium [159] superconducting leads. In both cases, they have used a short (20 to 30s) ion argon plasma etching prior to the superconductor deposition. Lee et al have used in addition a contact layer of titanium between the BSTS and the aluminum.

Both groups observed the superconducting proximity effect on the surface states of the crystal but did not prove its topological nature.

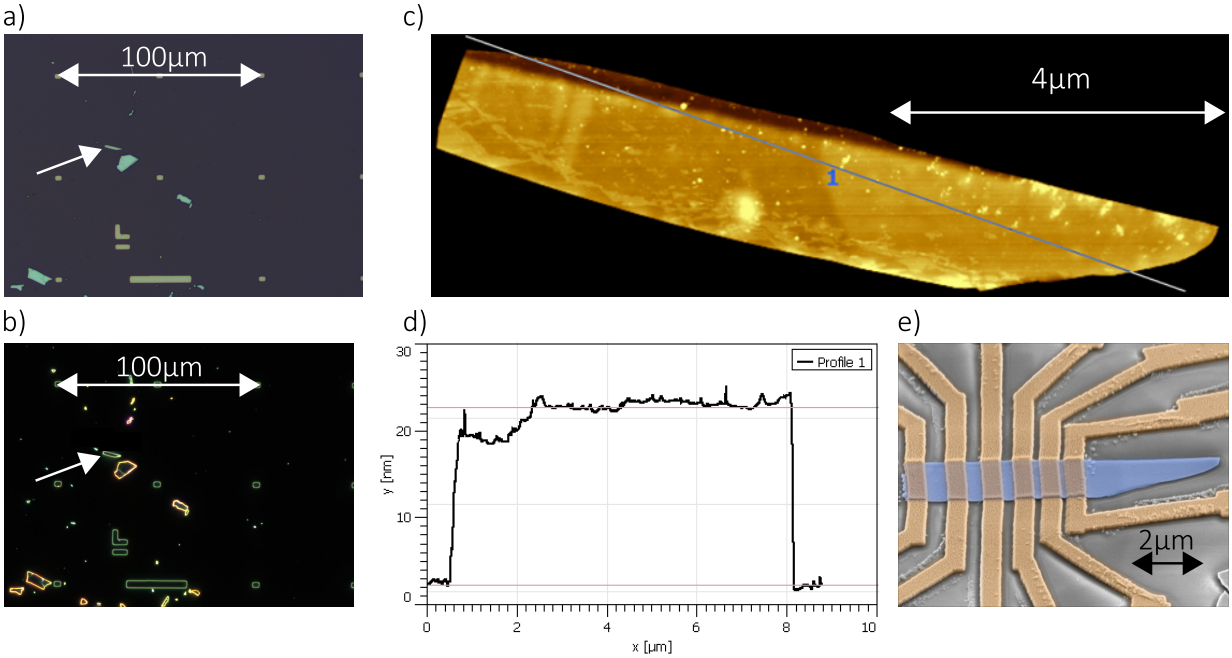

Figure 3.2. – Steps to select and contact a flake of crystal that has been exfoliated on a silicon/silica substrate. a) Bright field optical picture of the substrate with some flakes (light grey) dispersed around a prepared substrate with a patterned markerfield (gold). b) Dark field image of a). We recognize the thin flakes by their light green color. The white arrow points at one thin flake. c) Atomic force microscope image of the selected flake of a-b). d) Line profile taken along the blue line in c). The flake is 20 nm thin and has a surface with a low roughness. e) Scanning electron microscope image of the flake with false colors after lithography.

2 Production of mesoscopic devices

In order to fabricate a Josephson junction on a micrometer scale flake, a raw crystal is gradually cleaved and, hence, exfoliated onto a substrate. Superconducting leads are then placed onto the obtained thin flakes. In the following section, we explain in detail the different steps of the fabrication process starting with the crystal growth. Afterwards, the exfoliation and metal deposition are described putting especially the focus on our improvements to obtain high quality devices.

2.1 Crystal growth

Bi_2Se_3 crystals were synthesized by congruent melting growth method with high purity elements (5N) [2]: Bi and Se in an evacuated quartz tube. The tube is heated up to 770 °C then slowly cooled down to room temperature. The grown material is a boule of approximately 1 cm^3 that is easily cleavable (cf figure 3.1).

We have optimized the growth of BSTS. The details are given in chapter 2.

2. N is the number of 9 in the percentage of composition 99.99...%

2.2 Preparation of the substrate

We used degenerate Silicon substrate with 280 nm of thermal SiO_2. In order to precisely locate any device on the substrate, we have deposited a grid of gold markers that are visible in figure 3.1c. This marker-field has been lithographed by using an interferometric moving stage in order to have a precision better than 100 nm in the location of the device. We have used alternatively laser or electron beam lithography.

After this step of lithography, we clean the substrate before exfoliation. The inorganic dirt are removed by 10 minutes ultrasounds in a bath of acetone followed by a same duration bath of isopropanol. Once the substrate is well dried with N_2 , it is dipped in a Piranha solution (H_2SO_4/H_2O_2 3:1) for 5 minutes to remove all the organic residues of resist.

The substrates have to be stored in DI water and dried only right before the exfoliation of the crystal.

2.3 From chunk to flake

All the bismuth based topological insulators, are layered materials. Each layer is composed of five atoms coupled by covalent bond forming a quintuple layer (see chapter 2 figure 2.1). Two quintuple layers are coupled by van-der-Waals bond that make them easily cleavable perpendicularly to the c-axis. We use this property similar to the one of graphene to exfoliate our bismuth based compounds following the scotch-tape technique (see figure 3.1). This method consists in gradually cleaving the raw material using the glue of a scotch tape and then pressing the latter on a substrate. It gives flakes of thickness ranging from few nm to 1 µm randomly distributed on the substrate.

Once the exfoliation executed right after the piranha cleaning, we locate thin flakes with dark field mode of an optical microscope (see figure 3.2). We can discriminate thin flakes from their light green color (see figure 3.2b)

After optical search, we examine all selected flakes by atomic force microscopy (see figure 3.2c). Only flakes with atomically flat surfaces are suitable to build samples. In average, we find optically about 30 flakes per substrate. After AFM characterization, we select from 4 to 10 flakes for the next steps of fabrication.

2.4 Lithography and deposition of the leads

We use optical images of the flakes to determine their positions with respect to the designed markerfield. This step sets the precision of the alignment between the lithography and the flakes, which is of the order of 100 nm.

Once the design prepared on all the selected flakes, we use a standard electron-beam lithography technique with a PMMA 4% resist. The development is done with IPA/DI water (1:3) during 1min30s at room temperature. The deposition of the superconductor is performed by e-gun evaporation at a pressure of 1×10^{-7} mbar for the vanadium and

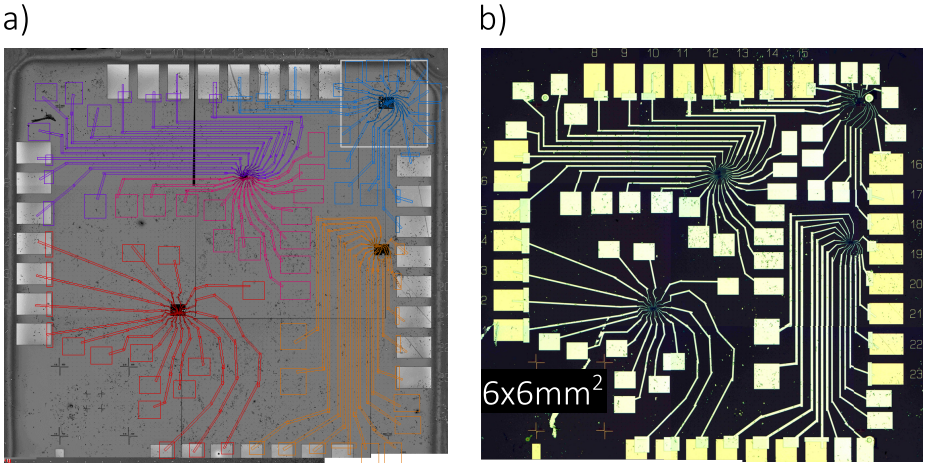

Figure 3.3. – a) Image of the design before lithography of the superconducting leads. b) Image of the sample after lithography steps.

around 1×10^{-6} mbar for the indium oxide. The lift-off is done in a bath of acetone overnight.

A typical sample after lithography process with five flakes contacted is shown in figure 3.3. On each flake there are two junctions and one Hall-bar. In total, we have hence patterned 75 lines and their associated pads to micro-bond the sample to the cryostat.

3 Superconducting contact on bismuth based topological insulators

We have studied different processes in order to optimize the interface quality between the crystal and the superconducting leads. These processes included different materials and surface preparations. The table 3.1 summarizes all samples of Bi_2Se_3 on which we have fabricated Josephson junctions.

We observe from the bibliography in section 1.1 that superconductors with high critical magnetic field (like amorphous indium oxide or NbN [17, 144]) have not been used yet to fabricated Josephson junctions on these bismuth based compounds. Moreover, we have access to vanadium that also has not been yet used.

We have used three types of superconductor : amorphous indium oxide, vanadium and aluminum.

Amorphous indium oxide (InO_x) is a disordered superconductor with a low critical temperature $T_c \approx 3\,K$, a superconducting energy gap $\Delta_{InO_x} = 0.55\,meV$ and a critical field that can be up to $14\,T$ [144].

Vanadium is a refractory metal with a higher critical temperature $T_c \approx 5\,K$ but a lower critical field $H_c \approx 0.28\,T$ and a superconducting energy gap $\Delta_V = 0.8\,meV$ [96, 156].

Aluminum is a superconductor with a low critical temperature $T_c = 1.6\,K$ and a low critical field $H_c \approx 0.01\,T$ [37].

From table 3.1, we observe that it is not a straightforward process to obtain a superconducting proximity effect in such topological insulator. If we do not etch the crystal before depositing the superconductor, only palladium is able to produce a superconducting coupling between the crystal and indium oxide.

During the different attempts, we have encountered two samples in which the contact presents a tunnel barrier (see figure 3.4a-b). This type of tunnel contact allows to probe the superconducting energy gap of the electrodes which has been evaluated to $\Delta_{\mathrm{InO_x}} \approx 0.7\,\mathrm{meV}$.

Preparing the surface of the crystal by a short argon etching (250 V excitation during 12 s), is the only way to have a high transparency contact with a superconducting coupling between vanadium and bismuth based topological insulators. In that case, a contact layer of titanium is not necessary. Using a titanium layer actually reduces the superconducting coupling.

The best recipe we have found is to etch in-situ with ion argon plasma and directly deposit vanadium and protect it with few nanometers of gold. The high quality contact leads to a superconducting proximity effect into the crystal and a supercurrent can set in (see figure 3.4c-d).

Sample	Crystal	Surface preparation	Contact material	Interface / I_c	L (nm)
LC046	Bi_2Se_3	∅	InO_x	No contact	
LC058	Bi_2Se_3	∅	InO_x	No contact	
LC059	Bi_2Se_3	∅	Pd/InO_x	$I_c = 60\,\mathrm{nA}$	200
LC060	Bi_2Se_3	∅	Ti/V/Au	No proximity effect	
LC066	Bi_2Se_3	∅	InO_x	Tunnel contact	
LC067	Bi_2Se_3	∅	Ti/Al	No contact	
LC079	Bi_2Se_3	RIE O_2 etching	InO_x	Tunnel contact	
LC081	Bi_2Se_3	IBE Ar etching	Ti/V/Au	$I_c = 1\,\mu\mathrm{A}$	450
LC099	Bi_2Se_3	IBE Ar etching	Ti/V/Au	$I_c = 450\,\mathrm{nA}$	200
LC106	Bi_2Se_3	IBE Ar etching	V/Au	$I_c = 7.5\,\mu\mathrm{A}$	150
LC092	$BiSbTeSe_2$	IBE Ar etching	Ti/V/Au	Small proximity effect, no I_c	400
LC111	$BiSbTeSe_2$	IBE Ar etching	V/Au	Small proximity effect, no I_c	150
LC134	$BiSbTeSe_2$	IBE Ar etching	V/Au	$I_c = 25\,\mathrm{nA}$	70

Table 3.1. – Summary of the junctions built on Bi_2Se_3 with different types of contact recipes: surface preparation and contact materials. RIE stands for reactive ion etching and IBE for ion beam etching. If we have a supercurrent, L is the length and I_c the critical current in the low temperature limit of the best Josephson junction of the sample. If not, we describe the type of interface there is between the leads and the flake.

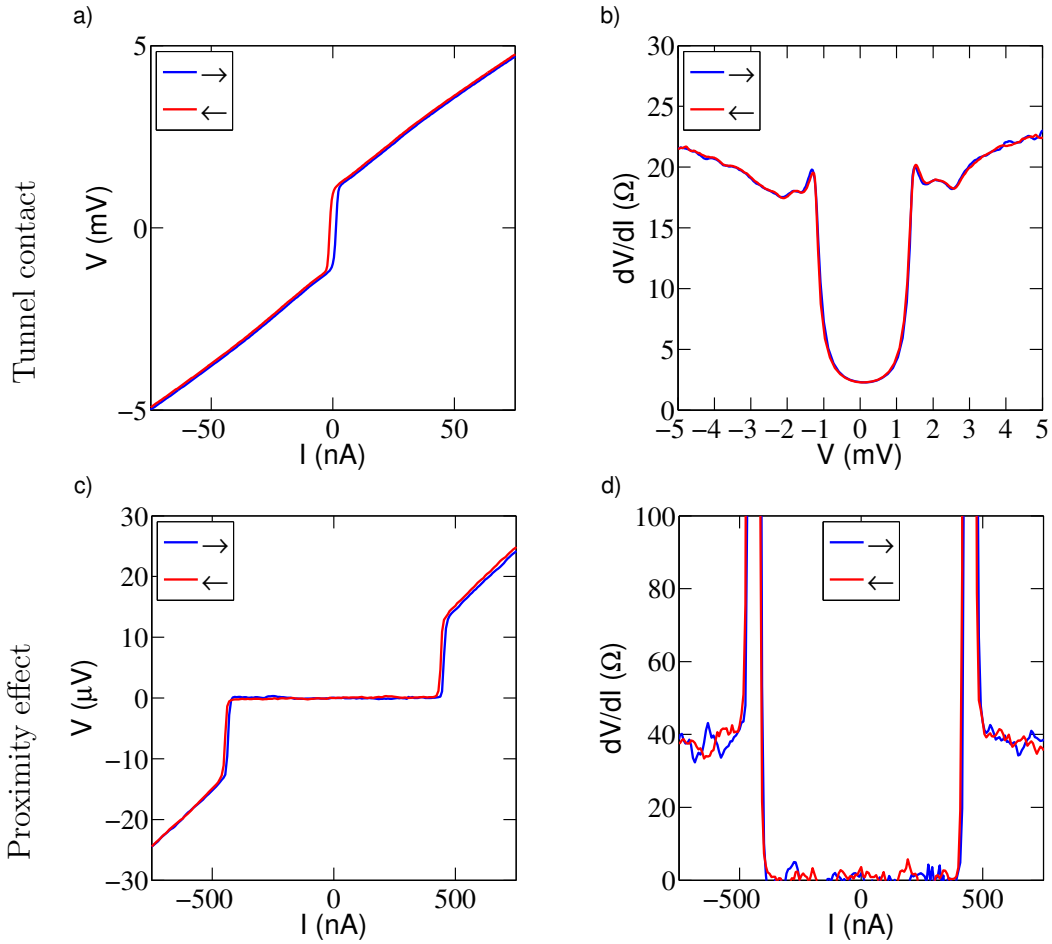

Figure 3.4. – Example of voltage-current characteristics a,c) and differential resistance b,d) of two junctions. The top line (a-b: sample LC079) displays a junction with a low quality contact that has produced a tunnel contact. The superconducting gap is half of the dip width in the differential resistance: $2\Delta_{InO_x} \approx 1.5\,\mu eV$. The bottom line (c-d: sample LC099) presents a junction in which we managed to induce superconductivity with a critical current of 450 nA.

Summary

In this chapter we have presented the fabrication process for our Josephson junction with a good interface on a bismuth-based topological insulator. We have first drawn a state of the art on the previous junctions made on the two materials Bi_2Se_3 and $BiSbTeSe_2$. We have noticed that vanadium has not been used yet as superconductor to produce junctions on such materials.

We have presented the protocol used during this thesis to exfoliate a layered crystal and then select and contact a nanometer range thin flake from it.

Finally we have reported on the optimization of the contact quality between the superconductor and Bi_2Se_3. The best recipe implies to in-situ argon etch the surface of the crystal before depositing vanadium.

Chapter 4

Topological Josephson junctions

A Josephson junction (JJ) consists in a weak link between two superconducting leads (S) through which a dissipationless current can flow without voltage drop [90, 91]. The weak link can be an insulating layer (I), a constriction (c), a normal metal (N) or a topological insulator (TI). The conventional Josephson junction (S-I-S, S-c-S and S-N-S) has been widely experimentally and theoretically investigated since its prediction by Brian D. Josephson in 1962. Since then the fundamental relation between the supercurrent through the junction and the phase difference between the left and right superconducting leads was believed to be a 2π periodic function ($I_S(\phi) = I_c \sin\phi$). Only recently with the discovery of topological insulators, the uniqueness of this periodicity is put in doubt.

Indeed, theory predicts that a Josephson junction in which the weak link is the surface state of a 3D topological insulator hosts a 4π periodic Andreev bound state (ABS) [63].

In this chapter, we first introduce the conventional Josephson junctions, which will be essential for the basic analysis of the experimental data. Then we develop the recent theories associated with Josephson junctions made of topological insulators: the so-called topological Josephson junction (TJJ). We derive part of this theoretical prediction based on ref [63, 107, 160]. First we show how a 3D topological insulator in contact with a conventional superconductor induces p-wave superconductivity. Then we discuss different possibilities to experimentally detect these topologically protected 4π periodic ABSs (4π-tABS). We establish the state of the art on the detection of the 4π periodic ABS with the AC Josephson effect. Finally, we review the physical phenomena called poisoning whose effect can alter the visibility of the 4π periodic ABS in DC measurements but also when probing the AC Josephson effect.

1 Introduction to Josephson junctions

We first introduce the Josephson effects and then discuss different transport regimes and their associated characteristic length scales. (inspired by [42, 114])

1.1 Basic phenomena in a Josephson junction

1.1.1 DC and AC Josephson effects

The simplest way to describe a Josephson junction [56] is by using a perturbative approach and define a weak coupling coefficient K between the two superconducting leads S_j, with j referring to lead 1 or 2 (see figure 4.1). Each lead is defined by its superconducting complex order parameter Ψ_j. This order parameter is a complex function that is uniform inside a homogeneous superconductor and vanishes outside the material over a finite length. When two superconductors are brought close enough, their order parameters can overlap leading to a Josephson coupling. The dynamics of the order parameters Ψ_1 and Ψ_2 is governed by the coupled Schrödinger equations [91]:

$$\begin{cases} i\hbar\frac{\partial\Psi_1}{\partial t} = \mu_1\Psi_1 + K\Psi_2 \\ i\hbar\frac{\partial\Psi_2}{\partial t} = \mu_2\Psi_2 + K\Psi_1 \end{cases} \tag{4.1}$$

with μ_j being the chemical potential of the side j, and $\hbar = \frac{h}{2\pi}$ the normalized Planck constant.

A solution of Eq. (4.1) reads :

$$\Psi_j = \sqrt{n_j}\, e^{i\phi_j} \tag{4.2}$$

with n_j the density of Cooper pairs and ϕ_j the phase of the superconducting state . We define the phase difference $\phi = \phi_2 - \phi_1$ and the voltage difference V between the two sides by $\mu_2 - \mu_1 = qV$ with $q = -2e$ the carrier charge. The supercurrent is defined as the number of Cooper pairs transferred from one side to the other by unit of time : $I_S = -2e\frac{dn_1}{dt}$. By assuming quasi-equilibrium, $n_1 \approx n_2$, we obtain the celebrated AC & DC Josephson relations :

$$\frac{d\phi}{dt} = \frac{2eV}{\hbar} \qquad \text{AC} \tag{4.3}$$

$$I_S(\phi) = I_c \sin\phi \qquad \text{DC} \tag{4.4}$$

The critical current I_c defines the maximum supercurrent that the junction can withstand before transitioning to the normal state. $I_S(\phi)$ is the fundamental relation of a JJ that relates the supercurrent flowing between the two leads to the phase difference across the JJ, also called the current-phase relation (CPR).

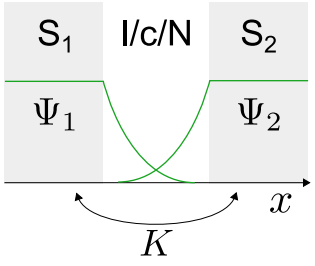

Figure 4.1 – Schematic of a Josephson junction. The order parameters of each lead decreases outside the superconducting region. The overlap between Ψ_1 and Ψ_2 defines the coupling constant K.

Current phase relation From Eq. (4.4), we see that the phase gradient is the driving force to supercurrent. The CPR has several straightforward, but important properties [71]:

— The current phase relation is 2π periodic.

— The supercurrent is an odd function with respect to the phase difference: $I_S(\phi) = -I_S(-\phi)$

— At a phase difference $\phi = 0, \pi$ there is no supercurrent.

In the case of strong coupling between the two leads, Eq. (4.1) is no more valid because higher order terms are involved. The CPR is no-longer sinusoidal and contains higher harmonics [1] :

$$I_S(\phi) = \sum_n I_{c,n} \sin(n\phi) \tag{4.5}$$

The aforementioned properties of the CPR have been irrevocably established since the discovery of the Josephson junction. We will see however that the discovery of topological insulators has led to a paradigm change on the 2π periodicity of this CPR.

AC Josephson effect Equation Eq. (4.3) shows that if we apply a DC voltage between the two leads, the phase will increase linearly with time and the supercurrent will oscillate at a frequency f_J determined by the applied voltage:

$$I_S(t) = I_c \sin(2\pi f_J t) \tag{4.6}$$

with $f_J \equiv \frac{2eV}{h}$ the Josephson frequency. This effect precisely relates voltage with frequency and is used as a frequency standard for metrology [19].

1.1.2 Andreev Bound States

We now address the physics of S-N-S Josephson junctions. For that we need to introduce a new effect that takes place at the interface between a normal metal and a superconductor: at an S-N interface, an electron coming from the N side with an energy below the superconducting gap (Δ) of the leads cannot enter the superconductor as a single electron due to the zero density of states (DOS) at this energy. Instead an electron is transmitted through the interface by a process called Andreev reflection [8, 45, 146], in which a hole of opposite momentum is backreflected into the N part and a Cooper pair is transmitted into the S region (cf figure 4.2). As this effect is present at both interfaces with the same coherent electron / hole, a bound state sets in between the two leads: the so-called Andreev Bound State (ABS) [24].

ABSs are key elements to describe supercurrent in a JJ. When occupied, each ABS of energy-phase relation $E(\phi)$, is a conduction channel that can carry a supercurrent at zero temperature given by [71]:

$$I_S(\phi) = \frac{2e}{\hbar} \frac{\partial E(\phi)}{\partial \phi} \tag{4.7}$$

1. This possible expression depicts $2\pi/n$ periodic components. The total sum is still 2π periodic.

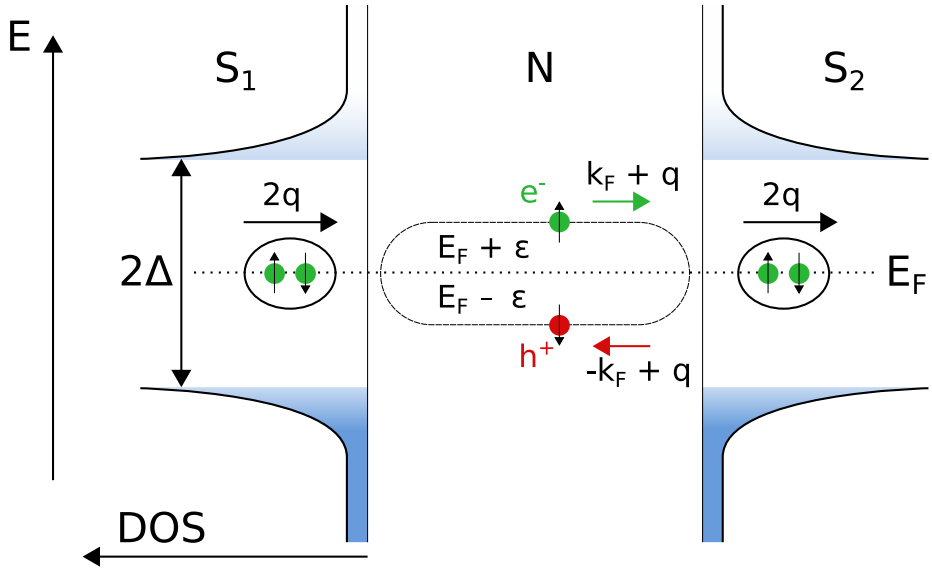

Figure 4.2. – Schematic of an SNS Josephson junction. The two superconducting leads have a gap (2Δ) in their density of states (DOS). The Andreev reflection on the right interface is as followed: in the weak link, a right moving electron (in green) has an energy $E_F + \epsilon$ and a wave vector $k_F + q$. It is back reflected as a hole (in red) with opposite spin, an energy $E_F - \epsilon$ and a wave vector $-k_F + q$. At the same time, a Cooper pair is transmitted into the S part. This phenomenon happening at both interfaces creates a coherent state called Andreev bound state and carries a total charge of $2e$ per cycle.

The critical current associated with this current-phase relation of a single channel is defined as the maximum value :

$$I_c = \max |I_S(\phi)|. \tag{4.8}$$

This physical quantity is easily accessible experimentally by standard DC transport measurement.

1.1.3 Transport regimes of a Josephson junction

The ABSs spectrum depends on the regime in which the superconducting transport sets in. That is why we want to focus on the different regime of transport in which a Josephson junction can be classified.

The phase coherence length l_ϕ is the mean distance over which an electron can travel before loosing its phase coherence. It corresponds usually to the inelastic mean free path. At low temperature this distance can be much greater than the elastic mean free path. Electrons can indeed elastically scatter multiple times before loosing their phase coherence through inelastic processes(phonons, electron-electron interaction, magnetic impurities). l_ϕ is the relevant length scale when talking about coherent effects in mesoscopic physics.

Following the discussion of Blanter and Büttiker [22], we consider a coherent mesoscopic system of length L connected to two leads : As long as the size of the conductor is shorter than the phase coherence length, it is possible to describe a conductor by a set of channels

of conduction with transmission coefficient $\mathcal{T}_\mathrm{i}$. The set of coefficients $\{\mathcal{T}_\mathrm{i}\}$ is called the personal identification number and defines the transport properties of any conductor of length $L < l_\phi$ [22]

In order to have superconducting transport between the two leads, electrons have to be coherent when traveling from the left to the right lead. Hence the condition $L < l_\phi$ is fulfilled as soon as we consider a Josephson junction.

The supercurrent transport of an SNS JJ can be divided into 2x2 different regimes: long/short and diffusive/ballistic. Each regime exhibits different energy-phase dispersion of the ABS.

Let us first define length scales that characterize these different regimes: ξ_S^N the superconducting coherence length in the normal part and l_e the elastic mean free path.

l_e is the average distance between two scattering centers in a material. When a device is smaller than l_e then the electron transport is *ballistic*. Conversely, when $L > l_\mathrm{e}$, then the electron transport is *diffusive* due to the multiple scattering [2].

ξ_S^N is the characteristic length over which the superconducting order parameter extends in the N region. When a junction is smaller (greater) than ξ_S^N, then it is defined as a *short* (*long*) junction. In a ballistic metal $\xi_\mathrm{S}^N = \frac{\hbar v_\mathrm{F}^N}{\Delta}$ whereas in a diffusive metal, $\xi_\mathrm{S}^N = \sqrt{\frac{\hbar D^N}{\Delta}}$ with v_F^N the Fermi velocity, D^N the diffusion coefficient of the N part and Δ the superconducting gap of the S leads.

ξ_S^S is the standard superconducting coherence length. It corresponds to the physical extension of a Cooper pair in the leads.

These different regimes are summarized in the following table:

	Short	Long
Ballistic	$L < l_\mathrm{e}, \xi_\mathrm{S}^N$	$\xi_\mathrm{S}^N < L < l_\mathrm{e}$
Diffusive	$l_\mathrm{e} < L < \xi_\mathrm{S}^N$	$l_\mathrm{e}, \xi_\mathrm{S}^N < L$

In the following section, we will use the formalism that consider transport as a set of channels with transmission coefficient $\{\mathcal{T}_\mathrm{i}\}$ (so-called Landauer-Büttiker formalism) that is valid in three out of four regimes (darken cells in previous table). For the long diffusive regime, that we develop in section 1.3, a different approach is more appropriate.

1.1.4 Critical current at zero temperature

At zero temperature, the amplitude of the critical current depends on the resistance of the normal metal R_N. In fact, the product $e \cdot R_\mathrm{N} \cdot I_\mathrm{c}$ gives an energy scale that is related to the energy gap or the Thouless energy of the junction. The Thouless energy is the energy scale that governs the energy of the ABSs in the regime of long junction. A precise definition of E_th is given in subsection 1.3.3. Here, we review the theoretical prediction for the zero temperature $e \cdot R_\mathrm{N} \cdot I_\mathrm{c}$ product in the four transport regimes.

2. Even in the case of ballistic transport, there can be a barrier of potential between the device and the lead. Hence the transmission coefficient is not necessary equal to 1 in ballistic junctions.

	Short		Long		
Ballistic	$eR_{\mathrm{N}}I_{\mathrm{c}} = \pi\Delta$	[103]	$eR_{\mathrm{N}}I_{\mathrm{c}} = E_{\mathrm{th}}$	with $E_{\mathrm{th}} = \hbar v_{\mathrm{F}}/L$	[102]
Diffusive	$eR_{\mathrm{N}}I_{\mathrm{c}} = 2.07\Delta$	[104]	$eR_{\mathrm{N}}I_{\mathrm{c}} = 10.82E_{\mathrm{th}}$	with $E_{\mathrm{th}} = \hbar D/L^2$	[51]

This estimation of the critical current at zero temperature will be used to confirm the transport regime and estimate the Thouless energy of the junctions measured in the experimental chapters (6 & 7).

1.2 Andreev bound states in ballistic short junctions

The regime of coherent transport ($L < l_\phi$) allows one to use the Landauer Büttiker formalism which supposes independent conduction channels. Each channel defined in the normal regime (without superconducting proximity effect) is able, once brought in contact with the S leads, to produce a resonant Andreev bound state (ABS) close to the Fermi energy. In this section we develop the Bogoliubov-de-Gennes equations that enables to describe the superconducting proximity effect in each conduction channel and find the energy dispersion of the ABSs.

1.2.1 Introduction to the Bogoliubov-de-Gennes equations

When the coupling between the two S leads is strong, the system cannot be described in a perturbative approach (as in section 1.1.1). The density of states (DOS) of the N part is strongly affected by the contact to the S part and vice-versa. The Bogoliubov-de-Gennes equations (BdG) provides the useful framework to study an SNS junction and to calculate the induced ABS [8, 16, 44]. These equations describe a single conduction channel defined by the two components wave function Ψ which contains the excitations of electron-like(u) and hole-like(v) quasi-particles:

$$\Psi = \begin{pmatrix} u \\ v \end{pmatrix} \tag{4.9}$$

u and v depend a priori on the energy E and position r. In one dimension, the evolution of Ψ is governed by the coupled Schrödinger equations [1]:

$$\begin{cases} Eu(x,E) = \left(-\frac{\hbar^2}{2m}\frac{d^2}{dx^2} + V(x) - E_{\mathrm{F}}\right) u(x,E) + \Delta(x)v(x,E) \\ Ev(x,E) = \left(-\frac{\hbar^2}{2m}\frac{d^2}{dx^2} + V(x) - E_{\mathrm{F}}\right) v(x,E) + \Delta^*(x)u(x,E) \end{cases} \tag{4.10}$$

with $\Delta(x)$ the position dependent pair potential, Δ^* its complex conjugate, m the effective mass of an electron, $V(x)$ the position dependent electrical potential and E_{F} the Fermi level. This approach enables to find the spatial variation of the pairing potential $\Delta(x)$ and the electrical potential $V(x)$ self-consistently [7]. Here we will not develop this self-consistent determination.

In the following we discuss some applications and examples of the BdG equations.

Uniform 1D ballistic superconductor In the case of a uniform one dimensional ballistic superconductor, we can separate the fast oscillation ($e^{ikx-i\frac{Et}{\hbar}}$) from the slow variations in space of the electron and hole components. Then the BdG equations admit the following solutions for $\Delta(x) = \Delta_0 e^{i\phi_S}$, $V(x) = 0$ with ϕ_S being the superconducting phase of the superconductor :

$$u = u_0 e^{ikx-i\frac{Et}{\hbar}} \quad , \quad v = v_0 e^{ikx-i\frac{Et}{\hbar}} \tag{4.11}$$

with k the wave vector of the quasi-particles and E their energy. The solution gives the usual energy dispersion of a superconductor with the opening of a superconducting gap Δ_0 in the density of states at the Fermi level E_F:

$$E = \pm\sqrt{\left(\frac{\hbar^2 k^2}{2m} - E_F\right)^2 + \Delta_0^2} \tag{4.12}$$

By inverting the energy dispersion, one finds the two possible wave vectors corresponding to the quasi-electron excitation k_+ above the Fermi energy and the quasi-hole excitation k_- below the Fermi energy :

$$k_\pm = k_F\sqrt{1 \pm \frac{\Delta_0}{E_F}\sqrt{\left(\frac{E}{\Delta_0}\right)^2 - 1}} \tag{4.13}$$

We notice from Eq. (4.12) that quasi-electron and quasi-hole are symmetric in energy. This symmetry will be again visible when studying the ABSs of a Josephson junction.

Interface between a superconductor and a normal metal In the case of an S-N interface, one can solve the BdG equations in the ballistic regime for which an incoming electron (Ψ_i) from the N part is either back reflected (Ψ_r) or transmitted(Ψ_t) to the S part (cf figure 4.3):

$$\begin{cases} \Psi_i = \left(1;0\right) e^{-ik_+^N x} \\ \Psi_r = a\left(0;1\right) e^{ik_-^N x} + b\left(1;0\right) e^{-ik_+^N x} \\ \Psi_t = c\left(u;v\right) e^{ik_+^S x} + d\left(v;u\right) e^{-ik_-^S x} \end{cases} \tag{4.14}$$

where k^N (k^S) corresponds to the wave vector of electrons k_+^N or holes k_-^N propagating in the N part (S part).

Using the Andreev approximation for $E_F \gg \Delta$, all wave vectors are considered to be close to the Fermi wave vector :$k_+^N \approx k_-^N \approx k_+^S \approx k_-^S \approx k_F$. If there is no barrier at the interface, then Ψ and its spatial derivative $\frac{d\Psi}{dx}$ are continuous. These boundary conditions give a perfect retro-reflection of

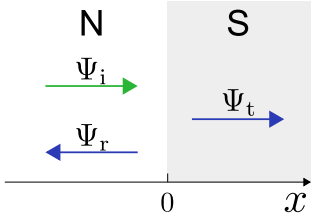

Figure 4.3. – Schematic of an SN interface. An incoming electron (green) can be back-reflected or transmitted.

the incoming electron into a back-reflected hole:

$$\begin{aligned} a &= e^{-i\phi_S}\left(\frac{E}{\Delta_0} - i\sqrt{1-\frac{E^2}{\Delta_0^2}}\right) \\ b &= c = d = 0 \end{aligned} \qquad (4.15)$$

with ϕ_S being the superconducting phase of the S side. This perfect retro-reflection illustrates a perfect Andreev reflection meaning the perfect transmission of a Cooper pair into the S part. Eq. (4.15) shows that the back-reflected hole is coherent with the incoming electron with an extra phase

$$d\phi = -\phi_S - \arccos(E/\Delta_0) \qquad (4.16)$$

We notice that for an incoming electron at zero energy, the dephasing is $d\phi = -\phi_S - \pi/2$. When the energy of the incoming electron is higher than the superconducting gap, the Andreev reflection process is not possible. In that case, energies of the quasi-particles are not discretized any-more and the dispersion relation is described by a continuum of states.

SNS junction In this subsection we review the properties of ABSs in the Landauer-Büttiker formalism by describing the normal part by a single conduction channel with a perfect transmission ($\mathcal{T}_i = 1$), then we introduce a scattering center in the transport channel ($\mathcal{T}_i \neq 1$) and finally we find a general solution for a Josephson junction.

In the case of an SNS junction, the Andreev reflection process is repeated on both interfaces. This means that the same coherent quasi-particle travels back and forth inside the N part making several loops. In order for this quasi-particle to generate a supercurrent, the total phase of a single loop has to be a multiple of 2π to produce constructive interferences.

Ballistic transport In the case of a one dimensional ballistic N part, the interference relation of channel i gives :

$$2\pi n = (k_+^N - k_-^N)L + \phi - 2\arccos(E_i/\Delta) \qquad (4.17)$$

with L being the total length of the N part and n an integer. The left part of Eq. (4.17) describes the constructive interference condition, the right part contains (1) the dephasing that the electron and the associated counter-propagating hole acquire by traveling in the N part over a distance L, (2) the two dephasings at the left and right interfaces according to Eq. (4.16).

One scattering center According to [13], if a scattering potential V_0 is present inside the junction at position $x = a$: $V(x) = V_0\ \delta(x-a)$, ϕ in equation Eq. (4.17) is replaced by α following :

$$\cos\alpha = \mathcal{T}_i\cos\phi + (1-\mathcal{T}_i)\cos\left(\frac{(L-2a)}{\xi_S^N}\frac{2E_i}{\Delta}\right) \qquad (4.18)$$

with $\mathcal{T}_\mathrm{i}$ the transmission probability of the channel i that depends on the scattering potential V_0. Replacing ϕ by α in Eq. (4.17) gives:

$$2\pi n = (k_+^N - k_-^N)L - 2\arccos(E_\mathrm{i}/\Delta) + \arccos\left(\mathcal{T}_\mathrm{i}\cos\phi + (1-\mathcal{T}_\mathrm{i})\cos\left(\frac{(L-2a)}{\xi_\mathrm{S}^N}\frac{2E_\mathrm{i}}{\Delta}\right)\right) \tag{4.19}$$

This equation does not have an analytical solution for the general case but would need to be solved for each regime of transport defined in section 1.1.3. In this section we only focus on the case of short Josephson junctions ($L \ll \xi_\mathrm{S}^N$). The approximations associated with the other transport regimes are used in section 1.3.

1.2.2 Energy-phase and current-phase relations

The knowledge of the energy-phase relation of the ABS allows one to deduce the current-phase relation from equation Eq. (4.7). In this subsection we calculate those two relations in the case of short junctions ($L \ll \xi_\mathrm{S}^N$), using the Andreev approximation. Eq. (4.19) simplifies to :

$$E_\mathrm{i}(\phi) = \pm\Delta\sqrt{1-\mathcal{T}_\mathrm{i}\sin^2(\phi/2)} \tag{4.20}$$

For a given transmission $\mathcal{T}_\mathrm{i}$, there are two ABSs available denoted $|-\rangle$ and $|+\rangle$ of opposite energies E^- and E^+ [3]. Both $|-\rangle$ and $|+\rangle$ can be empty of full of electrons [4] (cf figure 4.4). When both states are full or empty, the total energy of the system is zero and no net supercurrent flows through the junction.

There is a gap in the energy dispersion of the ABSs between $|-\rangle$ and $|+\rangle$ that depends on the phase difference $E_\mathrm{g}(\phi)$. This gap is minimum at $\phi = \pi$: $E_\mathrm{g}^{min} = 2\Delta\sqrt{1-\mathcal{T}_\mathrm{i}}$. This minimum gap is non zero because of the non perfect transmission: the two levels mix and an avoided crossing opens a gap at $\phi = \pi$. The opening of this gap leads to a 2π periodicity of each state.

In the Landauer-Büttiker formalism, a normal metal is fully described by its set of transmission channels $\{\mathcal{T}_\mathrm{i}\}$ [109]. As the ABS do not mix the normal conducting channels, we can apply the sum over all normal channels. Hence, using equation Eq. (4.7), the total supercurrent across the junction reads:

$$I_\mathrm{S} = \pm\sum_i \frac{2e\Delta}{\hbar}\frac{\mathcal{T}_\mathrm{i}\sin\phi}{\sqrt{1-\mathcal{T}_\mathrm{i}\sin^2(\phi/2)}} f(E_\mathrm{i}) \tag{4.21}$$

The energy dispersion and supercurrent of a single ABS are shown in figure 4.5 for different values of transmission $\mathcal{T}_\mathrm{i}$.

At zero temperature, only the energy states below E_F (ground state $|-\rangle$) are populated and the total current-phase relation simplifies to

3. Note the same symmetry of the states around zero energy as for the electron/hole symmetry
4. On top of the two available energy levels, both of them are spin degenerate.

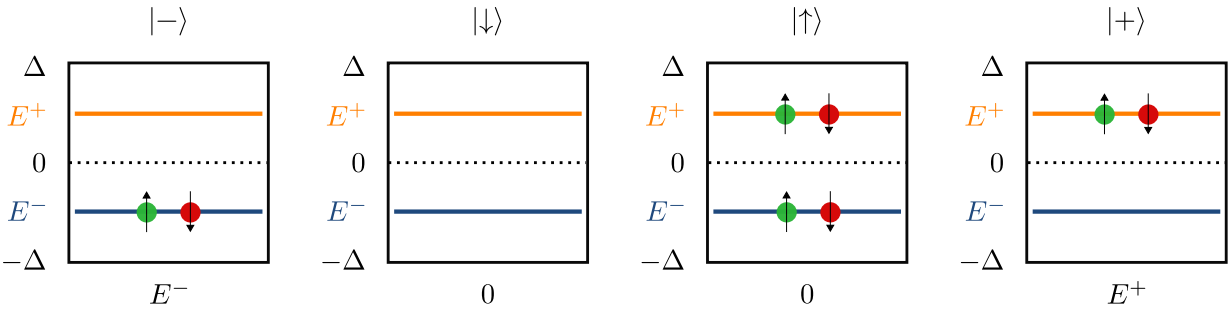

Figure 4.4. – Schematic of the possible occupancy of two Andreev bound states. For a given phase ϕ, E^- corresponds to a right moving electron and a left moving hole, whereas E^+ is a state where the electron moves to the left and the hole to the right. If the states E^- and E^+ are both occupied or empty, then the total energy and supercurrent are zero. Inspired by [27].

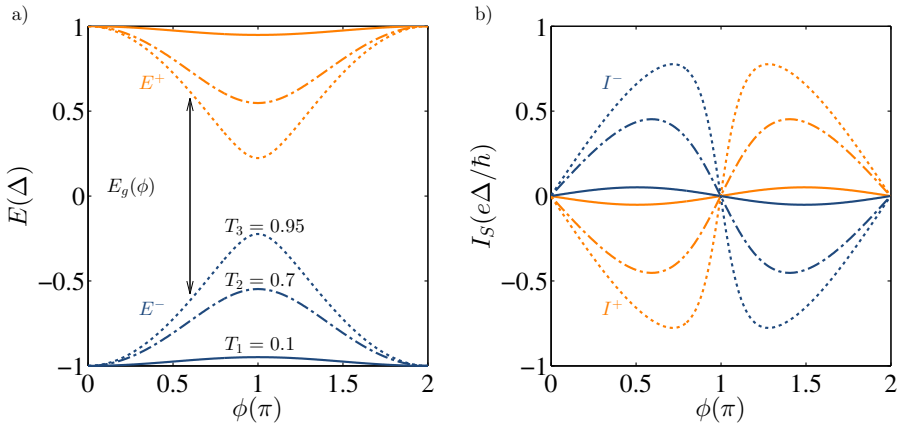

Figure 4.5. – a) Energy dispersion of ABSs of a short JJ for different transmission $\mathcal{T}_\mathrm{i}$. The zero energy corresponds to the Fermi energy. b) Supercurrent carried by the ABSs of a).

$$I_\mathrm{S} = \sum_i \frac{2e\Delta}{\hbar} \frac{\mathcal{T}_\mathrm{i} \sin\phi}{\sqrt{1 - \mathcal{T}_\mathrm{i} \sin^2(\phi/2)}} \tag{4.22}$$

We see in figure 4.5 ,that for $T = 0$ and $\phi = \pi$, the supercurrent is zero for every ABS of non perfect transmission ($\mathcal{T}_\mathrm{i} < 1$).

In the case of perfect transmission ($\mathcal{T}_\mathrm{i} = 1$, not shown in figure 4.5), the gap between E^+ and E^- vanishes and at a phase difference of $\phi = \pi$, both states are available. Therefore their resulting supercurrents compensate each other and no net supercurrent goes through the junction. If the transmission is almost perfect ($\mathcal{T}_\mathrm{i} \approx 1$), at finite temperature, some lower energy states can jump to the excited states due to Landau-Zener transitions [108, 186]. This aspect is discussed in detail in Appendix C.

1.3 Andreev bound states in other transport regimes

Now that we have reviewed the simple case of a short ballistic Josephson junction, in this section we describe the changes that arise in the three other transport regimes.

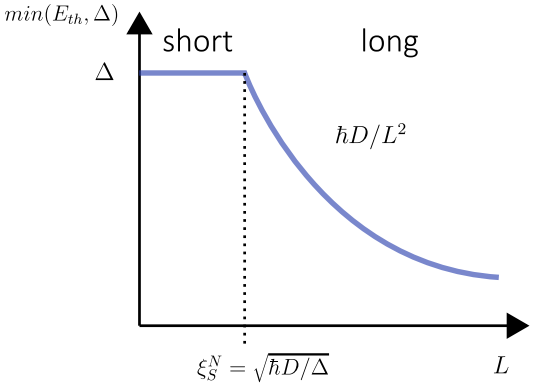

Figure 4.6. – Dependence of the governing energy scale of the ABSs versus the length of the junction in a diffusive Josephson junction. For $L < \xi_{\mathrm{S}}^N$ ($L > \xi_{\mathrm{S}}^N$), the junction is short (long).

1.3.1 ABS in short diffusive junctions

Experimentally, determining the personal identification number of a device with few channels (like an atomic point contact) can be done by fitting the current-voltage characteristic [153]. However, this technique is not adapted when the device has more channels. The transmission distribution of the set of channels in a diffusive junction is given by [50, 130]:

$$P(\mathcal{T}) = \frac{\pi}{2e^2 R_{\mathrm{N}}} \frac{1}{\mathcal{T}\sqrt{1-\mathcal{T}}} \tag{4.23}$$

We see that most channels have either a high transmission close to 1, or a poor transmission close to 0. An example of the energy dispersion of the ABSs in the case of a short ballistic JJ is shown in figure 4.7 c).

1.3.2 ABS in long ballistic junctions

The regime of long ballistic JJ has been theoretically studied by different groups [13, 15, 83, 102]. The basic idea of Andreev bound states living inside the junction is still correct. However, the minigap E_{g} does not reach Δ at $\phi = 0$ but only $\frac{\hbar v_{\mathrm{F}}}{L}$. This regime has been recently observed in graphene [26].

1.3.3 Energy-phase relation of a long and diffusive Josephson junction

In a long and diffusive JJ, the BdG equations describing scattering of independent channels are not easily solvable. A better approach relies on the Usadel equations and the Green functions formalism to describe the electronic transport [172]. We will not describe them in this work but only summarize the changes in the final results of the ABSs.

In the diffusive regime, an electron needs a time $t_{\mathrm{D}} = \frac{L^2}{D}$ in average to diffuse over a distance L. On the other hand, at an energy ϵ, it keeps its phase coherence during a time [5]

5. According to Heisenberg uncertainty.

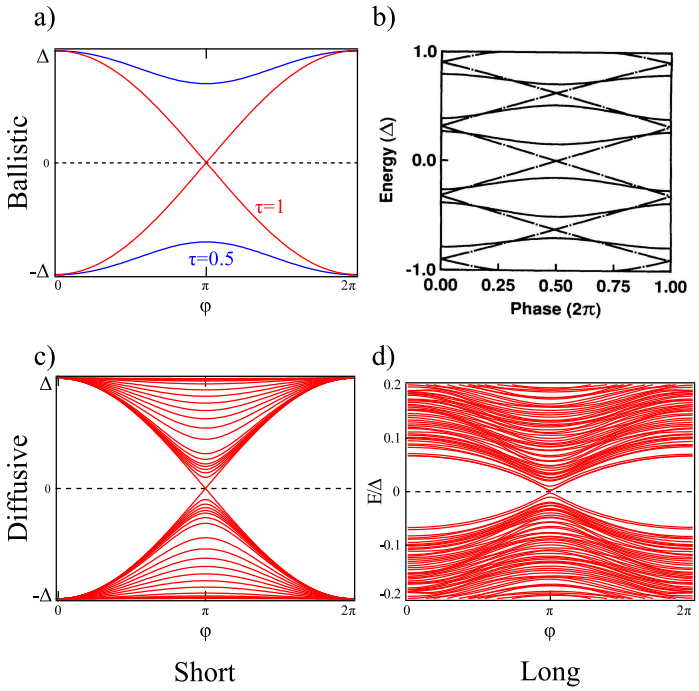

Figure 4.7. – Energy–phase relations of Andreev bound states in different regimes of a Josephson junction. a) Short and ballistic regime b) Long and ballistic regime [13] c) Short and diffusive regime d) Long and diffusive regime. Extracted from [42].

$t_\epsilon = \frac{\hbar}{\epsilon}$. Hence, in order to produce a coherent state between the two leads, the electron has to travel from one lead to the other before loosing its phase coherence ($t_\mathrm{D} < t_\epsilon$). This is described in terms of energy by $\epsilon < \frac{\hbar D}{L^2}$. In the case of short junctions, the energy of the Andreev bound states is limited by the superconducting gap Δ. Here, in long junctions, electrons at such high energy cannot produce coherent states. The maximum energy of the ABSs is the Thouless energy $E_\mathrm{th} = \frac{\hbar D}{L^2}$. The evolution of the governing energy scale of the ABSs is shown in figure 4.6.

In contrast to short ballistic junctions, the diffusive regime brings a new aspect. The density of states in the N part has a phase-dependent energy gap which closes at $\phi = \pi$ [84, 192]:

$$E_\mathrm{g}(\phi) \simeq 3.1 E_\mathrm{th} |\cos(\phi/2)| \tag{4.24}$$

This minigap has been confirmed experimentally by scanning tunneling microscopy [138] in Al-Ag-Al junctions. An example of simulated JJ in the long diffusive regime has been calculated in reference [42, 192] and is represented in figure 4.7 d). We see the gap in the density of states almost closing at π and opening up to a maximal value which is smaller than the superconducting gap (here about 0.07Δ). The gap does not totally close because the simulations have been done on a finite number of channels.

2 Topological superconductivity

A Topological Josephson junction has been predicted to involve an unconventional superconducting proximity effect which has a p-wave symmetry of the order parameter. The association of this p-wave symmetry and the absence of spin degeneracy of the surface states of a 3D TI leads to an appropriate environment to host an excitation at zero energy which resembles the yet elusive Majorana fermion particle.

In this section we introduce the Majorana fermions and show how it emerges in p-wave superconductors. We then describe the theoretical framework that predicts a p-wave superconducting proximity effect on the surface of a 3D TI. Finally, we discuss the possibility to distinguish the 4π-tABS from other conventional ABS also present inside a TJJ.

2.1 $p_x + ip_y$ superconductivity and Majorana bound states

2.1.1 Majorana fermion vs Majorana bound state

The Dirac equation describes fermionic particles in high energy physics. In 1937, Ettore Majorana developed a variation of Dirac equation with real solution which describes a spin 1/2 particle which is its own antiparticle : $\gamma = \gamma^\dagger$ [118]. This fermionic particle named Majorana fermion (MF) has not yet been observed as a fundamental particle.

In condensed matter, unlike high energy physics, a MF is not a particle but is predicted to appear as a non trivial *emergent* excitation of quasi-particles : denoted Majorana bound state (MBS). If these excitations do exist on a 2D surface [6], they are expected to obey a non-Abelian statistic and could serve as the building block for topological quantum computing [129]. Therefore finding the suitable experiment that would nail down the existence of MBS in condensed matter systems has attracted tremendous attention from the scientific community.

MBSs have been predicted to appear in the fractional quantum Hall effect $\nu = 5/2$ [139], in half quantum vortices of the spinful p-wave superconductor Sr_2RuO_4 [86], in cold atoms [148], superfluid Helium [122] and topological insulators [63]. The common theory describing these systems is the spinless $p_x + ip_y$ superconductivity.

A MF is visible by the decomposition of a complex fermionic state into real and imaginary parts:

$$\begin{aligned} c &= \frac{1}{2}(\gamma^a + i\gamma^b) \\ c^\dagger &= \frac{1}{2}(\gamma^a - i\gamma^b) \end{aligned} \tag{4.25}$$

with c and $c^\dagger$ being the annihilation and creation operators in the second quantization formalism. From this decomposition, we can inverse the definition :

6. This 2D surface can be, for instance, the topological surface state of a 3D topological insulator.

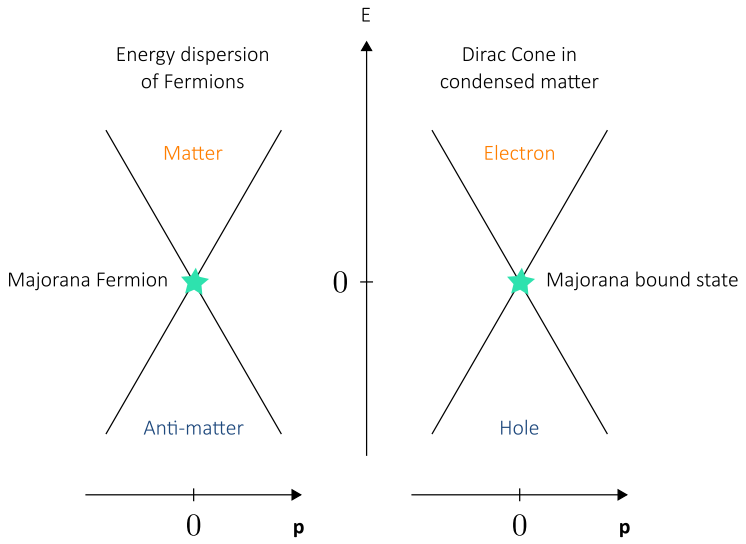

Figure 4.8. – Schematic representation of the analogy between the Majorana fermion predicted as massless fermionic particle and the Majorana bound state predicted in solid state physics.

$$\begin{aligned} \gamma^a &= c^\dagger + c \\ \gamma^b &= i(c^\dagger - c) \end{aligned} \tag{4.26}$$

We clearly see that $\gamma^{a\dagger} = c + c^\dagger = \gamma^a$ (and same for γ^b). This decomposition of MF shows that a MBS is the equal superposition of an electron and a hole in condensed matter. The analogy between a MF and a MBS is shown in figure 4.8. A MF is composed of both matter and anti-matter whereas a MBS is composed of both half an electron and half a hole: the MBS is located at the zero energy point of a Dirac Cone [7].

Particles that are equal superposition of holes and electrons is the core idea of the Bogoliubov formalism in superconductors. In this formalism, a quasiparticle is described by $uc^\dagger_\uparrow + vc_\downarrow$. Hence, a MBS would have an equal superposition [8]: $v = u$.

This peculiar aspect translated into the Bogoliubov approach means that the annihilation operator of a MBS reads : $\gamma = uc^\dagger_\sigma + u^* c_\sigma$.

So far we have not mentioned the spin of the electron. In fact, Eq. (4.26) reads $\gamma^a_\uparrow = c^\dagger_\uparrow + c_\uparrow$ for spin up electron and same for spin down electron. To create a MBS that behaves exactly like a Majorana fermion, we need to consider a spinless particle. The fermions which constitute the MBS are composed of a single spin. This condition is fulfilled by removing all type of degeneracies (spin and valleys in the case of graphene).

A MBS does not exist alone. As it is half a fermion, MBSs always appear in pairs γ^a and γ^b. If the two components of the pair interact, then both MBSs are destroyed and they are not at zero energy any-more. For the pair of MBS to be safe, they have to be created

7. The Dirac cone in condensed matter is described by the same Dirac equation in particle physics. The same equation that leads to the MF.

8. More precisely $v = u^*$

at two separate locations: two extremities of a wire or two sides of a Josephson junction.

Finding a reliable experiment to prove the presence of a MBS is a very challenging task. Recently, some experimentalists have claimed the observation of a MBS as a peak in the tunneling conductance at zero bias [41, 47, 125, 142, 179].

In the next paragraph, we introduce the basic ideas of unconventional superconductivity in order to better understand what is spinless $p_x + ip_y$ superconductivity. Then we show how a Majorana bound state arises at the borders of a 1D p-wave superconductor.

2.1.2 Short introduction on unconventional superconductivity

In a superconductor, the Cooper pair condensate is described by its complex wave function Ψ and a (integer) spin component $\mathcal{S}$. The Hamiltonian for conventional (s-wave) superconductivity couples two electrons of opposite spins: $H_S = \Delta\psi^\dagger_{k,\uparrow}\psi^\dagger_{-k\downarrow} + \Delta^*\psi_{-k\downarrow}\psi_{k,\uparrow}$.

It is also possible to form Cooper pairs of electrons of the same spin [121, 158]. The only limitation on superconductivity comes from the symmetry of Ψ: the wave function has to be anti-symmetric when inverting the two electrons of the Cooper pair [77]. The total spin $\mathcal{S}$ of the Cooper pair wave function can be either singlet ($\mathcal{S} = 0$), with pairs of opposite spins or triplet ($\mathcal{S} = 1$) with pairs of same spins and/or pairs of opposite spins. The general Hamiltonian describing the coupling reads : $H_S = \sum_{\sigma,\sigma'} \Delta_{k,\sigma,\sigma'}\psi^\dagger_{k,\sigma}\psi^\dagger_{-k,\sigma'} + H.c.$ [9] with σ and σ' the spin components of the electrons. The associated gap function $\Delta_{k,\sigma,\sigma'}$ can be expressed in term of a 2x2 matrix in the spin space :

$$H_S = \left(\psi^\dagger_{k,\uparrow}; \psi^\dagger_{k,\downarrow}\right) \mathbf{\Delta}_k \left(\psi^\dagger_{-k,\uparrow}; \psi^\dagger_{-k,\downarrow}\right)^t + H.c. \quad \text{with} \quad \mathbf{\Delta}_k = \begin{pmatrix} \Delta_{k,\uparrow,\uparrow} & \Delta_{k,\uparrow,\downarrow} \\ \Delta_{k,\downarrow,\uparrow} & \Delta_{k,\downarrow,\downarrow} \end{pmatrix} \tag{4.27}$$

The structure of the components of the gap function is related to the symmetry of $\Psi(k)$. In the s-wave case, the wave function of the Cooper pair is constant in k-space : $\Psi^s = \sqrt{n}e^{i\phi} = \Delta_0 e^{i\phi}$ (expression used in Eq. (4.2)) and

$$\mathbf{\Delta}^s_k = \begin{pmatrix} 0 & \Delta_0 \\ -\Delta_0 & 0 \end{pmatrix} \tag{4.28}$$

In the case of unconventional superconductivity, the superconducting gap is a 2x2 matrix in the spin space and each component of $\mathbf{\Delta}_k$ is k-dependent. A type of superconductivity is fully described by its superconducting gap $\mathbf{\Delta}_k$.

With these notations, the superconducting gap of the $p_x + ip_y$ superconductivity reads :

$$\mathbf{\Delta}^{p_x+ip_y}_k = \begin{pmatrix} \Delta_0(\frac{k_x+ik_y}{k_F}) & 0 \\ 0 & -\Delta_0(\frac{k_x-ik_y}{k_F}) \end{pmatrix} \tag{4.29}$$

9. Hermitian conjugate

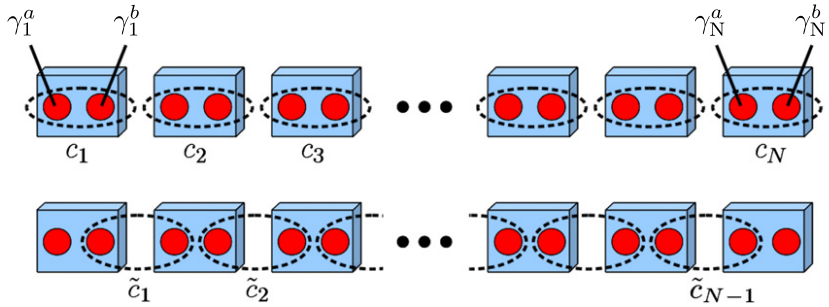

Figure 4.9. – Schematic of the Kitaev chain. Upper panel: the fermion operator c_j is composed of two Majorana fermion operator on the same site j. Lower panel: in the case of $\mu = 0$ and $t = \Delta$, two neighboring γ form a new fermion operator $\tilde{c}$ which sits on two different site. This new point of view leaves two Majorana operators unpaired: γ_1^a and γ_N^b. Extracted from [113].

2.1.3 The Kitaev toy model

The following part is mainly based on the review article [113]. In 2001, Kitaev proposed a simple model based on a 1D chain of N interacting electrons in which two MBSs appear at the end of the wire [95]. The Hamiltonian describes spinless electrons [113] :

$$H_{\text{chain}} = -\mu \sum_{j=1}^{N} n_j - \sum_{j=1}^{N-1} (t c_j^\dagger c_{j+1} + \Delta c_j c_{j+1} + H.c.) \tag{4.30}$$

with μ being the chemical potential, c_j the electron annihilation operator for site j, $n_j = c_j^\dagger c_j$ the associated number operator, t a hopping constant between the site $j+1$ and site j and Δ the superconducting paring potential. This Hamiltonian is spinless because it only operates on one type of spin . The coupling is p-wave because it pairs only electrons of the same spin.

Let us focus on the low energy physics ($\mu = 0$) in the simple case of $t = \Delta$. We introduce the γ and $\gamma^\dagger$ operators from Eq. (4.25) which decomposes c_j into two MBS sitting on the same site j ($c_j = \frac{1}{2}(\gamma_j^a + i\gamma_j^b)$). This new basis diagonalizes the Hamiltonian to :

$$H_{\text{chain}} = -it \sum_{j=1}^{N-1} \gamma_j^a \gamma_{j+1}^b \tag{4.31}$$

We can rewrite H_{chain} in another fermion basis composed of two MF that are located on two different sites :

$$\tilde{c}_j = \frac{\gamma_{j+1}^a + i\gamma_j^b}{2} \tag{4.32}$$

This new operator is sketched in figure 4.9 where we see that it couples electrons of different sites. In this new basis, the Hamiltonian reads [10]:

$$H_{\text{chain}} = 2t \sum_{j=1}^{N-1} \tilde{c}_j^\dagger \tilde{c}_j \tag{4.33}$$

10. $-i\gamma_j^a \gamma_{j+1}^b = 2\tilde{c}_j^\dagger \tilde{c}_j$

Writing the Hamiltonian in the basis of $\tilde{c}$ allows to add a component binding γ_1^a and γ_N^b. The associated operator reads:

$$\tilde{c}_{MF} = \frac{\gamma_N^b + i\gamma_1^a}{2} \tag{4.34}$$

This operator does not appear in the Hamiltonian because it does not cost energy to be created. The energy of the resulting fermion is hence zero. It is the superposition of two Majorana operators spatially located at the two ends of the wire. This fermion is non-local and hence is protected from disorder: as long as the left Majorana exists, the right Majorana cannot be destroyed by any *small* perturbation.

In general, two MBSs appear in pairs at the borders between a topological and a non-topological superconducting region for instance at the edges of a nanowire [95], on the two sides of a topological Josephson junction [63] or at the two extremities of a vortex core [82, 84, 101, 139].

We have shown so far how a Majorana bound state emerges from spinless p-wave superconductivity at the edge of the system. In the next section we will describe the consequence of such peculiar excitation in the current-phase relation of a p-wave Josephson junction.

2.1.4 4π periodic current-phase relation in Josephson junctions with p-wave superconductors

In this section we investigate the current-phase relation of a one dimensional S-I-S Josephson junction with a p-wave superconducting coupling based on the article of Kwon, Sengupta and Yakovenko [107] (cf figure 4.10).

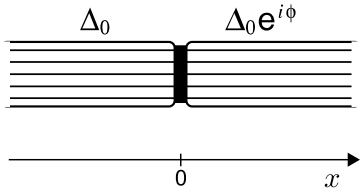

Figure 4.10. – Schematic a Josephson junction made of two quasi-one dimensional superconductors. Extracted from [107].

We use the one dimensional Bogoliubov-de-Gennes (BdG) Hamiltonian composed of a normal part $\mathcal{H}_N$:

$$\mathcal{H}_N(k_x) = \frac{\hbar^2 k_x^2}{2m} - \mu + U_0\delta(x) \tag{4.35}$$

and the superconducting coupling part $\mathcal{H}_S$:

$$\mathcal{H}_S(k_x) = \Delta_\beta \frac{k_x}{k_F} \tag{4.36}$$

with m being the effective mass, μ the Fermi energy, U_0 represents a barrier potential at the interface between the left and right electrode, β refers to the left or right electrode : $\Delta_L = \Delta_0$ and $\Delta_R = \Delta_0 e^{i\phi}$. The pairing potential changes its sign depending on the direction of propagation of the electron: it is a p-wave pairing.

With this notation, the Hamiltonian reads:

$$\begin{aligned}\mathcal{H} &= \begin{pmatrix} \mathcal{H}_{\mathrm{N},}(k_\mathrm{x}) & \mathcal{H}_\mathrm{S}(k_\mathrm{x}) \\ \mathcal{H}_\mathrm{S}^*(k_\mathrm{x}) & -\mathcal{H}_\mathrm{N}(k_\mathrm{x}) \end{pmatrix} \\ &= \begin{pmatrix} \frac{\hbar^2 k_\mathrm{x}^2}{2m} - \mu + U_0\delta(x) & \Delta_\beta \frac{k_\mathrm{x}}{k_\mathrm{F}} \\ \Delta_\beta^* \frac{k_\mathrm{x}}{k_\mathrm{F}} & -\frac{\hbar^2 k_\mathrm{x}^2}{2m} + \mu - U_0\delta(x) \end{pmatrix}\end{aligned} \tag{4.37}$$

We search solutions of the form :

$$\psi_\beta = e^{\beta\kappa x}\left[A_\beta\left(u_{\beta,+}; v_{\beta,+}\right)e^{ik_\mathrm{F}x} + B_\beta\left(u_{\beta,-}; v_{\beta,-}\right)e^{-ik_\mathrm{F}x}\right] \tag{4.38}$$

when used as a factor $\beta = +1$ (-1) for the left (right) electrode [11], the index + $(-)$ is for right (left) moving quasi-particles and $\kappa = \frac{\sqrt{\Delta_0^2 - |E|^2}}{\hbar v_\mathrm{F}}$ with E being the energy of the quasiparticle [12]. $1/\kappa$ represents the length scale over which the wave function decays away from the interface.

The wave-vectors of the quasi-electron and quasi-hole in the limit of $k_\mathrm{F} \gg \kappa$ and for zero barrier at the interface ($U_0 = 0$) are related by the conditions:

$$\begin{aligned}\eta_{\beta,+} &= \frac{v_{\beta,+}}{u_{\beta,+}} = \frac{E + i\beta\kappa\hbar v_\mathrm{F}}{\Delta_{\beta,+}} \\ \eta_{\beta,-} &= \frac{v_{\beta,-}}{u_{\beta,-}} = \frac{E - i\beta\kappa\hbar v_\mathrm{F}}{\Delta_{\beta,-}}\end{aligned} \tag{4.39}$$

with E the energy of the quasiparticle. In the case of p-wave superconductivity, we have:

$$\begin{aligned}\Delta_{\mathrm{L},+} = \quad \Delta_0 \quad &, \quad \Delta_{\mathrm{R},+} = \quad \Delta_0 e^{i\phi} \\ \Delta_{\mathrm{L},-} = -\Delta_0 \quad &, \quad \Delta_{\mathrm{R},-} = -\Delta_0 e^{i\phi}\end{aligned} \tag{4.40}$$

The geometry of a junction constrains the solutions of Eq. (4.37) with two boundary conditions at the interface ($x = 0$):

$$\begin{aligned}\psi_\mathrm{L}(x=0) &= \psi_\mathrm{R}(x=0) \\ \frac{\partial\psi_\mathrm{L}}{\partial x}(x=0) &= \frac{\partial\psi_\mathrm{R}}{\partial x}(x=0)\end{aligned} \tag{4.41}$$

Applying the boundary conditions to the solution implies the resolution of a 4x4 linear system whose determinant is zero [13]. Using again the hypothesis $k_\mathrm{F} \gg \kappa$ brings the following condition:

11. When used as an index, β refers to L or R electrode.
12. The energy of the states are the eigenvalues of $\mathcal{H}$
13. after using $k_\mathrm{F} \gg \kappa$, the 4x4 degenerated linear system of equation is :

$$\begin{cases} A_\mathrm{L}u_{\mathrm{L},+} + B_\mathrm{L}u_{\mathrm{L},-} & = A_\mathrm{R}u_{\mathrm{R},+} + B_\mathrm{R}u_{\mathrm{R},-} \\ A_\mathrm{L}v_{\mathrm{L},+} + B_\mathrm{L}v_{\mathrm{L},-} & = A_\mathrm{R}v_{\mathrm{R},+} + B_\mathrm{R}v_{\mathrm{R},-} \\ Z(A_\mathrm{L}u_{\mathrm{L},+} + B_\mathrm{L}u_{\mathrm{L},-}) & = i(A_\mathrm{R}u_{\mathrm{R},+} - B_\mathrm{R}u_{\mathrm{R},-} - A_\mathrm{L}u_{\mathrm{L},+} + B_\mathrm{L}u_{\mathrm{L},-}) \\ Z(A_\mathrm{L}v_{\mathrm{L},+} + B_\mathrm{L}v_{\mathrm{L},-}) & = i(A_\mathrm{R}v_{\mathrm{R},+} - B_\mathrm{R}v_{\mathrm{R},-} - A_\mathrm{L}v_{\mathrm{L},+} + B_\mathrm{L}v_{\mathrm{L},-}) \end{cases} \tag{4.42}$$

with $A_\mathrm{L}, B_\mathrm{L}, A_\mathrm{R}, B_\mathrm{R}$ the four unknown variables.

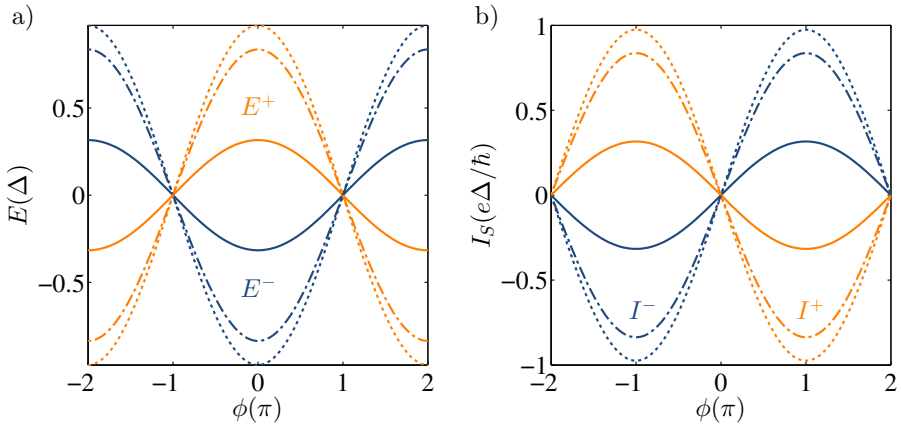

Figure 4.11. – Andreev bound state energy-phase (a) and current-phase (b) relations of a p-wave Josephson junction (drawn from eq. (4.44)) for different transmission coefficient: 0.1 (solid), 0.7 (dashed) and 0.95 (dotted). The ground (excited) state E^- (E^+) is represented in blue (orange)

$$\frac{(\eta_{\mathrm{R},-}-\eta_{\mathrm{L},-})(\eta_{\mathrm{R},+}-\eta_{\mathrm{L},+})}{(\eta_{\mathrm{R},+}-\eta_{\mathrm{L},-})(\eta_{\mathrm{R},-}-\eta_{\mathrm{L},+})}=1-D \tag{4.43}$$

with $D=\frac{4}{4+Z^2}$ the transmission of the barrier and $Z=\frac{2mU_0}{\hbar^2 k_{\mathrm{F}}}$

By combining Eq. (4.39) & Eq. (4.43) we obtain the energy-phase and current-phase relations of the Andreev Bound states :

$$\boxed{\begin{aligned} E^{(p)} &= -\Delta_0\sqrt{D}\cos(\phi/2) \\ I_{\mathrm{S}}^{(p)} &= \frac{e\Delta_0}{\hbar}\sqrt{D}\sin(\phi/2) \end{aligned}} \tag{4.44}$$

We see that a p-wave Josephson junction produces Andreev Bound states with 4π periodicity (see figure 4.11), contrarily to the expected 2π periodicity (seen in section 1.1.1) for conventional JJ. This 4π periodic ABS is composed of two interacting Majorana Bound states. When the phase difference is $\phi=\pi$, the two MBS are totally decoupled which sets them at zero energy.

We can understand this unusual periodicity by the following. A MBS is composed of half an electron and half a hole. After a conventional cycle of 2π by the phase, a single charge e is transferred from one electrode to the other. However, a single charge is not compatible with the $2e$ of the Cooper pair. Therefore, two cycles have to be executed by the phase in order to transfer the complete charge of a Cooper pair.

A more rigorous picture is given by the fermion parity anomaly of TJJs [62, 139]. The state of a Josephson junction is defined completely by the phase difference ϕ and the filling of the ABSs, or more precisely its fermion parity (the parity of the number of electrons inside the junction). In the particular case of TJJ, after a cycle of 2π, the fermion parity changes (from even to odd) [95]. Hence, for the system to go back to its initial state, it has to change its fermion parity two times, which makes it 4π periodic.

2.2 Superconducting proximity effect in 3D Topological Insulators

In 2008, Fu & Kane [63] proposed a theory of the superconducting proximity effect in the surface state of a 3D TI. They predicted that a superconductor with an s-wave symmetry of the pairing potential induces spinless p-wave superconductivity by proximity effect at the surface of the topological insulator.

The Hamiltonian describing the superconducting proximity effect in the surface states of a 3D TI is composed of the surface Hamiltonian H_{TI} and the superconducting part H_{S}: $H = H_{\mathrm{TI}} + H_{\mathrm{S}}$.

H_{S} is diagonal in a basis of quasi-electron and quasi-hole [14], whereas H_{TI} is diagonal in a basis containing spin up and spin down components [15]. To use a matrix notation for H, we need to use a basis that incorporate both the spins and electron/hole components. This basis called the Nambu space describes a quasiparticle by its spins and electron/hole components:

$$\Psi_{\mathrm{k}} = \begin{pmatrix} \psi_{\mathrm{k},\uparrow} \\ \psi_{\mathrm{k},\downarrow} \\ \psi^{\dagger}_{\mathrm{k},\downarrow} \\ -\psi^{\dagger}_{\mathrm{k},\uparrow} \end{pmatrix} \tag{4.45}$$

with ψ ($\psi^{\dagger}$) the annihilation (creation) operator of an electron with a spin up $\psi_{\uparrow}$ (resp. spin down $\psi_{\downarrow}$). Due to the spin-momentum locking effect at the surface of 3D TIs, a spin up electron necessarily moves to the right direction and vice-versa for spin down.

The total Hamiltonian is expressed by $H = {}^{\mathrm{t}}\Psi^{\dagger}_{-\mathrm{k}}\mathcal{H}\Psi_{\mathrm{k}}/2$, with $\mathcal{H}$ being a 4x4 matrix in the Nambu basis. We can write $\mathcal{H}$ in blocks of 2x2 elements. Each small block mixes the spin components whereas the global matrix couples the creation/annihilation components: $\psi_{\uparrow}$ and $\psi_{\downarrow}$ are coupled by the upper left small block of $\mathcal{H}$ and idem 3$^{\mathrm{rd}}$ and 4$^{\mathrm{th}}$ component of Eq. (4.45) are mixed by the lower right block. With this notation we have :

$$\mathcal{H} = \begin{pmatrix} \mathcal{H}_{\mathrm{TI,k}} & \mathcal{H}_{\mathrm{S}} \\ \mathcal{H}^{*}_{\mathrm{S}} & -\sigma^{y}\mathcal{H}^{*}_{\mathrm{TI},-\mathrm{k}}\sigma^{y} \end{pmatrix} \tag{4.46}$$

The 2x2 Hamiltonian of the topological surface state reads [63]:

$$\mathcal{H}_{\mathrm{TI,k}} = \hbar v_{\mathrm{F}} \boldsymbol{\sigma}.\boldsymbol{k} - \mu \mathbb{1}_2 \tag{4.47}$$

with μ being the chemical potential with respect to the Dirac point, $\boldsymbol{k} = (k_{\mathrm{x}}\mathbb{1}_2, k_{\mathrm{y}}\mathbb{1}_2)$ the electronic wave vector, $\mathbb{1}_2$ the 2x2 unitary matrix and the 2x2 Pauli matrices [16] $\boldsymbol{\sigma} = (\sigma^x, \sigma^y)$.

14. As described by the Bogoliubov-de-Gennes formalism of section 1.2.1
15. This is necessary to depict the spin-momentum locking in 3D TI.
16. let us recall the 2x2 Pauli matrices :

$$\sigma^x = \begin{pmatrix} 0 & 1 \\ 1 & 0 \end{pmatrix}, \quad \sigma^y = \begin{pmatrix} 0 & -i \\ i & 0 \end{pmatrix}, \quad \sigma^z = \begin{pmatrix} 1 & 0 \\ 0 & -1 \end{pmatrix}$$

The superconducting pairing potential part of $\mathcal{H}$ is $\mathcal{H}_{\rm S} = \Delta \mathbb{1}_2$, with $\Delta = \Delta_0 e^{i\phi}$ the superconducting order parameter.

It is useful to reduce the Hamiltonian [17] $\mathcal{H}$ in a compact form in order to find the associated eigenvalues. For that, we use the 2x2 Pauli matrices τ^i mixing the annihilation/creation components [18]:

$$\tau^x \otimes \mathbb{1}_2 = \begin{pmatrix} 0 & 0 & 1 & 0 \\ 0 & 0 & 0 & 1 \\ 1 & 0 & 0 & 0 \\ 0 & 1 & 0 & 0 \end{pmatrix} \quad , \quad \tau^y \otimes \mathbb{1}_2 = \begin{pmatrix} 0 & 0 & -i & 0 \\ 0 & 0 & 0 & -i \\ i & 0 & 0 & 0 \\ 0 & i & 0 & 0 \end{pmatrix} \quad , \quad \tau^z \otimes \mathbb{1}_2 = \begin{pmatrix} 1 & 0 & 0 & 0 \\ 0 & 1 & 0 & 0 \\ 0 & 0 & -1 & 0 \\ 0 & 0 & 0 & -1 \end{pmatrix} \tag{4.49}$$

with $\otimes$ being the tensor product. Let us recall the main property of the Pauli matrices: $\sigma^i\sigma^j = -\sigma^j\sigma^i = i\epsilon_{\rm ijk}\sigma^k + 2\delta_{\rm i,j}\mathbb{1}_2$, where $\epsilon_{\rm ijk}$ is the Levi-Civita symbol [19] and $\delta_{\rm i,j}$ is the Kronecker symbol [20].

The use of the τ^i matrices reduces the Hamiltonian to the following compact form :

$$\mathcal{H} = \hbar v_{\rm F} \tau^z \otimes \boldsymbol{\sigma}.\boldsymbol{k} - \mu\tau^z \otimes \mathbb{1}_2 + \Delta_0(\tau^x \cos\phi - \tau^y \sin\phi) \otimes \mathbb{1}_2 \tag{4.50}$$

We should comment on the fact that the scalar product $\boldsymbol{\sigma}.\boldsymbol{k}$ between two vectors of 2x2 matrices produces a 2x2 matrix. Hence, $\tau^z \otimes \boldsymbol{\sigma}.\boldsymbol{k}$ is a 4x4 matrix. It is now easier to find its eigenvalues by squaring $\mathcal{H}$ two times and thus transforming $\mathcal{H}$ into a diagonal matrix [21]:

$$\mathcal{H}^2 - (\hbar^2 v_{\rm F}^2 |\boldsymbol{k}|^2 + \mu^2 + \Delta_0^2) = -2\hbar v_{\rm F}\mu\boldsymbol{\sigma}.\boldsymbol{k}$$

$$\left[\mathcal{H}^2 - (\hbar^2 v_{\rm F}^2 |\boldsymbol{k}|^2 + \mu^2 + \Delta_0^2)\right]^2 = 4\hbar^2 v_{\rm F}^2 \mu^2 \boldsymbol{k}^2$$

The cross products between the same Pauli matrices give zero most of the time or $\mathbb{1}_2$. The cross product between the σ^i and τ^j matrices commutes because they do not act on

17. The expended notation of $\mathcal{H}$ taking in the Nambu basis is :

$$\mathcal{H} = \begin{pmatrix} -\mu & \hbar v_{\rm F}(k_{\rm x} - ik_{\rm y}) & \Delta_0 e^{i\phi} & 0 \\ \hbar v_{\rm F}(k_{\rm x} + ik_{\rm y}) & -\mu & 0 & \Delta_0 e^{i\phi} \\ \Delta_0 e^{-i\phi} & 0 & \mu & -\hbar v_{\rm F}(k_{\rm x} - ik_{\rm y}) \\ 0 & \Delta_0 e^{-i\phi} & -\hbar v_{\rm F}(k_{\rm x} + ik_{\rm y}) & \mu \end{pmatrix} \tag{4.48}$$

18. The σ^i and τ^i Pauli matrices are both 2x2 matrices that have the same expressions. However, they do not act on the same basis : σ^i acts on the spin $(\psi_\uparrow, \psi_\downarrow)$ whereas τ^i acts on the electron/hole components (first two components of Ψ Eq. (4.45) with respect to the last two components of Ψ).

19. $\epsilon_{\rm ijk} = \begin{cases} +1 & \text{if (i,j,k) is (1,2,3), (2,3,1) or (3,1,2)} \\ -1 & \text{if (i,j,k) is (3,2,1), (2,1,3) or (1,3,2)} \\ 0 & \text{if i=j, i=k or j=k} \end{cases}$

20. $\delta_{\rm i,j} = \begin{cases} 1 & \text{if i=j} \\ 0 & \text{else} \end{cases}$

21. We use the properties of the Pauli matrices: $\sigma^i\sigma^j + \sigma^j\sigma^i = [\sigma^i, \sigma^j] = 2\delta_{\rm i,j}$. The complete calculation is detailed in Appendix B.

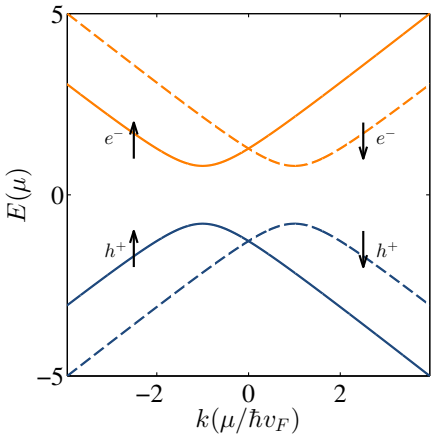

Figure 4.12 – Energy dispersion relation for the 4 energy states of (4.51) with the following parameters : $\mu = 1\,\text{meV}$, $v_\text{F} = 5 \times 10^5\,\text{m}\,\text{s}^{-1}$ and $\Delta = 800\,\mu\text{eV}$. Solid lines corresponds to, say, up spin, and dashed line to the opposite spin.

the same basis which thus simplifies the calculation. We thus obtain the following energy dispersion :

$$\boxed{E^{\pm}_{\uparrow,\downarrow} = \pm\sqrt{(\mu \pm \hbar v_\text{F}|\boldsymbol{k}|)^2 + \Delta_0^2}} \tag{4.51}$$

The $E^{\pm}_{\uparrow,\downarrow}$ of the 4 possible states is drawn in figure 4.12. The superconducting gap is opened at $\hbar v_\text{F} k = \mu$. Far away from the chemical potential, the dispersion relation is linear. There is a band crossing of spin polarized states around $k = 0$ at energy $\pm\mu$ that corresponds to the spin polarized Dirac cone.

Diagonalization of $\mathcal{H}$ Now that we have the energy of the eigenstates, we present in the following paragraph a method that uses a new basis which transform $\mathcal{H}$ into an effective p-wave superconducting Hamiltonian.

The normal part of the Hamiltonian can be more easily written using a basis that rotates with the momentum $\boldsymbol{k} = k_0(\cos\theta_\text{k}, \sin\theta_\text{k})$. In this new basis ($a_{\text{k},\uparrow}, a_{\text{k},\downarrow}$) the normal part of the Hamiltonian reads (full calculation is shown in Appendix B) :

$$\begin{aligned} H_\text{TI} &= \sum_\text{k} \psi^\dagger_{-\text{k}}(\hbar v_\text{F}\boldsymbol{\sigma}.\boldsymbol{k} - \mu)\psi_\text{k} \\ &= \sum_\text{k} a^\dagger_{-\text{k}}(\hbar v_\text{F} k_0 \sigma^z - \mu)a_\text{k} \end{aligned} \tag{4.52}$$

with

$$\left(a_{\text{k},\uparrow}; a_{\text{k},\downarrow}\right) = \frac{1}{\sqrt{2}}\begin{pmatrix} e^{i\theta_\text{k}/2} & e^{-i\theta_\text{k}/2} \\ -e^{i\theta_\text{k}/2} & e^{-i\theta_\text{k}/2} \end{pmatrix}\left(\psi_{\text{k},\uparrow}; \psi_{\text{k},\downarrow}\right) \tag{4.53}$$

The superconducting Hamiltonian in the same basis reads :

$$\begin{aligned}\mathcal{H}_{\mathrm{S}} = & \sum_k \Delta\psi^\dagger_{\mathrm{k},\uparrow}\psi^\dagger_{-\mathrm{k},\downarrow} + \Delta^*\psi_{-\mathrm{k},\downarrow}\psi_{\mathrm{k},\uparrow} \\ = & \frac{1}{2}\sum_k i\Delta\left[e^{i\theta_\mathrm{k}}a^\dagger_{\mathrm{k},\uparrow}a^\dagger_{-\mathrm{k},\uparrow} - e^{-i\theta_\mathrm{k}}a^\dagger_{\mathrm{k},\downarrow}a^\dagger_{-\mathrm{k},\downarrow}\right] \\ & -i\Delta^*\left[e^{-i\theta_\mathrm{k}}a_{-\mathrm{k},\uparrow}a_{\mathrm{k},\uparrow} - e^{i\theta_\mathrm{k}}a_{-\mathrm{k},\downarrow}a_{\mathrm{k},\downarrow}\right] \\ \boxed{\mathcal{H}_{\mathrm{S}} = \frac{1}{2}\sum_k i\Delta\left[\frac{(k_x+ik_y)}{k_0}a^\dagger_{\mathrm{k},\uparrow}a^\dagger_{-\mathrm{k},\uparrow} - \frac{(k_x-ik_y)}{k_0}a^\dagger_{\mathrm{k},\downarrow}a^\dagger_{-\mathrm{k},\downarrow} + H.c.\right]}\end{aligned} \tag{4.54}$$

This Hamiltonian in the new basis couples a pair of fermions of same spin ($\uparrow\uparrow$ and $\downarrow\downarrow$). We see that depending on the direction of propagation (θ_k), the coupling changes its sign. It describes a so-called $p_x + ip_y$ superconducting pairing symmetry. On top of that, as only one spin is available on the surface states of a 3D TI [22], the induced superconducting proximity effect is a **spinless p-wave superconductivity**.

2.3 S-TI-S Josephson junction

The model of the previous section considers the simple case of a 1D system. The generalization to the case of a Josephson junction made of a 3D topological insulator (S-TI-S), leads to similar conclusions with the formation of a 4π periodic topologically protected Andreev bound state (4π-tABS).

The case of a S-TI-S Josephson junction has been theoretically investigated in the regime of small doping ($\mu \approx 0$) [2, 61, 63, 116, 167] and large doping level ($\mu \gg \Delta$) [160]. Most of the theory studied an S-TI-S JJ with a ferromagnetic layer deposited on top of the 3D TI (cf figure 4.13). The results of Snelder [160] concluded that the ferromagnetic layer is not necessary to produce the 4π-tABS. The energy phase relation of the associated ABSs is drawn in figure 4.13a-d for different angles of incidence of the electronic modes on the surface of the 3D TI ($\theta = 0$ corresponds to a direction of propagation perpendicular to the S-TI interface). The parameters of the calculation are $\mu_{\mathrm{TI,S}}$ the chemical potential of the topological insulator and of the superconducting leads, Δ the superconducting gap, L the length of the junction and m_z the magnetization.

When no magnetization is applied and when the chemical potentials of the S leads and the TI are equal ($\mu_\mathrm{S} = \mu_\mathrm{TI}$), all ABS are 4π periodic. However, when there is a mismatch of the chemical potential at the interface, a barrier is formed and only the electronic mode perpendicular to the S-TI interface ($\theta = 0$) produces a 4π-tABS [23] (cf solid lines in figure 4.13 [a-c]).

The application of a magnetic field ($m_\mathrm{z} \neq 0$) breaks the time reversal symmetry and decreases the superconducting coupling of the ABSs which causes a decrease of their maximum energy (orange arrow shows $E(\phi = 0) < \Delta$). Applying a magnetic field also decreases

22. The spin is determined by the momentum of the quasiparticle

23. The 4π-tABS is perfectly transmitted whatever the quality of the (non-magnetic) interface or the mismatch of the chemical potential.

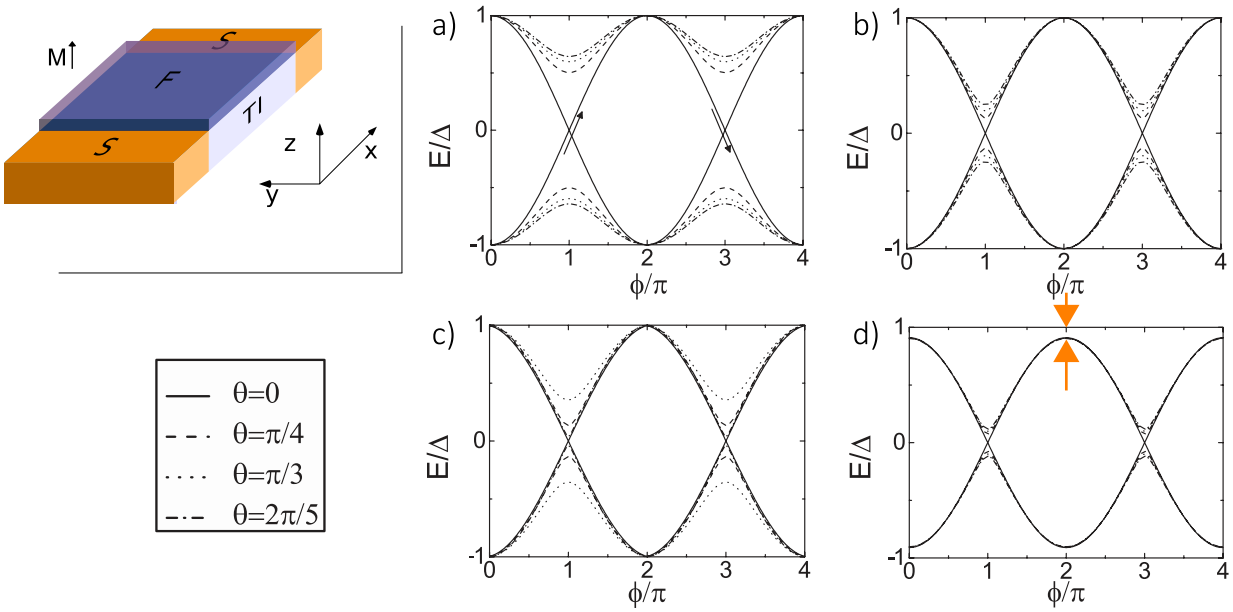

Figure 4.13. – (upper left) Schematic an S-TI-S Josephson junction. A ferromagnetic layer is deposited on top of the TI with a perpendicular magnetization. (right) Energy dependence of the ABS for different angle of incidence θ of the electronic surface mode in a S-TI-S Josephson junction. The legend in (a) applies for both graphs. (a) $\mu_{TI}/\Delta = 100$, $\mu_S/\Delta = 1000$ and $L/L_0 = 0.01$ with $L_0 = \hbar v_F/\mu_{TI}$. The arrows follow the 4π periodic topologically protected ABS. (b) $\mu_{TI}/\Delta = 100$, $\mu_S/\Delta = 120$ and $L/L_0 = 0.01$.(c) $\mu_{TI}/\Delta = 100$, $\mu_S/\Delta = 120$ and $L/L_0 = 0.1$.(d) $\mu_{TI}/\Delta = 100$, $\mu_S/\Delta = 120$, $m_z/\Delta = 60$ and $L/L_0 = 0.01$. Extracted from [160]

the transmission of all ABSs including the one of the 4π-tABS. This major aspect has an impact on the interaction between the 4π-tABS and the continuum of states living above the superconducting gap Δ. Indeed, at zero magnetic field and $\phi = 2\pi$, the 4π-tABS has a positive energy close to $+\Delta$. Around this position ($\pi < \phi < 3\pi$) the 4π-tABS is not in its lowest energy state. Any interaction between the 4π-tABS and the continuum of states forces its relaxation to the lowest energy states : switching from $E = +\Delta$ to $E = -\Delta$. This switching process, called quasiparticle poisoning, destroys the 4π periodicity of the 4π-tABS and will be discussed in details in section 4. Hence applying a magnetic field to the TJJ decouples the 4π-tABS from the continuum and conserves its 4π periodicity.

In conclusion, a **topological Josephson junction hosts a single topologically protected 4π periodic Andreev bound state**. In order to effectively measure the 4π periodicity of this peculiar ABS, one needs to decouple it from the continuum of states by applying a perpendicular magnetic field. On top of that, there will be other ABSs living inside the junction which are *not* topologically protected and are hence 2π periodic.

3 Experimental signatures of Majorana bound state

In the previous section we have seen how MBSs emerge in topological JJs. In fact, they are also predicted in many other geometries. To cite a few:

- In semiconducting nanowire in proximity with a superconductor
- In the vortex core of a p-wave superconductor
- In a wire of ferromagnetic atoms coupled to a superconductor
- ...

In this section we present recent experiments that reports on the observation of a MBS in proximity with superconductors. We first describe the detection of the zero energy mode with tunneling measurement of the density of states. Then we discuss measurements of energy-phase relation of the ABS of a TJJ. Finally we review the signature of MBS in the AC Josephson effect which will be the main focus of this PhD work.

3.1 Tunneling experiment

MBS are not only expected to appear in topological Josephson junctions made of 3D TIs. They are also predicted in semiconductors with strong spin-orbit coupling in proximity with a superconductor and with an applied magnetic field [57].

As the MBS is a state at zero energy, it is possible to reveal its presence by probing the density of states (DOS) of the junction and hence detecting a peak in the DOS at zero energy [57, 110]. The first experimental report on MBS was done by the group of Kouwenhoven (see figure 4.14) [125]. They measured the tunneling conductance through a barrier induced by a local gate beneath an InSb nanowire in contact with a superconductor. This pioneer measurement revealed a zero bias peak structure in the DOS at the extremity of the structure (see figure 4.14d).

The controversy of this result is that the observed zero bias conductance peak is not quantized at the value $2e^2/h$. Moreover, a MBS only exists if it is isolated from the continuum of energy. Here we see that the superconducting gap is not a sharp BCS-like gap and some states are present around zero energy. As many other physical phenomena could potentially explain this zero bias peak, this experimental result has dragged lots of attention to the scientific community in order to rule out other non-topological explanation for this result [40]. Soon after this work, two other groups observed the same zero bias anomaly in InAs nanowires [41, 111].

A second system revealing such clear and promising results is a chain of ferromagnetic atoms deposited on a superconductor. In 2014, the group of Yazdani observed in scanning tunneling spectroscopy a peak at zero energy in the DOS at the extremity of the chain (cf figure 4.15). A state at zero energy, located at the two ends of such nanowire is exactly the results of Kitaev's toy model (cf section 2.1.3).

One of the controversy on this observation is the short spatial location of the state in comparison to the expected size of a MBS, that is discussed in ref [135, 174].

3.2 Measurement of the current-phase relation

Instead of directly probing the Majorana zero mode in the density of states, one can measure the current phase relation (CPR) of a topological Josephson junction. As explained by Eq. (4.44), the current phase relation of such topological Josephson junction

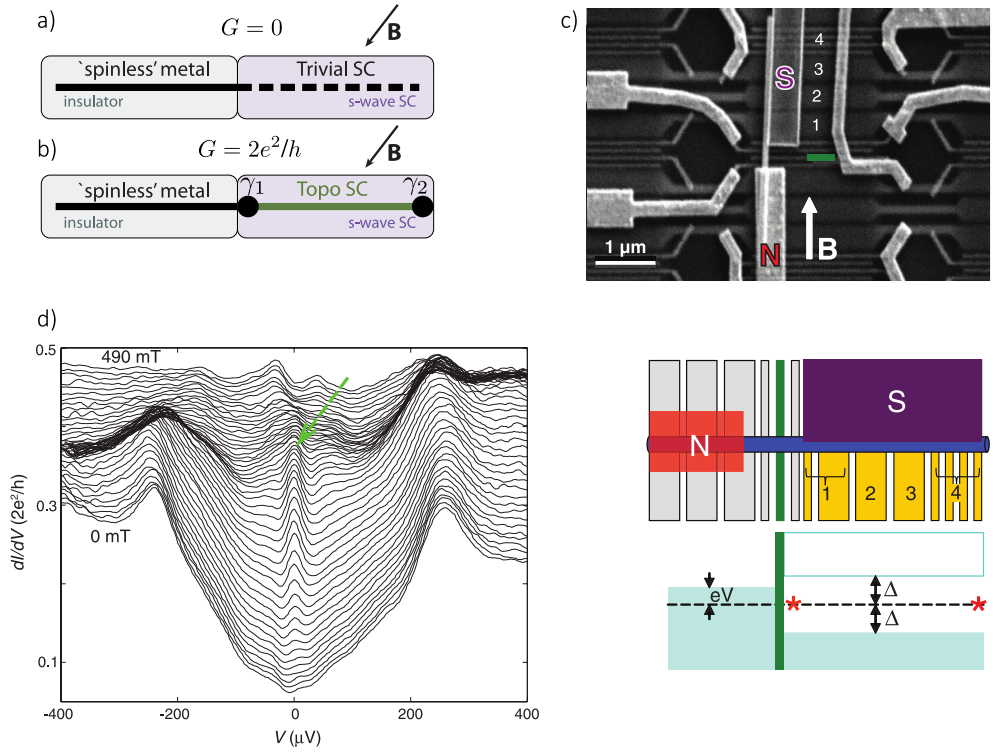

Figure 4.14. – Tunneling experiment to detect a Majorana fermion. A semiconducting nanowire is coupled to an s-wave superconductor (SC) on its right part. When no topological superconductivity is induced in the nanowire (a), the conductance of the wire is zero. However, if the proximity effect induces topological superconductivity, then the conductance of the wire at zero energy is $G = \frac{2e^2}{h}$. Extracted from [3].
(c-d) Experimental results of [125] based on the geometry of (b). (c) (upper) SEM picture of the device. We see the nanowire connected to an S lead and a normal contact. Gates are numbered from 1 to 4. The green gate is the one used to detect the zero bias anomaly. (lower) Schematic of the devices. d) Differential conductance versus voltage bias of the nanowire for increasing magnetic field. Each solid line has been shifted vertically for clarity. The green arrow points to the peak in the conductance at zero bias. This robust peak appears when the magnetic field is switched on.

should be partially composed of a 4π periodic component among 2π periodic components. This measurement can be done by using radiofrequency superconducting quantum interference device (RF-SQUID) [42, 60, 70], by direct measurement (DC-SQUID) [85] or by scanning-SQUID measurements [100]. A complete review about this subject has been made by Golubov [71].

CPRs have been measured by scanning SQUID on JJs made of Bi_2Se_3 [161] and on HgTe [162] and by transport measurement on Bi_2Se_3 [106]. However, even if an anomalous CPR has been detected in the latter measurement [24], no 4π periodic CPR on TJJs has been reported yet. This absence of doubled periodicity in the CPR measurement is understood to originate from the interaction between the 4π periodic ABS and the continuum of states

24. A 2π periodic non sinusoidal CPR is usually found in a short JJ with $2\pi/n$ periodic harmonics (cf eq. Eq. (4.5))

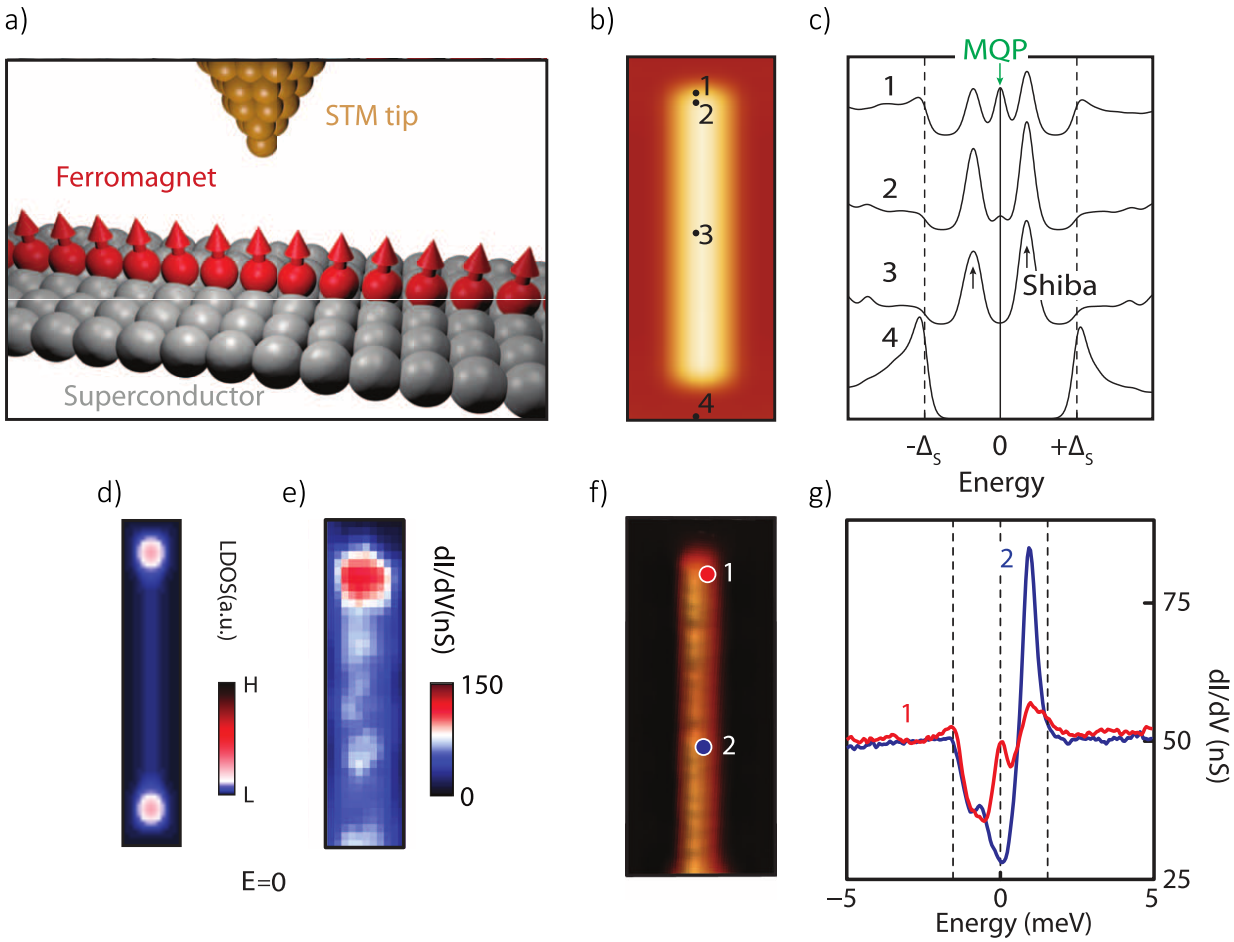

Figure 4.15. – Scanning tunneling experiment that has first measured a peak at zero energy in the density of states at the edge of a topological nanowire. a) A line of ferromagnetic atoms coupled by proximity to a superconductor is probed by an STM tip. b),c) and d) are theoretical simulations. e),f) and g) are experimental data. b) and f) represents the topographic top view of the nanowire with the position of the spectra shown in c) and g). d) and e) are the local density of states at zero biased. Extracted from [127]

at energy Δ which limits its lifetime. This interaction called quasiparticle poisoning is introduced in detail in section 4.

3.3 Fractional AC Josephson effect

The change of periodicity of the current phase relation in a TJJ implies a change in the AC Josephson effect. This changes can be measured either by performing a Shapiro measurement or by recording the electromagnetic environment of a biased JJ. After giving a short theoretical background on this so-called fractional AC Josephson effect, we present the state of the art on these two experimental techniques on topological JJ.

3.3.1 Theoretical prediction

As described in section 1.1.1, when a constant voltage (V_{DC}) is applied on a junction, an oscillating current appears across the junction and emits photons at the Josephson frequency $f_{\mathrm{J}} = 2eV/h$.

In the case of a topological JJ, one expect to measure half the Josephson frequency, that is, $f_{\mathrm{J}}^{4\pi} = \frac{eV}{h}$ resulting from the AC Josephson effect of the 4π periodic mode.

On the other hand, we can reverse the process by irradiating the junction with microwaves at frequency f_{RF}. The phase across the junction locks-in at the same frequency and the measured current voltage characteristic displays steps of equidistant voltages $\Delta V = hf_{\mathrm{RF}}/2e$. Those steps are nothing but the Shapiro steps [72, 157]. We now refer to this probe of the so-called Shapiro steps by a *Shapiro measurement*. In the case of a TJJ with only a 4π periodic ABS, Shapiro steps are expected with equidistant voltages $\Delta V = hf_{\mathrm{RF}}/e$ instead. This doubling of the voltage increment can be viewed as the presence of only even Shapiro steps :

$$V_{\mathrm{n}} = 2n\frac{hf_{\mathrm{RF}}}{2e} \quad n = 1, 2, 3, ... \tag{4.55}$$

Therefore the absence of the odd Shapiro steps provides evidence for the 4π periodic MBS. However, it is not obvious how a Josephson junction composed of one 4π periodic ABS and several conventional 2π ABSs behaves when irradiated with radio frequencies. Theory predicts that the *even/odd* effect only happens at low irradiation frequency [49]. In the next chapter we will review this study by using the resistively shunted junction model.

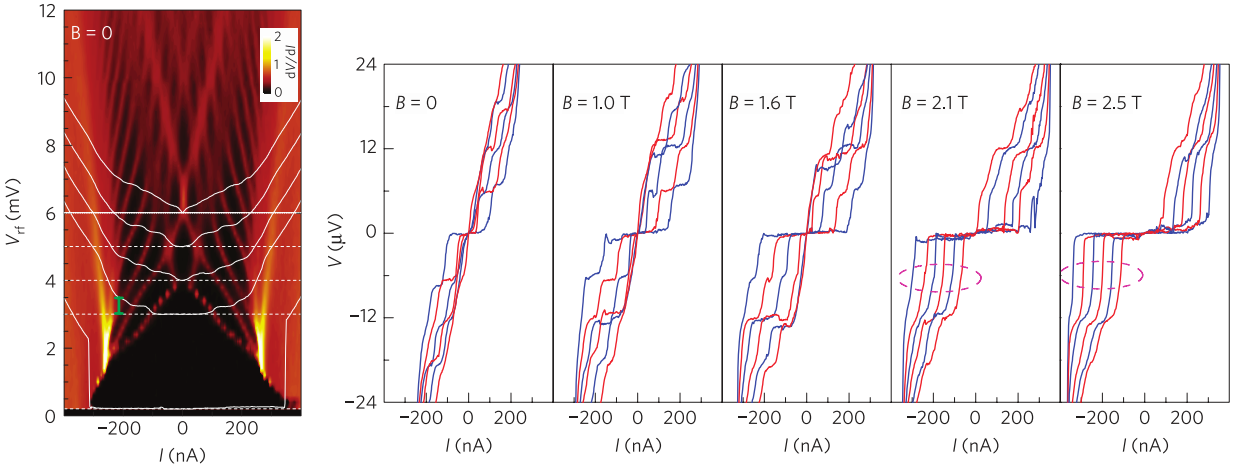

Figure 4.16. – Left panel: The colored plot shows the differential resistance (unit of kΩ) with respect to RF irradiation amplitude in mV at 3 GHz and DC current bias at zero magnetic field and dilution fridge temperature. The white doted lines are linecuts of the $|V(I)|$ characteristic at $V_{\mathrm{RF}} = 0.2, 3, 4, 5$ and 6 mV drawn in white solid lines. The green line represents a scale of 12 μV on the $|V(I)|$ curves. Right panel: $V(I)$ characteristics of the junction for increasing magnetic field. For B lower than 2 T, all Shapiro steps are visible at voltages $V_{\mathrm{n}} = n \cdot hf_{\mathrm{RF}}/2e = n \cdot 6\,\mu\mathrm{V}$. For magnetic field greater than 2 T, the step $n = 1$ at 6 μV disappears as emphasized by the dotted circles. This disappearance of an odd Shapiro step is an evidence of a topological superconductivity. Adapted from [142].

3.3.2 Shapiro measurement

Only two groups have been able to observe the fractional AC Josephson effect in Josephson junctions made of 3D topological insulators by measuring the photon emission of JJ or Shapiro steps.

The first experimental observation of this effect was reported by Rokhinson et al in 2012 [142]. They studied InSb nanowires in contact with superconducting niobium electrodes forming a JJ. InSb is a semiconductor with strong spin-orbit coupling which is one of the possible ingredients to produce a TJJ [151]. When applying a sufficiently high magnetic field, it undergoes a topological transition with the creation of a 4π periodic ABS. The main result of this work is described in figure 4.16. When the nanowire enters the topological phase, under RF irradiation, the Shapiro step $n = 1$ is absent. Which sounds as the beginning of the even/odd effect. However, all other odd Shapiro steps ($n \geq 3$) were observed. At that time, no explanation was given to explain the disappearance of *only* the step $n = 1$ and not all the odd steps, as expected from Eq. (4.55).

The second observation of the even/odd effect in a 3D TI was reported in strained HgTe by Molenkamp's group in 2015 whose main result is shown in figure 4.17. They also observed an unconventional effect of only the first Shapiro step ($n = 1$). At low irradiation frequency ($f_{\mathrm{RF}} = 5.3\,\mathrm{GHz}$), the first step appears at a higher excitation amplitude than the following steps ($n = 2, 3$, etc). Moreover, at lower frequency, the step $n = 1$ is totally absent from the low excitation part ($I_{\mathrm{RF}} < 0.7$). This effect is also concomitant with the absence of the first oscillation of the higher steps: diagonal dark blue region pointed by a gray arrow in figure 4.17a,g.

Some open questions remain about this experiment. If we look carefully on graph (a), the even step $n = 4$ also appears with a 'delay' in the RF excitation in comparison with the step $n = 3$ and $n = 5$ (see pink arrow). It is still unclear why only the first odd Shapiro step would be affected by the topological superconductivity and not the higher

Figure 4.17. *(facing page)* – The left, middle and right columns are measurements of a Josephson junction based on the 3D topological insulator HgTe in proximity with Nb superconducting leads irradiated with microwaves at frequency respectively $f = 2.7, 5.3$ and $11.2\,\mathrm{GHz}$. These graphs are base on the following set-up: At a fixed RF irradiation amplitude, a DC current is applied across the junction and the $V - I$ characteristic is recorded.
The first line graphs represents colored plots of the amount of measured point counted by the binning method with respect to the irradiation amplitude I_{RF} and the measured DC voltage V_{DC} in unit of the expected Shapiro steps $hf_{\mathrm{RF}}/2e$. Light colors represent a high density of measured data point at the V_{DC} voltage. Meaning that a plateau is present in the $V - I$ characteristic. Dark colored point in the graph means few points measured at this voltage hence no plateau in the $V - I$. Middle line graphs represents the differential resistance dV/dI versus the RF irradiation and the biased current I. Black area represent plateaus in the $V - I$ characteristic with zero differential resistance. The Shapiro step $n = 0, 1$ and 2 are labeled.
Lower line graphs shows the extracted size of the firsts (0 to 4) Shapiro step in µA.
The red arrows in the middle column represents the unconventional appearance of the Shapiro step $n = 1$. It is supposed to appear at a lower excitation than the step $n = 2$. The gray arrow in the left column represents the side effect on higher steps of the very late appearance of step $n = 1$. Adapted from [178].

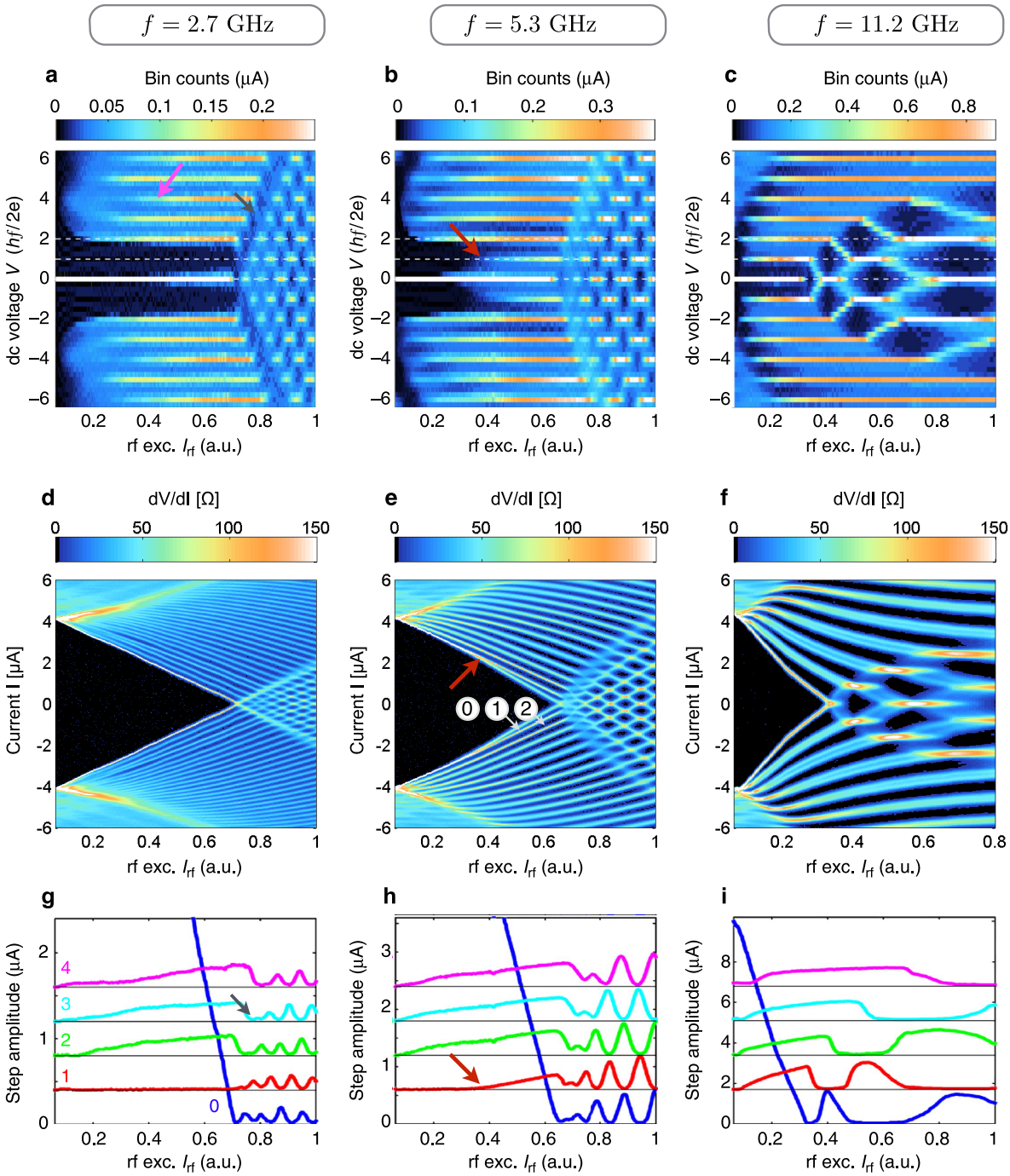
f = 2.7 GHz
f = 5.3 GHz
f = 11.2 GHz
a
b
c
Bin counts (μA)
dc voltage V (hf/2e)
rf exc. I_rf (a.u.)
d
e
f
dV/dI [Ω]
Current I [μA]
0 1 2
g
h
i
Step amplitude (μA)
4
3
2
1
0

odd steps ($n = 3, 5, 7$). The better visibility of the even/odd effect at lower frequency is understood by the fact that the 4π periodic ABS has a much longer phase adjustment time and therefore locks-in at the irradiation frequency only for a slow excitation.

We would expect to not see the effect of this single mode which carries a negligible amount of current in comparison with the conventional modes. However, as the physics describing this system is highly non-linear (cf chapter 5), when the driving irradiation f_{RF} becomes smaller than the characteristic frequency of the 4π periodic ABS $f_{4\pi} = eR_{\mathrm{n}}I_{4\pi}/h$, its contribution becomes greater than the one of the conventional ABSs. This physical effect will be extensively discussed in chapter 5.

It is worth mentioning the recent work of Bocquillon et al. They used HgTe as a 2D topo-

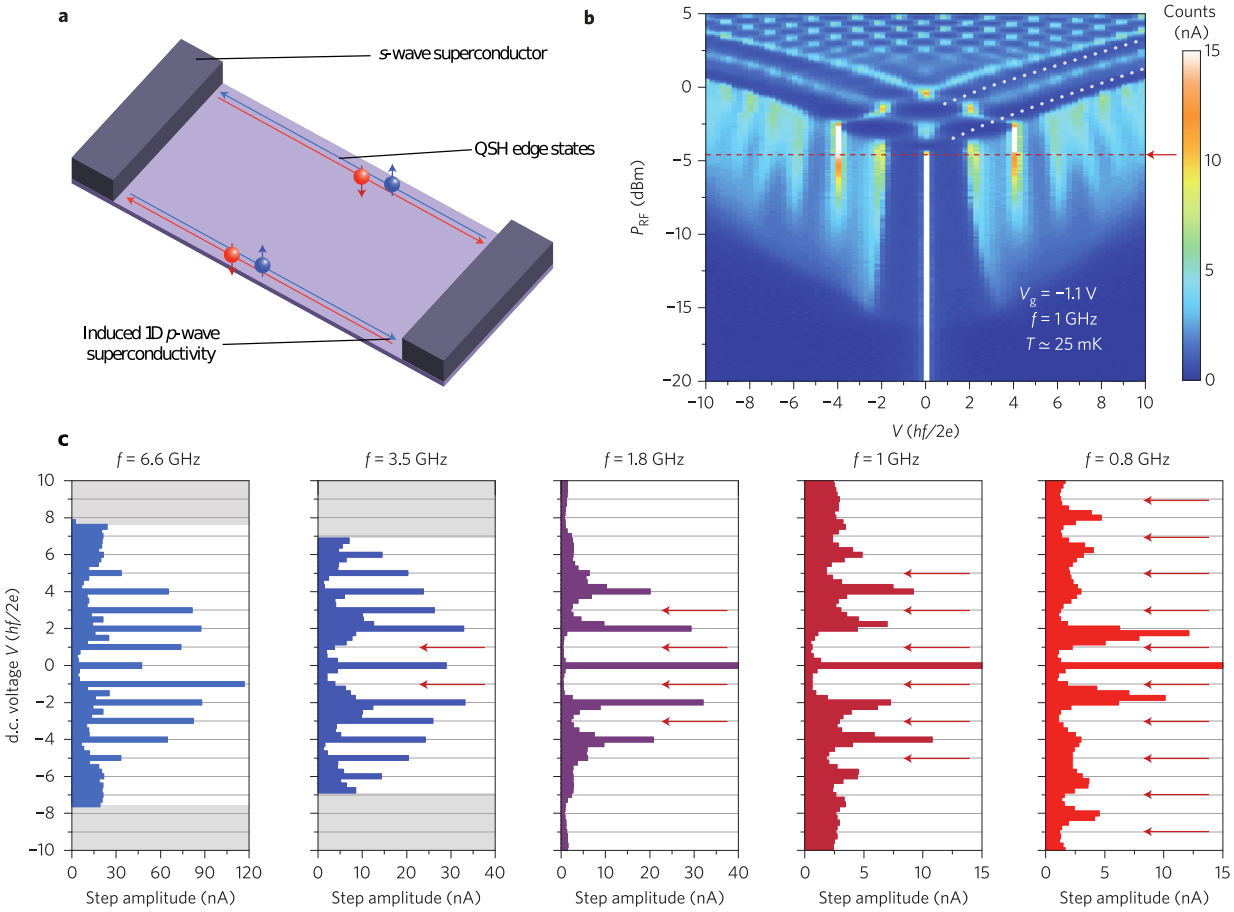

Figure 4.18. – a) Schematic of the device. The 2D topological insulator HgTe in contact with two s-wave superconducting leads produces a quantum spin Hall effect: Two counter propagating modes circulated at the border of the TI. These modes are spin polarized. b) Response to an RF excitation: Map of the voltage distributions with voltage bins in normalized units ($hf_{\mathrm{RF}}/2e$) versus the RF excitation power. Steps $n = 1$ and 3 are completely suppressed in the low power regime. In the oscillatory high RF power regime, dark fringes (white dotted lines) develop as the first and third oscillations are suppressed. The red dashed line indicates the RF power at which c) is applied. c) Histograms of the voltage distribution obtained for different irradiation frequencies. At high frequency, all the steps are visible whereas for lower frequencies, we observe the gradual disappearance of the odd steps. The red arrows point at the absence of the odd steps.Legend and figure extracted from [25].

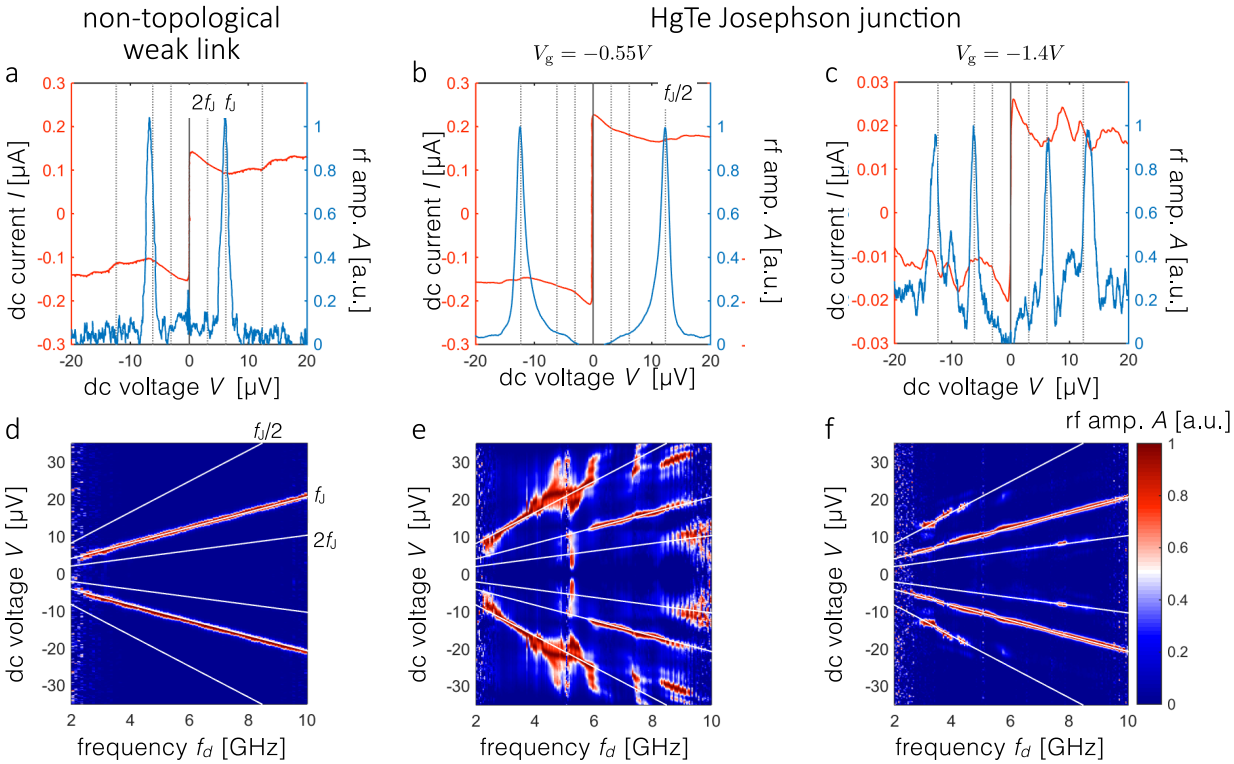

Figure 4.19. – Measurement of the AC Josephson effect of a JJ by probing its electromagnetic emission. The junction is made of a non-topological weak link on the left column and made of HgTe for the middle and right columns at two different back-gate voltages.
Upper part: the graphs represent $I-V$ characteristics (red lines) and emission spectrum at fixed detection frequency $f_\mathrm{d} = 3\,\mathrm{GHz}$ (blue lines). The gray dotted lines are guide line at frequency $2f_\mathrm{J}$ (innermost), f_J and $f_\mathrm{J}/2$ (outermost lines).
Lower part: colored plot of the power emitted by the junction versus the detection frequency f_d and the biased DC voltage V. The white lines are guides that represents the emission of the fractional ($f_\mathrm{J}/2$), conventional (f_J) and doubled ($2f_\mathrm{J}$) AC Josephson effect. Adapted from [46].

logical insulator in a quantum spin Hall regime. They performed Shapiro measurements and observed the progressive disappearance of all the even Shapiro steps when decreasing the irradiation frequency. Their results are shown in figure 4.18.

There exists no equivalent results as convincing as the latter on Josephson junctions on 3D topological insulators.

3.3.3 Emission measurement

The last observation of the fractional AC Josephson effect has been done by measuring the electromagnetic environment of a voltage biased 2D TJJ fabricated on HgTe. The results are shown in figure 4.19. One sees a conventional JJ on the left column which emits only at the Josephson frequency f_J. Whereas the HgTe Josephson junction has two regimes: at the gate voltage $V_\mathrm{g} = -0.55\,\mathrm{V}$, there is a clear emission at half the Josephson frequency that reduces drastically at lower gate voltage.

Measuring the emission at half the Josephson frequency is a very promising results. However, according to ref [152], the emission spectrum could resembles the fractional AC Josephson effect even in a non-topological system. In particular, Landau-Zener transitions can occur between high transmitted channels and have a similar signature as the 4π-tABS. This subject is discussed in Appendix C of this thesis.

Now that we have presented the state of the art on the possible observations of the coveted 4π-tABS, we present a phenomenon that explains the absence of signature of this state in the current-phase relation: quasiparticle poisoning. It will also be used in the next chapter to give a possible origin of the observation of the even/odd effect on only the first Shapiro step.

4 Poisoning

Quasiparticle poisoning describes the interaction of Andreev bound states with a continuum of states with the help of an external excitation (phonons, photons). This process is responsible for the relaxation of excited states to their ground states.

Poisoning plays an important role for studying the dynamics of a single ABS, or when, in particular, the junction parity has to be conserved.

4.1 What is Poisoning ?

The fermion parity of a Josephson junction is defined by the parity of the total number of electrons populating the ABS. It can be even or odd. Poisoning can change this parity when an excited Andreev bound state relaxes to a lower energy state by accepting or giving a quasi-particle to the continuum (see figure 4.20). This process has been first observed in 1994 in single-Cooper-pair devices [92]. Later the noise created by this switching process has been investigated theoretically in a quantum point contact by Averin [11, 12]. More recently, it has been possible to measure the dynamic associated to poisoning in spectroscopy measurements of the Andreev bound states [28, 187].

The case of conventional short ballistic JJ is drawn in figure 4.20 a). Excited ABSs can relax by accepting an electron (giving a hole) from the lower continuum of state or giving an electron to the upper continuum. This process is possible thanks to an external excitation of energy higher than the energy difference between the ABS and the continuum. The probability for this switching process is [11]:

$$p_{\mathrm{sw}}(\phi) \propto e^{\frac{\Delta - E(\phi)}{k_{\mathrm{B}}T}} \tag{4.56}$$

This phase dependent switching probability has been used to simulate the impact of poisoning on the current-voltage characteristic in ref [11].

4.2 How poisoning affects the 4π periodic ABS

Poisoning happens in a particular way with the 4π t-ABS. It is shown in figure 4.20 b) and has been theoretically studied in the case of topological JJs by [62, 79, 173]. The two main differences are (1) the state $|-\rangle$ is half of the time at a higher energy than state $|+\rangle$. Which means that the ground state is not always the same state. (2) As the state $|+\rangle$ is not spin degenerated, the two electrons of a Cooper pair can not populate simultaneously the topological ABS. This later can be used as a signature of the 4π-tABS by a fast measurement of the switching current of a TJJ [134].

In the case of a TJJ, the 4π-tABS has a maximum energy [25] $E'_J = \Delta_0\sqrt{D}$ given in Eq. (4.44) smaller than the conventional ABSs which have an energy close to the superconducting energy gap. Hence the topological ABS is isolated from the continuum of states by an almost constant energy gap Δ_{mini} (see figure 4.20 b)). The probability of switching from the upper state to the lower state simplifies to [62]:

$$p_{\text{sw}} \propto e^{-\frac{\Delta_{\text{mini}}}{k_B T}} \tag{4.57}$$

During each poisoning process, the fermion parity of the 4π-tABS is changed. Hence the resulting energy-phase relation becomes 2π periodic. This process explains why the measurement of the current-phase relation of TJJs is up to now unsuccessful (cf section 3.2) The only way to keep the 4π periodicity of the 4π-tABS is by driving the system

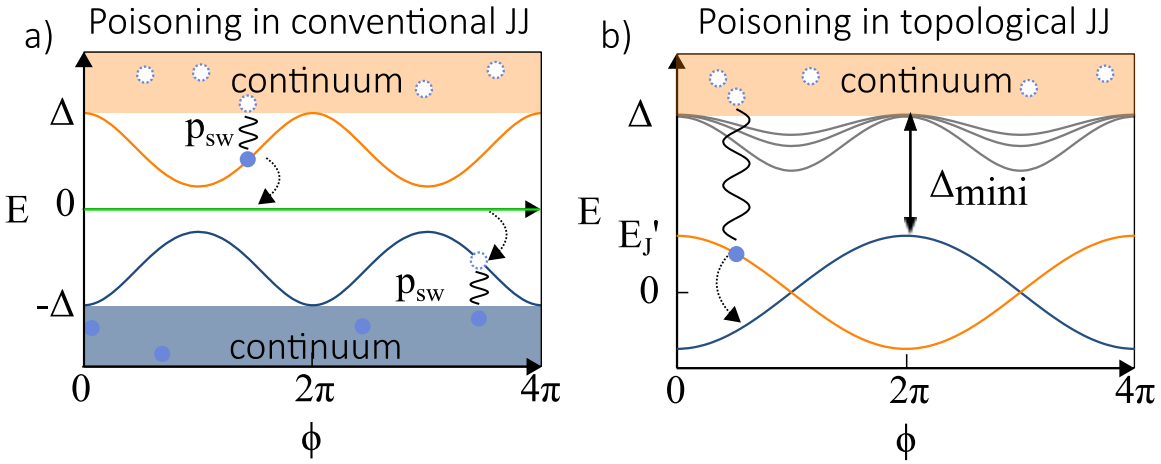

Figure 4.20. – a) Schematic of the poisoning process in a conventional short JJ. Excited ABSs (orange or green) can relax by interacting with available states present in the continuum (blue circles). Thanks to external excitations (phonons or photons), electrons are taken out from the ABSs to the continuum which changes the population of the ABSs. This process has a switching probability p_{sw} which depends on the (phase dependent) energy difference between the ABS and the continuum. When an ABS has the same energy as the continuum, it necessarily relaxes to its lowest energy state. b) In the case of a topological JJ, the 4π-tABS is either empty (blue) or occupied (orange). When the phase $\pi < \phi < 3\pi$, the occupied state is not the lowest energy state. The system can relax thanks to an external excitation by feeding the continuum with an electron.

25. The transmission is not perfect in the presence of a magnetic field.

faster than the time of poisoning processes. This condition is provided when probing the AC Josephson effect.

More precisely, the measurement time has to be shorter than the quasiparticle lifetime of the 4π-tABS. These considerations have been investigated theoretically by Badiane et al [79] in the case of a Shapiro measurement. They conclude that in order to detect the fractional AC Josephson effect in a Shapiro measurement, the adjustment time of the phase τ_{R} has to be shorter than the lifetime τ_{MF} of the 4π-tABS. τ_{R} depends on the driving frequency f_{RF} by the relation $\tau_{\mathrm{R}} = \frac{1}{e\mathcal{R}I_{\mathrm{n}}}$ with $\mathcal{R}$ the resistance of the electrical circuit in which the junction is embedded [26] and I_{n} is the height of n$^{\mathrm{th}}$ the Shapiro step at $V_{\mathrm{n}} = n\frac{hf_{\mathrm{RF}}}{2e}$. In the case of a voltage biased junction, this height is given by : $I_{\mathrm{n}} = I_{\mathrm{c}}|J_{\mathrm{n}}(\alpha)|$ with I_{c} the critical current, J_{n} the Bessel function and $\alpha = \frac{eV_{\mathrm{RF}}}{2\pi f_{\mathrm{RF}}}$ [27]. In the case of current biased Josephson junction, I_{n} has to be calculated. This will be done in next chapter.

This condition sets a lower limit on the excitation frequency to detect the 4π-tABS by Shapiro measurement. If we go too low in frequency, the 4π-tABS will be poisoned and loose its 4π periodicity.

26. We will see in next chapter that we suppose $\mathcal{R} \approx R_{\mathrm{N}}$ the normal state resistance of the junction.
27. This dependence is reviewed in detail in next chapter.

Summary

In this chapter we have introduced the physics of Josephson junctions. We have focused on the Bogoliubov-de-Gennes approach in the case of a short ballistic junction to study the Andreev bound states and then we have detailed the difference between the short junction regime and the other transport regimes.

Then we introduced the physics associated with the Majorana bound states in condensed matter. We have first discussed topological superconductivity and in particular the unconventional $p_x + ip_y$ superconductivity. We have seen how a topological Josephson junction exhibits a topologically protected 4π periodic Andreev bound state (4π-tABS) which leads to a 4π periodic current phase relation and thus a fractional AC Josephson effect.

We have reviewed some existing experimental observation of Majorana bound state. One of the best way to evidence the 4π-tABS is by performing a Shapiro steps measurement. A convincing signature is the observation of the even/odd effect when lowering the frequency of excitation f_{RF}. This effect was clearly observed in a quantum spin Hall system based on HgTe [25].

Finally, we have seen how quasiparticle poisoning can destroy the 4π-tABS. To prevent this poisoning to affect the 4π periodicity of the topological state, we need to probe the system in an AC experiment, like the Shapiro measurement, where the system is driven faster than the time-scale of quasiparticle poisoning.

Chapter 5

Resistively shunted junction model for topological Josephson junctions

BEFORE presenting our experimental observation of the fractional AC Josephson effect on a topological Josephson junction (TJJ), we introduce a simple model that gives, as we will see, a good description of SNS Josephson junctions. The so-called resistively shunted junction (RSJ) model is used to investigate the visibility of the fractional AC Josephson effect of a single topologically-protected 4π-periodic Andreev bound state (4π-tABS) among other conventional Andreev bound states (ABSs).

In this chapter we first introduce the RSJ model and use it to better understand a Shapiro measurement and decipher the exact behavior of a Josephson junction when irradiated with radio frequencies (RF).

A second aspect developed in this chapter is the impact of electron overheating. When driven out-of-equilibrium, the electronic bath of a junction is heated up by Joule heating. We include this consideration in the RSJ model in a self consistent manner.

Then we use the RSJ model to simulate a Shapiro measurement with (1) a single 4π-periodic mode and (2) a mix of conventional 2π-periodic supercurrent with a small 4π-periodic supercurrent. This leads us to a simple explanation to account for the absence of only the $n = 1$ Shapiro step in the fractional AC Josephson effect.

1 Introduction to the RSJ model

THE resistively Shunted Josephson junction (RSJ) model was first reported by McCumber, Stewart and Johnson [89, 120, 163]. The model considers an ideal Josephson junction in parallel with a resistor (cf figure 5.1). The resistor enables quasiparticle transport through the junction. This model allows us to have access to the dynamics of the superconducting phase ϕ and also to simulate the current-voltage (IV) characteristics of Josephson junctions. The parallel resistor is a parameter that is usually approximated by the normal state resistance R_N of the JJ [1].

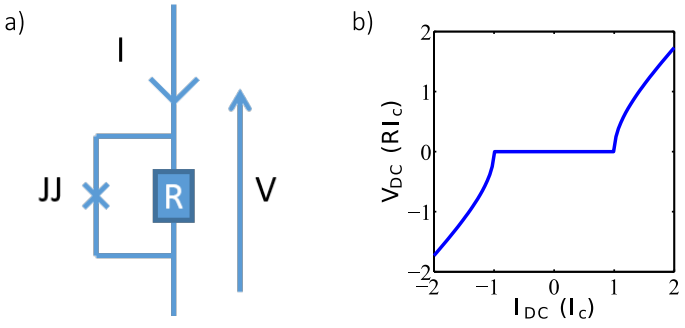

Figure 5.1. – a) Schematic of the RSJ model. The total current through the circuit is denoted by I and the voltage across the JJ by V. b) VI characteristic of a current biased Josephson junction modeled by the RSJ model.

1. In our experiments discussed in the next chapter, R_N is in the order of tens of Ohms.

In this section we use the RSJ model to simulate IV characteristics of a conventional Josephson junction. After a brief example, we add the key ingredient for Shapiro measurement: radio frequency (RF) irradiation.

1.1 DC biased junction

A Josephson junction can be either voltage or current biased. We review here both cases in the DC regime. In the next section will be add an AC component to the biasing.

Voltage biased junction The case of DC voltage biased junction is straightforward, using Eq. (4.3), the phase increases linearly with time and the supercurrent oscillates at the Josephson frequency $f_J \equiv \frac{2eV}{h}$. The resistive current follows Ohm's law. The total current through the device is the sum of the supercurrent and the resistive current :

$$I = I_c \sin(2\pi f_J t + \phi_{ini}) + \frac{V_{DC}}{R} \tag{5.1}$$

with ϕ_{ini} a phase offset that depends on the initial conditions. This equation has the general solution:

$$\begin{aligned} I_{DC} &= I_c \sin\phi_{ini} && \text{for } V_{DC} = 0 \\ I_{DC} &= \frac{V_{DC}}{R} && \text{for } V_{DC} \neq 0 \end{aligned} \tag{5.2}$$

Current biased junction In the DC current biased case, with the Josephson relations, the current flowing through the circuit follows:

$$\begin{aligned} I_{DC} &= \frac{V}{R} + I_c \sin\phi \\ \frac{d\phi}{dt} &= \frac{2eRI_c}{\hbar}(i_{DC} - \sin\phi) \end{aligned} \tag{5.3}$$

with $i_{DC} = \frac{I_{DC}}{I_c}$ the reduced DC current. This first order differential equation in ϕ has a characteristic relaxation time [2]:

$$\tau_J = \frac{\hbar}{2eRI_c} \tag{5.4}$$

For $i_{DC} > 1$, an analytical solution exists for this equation [3], that is periodic in time with

2. We can find this relaxation time by simplifying Eq. (5.3) for $I_{DC} = 0$ and using a first order approximation of the sine function: $\frac{d\phi}{dt} = -\frac{2eRI_c}{\hbar}\phi$

3. The analytical solution of Eq. (5.3) reads [16]:

$$\phi(t) = 2\,\mathrm{atan}\left[-i_{DC} + \frac{\sqrt{i_{DC}^2 - 1}}{i_{DC}} \tan\left(\frac{t\sqrt{i_{DC}^2 - 1}}{2\tau_J}\right)\right] \tag{5.5}$$

with $\tau_J = \frac{\hbar}{2eRI_c}$.

a period $T_\phi = \frac{h}{eR\sqrt{I_{\mathrm{DC}}^2 - I_c^2}}$. The average time derivative of ϕ gives the DC voltage across the junction:

$$V_{\mathrm{DC}} = R\sqrt{I_{\mathrm{DC}}^2 - I_c^2} \tag{5.6}$$

This simple VI characteristic is drawn in figure 5.1. We observe the absence of voltage until I_{DC} reaches the critical current. At high current bias, the voltage follows a linear increase close to the Ohm's law.

1.2 AC biased junction

The RSJ model becomes more complex when adding an AC component to the DC bias. There still exists an analytical solution in the case of voltage biased junction. However, for the current bias case, we need to use numerics to obtain the current-voltage characteristic.

1.2.1 Shapiro steps of a voltage biased junction : Analytical solution

In the case of a voltage biased junction, the RF irradiation is taken into account by adding an oscillating voltage at frequency f_{RF} : $V_{\mathrm{RF}}\cos(2\pi f_{\mathrm{RF}}t)$ to the DC voltage V_{DC}. The phase dynamic follows :

$$\frac{\hbar}{2e}\frac{d\phi(t)}{dt} = V_{\mathrm{DC}} + V_{\mathrm{RF}}\cos(2\pi f_{\mathrm{RF}}t) \tag{5.7}$$

Integrating over time gives :

$$\phi(t) = \phi_{ini} + 2\pi f_{\mathrm{J}}\cdot t + \frac{V_{\mathrm{RF}}}{V_{\mathrm{DC}}}\frac{f_{\mathrm{J}}}{f_{\mathrm{RF}}}\sin(2\pi f_{\mathrm{RF}}t) \tag{5.8}$$

with ϕ_{ini} an arbitrary phase shift and $f_{\mathrm{J}} = \frac{2eV_{\mathrm{DC}}}{h}$ the Josephson frequency. In a voltage biased junction, the phase increases linearly (due to V_{DC}) with an oscillatory part coming from the RF irradiation. Thus, the supercurrent I_{S} reads:

$$I_{\mathrm{S}}(t) = I_{\mathrm{c}}\sin\left(\phi_0 + 2\pi f_{\mathrm{J}}\cdot t + \frac{V_{\mathrm{RF}}}{V_{\mathrm{DC}}}\frac{f_J}{f_{\mathrm{RF}}}\sin(2\pi f_{\mathrm{RF}}t)\right) \tag{5.9}$$

This expression can be rewritten as a sum of Bessel function (cf p.292 in [16]):

$$I_{\mathrm{S}}(t) = I_{\mathrm{c}}\sum_{n=-\infty}^{n=+\infty}(-1)^n\cdot J_{\mathrm{n}}\left(\frac{2eV_{\mathrm{RF}}}{hf_{\mathrm{RF}}}\right)\cdot\sin(\phi_0 + 2\pi t(f_{\mathrm{J}} - nf_{\mathrm{RF}})) \tag{5.10}$$

with $n \in \mathbb{N}$ and J_{n} is the n^{th} Bessel function of the first kind. In order for the supercurrent to have a non zero average value ($< I_{\mathrm{S}} >_t \neq 0$) the sine should not oscillate in time :

$$\boxed{nf_{\mathrm{RF}} = f_{\mathrm{J}} \;\Leftrightarrow\; V_{\mathrm{DC}} = n\cdot\frac{hf_{\mathrm{RF}}}{2e} \equiv V_{\mathrm{n}}} \tag{5.11}$$

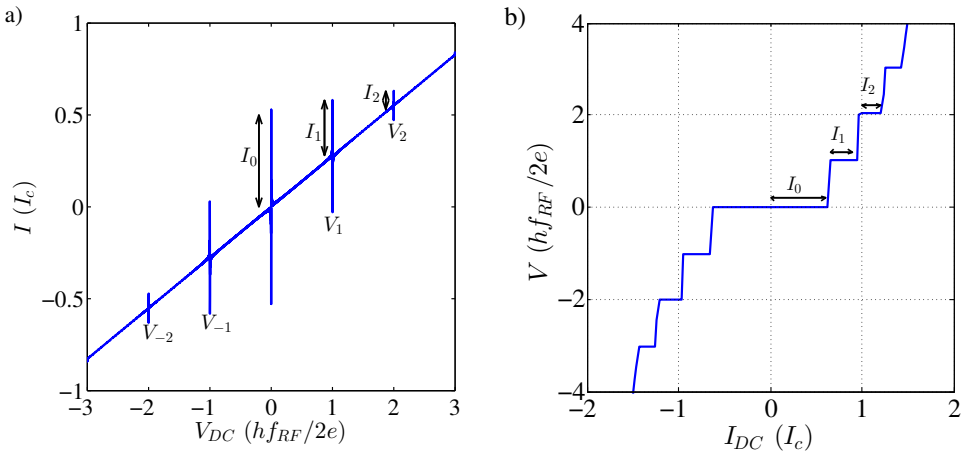

Figure 5.2. – Simulation of a voltage (a) and current (b) biased Josephson junction irradiated with a 2 GHz radio frequency, a bias resistance $R = 30\,\Omega$, a critical current $I_c = 500\,\text{nA}$, an RF voltage $V_{RF} = 4\,\mu\text{V}$ and an RF current $I_{RF} = 0.3\,\mu\text{A}$.

If the applied voltage is $V_{DC} = V_n$, a voltage plateau at V_n with a width in current I_n is obtained :

$$I_n(V_{RF}) = 2I_c J_n\left(\frac{2eV_{RF}}{hf_{RF}}\right) \tag{5.12}$$

This analytical solution gives a general idea of the behavior of such a system: When irradiating a JJ at a frequency f_{RF}, the superconducting phase ϕ locks-in at multiples of the irradiation frequency. In this case, the only possible DC voltages across the JJ are Shapiro voltages $V_n = n\frac{hf_{RF}}{2e}$. This results experimentally as equidistant steps in the current-voltage (IV) characteristics [157]. Each step has a current width I_n (cf figure 5.2) which follows a Bessel function.

1.2.2 Shapiro steps of a current biased junction: numerics

There is no analytical solution describing a current biased junction under radio frequencies. However we can still use the RSJ model to predict its behavior. The RF irradiation is taken into account in the RSJ model by adding an oscillating current ($I_{RF}\cos(2\pi f_{RF}t)$) to the bias current (I_{DC}). Summing up all contributions leads to :

$$I_{tot}(t) = I_{DC} + I_{RF}\sin(2\pi f_{RF}t) = \frac{\hbar}{2eR}\frac{d\phi}{dt} + I_c\sin(\phi) \tag{5.13}$$

which gives :

$$\boxed{\frac{d\phi}{dt} = \frac{1}{\tau_J}\left[i_{DC} + i_{RF}\sin(2\pi f_{RF}t) - \sin(\phi)\right]} \tag{5.14}$$

with i being the reduced current $i = \frac{I}{I_c}$ and $\tau_J = \frac{\hbar}{2eRI_c}$ the phase relaxation time. This is a non-linear first-order differential equation which has to be solved numerically for each pair of variables (I_{DC}, I_{RF}).

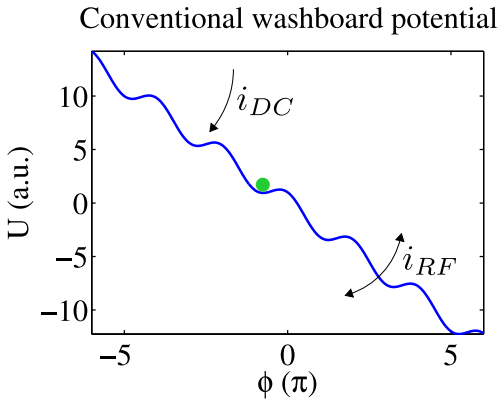

Figure 5.3. – Schematic of the tilted washboard potential. The motion of a particle in this potential has the same behavior of a JJ described by the RSJ model. The linear tilt of the potential is proportional to i_{DC} and an RF component i_{RF} changes slightly this tilt periodically in time.

Tilted washboard potential To have a better understanding of the system, we can use the standard picture of a rolling massless particle at position ϕ on a tilted washboard potential[4] $U(\phi) = \phi(i_{\mathrm{DC}} + i_{\mathrm{RF}} \sin(2\pi f_{\mathrm{RF}} t)) + \cos\phi$ represented in figure 5.3.

In the DC biased case, as long as $i_{\mathrm{DC}} < 1$, the particle is trapped inside a potential minimum and the phase is constant over time: No voltage appears across the junction. When $i_{\mathrm{DC}} > 1$, the tilt is large enough to cancel the barrier potential and the particle rolls down the washboard. A finite voltage appears at the junction.

Applying an RF irradiation makes the washboard to oscillate in time with an amplitude i_{RF}. If during an RF oscillation the tilt of the washboard is larger than the barrier, the particle will roll down by a few minima before the tilt decreases at the end of the RF period. The number n of minima over which the particle has rolled down during an RF period determines the voltage V_n across the junction.

Simulation of Shapiro steps We present in figure 5.4 the numerical simulation for the RSJ model Eq. (5.14) with $R = 30\,\Omega$, $I_{\mathrm{c}} = 500\,\mathrm{nA}$ and an RF current at $f = 2\,\mathrm{GHz}$. These parameters are close to the experimental ones seen in chapter 6 of sample LC099-JJ4. We solved the time-differential equation by using the 4^{th} order of the Runge-Kutta algorithm.

The resulting VI characteristics (figure 5.4b) shows plateaus in voltage at the expected values V_{n} for Shapiro steps. To study the evolution of these steps as a function of the RF power and the DC biased current, a colored plot of the differential resistance dV/dI is shown in figure 5.4a. Each black region corresponds to a Shapiro step in the VI characteristic. At low RF power (lower part of the figure), the influence of the irradiation is negligible and only the plateau at zero voltage is seen up to the critical current, corresponding to the usual superconducting branch of a VI characteristic. On increasing RF power, the Shapiro

4. By integrating over the phase Eq. (5.14) we get : $\frac{1}{2}\left(\frac{d\phi}{dt}\right)^2 = \frac{2eRI_{\mathrm{c}}}{\hbar}\left[\phi(i_{\mathrm{DC}} + i_{\mathrm{RF}}\sin(2\pi f_{\mathrm{RF}} t)) + \cos\phi\right]$

5. $P_{\mathrm{RF}}[\mathrm{dB\,m}] = 10\log\left(10^3 \cdot P_{\mathrm{RF}}[\mathrm{W}]\right) = 30 + 10\log\left(I^2_{\mathrm{RF}}[\mathrm{A}]\right)$

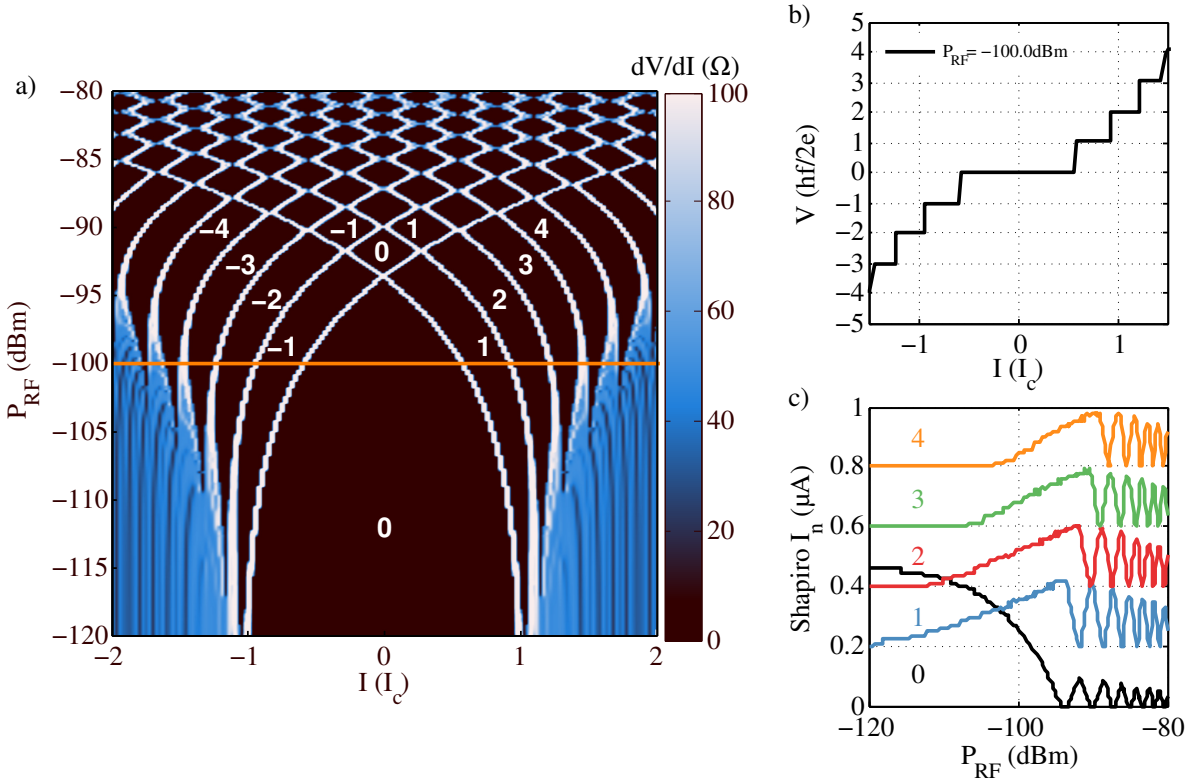

Figure 5.4. – Results of the RSJ model on current-biased junction irradiated at 2 GHz, with $R = 30\,\Omega$ and $I_c = 500\,\text{nA}$. a) Differential resistance versus current bias and RF power [5]. The black regions correspond to plateaus in the voltage-current characteristic. The horizontal orange line indicates the line-cut corresponding to b) and the first plateaus are indexed with their numbers. b) Current–voltage characteristic of a JJ at an irradiation power of $-100\,\text{dB m}$. The voltage is in units of $hf_{\text{RF}}/2e$ and the bias current in units of I_c. c) Amplitude of each Shapiro step versus radio-frequency power.

steps appear gradually starting from step $n = 1$.

The amplitude in current of each voltage plateau $I_n(P_{\text{RF}})$ is shown in figure 5.4c. This amplitude does not follow the expected Bessel oscillations from the voltage-bias solution (5.12). The system tends to the 'Bessel like' dependency at a higher RF frequency (good agreement at 5 GHz cf figure 5.12 right panel).

This behavior can be explained by comparing the phase adjustment time τ_J and the period of the driving frequency $1/f_{\text{RF}}$ through the parameter Ω defined as :

$$\Omega = f_{\text{RF}} \cdot \tau_J \tag{5.15}$$

When $\Omega \ll 1$ the junction has enough time to relax and to be in quasi equilibrium during one RF oscillation. For a faster driving frequency, $\Omega \lesssim 1$, the system is close to the voltage bias solution with $I_n(I_{\text{RF}})$ that oscillates like Bessel functions with rounded lobes. However, if we drive the system in a regime much faster than the phase relaxation time ($\Omega \gg 1$), then the Shapiro steps are suppressed [6].

6. We have simulated a JJ in a regime where $\Omega = 500\,\text{GHz} \cdot 0.14\,\text{ns} = 69$. The Shapiro steps are not visible any more but only appear as kinks in the voltage–current characteristic.

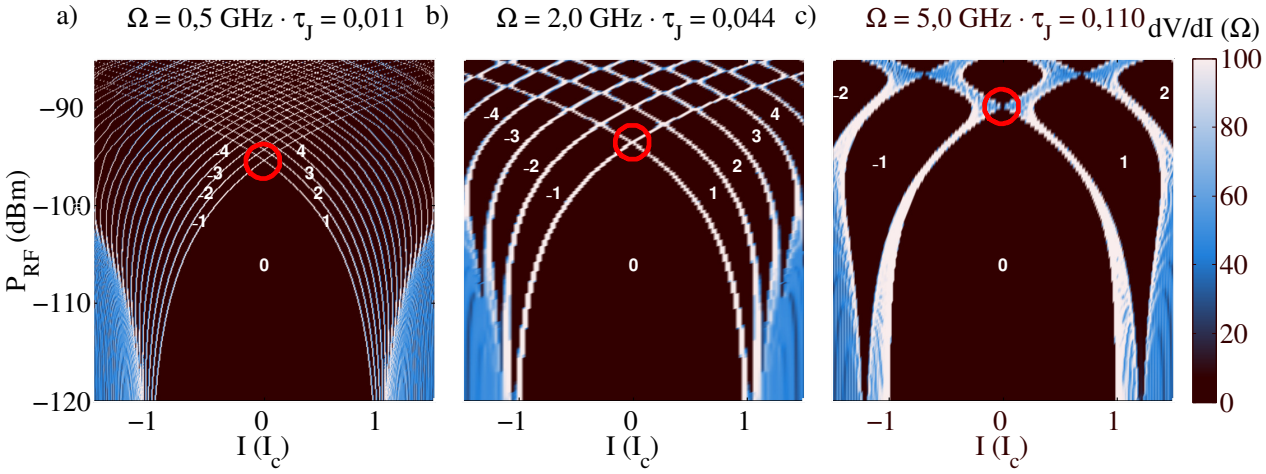

Figure 5.5. – Results of the RSJ model of a conventional JJ at three different frequencies with $R = 30\,\Omega$ and $I_c = 500\,\mathrm{nA}$. The power for which the critical current vanishes (red circle) depends on the frequency.

Finally, depending on the RF frequency, there is a varying minimum power for Shapiro steps to show up. This power is less at low frequency than at high frequency, as be seen in figure 5.5.

The red circle in figure 5.5 in the color-map indicates the RF power necessary to affect the system. No theoretical prediction exists on its position in the (I_c, P_{RF}) map. In fact, the position of this point also depends on the phase adjustment time. The smaller the τ_J, the less the position of this point is shifted at high frequency.

Despite the simplicity of the RSJ model, it enables a dynamical description of the Josephson junction. Experimentally, Josephson junctions cannot be always described by this RSJ model. Hysteretic VI characteristics for instance are not compatible with the model described in this section. In the next section, we introduce thermal effects that can account for this hysteresis.

2 Hot electrons effect in the RSJ model

The thermodynamic of a mesoscopic electronic device can be decomposed into two interacting subsystems: the electron bath and the phonon bath at the temperatures T_{el} and T_{ph} respectively. Most of the time, a device is resting on a substrate which has a constant phonon temperature T_{bath} [7]. A thermal equilibrium between the phonons of the system and the one from the substrate is expected (cf figure 5.6).

The standard behavior of SNS junction described in figure 5.1b is only occasionally observed. Frequently, the experimental VI characteristics is hysteretic as shown in figure 5.7. This behavior was interpreted by ref [38] to originate from electron overheating. The interpretation is the following. Electrons heat up when the junction is in the resistive

7. This general bath also contains the temperature of the electrodes connected to the mesoscopic system.

branch ($V \neq 0$) and cool down to the phonon temperature in the superconducting branch ($V = 0$). Hence, in the superconducting branch, the electrons have a temperature T_{cold} and can withstand a large amount of supercurrent up to the switching current [8] $I_{\text{sw}} \approx I_{\text{c}}(T_{\text{cold}})$, whereas in the resistive branch, the junction is hot and transitions only at the retrapping current $I_{\text{r}} \approx I_{\text{c}}(T_{\text{hot}}) < I_{\text{c}}(T_{\text{cold}})$.

2.1 Thermal effects model

In this section we consider a current biased Josephson junction modeled by the RSJ model. We estimate the power dissipated by Joule heating and calculate the heat balance inside this system to simulate the effective electronic temperature during a Shapiro measurement.

Joule heating in Josephson junctions In a current biased junction, the source of heat mainly originates from Joule heating [9].

$$P_{\text{Joule}}(t) = I(t) \cdot V(t) \tag{5.16}$$

Using Eq. (5.14) with DC and AC current biasing, the Joule power reads:

$$\begin{aligned} P_{\text{Joule}}(t) =& \frac{\hbar}{2e}\frac{d\phi}{dt} \cdot I_{\text{c}}[i_{\text{DC}} + i_{\text{RF}} \sin(2\pi f_{\text{RF}} t)] \\ =& RI_{\text{c}}^2 \left[i_{\text{DC}} + i_{\text{RF}} \sin(2\pi f_{\text{RF}} t) - \sin\phi(t)\right] \cdot \left[i_{DC} + i_{\text{RF}} \sin(2\pi f_{\text{RF}} t)\right] \end{aligned} \tag{5.17}$$

The time average of the heating power reads :

$$< P_{\text{Joule}} >_t = RI_{\text{c}}^2 \left[i_{\text{DC}}^2 + \frac{i_{\text{RF}}^2}{2} - i_{\text{RF}} < \sin\phi(t) \cdot \sin\left(2\pi f_{\text{RF}} t\right) >_t \right] \tag{5.18}$$

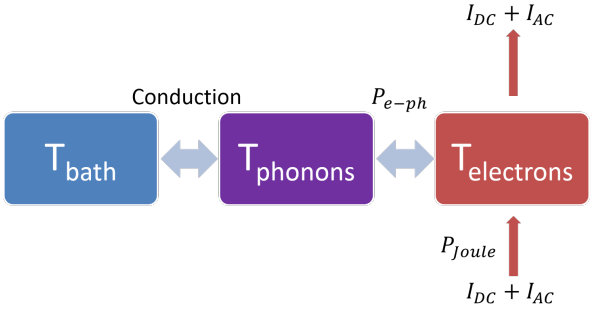

Figure 5.6. – Schematic of heat transfer between the three baths at different temperatures defined in a mesoscopic system. Heating comes mainly from Joule heating and is dissipated through the phonons of the system and the substrate.

8. The critical current is the theoretical maximal current a junction can withstand at finite temperature whereas the switching current is the measured value. We have $\max I_{\text{sw}} = I_{\text{c}}$

9. This means that the bath temperature is constant. We will see that it is not always the case experimentally.

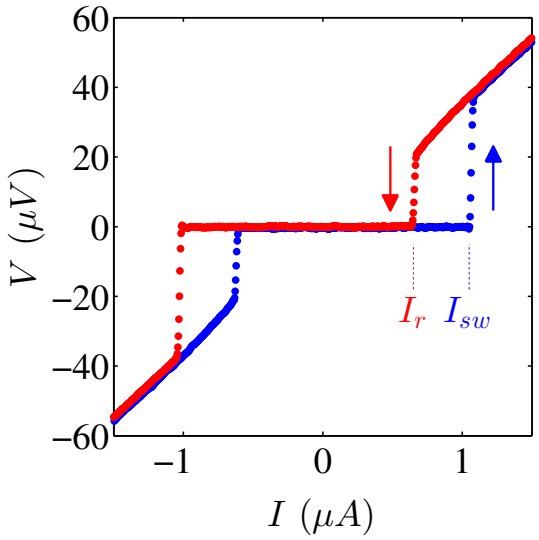

Figure 5.7. – Measured voltage–current characteristic of a Josephson junction. The up and down current sweeps do not overlap: The switching current I_{sw} is higher than the retrapping current I_{r}.

If Shapiro steps are visible in the VI characteristics, then the phase is locked at a multiple n of the RF frequency: $\phi(t) = n \cdot \frac{hf_{\mathrm{RF}}}{2e} t$. In that case, Joule heating has a specific expression :

$$< P_{\mathrm{Joule,n}} >_t = RI_{\mathrm{c}}^2 \left[i_{\mathrm{DC}}^2 + \frac{i_{\mathrm{RF}}^2}{2} - i_{\mathrm{RF}} \delta_{n,1}/2 \right] \tag{5.19}$$

with $\delta_{m,n}$ the Dirac delta function. We can draw two conclusions from this equation: (1) Even without DC voltage across the junction ($n = 0$), the RF irradiation has a heating effect. (2) The plateau $n = 1$ is slightly less heated than the other Shapiro steps.

Heat balance When driven out of equilibrium, the Joule heating is compensated by the electron-phonon coupling [68, 177]:

$$P_{\mathrm{el-ph}} = \Sigma \mathcal{V} (T_{\mathrm{el}}^5 - T_{\mathrm{ph}}^5) \tag{5.20}$$

with $\mathcal{V}$ being the volume of the Josephson junction and Σ the electron-phonon coupling constant of the normal material [10].

As long as the RF excitation is faster than the electron-phonon scattering rate, the temperature can be considered as almost constant at a given pair (I_{DC}, I_{RF}). A constant T_{el} means that $P_{\mathrm{el-ph}} =< P_{\mathrm{Joule}} >_t$. In conclusion, the electronic temperature can be estimated by :

$$T_{\mathrm{el}} = \sqrt[5]{T_{\mathrm{ph}}^5 + \frac{< P_{\mathrm{Joule}} >_t}{\Sigma V_{\mathrm{JJ}}}} \tag{5.21}$$

10. Σ is around $1 \times 10^9\,\mathrm{WK^{-5}m^{-3}}$ in metals [54].

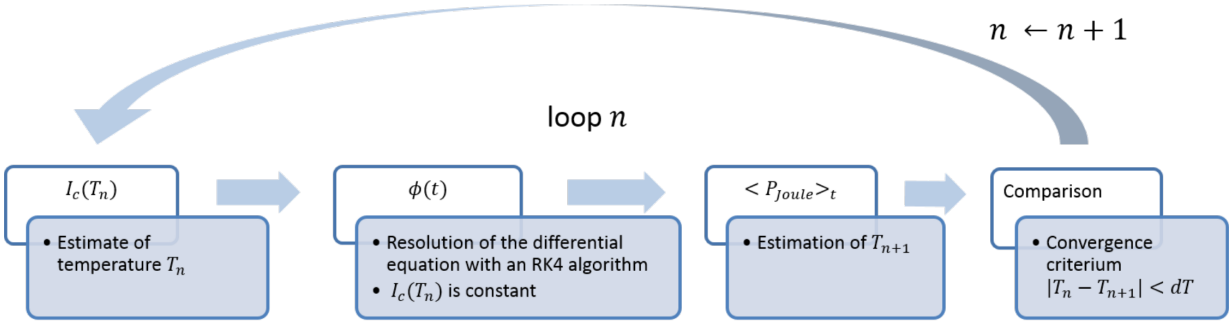

Figure 5.8. – Schematic of the algorithm used to self-consistently determine the temperature for each pair of parameter $(I_{\mathrm{DC}}, I_{\mathrm{RF}})$. We start by supposing a temperature T_{n} (The first iteration is with the bath temperature $T_0 = T_{\mathrm{bath}} = 100\,\mathrm{mK}$) which gives a critical current $I_{\mathrm{c}}(T_{\mathrm{n}})$. We solve Eq. (5.14) during a long period of time (greater than $1/f_{\mathrm{RF}}$). From $\phi(t)$ we estimate the Joule heating which gives us a new estimation of the temperature ($T_{\mathrm{n+1}}$ using Eq. (5.21)). If $|T_{\mathrm{n+1}} - T_{\mathrm{n}}|$ is small enough, we exit the convergence loop and start again for the next pair of parameter $(I_{\mathrm{DC}}, I_{\mathrm{RF}})$. If not, the calculation starts again with $T_{\mathrm{n+1}}$.

2.2 Application to the SNS junction

We have included a temperature dependence of the critical current in the RSJ model in order to understand the role of heating on the AC Josephson effect.

The algorithm used in the simulations to estimate the electron temperature is presented in figure 5.8. This algorithm calculates the theoretical temperature T_{el} for each couple (I_{DC}, I_{RF}) in the color-map of figure 5.4. Assuming a given electronic temperature T_{n}, we first estimate the critical current [11] $I_{\mathrm{c}}(T_{\mathrm{n}})$ and then solve the differential equation Eq. (5.14) that governs $\phi(t)$. From this solution, we calculate the associated Joule heating, which gives a new estimation of the electronic temperature $T_{\mathrm{n+1}}$. If the new temperature is different than the first estimated one, we iterate this process with the new temperature $T_{\mathrm{n+1}}$.

In the following paragraph, we compare this RSJ model with electron overheating to data obtained by De Cecco et al on Nb/Au/Nb long SNS Josephson junctions. The results shown in figure 5.9 are published in [43]. The junction is a gold island contacted with niobium electrodes. In figure 5.9a we observe the temperature dependence of the switching and retrapping currents. They differ below 3 K which is associated to an hysteretic behavior visible in the VI characteristics (graph c & d). This phenomenon due to heating effects is already well understood [38].

This hysteresis has an impact on the Shapiro measurement presented in graph b: We identify a clear discontinuity at $I_{\mathrm{RF}} = 0.04$. The VI characteristic hysteresis shows up at lower RF current but disappears above at higher RF current. We can easily presume that the electronic temperature in the latter regime ($I_{\mathrm{RF}} > 0.04$) is higher than 3 K.

Let us now focus on the low RF power regime ($I_{\mathrm{RF}} < 0.04$): On the positive current bias

11. To best describe the experimental conditions, we have used the experimental $I_{\mathrm{c}}(T)$ dependence in figure 5.9a which does not correspond perfectly to one of the model described in chapter 1.

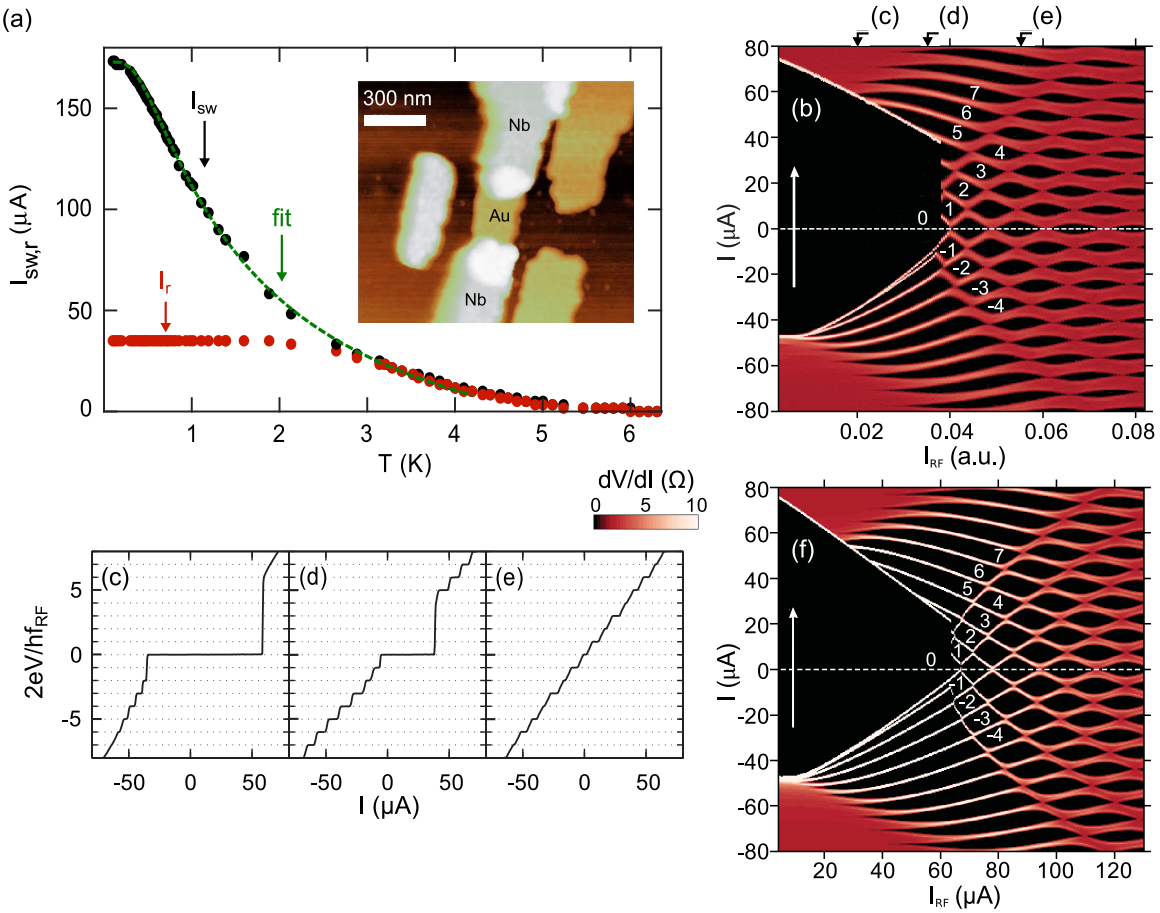

Figure 5.9. – Adapted from [43] (a) Temperature dependence of the switching current I_{sw} (black dots) and retrapping current I_{r} (red dots). The green line corresponds to a fit of Eq. (3) from [51] with the normal state resistance $R_{\mathrm{N}} = 1.7\,\Omega$ and the Thouless energy $E_{\mathrm{th}} = 49.6\,\mu\mathrm{eV}$. Inset: Atomic force microscopy image of the Nb-Au-Nb Josephson junction. (b) Differential resistance map as a function of the DC current bias I and the microwave excitation amplitude I_{RF} for a frequency $f_{\mathrm{RF}} = 6\,\mathrm{GHz}$ measured at 100 mK. The white arrow indicates the sweeping direction of the DC current bias and the white numbers index the Shapiro steps. The top black arrows point to the individual V-I curves taken at microwave drives of (c) 0.020, (d) 0.035, and (e) 0.056 (a.u.) where the measured voltage is normalized to $\frac{hf_{\mathrm{RF}}}{2e}$. (f) Simulated differential resistance map, including thermal effects following procedure described in section 2.

side ($I > 0$), the low order Shapiro plateaus are not visible. Indeed, when the junction transitions from the superconducting branch to the resistive branch, the voltage is $V \approx R_{\mathrm{N}} I_{\mathrm{sw}} = 1.7\,\Omega \cdot 40\,\mu\mathrm{A} = 68\,\mu\mathrm{V}$. This voltage corresponds to a Shapiro steps index $n \approx \frac{68\,\mu\mathrm{V}}{hf_{\mathrm{RF}}/2e} \approx 5$, which is the step that appears in line-cut d. On the negative current biased side, the step $n = -3$ is the first step visible for increasing RF current. We find exactly the same behavior in the simulations (f) and the experimental (b) Shapiro graphs.

Therefore, we believe **our model provides a remarkably good description of the VI characteristics under RF irradiation and DC bias**.

We can now consider the temperature calculated during this simulation. The electronic temperature is shown in figure 5.10a where we observe two distinct regions. At the zeroth

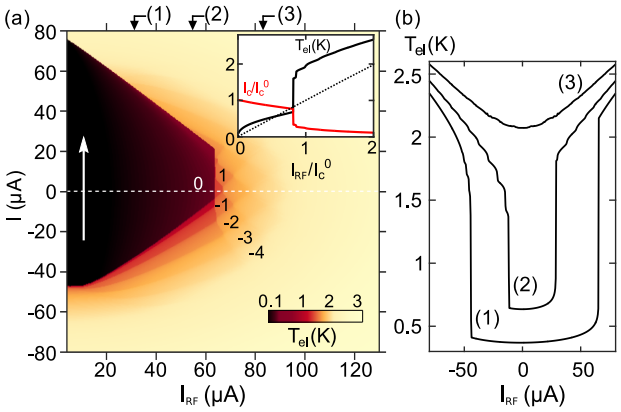

Figure 5.10 – (a) Calculated electronic temperature T_{el} map corresponding to the situation of figure 5.9, i.e. for a device at $T_{\mathrm{bath}} = 100\,\mathrm{mK}$. The first Shapiro steps are labeled. The white arrow indicates the direction of the sweep in the simulation. Inset: Line cut of this map showing the electronic temperature at zero DC bias current as a function of the microwave current and calculated value of the critical current at this electronic temperature. The dashed line indicates the $I_{\mathrm{c}}(T_{\mathrm{el}}) = I_{\mathrm{RF}}$ correspondence. (b) Line cuts of the map (a) showing the dependence of the electronic temperature as a function of the DC bias current I at different values of the microwave current I_{RF} indicated by arrows at the top of the map. Extracted from [43].

Shapiro step, T_{el} is below 1 K. As soon as $I_{\mathrm{c}}(T_{\mathrm{el}}) = I_{\mathrm{RF}}$, the system switches to a much higher temperature (close to 2 K) and is not hysteretic any-more.

The large temperature difference between the step at zero voltage and the high order steps is underlined by the graph 5.10b where line-cuts of the temperature profile are drawn.

To conclude on this study, an hysteretic behavior of a conventional JJ can be explained by a simple overheating of the electrons bath. In that case, the first Shapiro steps are absent at low radio frequency irradiation power. The very good agreement between the two colormaps (experiment and theory) bears out the validity of our model which will be insightful for our study on topological Josephson junctions.

3 RSJ model with 2π and 4π periodic current-phase relations

A topologically protected 4π periodic Andreev bound state (4π-tABS) is expected to display a fractional AC Josephson effect : $\frac{d\phi}{dt} = \frac{eV}{\hbar}$ with only even Shapiro steps. This is the so-called even/odd effect or fractional AC Josephson effect.

However, in real devices, both 2π and 4π periodic ABSs can be present (as described in chapter 4). Based on the RSJ model, this section aims at understanding the effect of the mixing of 2π and 4π periodic CPRs and discusses the condition of visibility of the even/odd effect in Shapiro measurements.

3.1 Frequency dependence of the even/odd effect

We model a TJJ composed of 2π and 4π periodic modes by two junctions in parallel (cf Figure 5.11). The junction JJ1 is conventional : $I_{\mathrm{S}}^{2\pi} = I_{\mathrm{c}}^{2\pi} \sin\phi$ and the junction JJ2 has a 4π-periodic CPR : $I_{\mathrm{S}}^{4\pi} = I_{\mathrm{c}}^{4\pi} \sin\phi/2$.

Following the same procedure as in section 1.2, the distribution of the current flowing inside the circuit leads to a 1st order differential equation for the phase [12] :

$$\frac{d\phi}{dt} = \frac{1}{\tau_{\mathrm{J}}^{tot}}\left[i_{\mathrm{DC}} + i_{\mathrm{RF}}\sin(2\pi f_{\mathrm{RF}}t) - i_{\mathrm{c}}^{2\pi}\sin(\phi) - i_{\mathrm{c}}^{4\pi}\sin(\phi/2)\right] \tag{5.22}$$

with $\tau_{\mathrm{J}}^{tot} = \frac{\hbar}{2eR(I_{\mathrm{c}}^{2\pi}+I_{\mathrm{c}}^{4\pi})}$ and all currents are normalized by the total critical current $I_{\mathrm{c}}^{tot} = I_{\mathrm{c}}^{2\pi} + I_{\mathrm{c}}^{4\pi}$. Here, $i_{\mathrm{c}}^{4\pi} = \frac{I_{\mathrm{c}}^{4\pi}}{I_{\mathrm{c}}^{2\pi}+I_{\mathrm{c}}^{4\pi}}$ gives the relative contribution of the 4π periodic supercurrent.

We have computed several simulations at a fixed normal state resistance $R = 30\,\Omega$ and critical current $I_{\mathrm{c}} = 500\,\mathrm{nA}$ for various contributions of 4π periodic supercurrent $i_{\mathrm{c}}^{4\pi}$ and at different driving frequency f_{RF}.

Figure 5.12 presents the results of simulations for 5% of 4π periodic supercurrent. At a high excitation frequency $f_{\mathrm{RF}} \geq 2\,\mathrm{GHz}$, the appearance order of the Shapiro steps is regular : the first step appearing with raising RF power is step $n = 1$, then step $n = 2$ is visible in the VI characteristic, etc... At a lower driving frequency ($f_{\mathrm{RF}} \leq 0.5\,\mathrm{GHz}$), the appearance order is drastically changed. Only even steps are visible at a low driving amplitude. Hence, the appearance order is step $n = 2$, then step $n = 4$ and, only after, the odd steps are visible.

Thus **the presence of a 4π periodic component leads at low enough frequency to a delay in the appearance order of odd Shapiro steps upon increasing P_{RF}.**

Importantly, within our studies, we observe that, whatever tiny is the 4π contribution, there will always be a **driving frequency threshold below which the even/odd effect is visible**. This threshold can be determined by comparing the relevant time scales. For a 4π periodic ABS the phase relaxation time is $\tau_{\mathrm{J}}^{4\pi} = \frac{\hbar}{eRI_{\mathrm{c}}^{4\pi}}$ (notice the absence of factor 1/2). As long as $\tau_{\mathrm{J}}^{4\pi} > 1/f_{\mathrm{RF}}$ the effects of the 4π-ABS are not visible. However, as soon as $\tau_{\mathrm{J}}^{4\pi} < 1/f_{\mathrm{RF}}$, the Shapiro pattern changes and the even steps appear at a lower driving amplitude than the odd steps : the even/odd effect appears. The range of observation of the even-odd effect is summarized in figure 5.13. The presence of only even Shapiro steps is possible for a low excitation frequency ($\Omega^{4\pi} < 1$) and a low excitation power.

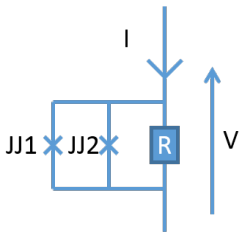

Figure 5.11. – RSJ model with two types of Josephson junctions: JJ1 has a 2π periodic current–phase relation whereas JJ2 has a 4π periodic one.

12. We choose to not have any constant dephasing between JJ1 and JJ2. In fact, a constant dephasing changes the simulations insignificantly.

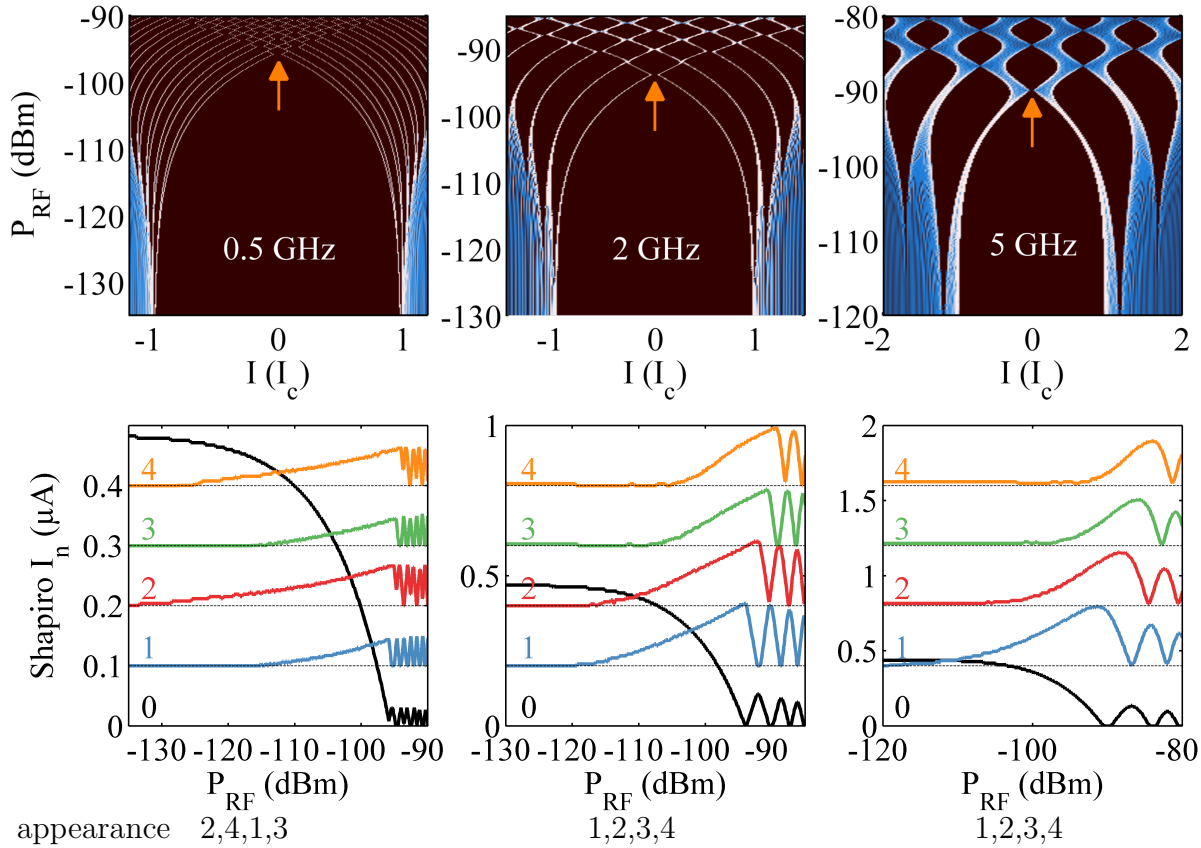

Figure 5.12. – Results of the RSJ model with two types of current–phase relations with 5% (95%) of 4π (2π) supercurrent at different irradiation frequencies. (top line graphs) Differential resistance versus DC current bias and RF power. The orange arrows point at the non vanishing supercurrent at low current bias denoted $\tilde{I}_c$ and discussed in section 3.2. (bottom line graphs) Current amplitude I_n of each Shapiro step versus radio frequency power. The numbers below each figure represent the appearance order of the Shapiro steps when gradually increasing the RF power.

3.2 Anomaly at zero current bias at even Shapiro steps crossing

The crossing point between the switching and retrapping current is modified by the inclusion of a 4π periodic component in the RSJ model. Indeed, as pointed out by the orange arrows in figure 5.12, at low irradiation frequency, the supercurrent does not vanish anymore at low current bias [13]. The remaining supercurrent denoted $\tilde{I}_c$ seems to originate from the 4π periodic component and depends on the frequency f_{RF}. This $\tilde{I}_c$ is sketched in figure 5.14a.

The figure 5.14b represents the ratio between the observed $\tilde{I}_c$ and the 4π contribution used for the simulation: $\frac{\tilde{I}_c}{I_c^{4\pi}}$. At low $\Omega^{4\pi} = f_{RF} \cdot \frac{\hbar}{eRI_c^{4\pi}}$, independently of the other parameters (R,I_c,$I_c^{4\pi}$), $\tilde{I}_c$ saturates to about 70% of the 4π contribution. Therefore, if we

13. This effect is also visible on all even steps but we choose to focus on the most visible one in this thesis.

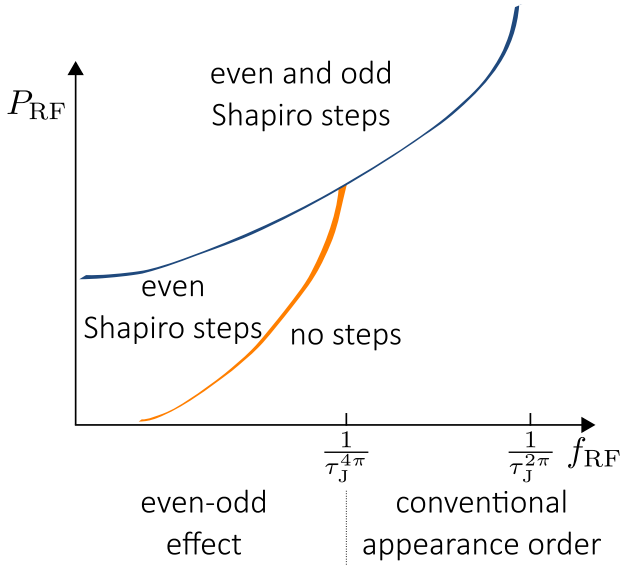

Figure 5.13 – Schematic description of the even–odd effect: the appearance of the even Shapiro steps at low RF power. The lines represent the minimal RF power to observe Shapiro steps. A large phase adjustment time τ_J increases the slope of a given line. The blue (resp. orange) one corresponds to the limit to observe the Shapiro steps associated to conventional (topological 4π periodic) ABSs. As we have $\tau_{\mathrm{J}}^{4\pi} > \tau_{\mathrm{J}}^{2\pi}$, the orange line has a steeper slope than the blue line. For a frequency $f_{\mathrm{RF}} < 1/\tau_{\mathrm{J}}^{4\pi}$, the even-odd effect is visible.

observe experimentally the frequency dependence of $\tilde{I}_{\mathrm{c}}$, we can deduce the associated 4π supercurrent.

If we do not have access to the saturation of $\tilde{I}_{\mathrm{c}}(f_{\mathrm{RF}})$, we can still estimate $I_{\mathrm{c}}^{4\pi}$ by the following method. We present in figure 5.14c the frequency dependence of the ratio $\frac{\tilde{I}_{\mathrm{c}}}{\max(I_0)}$, with I_0 being the amplitude of the Shapiro step $n = 0$. The simulated ratio presents an exponential dependence versus $\Omega^{4\pi}$:

$$\frac{\tilde{I}_{\mathrm{c}}}{\max(I_0)} \approx \alpha e^{-\beta\Omega^{4\pi}} \tag{5.23}$$

with $\alpha \approx 1.3$ a factor that apparently slightly increases with frequency f_{RF} and β which is independent close to $\beta \approx 2.2$. **As $\tilde{I}_{\mathrm{c}}$ and $\max(I_0)$ are both measurable quantities, we can estimate the ratio of the two and therefore estimate the associated $\Omega^{4\pi}$ by using Eq. (5.23) and deduce the contribution of the $I_{\mathrm{c}}^{4\pi}$ supercurrent.**

3.3 Discussion on the even-odd effect

Two effects justify the low-frequency appearance of the even/odd effects:

First, as long as $I_{\mathrm{c}}^{4\pi} \ll I_{\mathrm{c}}^{2\pi}$, the phase adjustment time of the 4π-tABS $\tau_{\mathrm{J}}^{4\pi}$ is much longer than the one from the conventional ABS $\tau_{\mathrm{J}}^{2\pi}$. Hence, at a given RF frequency, the ratio $\Omega^{4\pi} = f_{\mathrm{RF}} \cdot \tau_{\mathrm{J}}^{4\pi}$ is much bigger than the $\Omega^{2\pi} = f_{\mathrm{RF}} \cdot \tau_{\mathrm{J}}^{2\pi}$. At a given frequency, the plateaus associated with the 4π-tABS will be less defined than the conventional ones (as mentioned in footnote 6).

Second, depending on the RF frequency, the system needs a different minimum power to exhibit Shapiro steps (see the description of figure 5.5)). If τ_{J} is large, the RF frequency will have a great impact on the shift of the position of the crossing point between the retrapping and switching branch (red circle in figure 5.5). As we have $\tau_{\mathrm{J}}^{4\pi} > \tau_{\mathrm{J}}^{2\pi}$ ($\Omega^{4\pi} > \Omega^{2\pi}$), a smaller power is needed to induce Shapiro steps on the 4π-tABS than on the conventional ABS.

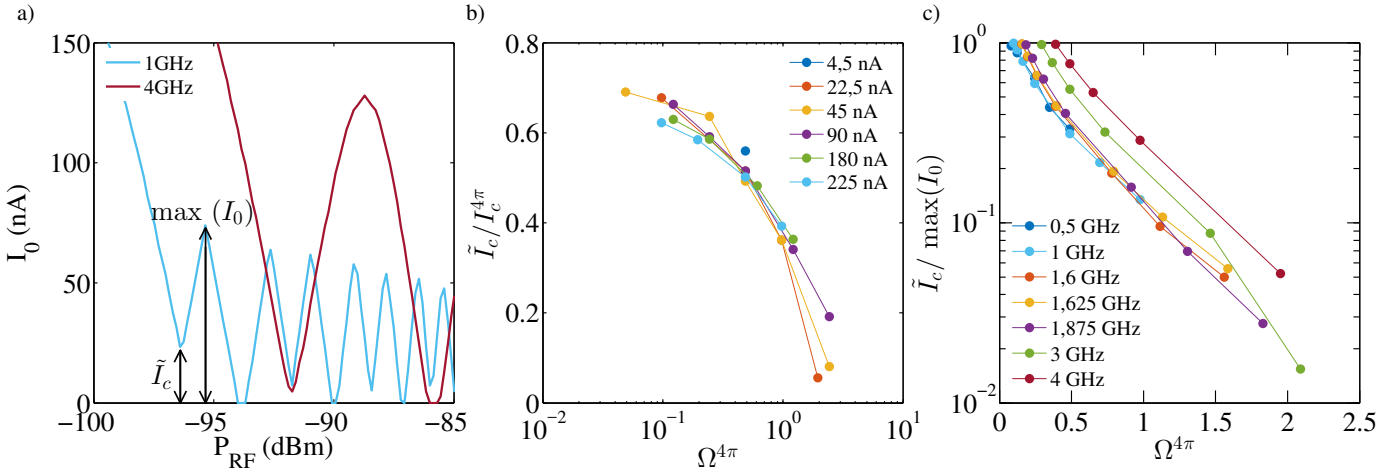

Figure 5.14. – a) Definition of the remaining supercurrent $\tilde{I}_c$ and the quantity $\max(I_0)$ by presenting the step amplitude of the Shapiro step $n = 0$ versus the RF power at two RF irradiations. b) Frequency dependence of the ratio $\tilde{I}_c$ over the 4π contribution versus $\Omega^{4\pi} = f_{RF} \cdot \tau_J^{4\pi}$ for several 4π supercurrent contribution $I_c^{4\pi}$. With $\tau_J^{4\pi} = \frac{\hbar}{eRI_c^{4\pi}}$ the phase adjustment time of the 4π-tABS. c) Relative amplitude of $\tilde{I}_c$ with respect to the amplitude of the first oscillation of I_0 versus $\Omega^{4\pi}$ for different irradiation frequencies f_{RF}.

4 Influence of thermal poisoning of the 4π periodic mode to the even/odd effect

RECENTLY, the absence of many odd Shapiro steps has been observed in a 2D quantum spin hall insulator HgTe [25]. This observation confirms the presence of a 4π-tABS. However, only the absence of the first step $n = 1$ has been seen in *three dimensional* systems that are predicted to host a 4π-tABS [29, 178]. In fact, the step $n = 1$ appears at a higher RF amplitude than the other steps (appearance order : 2,3,4,5,6,1 as shown in figure 4.17 (a) and (b)). This Shapiro pattern cannot be explained by the simple RSJ model with both 2π and 4π supercurrent contributions nor by the even-odd effect. The aim of the following section is to find a model that can explain an effect of the 4π ABS uniquely on the $n = 1$ Shapiro step. For that, we propose to include the overheating model used in section 2 as a source of poisoning.

In this section we will describe how temperature decreases the efficiency of the 4π-tABS to carry a supercurrent.

4.1 Switching probability of the 4π periodic mode

Figure 5.15 presents a schematic of the switching process on the 4π-tABS. This state is either in the $|+\rangle$ state (orange line) or $|-\rangle$ state (blue line). When the system is in the $|+\rangle$ state and $-\pi < \phi < \pi$, then the system is excited. Any relaxation process, like quasiparticle poisoning, could switch the system to its ground state. Temperature activates such a quasiparticle poisoning and hence suppresses the supercurrent carried by

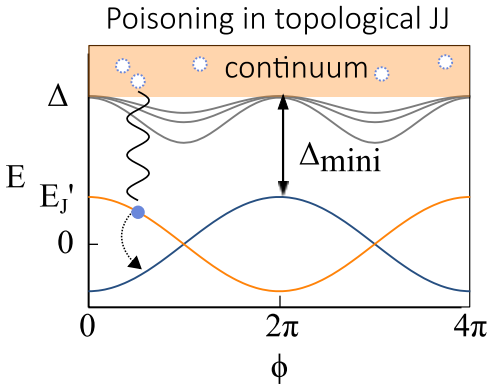

Figure 5.15. – Energy dispersion of a topological Josephson junction containing multiple conventional Andreev bound states (gray lines) and two topologically protected 4π periodic ABS (blue $|-\rangle$ and orange $|+\rangle$ lines). The energy is defined with respect to the Fermi level.
Quasiparticle poisoning makes the system transition from $|-\rangle$ to $|+\rangle$ or conversely by interacting with the continuum of conventional states close to Δ. The energy difference between the continuum of states and the topological states referred to as Δ_{mini} is almost constant.

the 4π-tABS.

We take into account quasiparticle poisoning in the RSJ by defining the lifetime τ_{sw} of the 4π-tABS following Eq. (4.57):

$$\tau_{sw} = \tau_0 e^{\frac{\Delta_{\text{mini}}}{k_B T}} \tag{5.24}$$

with Δ_{mini} being the relevant energy scale of the poisoning process and τ_0 a phenomenological time scale. Δ_{mini} represents the energy difference between the 4π ABS and the continuum of states. The latter is at Δ for short junctions or at the Thouless energy for long junctions. So that $\Delta_{\text{mini}} < \min\{E_{\text{th}}, \Delta\}$ cf (Eq. (4.24)).

Once the lifetime τ_{sw} is defined we solve the time dependent differential equation Eq. (5.22) with a time sampling dt. For each time step the probability for the 4π-tABS to switch is given by dt/τ_{sw}. The current associated with the 4π state switches sign according to :

$$I_{\text{S}}^{4\pi}(t) = (-1)^{n_{\text{sw}}(t)} I_{\text{c}}^{4\pi} \sin\left(\frac{\phi(t)}{2}\right) \tag{5.25}$$

with n_{sw} being the number of switching events during the time of the simulation. Each time a switching happens, the sign of the current–phase relation is changed. This corresponds to a stochastic transition from $|-\rangle$ to $|+\rangle$ as illustrated in figure 5.15. To know the time evolution of n_{sw}, we pick a uniformly distributed random number $x \in [0\ 1]$ and thus have the next value of n_{sw} :

$$n_{\text{sw}}(t + dt) = n_{\text{sw}}(t) + integer(x + 1 - \frac{dt}{\tau_{\text{sw}}}) \tag{5.26}$$

With this method, we can see how the 4π-tABS and its associated Shapiro steps survive during a Shapiro measurement.

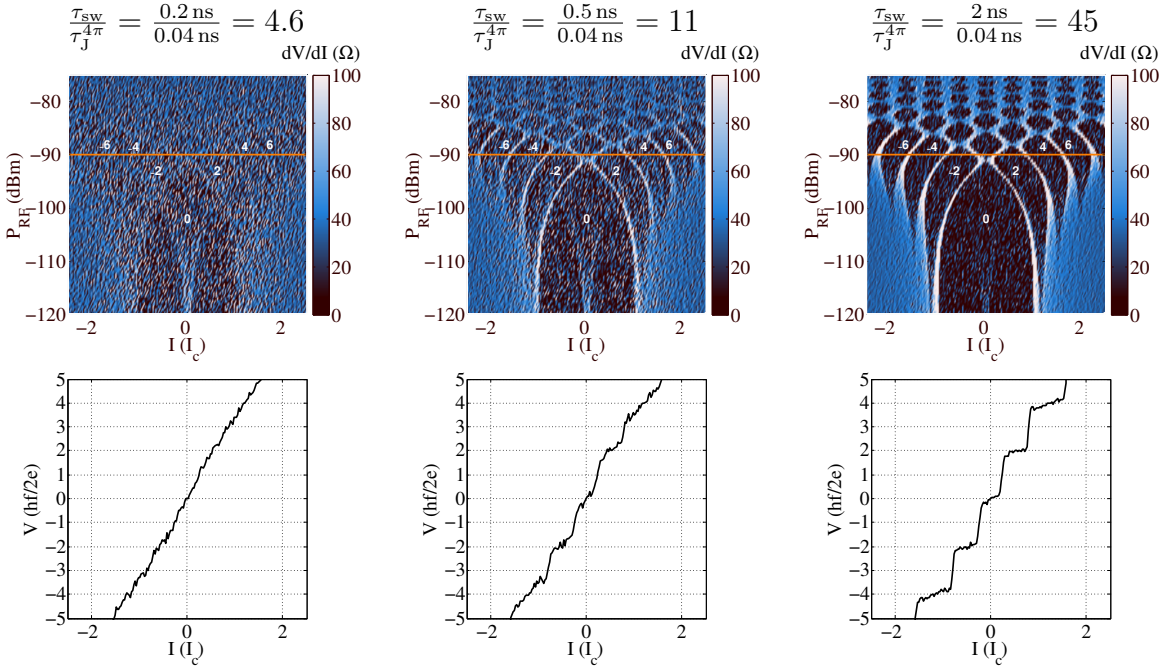

Figure 5.16. – Shapiro simulation at 2 GHz using the RSJ model of a 4π periodic ABS subject to switching processes. The switching time is, from left to right, 0.2 ns, 0.5 ns and 2 ns. (top line) Color-map of the differential resistance versus biased current I and RF power P_{RF}. (bottom line) Voltage–current characteristic at a fixed RF power indicated by the orange line of the top line graphs.

Figure 5.17 – Schematic of visibility of the Shapiro steps. When the switching time is longer than the phase adjustment time, then Shapiro steps can form.

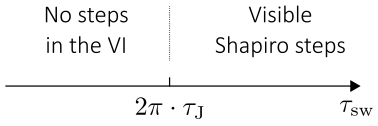

In figure 5.16 we have simulated a current-biased Josephson junction composed of only a 4π-tABS (without conventional 2π-ABSs) that encounters a uniform poisoning with a lifetime τ_{sw} fixed during a complete simulation. We observe, for a short lifetime, the absence of any plateau in the VI characteristic. Shapiro steps gradually appear only for a lifetime $\tau_{sw} > 2\pi \cdot \tau_J^{4\pi}$ with $\tau_J^{4\pi} = \frac{\hbar}{eRI_c^{4\pi}}$ the phase adjustment time of the topological ABS (see figure 5.17). The plateaus are still noisy because of the finite time over which the simulation has run.

In these simulations we also observe a spike in the differential resistance close to zero current bias and low RF power. It is not clear why this spike appears in a system subject to a lot of switching processes.

As we have found the threshold lifetime above which Shapiro steps are visible, we can include the temperature dependence of τ_{sw} in a thermal model as used in section 2.

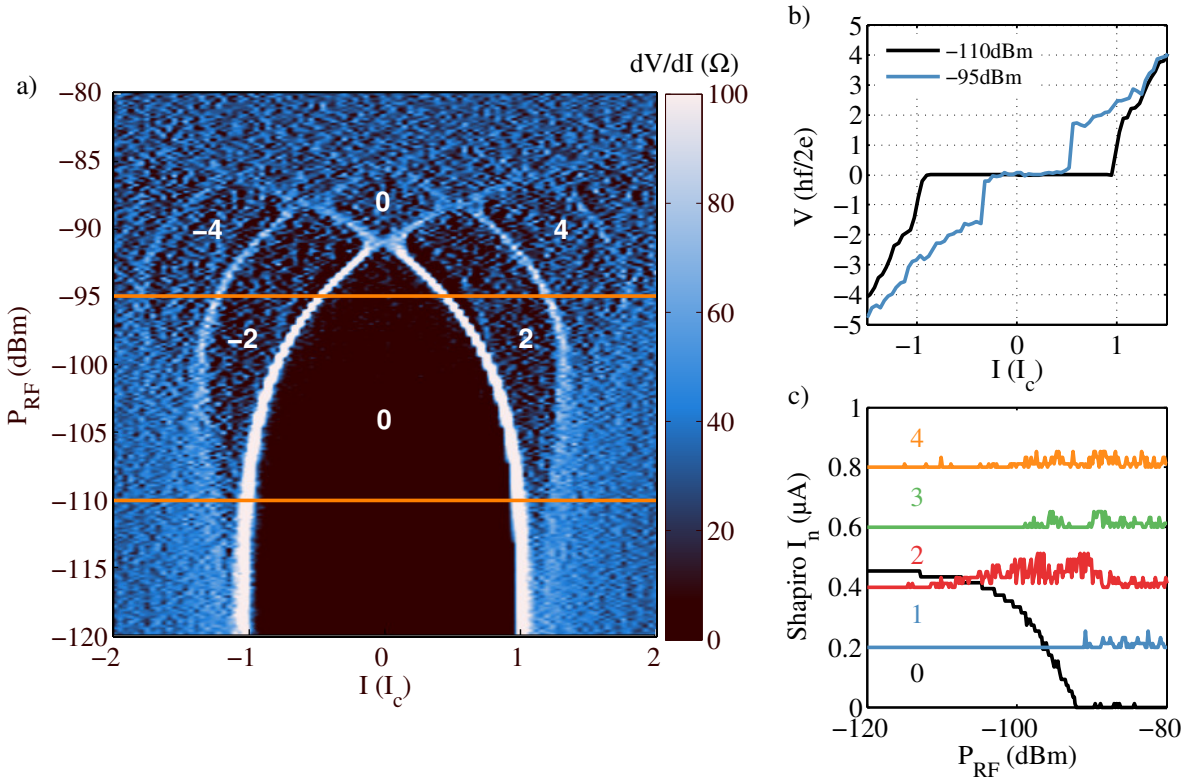

Figure 5.18. – Result of RSJ model with one 4π-JJ irradiated at 2 GHz with $R = 30\,\Omega$, $I_c^{4\pi} = 500\,\text{nA}$, $\mathcal{V} = 0.20\,\mu\text{m}^3$, $\Delta_{\text{mini}} = 160\,\mu\text{eV}$ and $\tau_0 = 0.01\,\text{ns}$. a) Differential resistance map vs biased current I and RF power P_{RF}. The orange lines show the line-cut corresponding to b) and the firsts plateaus are indexed with their numbers. b) VI characteristic at two different irradiation powers. c) Amplitude of each Shapiro step versus radio frequency power.

4.2 Thermally activated poisoning of the 4π state

We develop a model that aims at explaining the reduction the even-odd effect on high index Shapiro steps ($2n+1$ with $n \geq 1$) and hence the experimental observation in which only the $n = 1$ Shapiro step is delayed. We have seen in the previous section that poisoning due to finite temperature reduces the visibility of the Shapiro plateaus. As electronic temperature T_{el} increases significantly on high index Shapiro steps, poisoning will be stronger, thus reducing the even-odd effect. In this subsection we include heating effects in the RSJ model modeling a Josephson junction comprising only a 4π-tABS.

The switching time has to be large so that one can observe clear plateaus: $\tau_{sw} > 2\pi \cdot \tau_{\text{J}}^{4\pi}$. When a junction is biased, its electron bath is heated up and the associated switching time is thus reduced following Eq. (5.24). During a single VI measurement, the temperature and hence τ_{sw} will vary as a function of I_{DC}. The higher the Shapiro index, the more poisoning will destroy the 4π-contribution.

We have simulated the electron overheating in a 4π-periodic JJ following the same procedure as section 2 with a constant critical current $I_c^{4\pi}$ and thermally activated switching processes. The results of RSJ simulation are shown in figure 5.18 with $\tau_0 = 0.01\,\text{ns}$ and

$\Delta_{\text{mini}} = 160\,\mu\text{eV}$, $I_c^{4\pi} = 500\,\text{nA}$. As expected, only the even Shapiro steps are present in the VI characteristics. However the plateaus are more noisy than in the previous simulations due to the poisoning (Figure 5.18b). As temperature increases on the high-indexed plateaus, the lifetime is reduced and the plateaus are more and more smeared out.

The even/odd effect could then be strongly reduced on high order Shapiro plateaus due to electron overheating and thermally activated poisoning. This heating effect could be the reason why, experimentally, only the first Shapiro plateau is affected by the even/odd effect.

4.3 Odd Shapiro steps recovery due to thermal poisoning in S-TI-S Josephson junction

Let us now consider a Josephson junction containing both conventional (2π periodic) and a topological (4π periodic) components of the current–phase relation with electron overheating. In the simulations, temperature impacts the 4π-tABS through switching processes following Eq. (5.24) whereas the conventional supercurrent is affected by temperature through usual electronic overheating.

We have simulated a Josephson junction irradiated at 2 GHz with $i_c^{4\pi} = 20\%$ and the parameters : $R = 30\,\Omega$, $I_c^{tot} = 500\,\text{nA}$, $\tau_0 = 1.9\,\text{fs}$ and $\Delta_{\text{mini}} = 500\,\mu\text{eV}$. Figure 5.19 presents the main result of this chapter. Figures 5.19a-c present the results of three simulations with the same parameters. Figure a shows a simulation without heating effects. Figure b includes heating effects only on the conventional ABS and finally figure c includes heating effects and thermally activated poisoning on the 4π periodic ABS.

The difference between figure a and figure b is visible on the high excitation power part ($P_{\text{RF}} > -95\,\text{dB m}$) by a broadening of the transition between the steps. In addition, the appearance order of the Shapiro steps is similar for both simulations with a clear even/odd effect on all steps: $n = 2, 1, 4, 3, 6, 5, ...$ Therefore, **our heating model applied only on the conventional ABSs does not influence the even/odd effect**.

Figure c shows the simulation with poisoning. We clearly see that the appearance order of the steps has now changed under the influence of poisoning. We obtain an inversion between $n = 1$ and 2, indicating that the even odd effect operates on the low-index steps, but the sequence of appearance is regularized for any $n > 2$. **We therefore obtain with our thermal poisoning model the even/odd effect only on the first step, the higher order plateaus appearing with regular order.**

Quantitative analysis can be made by extracting the critical currents of each Shapiro steps I_n for figure b and c. Those I_n are shown in figure 5.19g as dotted and continuous lines respectively. The onset of the steps are pointed by vertical arrows, in gray for the simulation without poisoning and in black for the simulation with poisoning. Without poisoning (gray arrows), we observe a clear even/odd effect effect on all Shapiro steps with an appearance order $n = 2, 1, 4, 3, 6, 5, 8, 7$.

When adding poisoning to the simulation, only the even steps are shifted to higher RF amplitude. As the 4π mode contributes only to the even steps, leading to an appearance

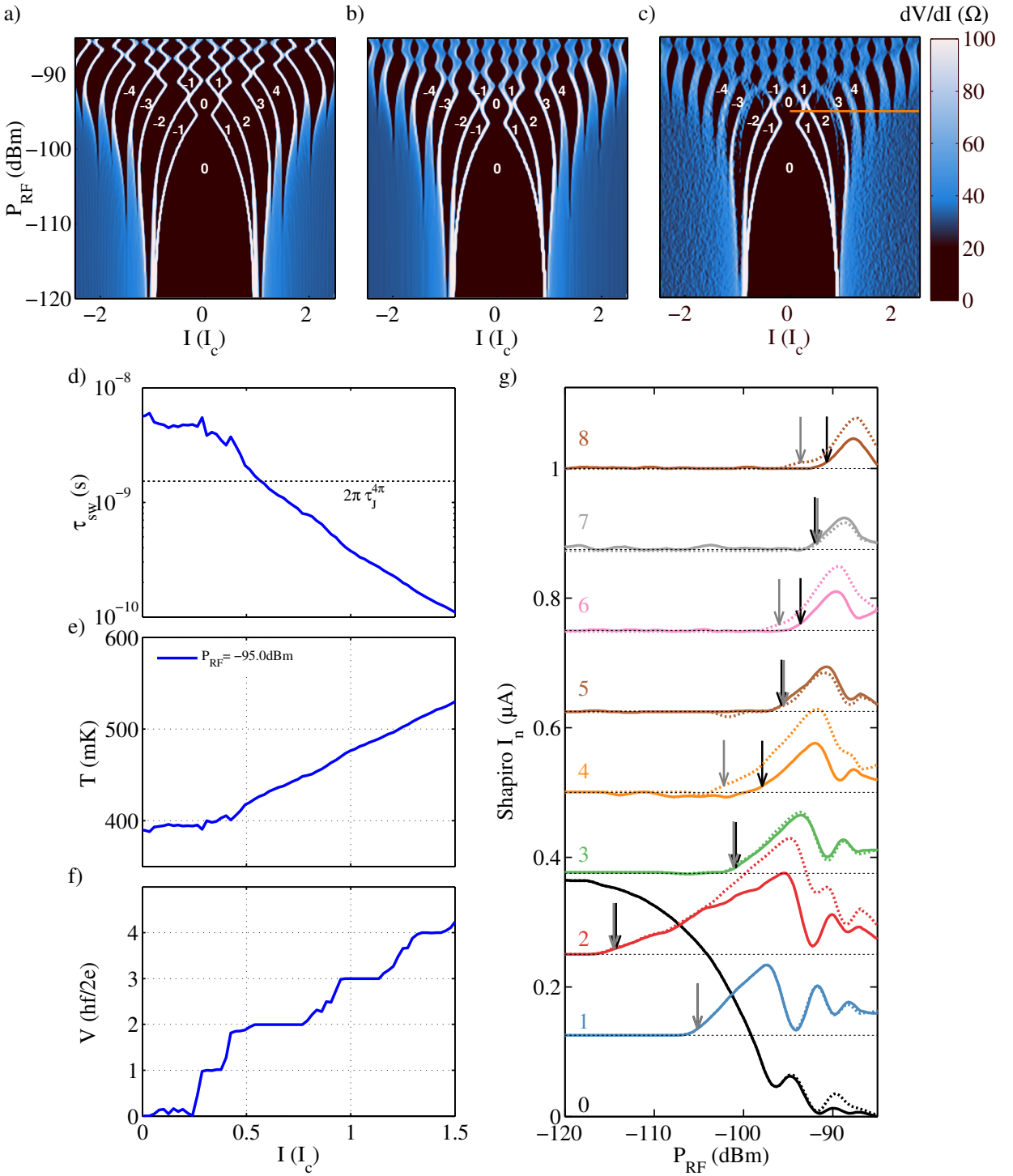

Figure 5.19. – Result of RSJ model of two JJ with 20% (80%) of 4π (2π) supercurrent, irradiated at 2 GHz, with $R = 30\,\Omega$, $I_c^{4\pi} = 500\,\text{nA}$. a-c) Differential resistance maps vs the bias current I_{DC} and the RF power P_{RF} of simulations a) without heating effects, b) with Joule heating on the conventional supercurrent, c) with Joule heating and thermally activated poisoning. The thermodynamic parameters are the following : $\mathcal{V} = 0.20\,\mu\text{m}^3$, $\Delta_{\text{mini}} = 500\,\mu\text{eV}$ and $\tau_0 = 1.9\,\text{fs}$. The indexes label the first Shapiro steps. The orange line show the line-cut corresponding to d-f). d-f) Current dependence at $-95\,\text{dB m}$ of the switching time (d), the electronic temperature (e) and the DC voltage (f). g) Amplitude of each Shapiro step versus radio frequency amplitude. The continuous lines correspond to the extracted I_n from figure c) (with poisoning) while the dotted lines correspond to the same simulation without poisoning effects b) (but still with heating on the 2π supercurrent). We indicate the appearance of each steps by black (gray) arrows corresponding to the simulation with (without) poisoning.

at lower RF power of the even steps (that is usually seen as a delay in appearance of the odd steps), suppressing the 4π contribution with poisoning restores the normal appearance order of the 2π modes. The ensuing shift is highlighted by the black arrows in figure 5.19g. The even/odd is still clear between steps 1 and 2 and is absent for the steps 3, and for all other high order steps. Indeed, the appearance order is now $n = 2, 1, 3, 4, 5, 6, 7, 8$.

To gain further insight into our model, we display in figure 5.19d-f the switching time, the electronic temperature and the DC voltage, all versus bias current. We see in figure 5.19e that the electronic temperature raises from $0.4K$ (overheating at zero bias due to the ac current), up to nearly $0.55K$. This temperature raises leads to an exponential suppression of the switching time, which becomes shorter than the typical phase relaxation time of the 4π mode, $2\pi \cdot \tau_{\mathrm{J}}^{4\pi}$, when the bias current reaches the step $n = 2$. This transition thus sets the suppression of the contribution of the 4π mode, and therefore leads to the disappearance of the even/odd effect at higher current bias.

To conclude, our model provides a possible explanation for the experimental observation of the even/odd effect on only the step $n = 1$ in topological Josephson junctions on 3D topological insulators.

Summary

In this chapter we have introduced the resistively shunted Josephson junction model to simulate a Shapiro experiment on a voltage- or current-biased Josephson junction. In the voltage-biased case, we give an analytical solution, whereas the current-biased one needs to be solved numerically.

We have then focused on the current biased model and have included a thermal model that can explain hysteresis effects due to hot electrons. This model can precisely estimate the electron temperature during a simple voltage–current characteristic or a more complex Shapiro measurement. This model presents a convincing simulation of a Shapiro experiment on a conventional Josephson junction.

Following the study of [49] we have evaluated the impact of a single topological 4π periodic channel among many conventional ABSs. We concluded that the even/odd effect appears more clearly at low frequency irradiation: The even Shapiro steps will be more visible than the odd steps for $f_{\mathrm{RF}} < 1/\tau_{\mathrm{J}}^{4\pi}$.

We have then adapted the heating model to the topological Josephson junction case. Indeed, temperature affects the topologically protected 4π periodic Andreev bound state by inducing quasiparticle poisoning. This poisoning reduces the overall supercurrent carried by the 4π-tABS and hence the associated Shapiro steps.

As we have assumed a thermally activated poisoning, hot electrons are more subject to switching events. When a junction is biased, electrons are overheated and induce more switching at high bias. Consequently, during a Shapiro experiment, the low index steps can show the even/odd effect but not the high index ones. We have simulated a topological Josephson junction subject to hot electron effects. We have been able to suppress the even/odd effect for the high order Shapiro steps while keeping it for the first step $n = 1$.

Therefore, our thermal poisoning model explains the elusive even/odd effect seen only on the low index Shapiro steps.

Chapter 6

Even-odd effect in Bi_2Se_3 Josephson junctions

JOSEPHSON junctions formed by coupling superconducting electrodes (S) to topological insulators (TI) have attracted considerable attention due to the prospect of observing and manipulating Majorana fermions in suitably designed devices [63]. Experimentally, indications of Majorana states in different systems and configurations were reported by tunneling in superconductivity-proximitised semiconducting nanowires, vortices in 3D TIs, and atomic chains of magnetic atoms. In transport measurement however, hunt for evidences is still challenging mainly due to the fact that any parallel conduction channel stemming from material imperfection can conceal the contribution of the Majorana bound state.

Soon after the discovery of TIs, S-TI-S Josephson junction were proposed as a testbed for Majorana physics. Theory indeed predicts that S-TI-S junctions covered with a ferromagnetic layer host Majorana fermions in the form of a perfectly transmitted Andreev bound-state of 4π-periodic current-phase relation [63]. This 4π-periodicity can profoundly

affect the a.c. Josephson effect and the resulting Shapiro steps that arise in current-biased junctions under RF excitation. Whereas the usual 2π-periodic current-phase relation leads to a series of steps at voltages $V_n = n\frac{hf_{\mathrm{RF}}}{2e}$ (h the Planck constant, f_{RF} the RF excitation frequency, e the electron charge) where n is the integer index of the Shapiro step, the new 4π-periodic Andreev mode implies only even Shapiro step of index $2n$ [49, 79, 173].

Initial measurements performed on Bi-based TI showed usual Shapiro steps in current biased S-TI-S Josephson junctions [66, 123, 145, 170]. Recently, two experiments performed on InSb and strained HgTe have reported an anomalous sequence of Shapiro steps on increasing RF power [142, 178]. In both cases, the $n = 1$ step is conspicuously absent in a given range of RF power and frequencies, pointing to a possible, though incomplete, contribution of the topological 4π-periodic Andreev bound state.

In this chapter we report on Josephson junctions made of the 3D topological insulator Bi_2Se_3 with large bulk conduction exhibiting anomalous sequences of Shapiro steps.

We first present how we have produced Josephson junction on thin flakes of Bi_2Se_3. Then we characterize the regime of conduction in which the superconducting proximity effect develops. We show that the whole flake is coupled by proximity effect of the superconducting leads. Finally we perform a Shapiro experiment and observe the even/odd effect on the first Shapiro step. We compare the experimental observations and the simulations developed in previous chapter to evaluate the origin of this effect and answer the question : Is the observed delay of the first step due to a 4π Andreev mode ?

1 Josephson junctions on Bi_2Se_3

1.1 Bi_2Se_3 a topological insulator with a conducting bulk

Before going into details of the superconducting transport occurring inside the topological insulator crystal, we first present the electronic properties of our Bi_2Se_3 crystal.

Bi_2Se_3 is a widely used topological insulator with a large band gap of 300 meV. We reviewed its crystallographic properties and history in chapter 2. The compound is known to have its Fermi level in the conduction band. The material used in this thesis has been grown by J. Marcus at Institut Néel. It has been characterized by angle resolved photoemission spectroscopy (ARPES) and magnetotransport measurements.

In ARPES measurement in figure 6.1, we see that the Fermi energy is located inside the conduction band, which makes the bulk of Bi_2Se_3 conducting. The Dirac cone of the surface states is clearly visible inside the band gap.

We have measured the electron transport properties in two different samples extracted from the same mother crystal (figure 6.2). Both of them show Shubnikov-de-Haas oscillations. Sample 1 has been dedicated to Hall measurements and exhibits clear oscillations at frequency $f_{\mathrm{SdH}} = 123.7\,\mathrm{T}$, whereas sample 2 is a Hall bar designed next to a Josephson junction. From Hall measurement and Shubnikov-de-Haas oscillations we extract the

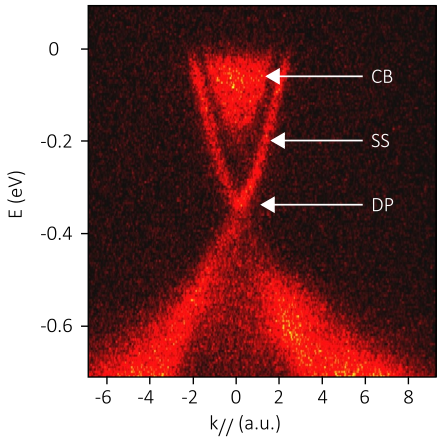

Figure 6.1. – Angle resolved photo-emission spectroscopy of Bi_2Se_3 measured at SOLEIL (collaboration J.-Y. Veuillen, J. Avila and M. C. Asensio). The energy is measured with respect to the Fermi level ($E_F = 25.7\,eV$) versus the parallel wave vector. The surface states (SS) cross in a linear way at the Dirac point (DP) 0.35 eV below the Fermi level. The latter is placed in the bulk conduction band (CB) which leads to a bulk metallic behavior.

Sample	f_{SdH} (T)	n_e (cm^{-3})	ρ (mΩ cm)	μ_e ($cm^2/V/s$)	D (cm^2/s)	l_e (nm)
1	123.7	7.8×10^{18}	~ 0.5	1600	170	60
2	163	1.2×10^{19}	0.7	760	64	35

Table 6.1. – Transport properties of the two samples of figure 6.2.

Drude transport properties that are summarized in table 6.1 [1].

The high electron density n_e and the low resistivity ρ are consistent with a crystal that has a metallic bulk. The short electron mean free path l_e of few tens of nanometers implies practical Josephson junctions in the diffusive limit. The large dispersion of values indicates the inhomogeneity of our crystal.

Now that we have characterized the normal transport properties of our Bi_2Se_3, we can build Josephson junctions out of it. The sample fabrication is presented in chapter 3.

1.2 Long SNS junction in the diffusive regime

Josephson junction devices have been characterized by current biasing the junction and measuring the voltage between the two leads. The following results have been similarly observed on two different samples (chips LC099 and LC106 on which there are several junctions). We mainly focus on sample LC099-JJ4. The junction is made out of a 20 nm thick flake of Bi_2Se_3 (shown in Figure 6.3a), is 140 nm long (spacing between electrodes) and 1.45 µm wide. Superconducting electrodes are composed of vanadium capped with few nanometers of gold.

1. From the 3D Drude model we have: the carrier density $n_e^{3D} = (\frac{2ef_{SdH}}{\hbar})^{3/2}$, the electron mobility $\mu_e^{3D} = \frac{1}{\rho n_e^{3D} e}$, the mean free path is $l_e = \frac{\hbar k_F \mu_e}{e}$ and the diffusion coefficient $D = \frac{1}{3} v_F l_e$ with $v_F = \frac{\hbar k_F}{m_e}$ the Fermi velocity.

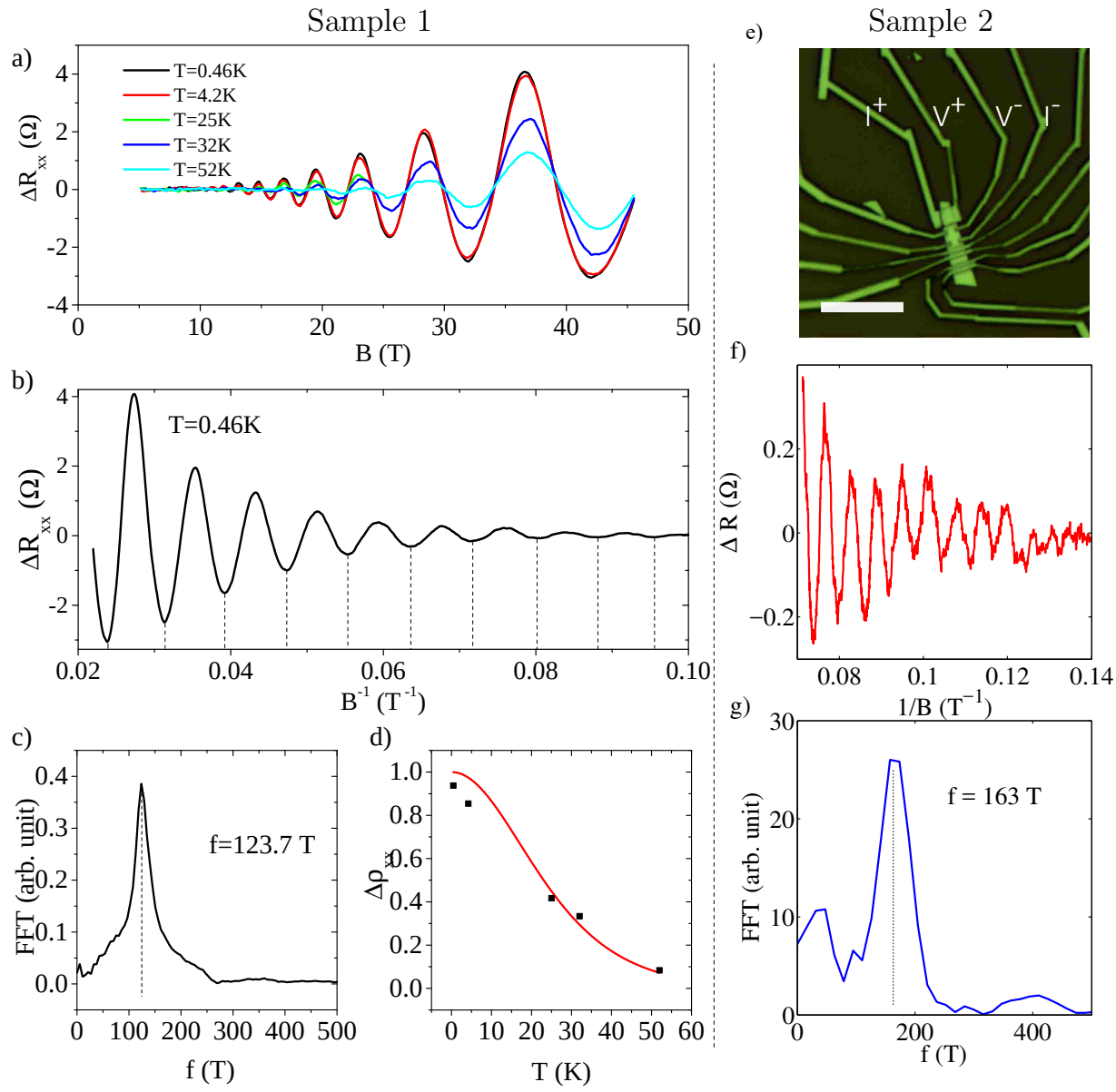

Figure 6.2. – Shubnikov-de-Haas oscillations in two different samples extracted from the same crystal of Bi_2Se_3.
Sample 1 (collaboration W. Escoffier and F. Iacovella LNCMI Toulouse) : a) Variation of longitudinal resistance ΔR_{xx} versus perpendicular magnetic field at different temperatures. b) Variations of ΔR_{xx} versus inverse magnetic field at 460 mK. c) Fourier transform of b). d) Temperature dependence the oscillation amplitude. The red curve is a fit following $\Delta\rho_{xx} = \frac{\alpha T}{\sinh(\alpha T)}$ with $\alpha = \frac{2\pi^2 m^*}{he}$. It gives an estimation of the electron mass $m^* = 0.15 m_e$.
Sample 2 (LC106) : magneto-transport performed next to Josephson junctions presented in this chapter: e) Optical picture of sample 2. The Hall bar is defined by the current source (I^+) and drain (I^-) in-between the voltage probes (V^+ and V^-). White line for scale is 10 µm. f) Variations of longitudinal resistance versus inverse magnetic field. g) Fourier transform of f).

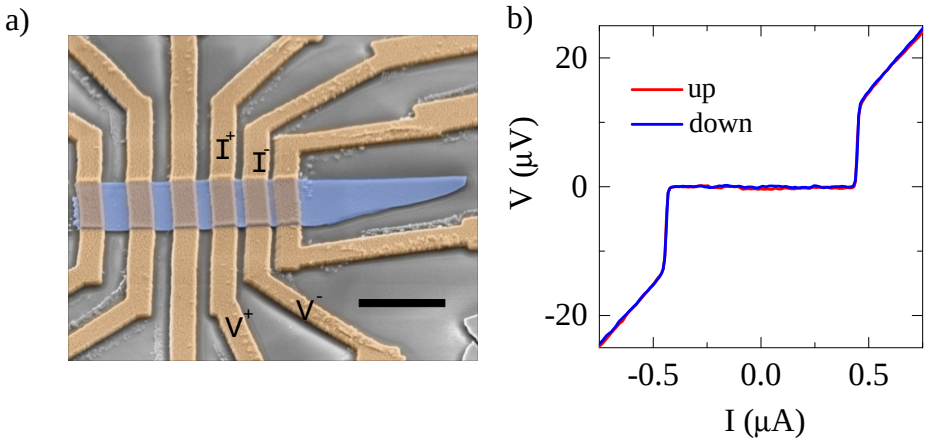

Figure 6.3. – a) Scanning electron microscopy image of the sample LC099 with false colours. The crystal of Bi_2Se_3 is in blue and the vanadium electrodes are in orange. The black line is 1 µm for scale. The current source/drain and voltage probes indicate the location of the junction LC099-JJ4 b) Voltage versus current measurement of the device at 80 mK.

Name	L (nm)	R_n (Ω)	I_c (nA)	eR_nI_c (µeV)	E_{th} (µeV)	eR_nI_c/E_{th}
LC099-JJ1	500	80	50	4	17	0.24
LC099-JJ2	400	60	80	5	27	0.19
LC099-JJ3	300	46	190	8.7	48	0.18
LC099-JJ4	140	30	450	13	220	0.06
LC106-JJ1	250	10	2600	26	68	0.38
LC106-JJ2	150	12	2750	33	190	0.17

Table 6.2. – Summary of the Josephson junctions fabricated on Bi_2Se_3 with their superconducting properties.

The length of the junction is much greater than the mean free path, which classifies the junction in the diffusive limit. Figure 6.3b presents the current-voltage (IV) characteristics at 80 mK. The IV shows a switching current $I_{sw} = 450\,nA$ and is non-hysteretic. The $e \cdot R_n \cdot I_c$ product at base temperature (80 mK) is 14.5 µeV. The estimated Thouless energy is $E_{th} = \frac{\hbar D}{L^2} = 220$ µeV. As E_{th} is smaller than the superconducting energy gap of vanadium [18] $\Delta_V = 800$ µeV, the junction is in the long limit. Table 6.2 summarizes the properties of the different junctions studied. All of them belong to the **long diffusive limit**. However, the base temperature ratio eR_nI_c/E_{th} is much smaller than 10.8 predicted in a (non topological) JJ with perfect interfaces.

1.3 Estimation of interface transparency

To estimate the barrier transparency between the superconducting lead and the crystal, we use two independent methods. The first method uses the temperature dependence of the switching current that we fit with the Thouless energy and a prefactor. The second uses the excess current in the framework of the Blonder-Tinkham-Klapwijk theory [24].

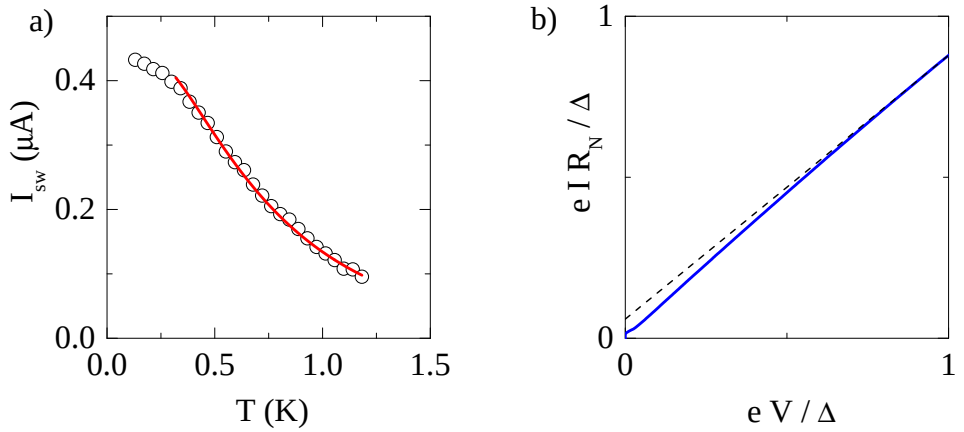

Figure 6.4. – Sample LC099-JJ4. a) Switching current vs temperature (black circles). A fit of the high temperature part according to Eq. (6.1) is added in red with the parameters: $E_{\mathrm{th}}^{fit} = 13\,\mu\mathrm{eV}$ and $\alpha = 14\%$. b) Measurement of the excess current at high voltage bias. Dotted line is a linear fits at high (several times the gap) voltage bias.

Transparency using $I_{\mathrm{sw}}(T)$ The temperature dependence $I_{\mathrm{c}}(T)$ in the long and diffusive regime at temperature $T > E_{\mathrm{th}}/k_{\mathrm{B}}$ reads [51]:

$$eR_{\mathrm{N}}I_{\mathrm{c}}(T) = \alpha\frac{32}{3+2\sqrt{2}}(2\pi k_{\mathrm{B}}T)^{3/2}E_{\mathrm{th}}^{-1/2}\exp\left(-\sqrt{\frac{2\pi k_{\mathrm{B}}T}{E_{\mathrm{th}}}}\right) \tag{6.1}$$

The phenomenological coefficient α characterizes the interface transparency. The measured $I_{\mathrm{sw}}(T)$ of LC099-JJ4 is presented in figure 6.4a with the associated fit according to Eq. (6.1). We find a parameter α of 14%. We can notice the large discrepancy between the calculated Thouless energy $E_{\mathrm{th}} = 220\,\mu\mathrm{eV}$ and the one obtained from the fit $E_{\mathrm{th}}^{fit} = 13\,\mu\mathrm{eV}$.

Transparency using the BTK theory A second estimation of the transparency is possible by studying the excess current. Indeed, according to the Blonder-Tinkham-Klapwijk theory [24], an interface between a normal metal and a superconductor has a linear current voltage relation at high voltage bias with an offset called I_{excess} that depends on the interface transparency. An S-N-S junction seen as two N-S interfaces in series gives $I_{excess}^{tot} = I_{excess}^{NS}$. The measured $eI_{excess}^{tot}R_{\mathrm{N}}/\Delta = 0.086$ implies that the junction has two barriers with a mean strength value $Z = 2.0$ which means a transparency of 20 % (cf figure 6 in [24]). The superconducting gap of the thin film may be overestimated, nevertheless the transparency little depends on it.

Through two different ways, in this section, we have found an interface transparency between the superconductors and the topological insulator around 15%.

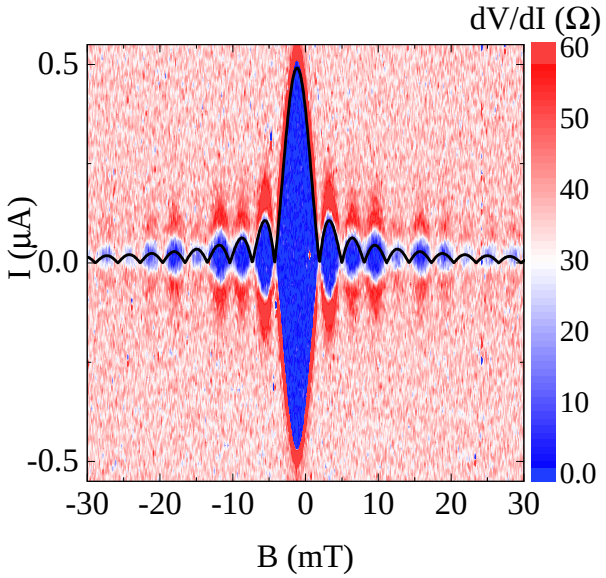

Figure 6.5. – Differential resistance of the junction LC099-JJ4 under a perpendicular magnetic field. The black line represents a fit of the Fraunhofer pattern with a uniform supercurrent distribution : $I_c = I_c^0|\mathrm{sinc}(\pi BS/\phi_0)|$.

1.4 Uniformly distributed supercurrent

In order to estimate the spatial distribution of the supercurrent through the Josephson junction, we apply a perpendicular magnetic field and measure the switching current.

The result is presented in figure 6.5. Under a perpendicular magnetic field, the switching current of the junction displays a Fraunhofer interference pattern with a period [2] $S = 1.45\,\mu\mathrm{m} \times 465\,\mathrm{nm}$. The difference between the geometrical length between the electrodes $L = 140\,\mathrm{nm}$ and the effective length $465\,\mathrm{nm}$ measured with the Fraunhofer pattern is explained by the penetration of the magnetic field inside the leads on the superconducting magnetic length. The good agreement between measured data and fit demonstrates an homogeneous supercurrent inside the BS flake.

2 Fractional AC Josephson effect

HERE we report on the non monotonic appearance of the Shapiro steps sequence on a topological Josephson junction. We first present the results measured on two different junctions, and then compare the measurement with the Shapiro simulation of previous chapter. Finally we discuss the origin of this observed even/odd effect.

2. Theoretical explanation are given in appendix A.

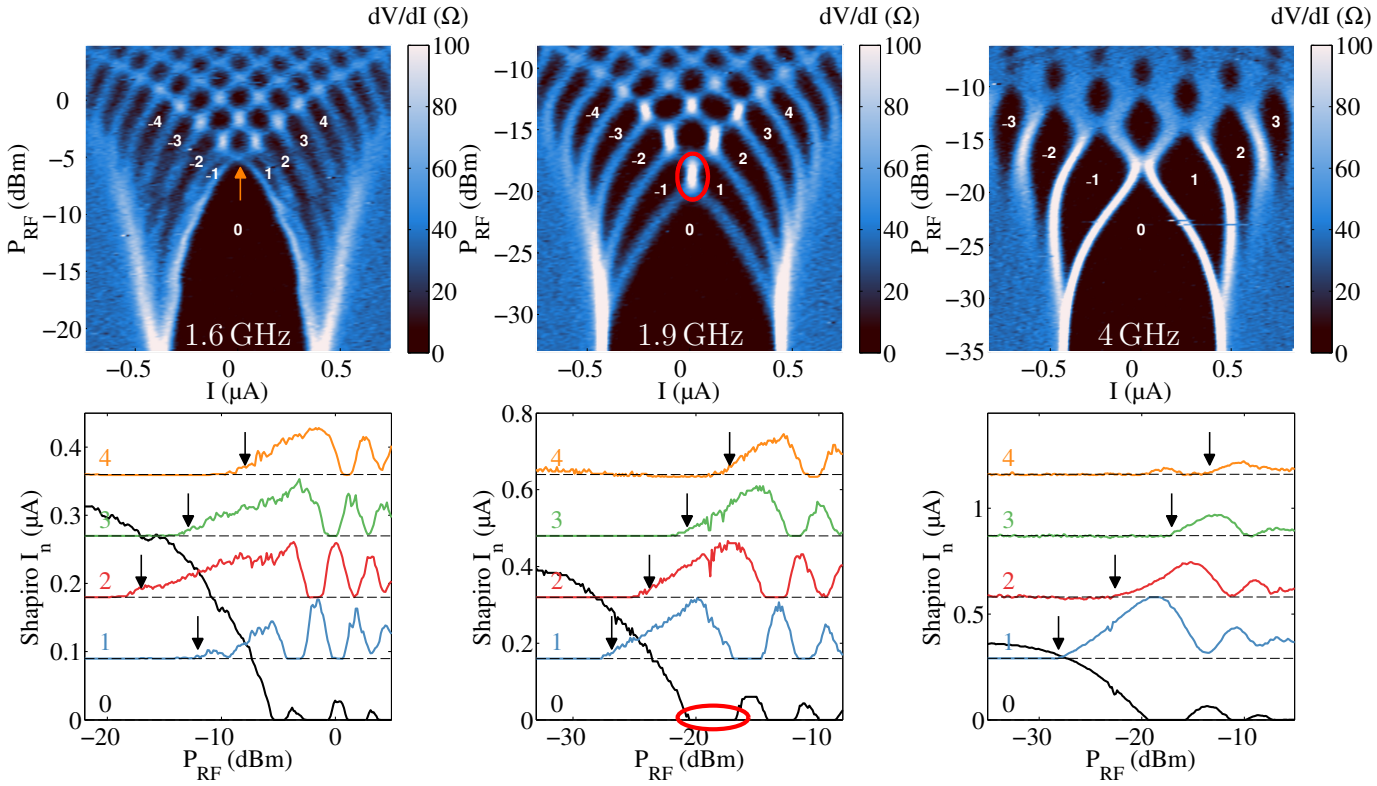

Figure 6.6. – (top graphs) Differential resistance of the junction LC099-JJ4 under RF irradiation at 1.6, 1.9 and 4 GHz. The first Shapiro steps are labeled. The orange arrow and the red circle point at an anomaly at the crossing point between the switching branch and the retrapping branch. It is further discussed in the main text. (bottom graphs) Amplitude I_n of the first Shapiro steps versus the RF power. The arrows point at the RF power where every step appears.

2.1 Even/odd effect in the Shapiro measurement

We have shined radio frequencies on Bi_2Se_3 Josephson junction and recorded the differential resistance versus bias current at various RF power. The results on the junction LC099-JJ4 at three different frequencies are presented in figure 6.6. We first note that the Shapiro map is non-hysteretic at all frequencies.

High frequency : $f_{RF} = 4\,\mathrm{GHz}$ At high frequency (right graphs of figure 6.6), the first Shapiro step that forms at low RF power is the step $n = \pm 1$ at $P_{RF} = -29\,\mathrm{dB\,m}$. At $P_{RF} = -22\,\mathrm{dB\,m}$, the second step $n = 2$ starts to be visible and so on for the next steps. The steps are thus appearing in a monotonic way, as expected in a standard JJ.

On top of the expected oscillations, we observe at high RF power the decrease of the step size: on the right lower graph, I_1 (blue line) is significantly smaller at $-11\,\mathrm{dB\,m}$ than at $-15\,\mathrm{dB\,m}$. This can be understood by the increasing heating coming from the RF irradiation which globally decreases $I_c(T)$.

Intermediate frequency : $f_{\mathrm{RF}} = 1.9\,\mathrm{GHz}$ At intermediate frequency (center graphs of figure 6.6), the appearance order of the Shapiro steps is the same as the one at high frequency: $n = 1, 2, 3, 4, 5, ...$ However, we notice an anomaly which has not been anticipated in the simulations. The crossing point of the retrapping and switching branches (red circle in the graphs) is not a point anymore but is rather stretched over a wide range of RF power. This phenomenon is visible not only on the zeros step but for all the low index Shapiro plateaus : $n = 0, 1, 2, 3$.

Low frequency : $f_{\mathrm{RF}} = 1.6\,\mathrm{GHz}$ At low frequency (left graphs of figure 6.6), the steps are less defined because the voltage $\Delta V = \frac{hf_{\mathrm{RF}}}{2e}$ is smaller and so is the associated energy. However, two aspects are clearly visible in the two graphs.

At the crossing point between the retrapping and switching branch (indicated by an orange arrow), the differential resistance decreases in comparison to the other crossings (it is not as white as the other crossing points).

Second, if we focus on the amplitude of the Shapiro steps (bottom graph), we observe the appearance of the step $n = 1$ only at RF power $P_{\mathrm{RF}} = -12\,\mathrm{dB\,m}$ which is higher than the one needed to observe the step $n = 2$ at $P_{\mathrm{RF}} = -18\,\mathrm{dB\,m}$. The appearance order is hence $n = 2, 3, \mathbf{1}, 4, 5, 6$. This behavior resembles the one measured on HgTe 3D TI [178] (in this thesis Figure 4.17e). This non-monotonic appearance order of the Shapiro steps is visible in this junction for an irradiation frequency lower than $f_{\mathrm{RF}} \leq 1.6\,\mathrm{GHz}$. If this even/odd effect stems from a 4π periodic ABS, the threshold frequency 1.6 GHz is then associated to a relaxation time : $\tau_{\mathrm{J}}^{4\pi} = \frac{\hbar}{eRI_{\mathrm{c}}^{4\pi}}$ within the RSJ model. Considering the resistance of the RSJ model as the measured normal resistance, then we can estimate the 4π periodic current: $I_{\mathrm{c}}^{4\pi} = 35\,\mathrm{nA}$. Compared to the measured critical current, this corresponds to 7% of the total supercurrent.

A single superconducting channel in a JJ can carry up to $I_{\mathrm{c}}^{theory} = \frac{e\Delta}{h} = 35\,\mathrm{nA}$, with $\Delta = 800\,\mu\mathrm{eV}$ the superconducting energy gap of the vanadium. This perfect consistency between our estimation and the theoretical value is astonishing. To confirm this observation, we measured a second Josephson junction (LC106-JJ2) and observed the same behavior.

This second sample has an hysteretic behavior and a larger switching current $I_{\mathrm{sw}} = 2.7\,\mu\mathrm{A}$. The Shapiro measurements are displayed in figure 6.7 with the same color code. For this junction, the frequency threshold 1 GHz gives $I_{\mathrm{c}}^{4\pi} = 55\,\mathrm{nA}$ which corresponds to 2% of the supercurrent.

For this second sample we also observe a remaining supercurrent at low current bias pointed by the orange arrow in figure 6.7 at 1 GHz. From this clear feature, we can give a second estimation of $I_{\mathrm{c}}^{4\pi}$ following Eq. (5.23) which gives a ratio $\Omega^{4\pi} = \frac{-1}{\beta}\ln\left(\frac{1}{\alpha}\frac{\tilde{I}_{\mathrm{c}}}{\max I_0}\right) = 0.24$ with $\alpha = 1.33$, $\beta = 2.2$ and the ratio $\frac{\tilde{I}_{\mathrm{c}}}{\max I_0} = 0.78$. Therefore the 4π supercurrent reads $I_{\mathrm{c}}^{4\pi} = 220\,\mathrm{nA}$.

There is thus a factor 4 between the last two estimations of the 4π periodic supercurrent. This discrepancy could be explained by the large uncertainty of the method using the remaining supercurrent $\tilde{I}_{\mathrm{c}}$ as seen in figure 5.14c.

Besides, we notice that the supercurrent does not vanish at the crossing points between

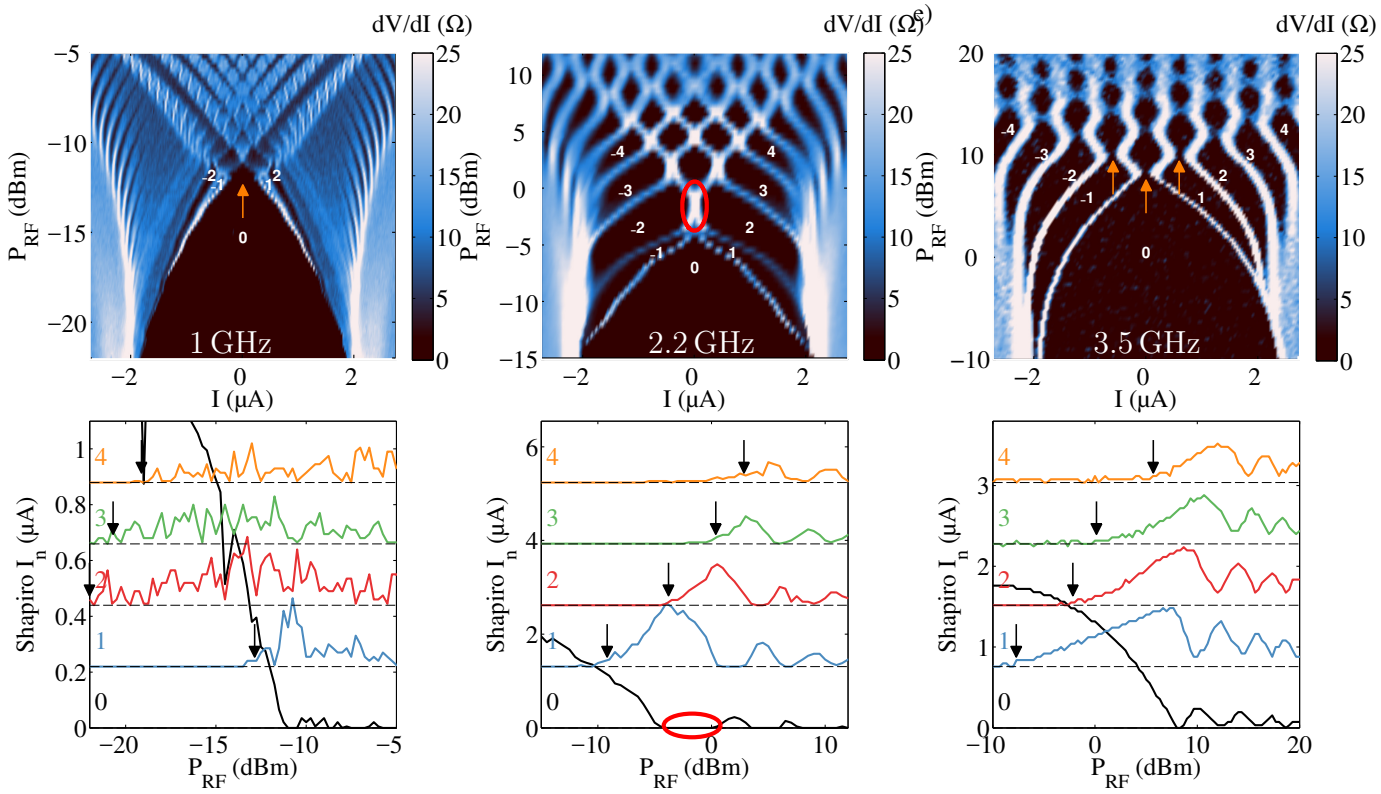

Figure 6.7. – (top graphs) Differential resistance of the junction LC106-JJ1 under RF at 1.6, 1.9 and 4 GHz. The first Shapiro steps are labeled. The orange arrow and the red circle point at an anomaly at the crossing point between the switching branch and the retrapping branch. It is furthered discussed in the main text. (bottom graphs) Amplitude I_n of the first Shapiro steps versus the RF power. The arrows points at the RF power where the step appear.

higher order lobes for the 3.5 GHz map. This remaining supercurrent is indicated by orange arrows in figure 6.7. As this effect is visible at even and odd crossings of Shapiro steps, it thus cannot originate from a possible 4π ABS. We do not have any explanation for this gap opening.

The estimation of the supercurrent carried by a topologically protected 4π periodic ABS for LC099 is consistent with the theoretical prediction, still both estimations of LC106 are not consistent with the theoretical estimation. We do not have a clear explanation for this unexpectedly large 4π periodic supercurrent.

2.2 Comparison experimental observation & simulation

Let us now use our thermal model introduced in chapter 5, to reproduce the Shapiro map of our topological Josephson junctions.

We have estimated the phonon coupling constant of bismuth selenide $\Sigma_{Bi_2Se_3}$ using the formula proposed in ref. [54] :

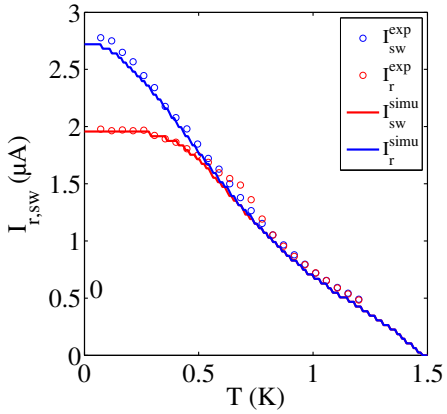

Figure 6.8. – Estimation of the volume of the junction. The circles display the measured switching and retrapping currents of junction LC106. The curves represent the simulated switching and retrapping currents with a volume $\mathcal{V}_{\mathrm{LC106}} = 2.4\,\mu\mathrm{m} \cdot 30\,\mathrm{nm} \cdot (150\,\mathrm{nm} + 400\,\mathrm{nm}) = 4 \times 10^{-2}\,\mu\mathrm{m}^3$.

$$\Sigma = \left(\frac{k_\mathrm{B}}{\hbar}\right)^5 \frac{4\hbar\beta_\mathrm{l}}{5\pi^4} \frac{\Gamma(5)\zeta(5)}{v_\mathrm{F} u_\mathrm{l}^2} \frac{l_\mathrm{e}}{d} \left(1 + \frac{3}{2}\left(\frac{u_\mathrm{l}}{u_\mathrm{t}}\right)^5\right) \tag{6.2}$$

with $u_{\mathrm{l,t}}$ being the longitudinal and transverse sound velocities, v_F the Fermi velocity l_e the electronic mean free path, d the film thickness, Γ and ζ the gamma and zeta functions and β_l a dimensionless parameter. The estimated electron-phonon coupling constant is then [3]: $\Sigma_{\mathrm{Bi_2Se_3}} = 27 \times 10^9\,\mathrm{Wm^{-3}K^{-5}}$.

The JJ thermodynamics depends on the microwave excitation and on the electron-phonon scattering time $\tau_{\mathrm{el-ph}}$. The latter is estimated from the electron-phonon coupling constant at low temperature in Bi_2Se_3 by [69] $\tau_{\mathrm{el-ph}}^{-1} \approx 1.08\ T^2$ GHz. At 100 mK, the rate is 11 MHz. As long as the RF excitation is faster than the electron-phonon scattering rate, the electronic temperature can be considered as almost constant at a given pair (I_{DC}, I_{RF}). A constant T_el means that the thermal balance can be written as $P_{\mathrm{el-ph}} =< P_{\mathrm{Joule}} >_t$.

To estimate the volume $\mathcal{V}$ of the system, we have used the experimental measurement of $I_{\mathrm{sw,r}}$ as a function of temperature and compared it with several simulations with different volumes. Figure 6.8 presents the fits of $I_{\mathrm{sw,r}}$ allowing for the final estimation of the volume of the second topological JJ (LC106). The volume corresponds to product of the thickness t, the width W and the sum of L and two half of the electrodes width (400 nm). We observe a good agreement between the simulation and the experimental measurement which validates our estimation of the volume of the junction. One should note that for a temperature above 500 mK, both the simulation and the experiment show the merging of the switching and retrapping currents. Hence the junction is not hysteretic anymore above this temperature.

Josephson junction LC099-JJ4 To determine the thermal dependence of the poisoning, we simulate the junction using our thermally activated poisoning model.

3. For comparison $\Sigma_{\mathrm{Au}} = 2 \times 10^9\,\mathrm{Wm^{-3}K^{-5}}$

In the simulation we use the estimated amount of 4π periodic supercurrent of the junction : $I_c^{4\pi} = 35\,\mathrm{nA}$ and the transport parameters: $R = 30\,\Omega$ and $I_c^{tot} = 450\,\mathrm{nA}$. With these parameter values, we have found an appropriate temperature dependence of the switching time $\tau_{sw} = \tau_0 e^{\frac{\Delta_{\mathrm{mini}}}{k_B T}}$ with $\tau_0 = 0.1\,\mathrm{ns}$ and [4] $\Delta_{\mathrm{mini}} = 160\,\mu\mathrm{eV}$ that reproduces the measured Shapiro maps. The cooling power is calculated by using the estimated electron-phonon coupling constant $\Sigma_{Bi_2Se_3} = 27 \times 10^9\,\mathrm{Wm^{-3}K^{-5}}$ and a coupled volume of $V_{JJ} = 20\,\mathrm{nm} \cdot 1.45\,\mu\mathrm{m} \cdot 540\,\mathrm{nm} = 0.016\,\mu\mathrm{m}^3$.

To our knowledge, the prefactor τ_0 has not been estimated in literature. However, the energy Δ_{mini} is supposed to be in the order or smaller than the Thouless energy. Experimentally $E_{\mathrm{th}} = 220\,\mu\mathrm{eV}$ which is consistent with the parameters used in the simulation ($\Delta_{\mathrm{mini}} = 160\,\mu\mathrm{eV}$).

In figure 6.9, we display the experimental measurement of LC099-JJ4 and the associated simulations at the same irradiation frequencies. We propose two types of simulations both with the effect of heating on the contribution of the conventional supercurrent (as for section 2 of chapter 5) and either a constant 4π supercurrent $I_c^{4\pi} = 35\,\mathrm{nA}$, or with thermally activated poisoning on the 4π supercurrent.

At 1.6 GHz, we observe in the first simulation that the appearance order of the Shapiro steps is $n = 2, \mathbf{1}, 3, 4$ which is not the same as the experiment: $n = 2, 3, \mathbf{1}, 4$. However, the steps $n = 1$ and $n = 3$ appear almost at the same irradiation power. Adding poisoning does not change this appearance order, but rather slightly delays the appearance of step $n = 4$.

Experimentally, the decrease of the resistance at zero current bias (orange arrow of graph a) is observed in the simulation by the opening of a gap at the crossing of the resistive branches (orange arrows of graph g). This effect is observed in experiment only at zero current bias. However, the simulation with a constant 4π supercurrent displays a gap opening at all the even crossings pointed by the orange arrows of graph g. Poisoning removes this gap opening on the high index Shapiro steps (brown arrows in graph m).

At 1.9 GHz, the anomaly observed at zero current bias (red ellipse) cannot be reproduced

Figure 6.9. *(facing page)* – Differential resistance of the junction LC099-JJ4 under RF irradiation at 1.6, 1.9 and 4 GHz and the associated amplitude of the Shapiro first steps I_n. The first Shapiro steps are labeled. The orange arrows and the red circle point at anomalies at the crossing point between the switching branch and the retrapping branch. It is further discussed in the main text. The brown arrows point at the effect of poisoning between the second and third line graphs. The black arrows points at the RF power where the step appear.
(top row graphs) Experimental measurement of LC099-JJ4.
(middle row graphs) Simulations using the RSJ model with conventional Andreev bound states (ABSs) that are subject to heating following the model presented in chapter 5 section 2. In addition to these conventional modes, we add a 4π periodic mode that carries 35 nA.
(bottom row graphs) Simulations using the RSJ model similar to the middle row graphs. The 4π periodic mode are here subject to thermally activated poisoning following (5.24).

4. A wrong estimation of E_{th} lead us to perform some simulations with $\Delta_{\mathrm{mini}} = 160\,\mu\mathrm{eV}$. Currently, we are repeating these simulation with the corrected estimation: $\Delta_{\mathrm{mini}} = E_{\mathrm{th}} = 220\,\mu\mathrm{eV}$.

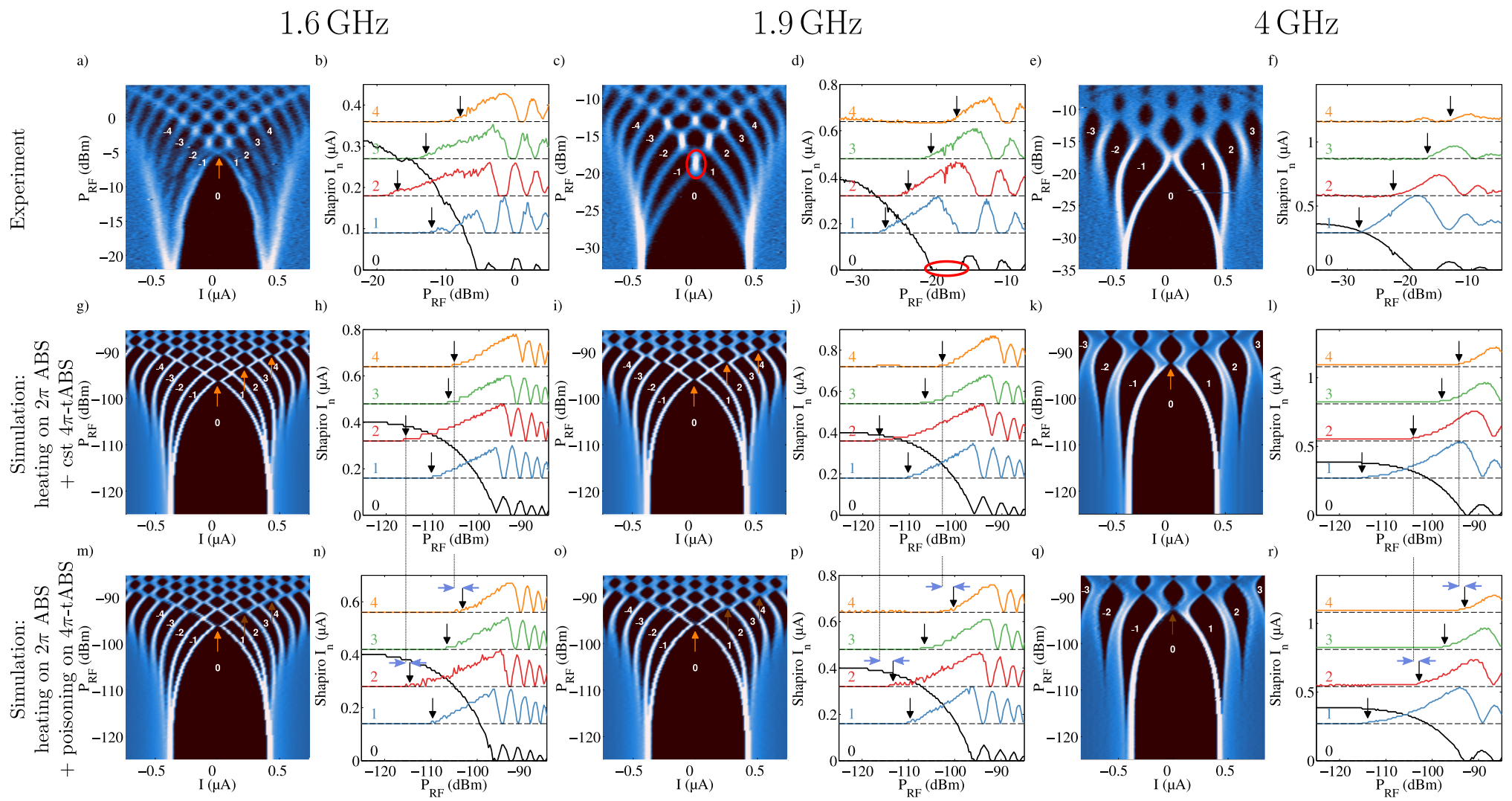
1.6 GHz
1.9 GHz
4 GHz
Experiment
Simulation: heating on 2π ABS + cst 4π-tABS
Simulation: heating on 2π ABS + poisoning on 4π-tABS
a)
b)
c)
d)
e)
f)
g)
h)
i)
j)
k)
l)
m)
n)
o)
p)
q)
r)
P_RF (dBm)
I (μA)
Shapiro I_n (μA)

by the simulation neither with nor without poisoning. Furthermore, the simulation predicts an even–odd effect on the appearance order of the Shapiro steps which is not observed experimentally.

At 4 GHz, poisoning enables one to cancel the opening of the gap at zero current bias (orange arrow in k becomes a brown arrow in graph r).

Josephson junction LC106-JJ2 In order to validate the model, we also compare the experimental measurement of LC106-JJ2 to the simulation [5].

Before presenting the comparison between the simulations and experiment for the second junction LC106-JJ2, we need to observe carefully the three Shapiro measurements of LC106 in figure 6.7. We observe that the switching and retrapping current are not the same depending on the irradiation frequency. In addition, the high frequency irradiation (3.5 GHz) presents an hysteresis at low irradiation power (-10 dB m). This difference of behavior depending on f_{RF} is explained by a change in the electronic temperature. Therefore, the RF irradiation does not have the same impact on T_{el} depending on the RF frequency.

We estimate the electronic temperature at the low RF power part of the Shapiro measurements by comparing the values of the switching and retrapping currents with the experimental temperature dependence measured and shown in figure 6.8. The estimated electronic temperatures are given in table 6.3.

f_{RF}	1 GHz	2.2 GHz	3.5 GHz
$\min(P_{\mathrm{RF}})$	-22 dB m	-15 dB m	-10 dB m
$T_{\mathrm{el}}(\ \min(P_{\mathrm{RF}})\ )$	500 mK	375 mK	200 mK

Table 6.3. – Temperatures of the electron bath estimated at low RF power for the three Shapiro measurements on LC106.

To take into account this shift of the electronic temperature, we offset the phonon temperature so that the electronic temperature is artificially elevated. This ad-hoc elevation indicates the limitation of our thermal model. Indeed, without this offset, we underestimate the electronic temperature during a Shapiro measurement.

Figure 6.10 compares the Shapiro measurement with the simulated one. We do not include poisoning but it could be included for a deeper analysis. We include heating only.

At 1 GHz in the simulation figure g), the appearance order of the Shapiro steps shows an the even-odd effect : $n = 2, 4, 1, 3$. This is not observed experimentally: only the step $n = 1$ is shifted to higher RF power, see figure a).

The opening of a gap at zero current bias visible experimentally (orange arrow) is also reproduced in the simulation at the same magnitude.

As for the previous junction, our simulation of the intermediate irradiation frequency (2.2 GHz) does not explain the feature highlighted by the red circle. However, the appearance order of the steps is regular both experimentally and in the simulation.

5. This last sample has been measured during the redaction of this manuscript. Therefore, the simulations using poisoning are currently running.

At 3.5 GHz, the Shapiro steps are conventional. We note that the hysteresis seen in the experiment is reproduced by the heating model on the conventional ABS see figure k). The appearance order of the steps should be studied on the retrapping side ($I < 0$) to remove any artefact due to Joule heating.

The simulation does not predict every feature of the experimental observations, as the elongated crossing point at intermediate irradiation frequency (red circle). However, poisoning could explain the absence of signatures of the 4π ABS at high irradiation power and the closing of the gaps at the even crossing points (brown arrow).

Including heating effects to perfectly match the experimental observation is a delicate task. We could estimate the temperature evolution of $T_{\text{phonon}}(P_{\text{RF}})$ by a polynomial law but there is no guaranty that this estimation reflects reality. This heating is poorly evaluated by the thermometer placed on the sample holder that measures T_{bath} (cf figure 6.11). Our thermal model supposed that $T_{\text{bath}} = T_{\text{phonon}} = C^{st}$, but apparently this hypothesis is not valid anymore during Shapiro measurements. T_{bath} increases when increasing P_{RF} and the underestimation of T_{el} could originate from the non perfect coupling between T_{phonons} and T_{bath}.

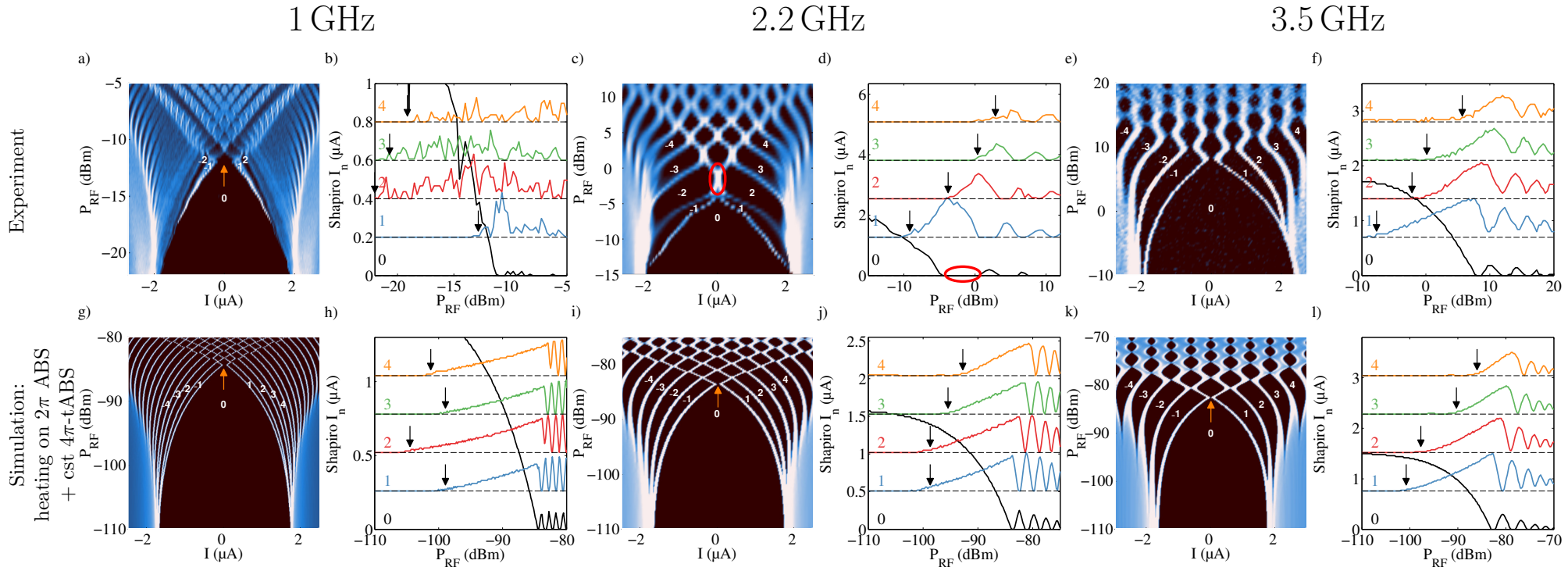

Figure 6.10. – Differential resistance of the junction LC106-JJ2 under RF irradiation at 1, 2.2 and 3.5 GHz and the associated amplitude of the Shapiro first steps I_n. The first Shapiro steps are labeled. The orange arrow and the red circle point at anomalies at the crossing point between the switching branch and the retrapping branch. It is furthered discussed in the main text. The arrows points at the RF power where the step appear.
(top row graphs) Experimental measurement of LC106-JJ2.
(bottom row graphs) Simulations using the RSJ model with conventional Andreev bound states (ABSs) that are subject to heating following the model presented in chapter 5 section 2. In addition to these conventional modes, we add a 4π periodic mode that carries 50 nA.

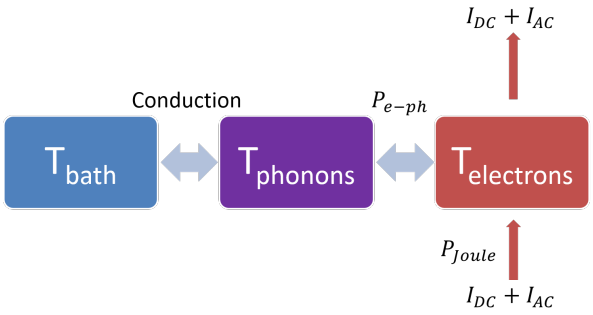

Figure 6.11. – Schematic of heat transfer between the three baths at different temperatures defined in a mesoscopic system. Heating comes mainly from Joule heating and is dissipated through the phonons of the system and the substrate.

2.3 Discussions

Let us here discuss the validity of the signature of a possible 4π ABS in our systems. We recall the estimated amounts of 4π ABS by using the observation of frequency threshold of the even–odd effect and the gap opening $\tilde{I}_c$ at the crossing point of the switching and retrapping branches :

Josephson junction	I_c^{tot}(nA)	$I_c^{4\pi}$(nA) (from the even-odd effect)	$I_c^{4\pi}$(nA) (from $\tilde{I}_c$)
LC099-JJ4	450	35	
LC106-JJ2	2700	55	220

Partial description of Shapiro measurement The even-odd effect we have observed is limited to the shift to higher RF power on the appearance of the Shapiro step $n = 1$. We did not observe any even–odd effect on higher index steps. This sole observation is a weak signature as it could originate from heating effects as observed in the lower parts of figure 5.9b,f.

However, we have predicted and observed experimentally a second signature of the 4π ABS, that is the opening of a gap at the crossing between the switching and retrapping branches. This opening is supposed to reproduce at all even crossings which we did not observe.

With our model of thermal poisoning we can explain the absence of the even-odd effect and the gap opening on high order Shapiro steps. With our simulations, we can confidently say that a 4π periodic ABS that is subject to thermal poisoning would give similar features as the ones observed experimentally.

There is still a characteristics that does not match with the explanation we propose. Indeed, a single ABS can theoretically carry up to 35 nA that is way less than our estimations of $I_c^{4\pi}$.

Where is the magnetic layer in our junctions? The attentive reader may have noticed that the system we are dealing with does not contain a magnetic layer. As far as

we know, all theories predicting the presence of a 4π ABS require a magnetic layer.

As described in chapter 3, vanadium has never been used to induce superconductivity by proximity effect in bismuth based TIs. In addition, the anomalous effects we have reported here in Shapiro measurement have also never been observed in previous reports on bismuth based TIs. We think vanadium could be the key ingredient that enabled the apparition of a 4π periodic ABS in our system.

Indeed, vanadium doping is known to induce a quantum anomalous Hall regime in $BiSbTe_3$, Bi_2Te_3 and Sb_2Te_3 [32, 35, 52]. As we have etched the TI crystal prior to vanadium deposition, the atoms of vanadium may have slightly doped the crystal at its surface, thus inducing magnetic moment at the interface between Bi_2Se_3 and the vanadium. Such particular geometry has not been simulated yet in literature but we can think that it resembles the one studied in this thesis in section 2.3 of chapter 4.

Furthermore, even if we have deposited a protection layer of gold on top of the vanadium electrodes, the side surfaces of the electrodes are in certainly oxidized. Vanadium is a transition metal that oxides in various ways: VO (II), V_2O_3(III), VO_2(IV), V_2O_5(V), and others. Those oxides have been widely studied and are known for having various magnetic order [81] (VO_2 [191], VO_3 [39]).

Therefore, there is most probably a strong magnetic field close to the junction that plays the same role as the ferromagnetic layer used in the literature to decouple the topologically protected 4π periodic ABS from the continuum of states and hence keep its 4π periodicity.

We thus believe that our JJ are actually S-M-TI-M-S (with M the magnetic barrier), a geometry that has not yet been studied theoretically.

Summary

In this chapter we have presented the observation of the even/odd effect on the first step of the Shapiro measurement on topological Josephson junctions designed on Bi_2Se_3. Because of the short electronic mean free path in Bi_2Se_3 and the small Thouless energy compared to the superconducting gap of the vanadium electrodes, the superconducting transport occurs in the long diffusive regime.

We have probed the supercurrent profile of the junctions with Fraunhofer measurement and concluded that the supercurrent flows uniformly inside the Josephson junction. This can be understood by the superconducting coupling of the complete bulk of the crystal.

For the Shapiro measurement, we have observed, at high radio frequency irradiation a conventional appearance order of the Shapiro steps. At low frequency irradiation we observed the predicted even/odd effect by the non-monotonic appearance order of the Shapiro steps : $n = 2, 1, 3, 4, 5$. This effect is however only visible on the low index steps : there is no inversion between $n = 3$ and $n = 4$... This non regular appearance order can be explained by our thermally activated poisoning model introduced in chapter 5. However, at intermediate frequency, we observed anomalies in the Shapiro measurements at the crossing point between the switching and the retrapping branch that cannot be explained by the model.

Chapter 7

Superconducting proximity effect through the surface states of $BiSbTeSe_2$

Most of bismuth based topological insulators have a metallic bulk. As a result, signatures of surface states in transport are always spoiled by the bulk conductance. With a significant bulk contribution, the observation of an even-odd effect in the Shapiro measurement is thus delicate.

Recently, the TI $BiSbTeSe_2$ (BSTS) has shown clear evidence of surface transport only [182]. For this reason we have focused our growth efforts on this material (cf chapter 2) to study topological Josephson junction.

In this chapter we present the observation of a superconducting proximity effect in the surface states of a topological insulator without bulk conductivity. We first characterize the transport properties of the BSTS crystal used to fabricate the junctions, then we study the regime of conduction in which the superconducting proximity effect develops. By probing the Fraunhofer pattern, we prove the two-dimensional nature of the superconducting proximity effect. We observe resonances of the environment that affect the transport properties of the junctions and forbid to properly perform Shapiro measurement.

1 State-of-the-art of Josephson junctions on $BiSbTeSe_2$

BSTS has been already used to fabricate topological Josephson junctions by Lee et al [112] and Snelder et al [159]. Both groups have observed the superconducting proximity effect inside the surface states of the crystal but did not prove its topological nature.

While Lee et al [112] measured the non-local transport originating from the surface states, Snelder et al [159] made small Josephson junctions (40 nm long). The authors have shown a surface–dominated normal transport that turns into a superconducting transport when coupled to superconducting leads.

Up to now, no clear evidence has been found for the topological nature of the proximity induced superconductivity on the bismuth-based topological insulators. In addition, the fractional AC Josephson effect was probed in BSTS Josephson junctions by the group of A. Brinkmann but they did not observe the even-odd effect.

2 Josephson junctions on $BiSbTeSe_2$

In this section we first describe the normal transport properties of BSTS. Then we find the superconducting transport regime in which the superconducting proximity effect occurs in a Josephson junction geometry.

2.1 $BiSbTeSe_2$ a topological insulator without bulk conduction

BSTS as a topological insulator has been first grown and characterized in 2011 by Taskin et al [168]. Only three years later, Xu et al have observed quantum Hall effect in this material [182]. They characterized its electronic band structure by performing an ARPES measurement displayed in figure 7.1. In this figure we see the Fermi level lying at the Dirac point inside the bulk band gap. They also estimated the Fermi velocity $v_F^{BSTS} = 3 \times 10^5\,m/s$, which is close to the one of Bi_2Se_3: $v_F^{Bi_2Se_3} = 5 \times 10^5\,m/s$ [190].

Our BSTS crystals also show surface conduction that has been characterized in chapter 2. In table 7.1 we summarize the transport properties of our material and compare them with the properties of the one that displayed quantum Hall effect [182].

Material	n^{2D}	μ^{2D}	D^{2D}	l_e^{2D}
BSTS from Xu et al [182]	$2 \times 10^{12}\,cm^{-2}$	$3000\,cm^2/V/s$	$65\,cm^2/s$	37 nm
our BSTS	$2.5 \times 10^{13}\,cm^{-2}$	$106\,cm^2/V/s$	$12\,cm^2/s$	6.8 nm

Table 7.1. – Transport properties of two $BiSbTeSe_2$, with n^{2D} being the surface carrier density, μ^{2D} the surface electron mobility,D^{2D} the associated diffusion coefficient and l_e^{2D} the electronic mean free path.

We see that the quality of the two crystals is much different. There is a factor 10 in the carrier densities. The electron mobility of our crystal is poor in comparison to the

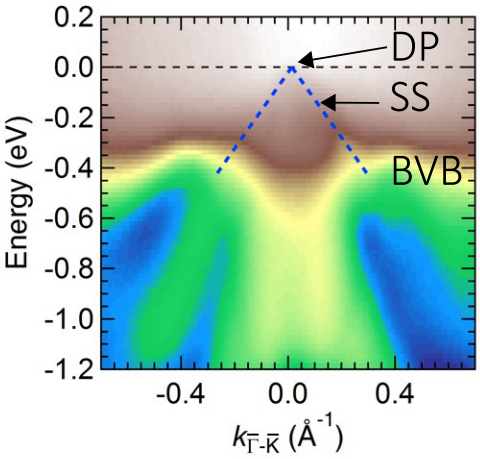

Figure 7.1 – Angle resolved photo-emission spectroscopy of $BiSbTeSe_2$. The blue dashed lines are guide lines to highlight the linear dispersion relation of the surface states (SS) which are decoupled from the bulk valence band (BVB). The energy is measured with respect to the Fermi level. The Dirac point (DP) is the crossing point of the linear surface states. Extracted from [182].

state of the art. This low mobility implies a low diffusion coefficient and a short mean free path. This electron mobility explains the absence of any Shubnikov-de-Haas oscillations in magneto-transport. Moreover, the short mean free path leads to a diffusive regime when building a Josephson junction of few tens of nanometer long.

2.2 Long junction in diffusive regime

Despite the low mobility of our crystal, we have managed to produce Josephson junctions with vanadium leads. Table 7.2 summarizes the geometric characteristics of the junctions that present a supercurrent. In all cases, the supercurrent is small ($\leq 50\,\mathrm{nA}$ for a width of $\approx 2\,\mu\mathrm{m}$) in comparison to the junctions made on Bi_2Se_3 ($\approx 1\,\mu\mathrm{A}$ with the same geometry).

Name	L(nm)	$W(\mu$m)	t(nm)	I_c(nA)	$R_N(\Omega)$	$eR_NI_c(\mu$eV)	$E_{th}(\mu$eV)	$\frac{eR_NI_c}{E_{th}}$
LC111	150	2	19	0	390	0	22	0
JJ2	60	1.6	39	35	335	11.7	81	0.15
JJ3	60	0.2	17	10	1200	12.0	178	0.067
JJ4	60	1.9	38	33	325	10.7	69	0.18
JJ5	50	1.9	38	47	280	3.2	97	0.14
JJ6	60	2.0	23	30	250	7.5	86	0.088
JJ7	70	2.0	23	12	470	5.6	40	0.14
JJ8	60	0.9	26	18	550	9.9	86	0.12
JJ9	70	0.9	26	21	225	4.7	181	0.026
JJ12	70	0.5	37	3	1250	3.1	59	0.053
JJ13	60	0.7	59	15	480	7.2	127	0.057

Table 7.2. – Table summarizing the characteristics of all the Josephson junctions we have produced on BSTS. With L being the length between the superconducting electrodes, W and t the width and thickness of the crystal, I_c the critical current at base temperature (60 mK) and R_N the normal state resistance of the junction. We estimate the Thouless energy $E_{th} = \frac{\hbar D}{L^2}$ by using the normal state resistance to evaluate the diffusion coefficient for each flake.

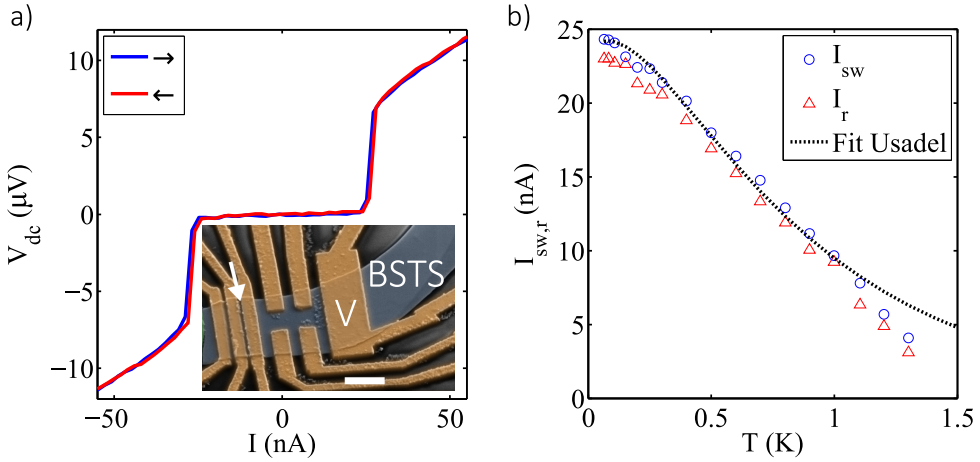

Figure 7.2. – a) Voltage-current characteristic of the Josephson junction JJ6 built on $BiSbTeSe_2$ (BSTS). A small hysteresis is noticeable between the up (blue) and down (red) current sweeps. (Inset) Scanning electron microscopy image of the device with false colors. The vanadium contacts are in orange and the blue flake is the BSTS crystal. The white line is 1 µm for scale. An arrow points at the junction JJ6. b) Switching and retrapping current versus temperature. A fit is added following Eq.(6.1) with a Thouless energy $E_{\mathrm{th}}^{fit} = 27\,\mu\mathrm{eV}$ and a prefactor $\alpha = 2.6\%$.

But the $eR_{\mathrm{N}}I_{\mathrm{c}}$ product is comparable for both Bi_2Se_3 and BSTS material. We also had to place the leads much closer on BSTS than on Bi_2Se_3 to have a measurable supercurrent.

We estimate the Thouless energy by using the equation $E_{\mathrm{th}} = \frac{\hbar D}{L^2}$ that gives an energy much smaller $(40 - 180\,\mu\mathrm{eV})$ than the superconducting energy gap of the electrodes $\Delta_V \approx 800\,\mu\mathrm{eV}$. This categorizes these junctions in the long diffusive limit.

The $eR_{\mathrm{N}}I_{\mathrm{c}}$ product is much smaller $(3 - 12\,\mu\mathrm{eV})$ than the estimated Thouless energy and does not follow the expected ratio of 10.8 (see chapter 1 section 1.1.4).

We can also estimate the Thouless energy with the temperature dependence of the critical current. In figure 7.2, we present the voltage-current characteristic of one of the junctions (JJ6) and its associated $I_{\mathrm{c}}(T)$. We fit the dependence using the Usadel formula Eq. (6.1). This gives a Thouless energy $E_{\mathrm{th}}^{fit} = 27\,\mu\mathrm{eV}$ and a transparency coefficient $\alpha = 2.6\%$. This second estimation of the Thouless energy ($27\,\mu\mathrm{eV}$) is much smaller than the calculated one ($86\,\mu\mathrm{eV}$). In both cases, the transport occurs across a long diffusive junction ($E_{\mathrm{th}} \ll \Delta_{\mathrm{V}}$).

3 Supercurrent in surface states

In order to show that the Josephson supercurrent is located on the surface of the BSTS crystal, we first study the critical current dependence with respect to the thickness of the different junctions. Then we analyze the supercurrent profile by performing a Fraunhofer measurement of the junction.

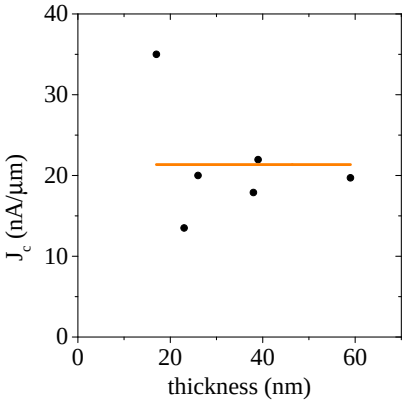

Figure 7.3 – Critical current density $J_c = I_c/W$ versus the thickness of the crystal for all junctions of length $L = 60\,\text{nm}$ produced on BSTS, with W being the width of the crystal. In orange is the mean value at $21\,\text{nA}/\mu\text{m}$.

3.1 Thickness independent critical current

If the supercurrent develops in the whole crystal, then the critical current density I_c/W would scale linearly with the thickness of the crystal [1]. In figure 7.3, we have plotted this quantity for different thickness for a fixed junction's length. We observe that the quantity I_c/W does not increase linearly but is rather constant. Having a supercurrent density independent of the thickness of the crystal is consistent with a supercurrent flowing only at the surface of the crystal.

To directly probe this non uniform supercurrent density, we can use the Fraunhofer pattern to extract the spatial dependence of the supercurrent profile $J_c(x)$.

3.2 Non conventional Fraunhofer pattern

We apply a magnetic field perpendicular to the surface of the normal part of the JJ (cf figure 7.4a). If the supercurrent is homogeneous inside the BSTS crystal, then the critical current dependence $I_c(B)$ should follow the regular Fraunhofer pattern $I_c\left|\text{sinc}(\frac{\pi WB}{L\phi_0})\right|$, with the flux quantum $\phi_0 = \frac{h}{2e}$ as presented in Appendix A section 1.

We focus in this section on the results of junction JJ6. The same phenomenon has been observed on several junctions. The differential resistance versus perpendicular magnetic field and the current bias is displayed in figure 7.5a. We observe many oscillations of the critical current up to a large magnetic field. The critical current almost cancels at 80 mT and increases again up to a maximum at 140 mT. This second oscillation is understood by a SQUID [2]-like profile of the supercurrent [3].

Following the method based on a Fourier transform described in Appendix A section 2, we estimate the supercurrent profile $J_c(x)$. It is shown in figure 7.5b. We observe a finite

1. We call current density the amount of current per unit of width W and not per unit of surface. With W the width, t the thickness and L the length of the junction, the hypothesis $eR_N I_c = C^{st}$ gives $\frac{I_c}{W} = t\frac{C^{st}}{e\rho L}$.

2. Superconducting quantum interference device

3. A similar behavior has been observed in graphene [4], and 2D HgTe [74, 136] in a regime of quantum spin Hall effect.

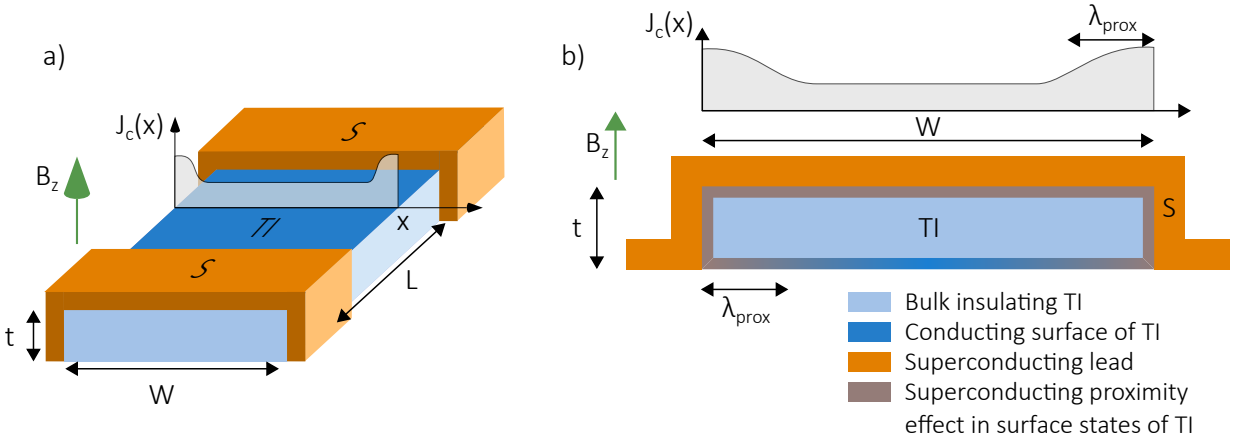

Figure 7.4. – a) Schematic of the ideal set-up to probe the supercurrent profile $J_c(x)$ inside the Josephson junction. We apply a perpendicular magnetic field while recording the critical current I_c. b) Schematic of the model we propose to explain the non uniform supercurrent distribution $J_c(x)$. Side view of the topological insulator (TI) flake in blue, contacted with a superconducting (S) electrode in orange. The flake has a width W and a thickness t. Only the surface states of the TI are superconductively coupled. The proximity effect extends in the surface states of the bottom surface over a distance λ_{prox}.

supercurrent in-between $\pm 1\,\mu m$ that corresponds to the physical boundary of the crystal of BSTS. Outside this position, the supercurrent is supposed to be zero, which gives an estimation of the uncertainty of the estimation.

In addition to the finite supercurrent density in the middle of the flake, we observe a large current density at its border. Still in our system, no quantum spin Hall effect is expected. We propose a simple model that explains this behavior: If the supercurrent only flows in the surface states, then it can also flow at the bottom surface due to proximity effect on the bottom over a small distance λ_{prox}. A schematic of this model is drawn in figure 7.4b. The perfect theoretical supercurrent profile $J_c^{model}(x)$ and the critical current $I_c^{model}(B)$ of this model are drawn in figure 7.5 with black lines [4]. The parameters used are $\lambda_{prox} = 75\,nm$ and the supercurrent profile in the surface states is $13\,nA/\mu m$.

4 Resonances from the environment

In the previous section we have shown that the superconducting proximity effect in the TJJ develops at the surface of the BSTS crystal. This system thus seems ideal to investigate the even-odd effect without contribution from the bulk. However, the Josephson junctions on our sample all displayed voltage steps as if they were irradiated by radio frequencies. This unexpected behavior prevented us to properly observe any even-odd effect in the Shapiro measurement at low frequency. In this section we first expose this observation, then present the origin of the self resonant voltage steps and finally show the

4. Here we neglect the supercurrent which comes from the side surfaces. It has a negligible impact on $I_c^{model}(B)$ and cannot be the only explanation of the supercurrent profile.

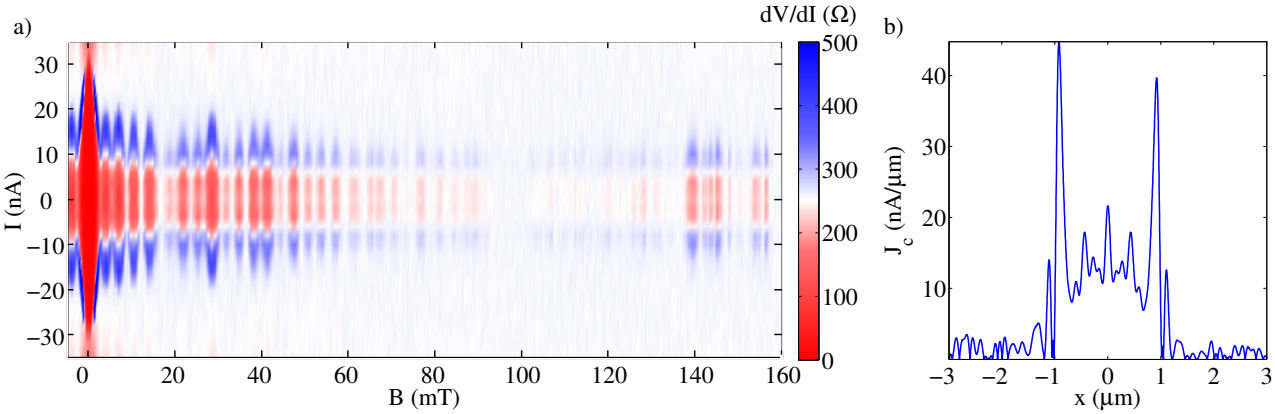

Figure 7.5. – Fraunhofer measurement of the topological Josephson junction JJ6 built on BSTS. a) Differential resistance colored map versus the perpendicular magnetic field and the DC current bias. b) Supercurrent profile estimated by using a) and following the method proposed in Appendix A. In a) and b), the black line corresponds to the critical current and the supercurrent profile of the model proposed in main text.

Shapiro measurement that we have performed.

4.1 Equidistant voltage steps in the VI characteristics

We have observed some self-induced voltage steps without RF irradiation in every junction of the sample. We focus here on the Josephson junction JJ6 whose voltage–current characteristics is shown in figure 7.6. We see some plateau-like features. By plotting the differential resistance versus the measured DC voltage, we see that the plateaus are equidistant in voltage. We have found for JJ6 a distance between each plateau of $\Delta V = 8.66\,\mu\text{V}$. Such voltage step would correspond to an irradiation by an antenna at $f_{\text{res}} = \frac{2eV_{\text{step}}}{h} = 4.1\,\text{GHz}$. This value is different for each junction on the same substrate (LC134) and does not scale with any estimated physical quantity of the junctions such as $e \cdot R_{\text{N}} \cdot I_{\text{c}}$, E_{th}, L, W or t.

The same type of resonances have already been observed and studied by Fiske et al [58] where the Josephson junction itself forms a resonant electromagnetic cavity in which the resonant modes interact with the Josephson effect. This type of resonance is visible when the junction is under a perpendicular magnetic field or when the supercurrent profile is inhomogeneous [33, 166]. A theoretical explanation is given in chapter 9 of ref [16]. However, the size of the cavity has to be a multiple of the electromagnetic wavelength. In our case, the GHz frequency resonance would correspond to a cavity of size [5] 3 cm, which is 4 order of magnitude larger than the width of the junction. Therefore, our observation cannot be compatible with the well known self resonant Fiske steps.

5. The so-called Fiske–steps or zero–field steps are voltage plateaus at voltage $V_{\text{Fiske,n}} = \frac{h}{2e}\frac{\tilde{c}}{2W}n$ with n being an integer, W the length of the resonant cavity (the width of the Josephson junction) and the wave velocity $\tilde{c} = c\sqrt{\frac{L}{\epsilon_{\text{r}} t}}$, with c the speed of light, ϵ_{r} the relative permittivity of the normal metal of the junction, L the length of the junction and $d = L + 2\lambda_{\text{B}}$, with λ_{B} the magnetic penetration depth inside the superconducting electrodes.

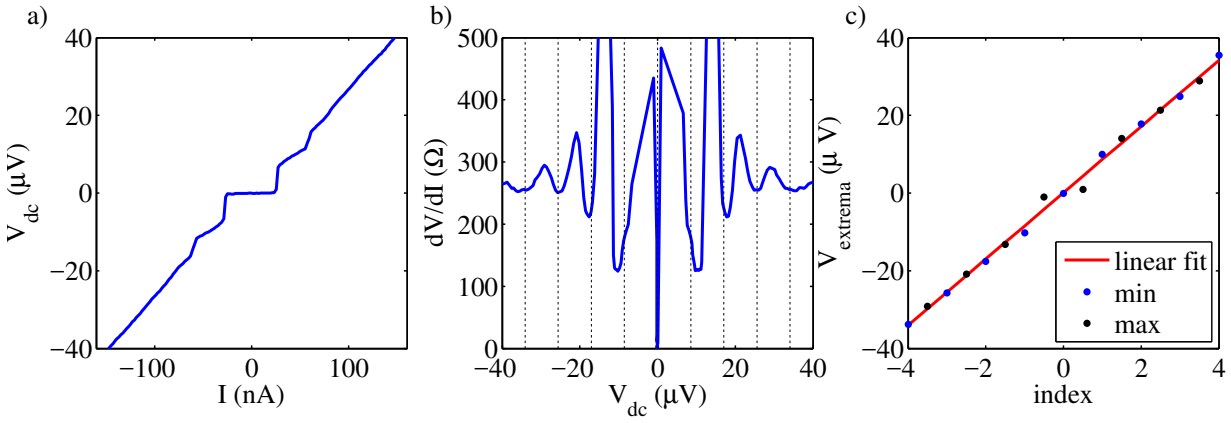

Figure 7.6. – Observation of self-induced voltage steps on junction JJ6. During this measurement, no antenna is placed near the junction. We simply current bias the device and observe equidistant voltage steps. a) Voltage–current characteristics. Some step-like features are visible above the critical current. b) Differential resistance of the junction versus the measured DC voltage during a current biased sweep. The dotted vertical lines are located at multiples of V_{step}. c) Voltages of each extrema of the differential resistance versus their index. In red is plotted a linear fit with a slope of $V_{\text{step}} = 8.66\,\mu\text{V}$.

4.2 Resonance from the environment to the junction

To understand the origin of the irradiation, we had to find a resonant cavity of size in the centimeter range. The resonance frequency is independent of the cryostat geometry and of the filter we use on the measurement lines.

Exceptionally, during the fabrication process of those Josephson junctions on BSTS, we have used superconducting lines of vanadium from the junction up to the bonding pads (see figure 7.7a). Those lines have a kinetic inductance $L_{\text{kin}} \approx 370\,\text{fH}/\square$ at $3.5\,\text{GHz}$ [6] and are capacitively coupled to the SiO_2 back gate and between them forming LC resonators.

In collaboration with C. Hoarau (Institut Néel, pôle électronique), the RF response of our sample design has been simulated. The circuit is composed of four input ports with a $50\,\Omega$ impedance to which we send or receive a signal [7]. The results are shown in figure 7.7. We choose to plot only the transmission coefficients from port 1 to port 2 which presents the largest resonant dip in frequency. At $4.78\,\text{GHz}$, the system transmits poorly the electromagnetic excitations. Therefore, any irradiation at this frequency will stay trapped at the surface of the substrate. This resonance frequency is close to the observed voltage plateau in the VI characteristics of JJ6: $\frac{h \cdot 4.78\,\text{GHz}}{2e} = 9.88\,\mu\text{eV}$.

Because of the AC Josephson relation Eq. (4.3), a biased junction irradiates photons at the Josephson frequency $f_{\text{J}} = \frac{2eV}{h}$. During a current sweep, the junction will irradiate at an increasing frequency $f_{\text{J}}(V)$. When the voltage across the junction reaches $\frac{hf_{\text{res}}}{2e}$, then the environment resonates and the phase locks-in at the same frequency f_{res}, thus leading

6. $L_{\text{kin}} = \frac{\hbar R_{\text{sq}}}{\pi \Delta}$ with R_{sq} the sheet resistance. We have performed several simulation with different value of the kinetic inductance by a factor 10 and 0.1 which gives a variation of the resonance frequency of about 5%.

7. The input impedance is unknown and therefore induce an uncertainty on the resonance frequency.

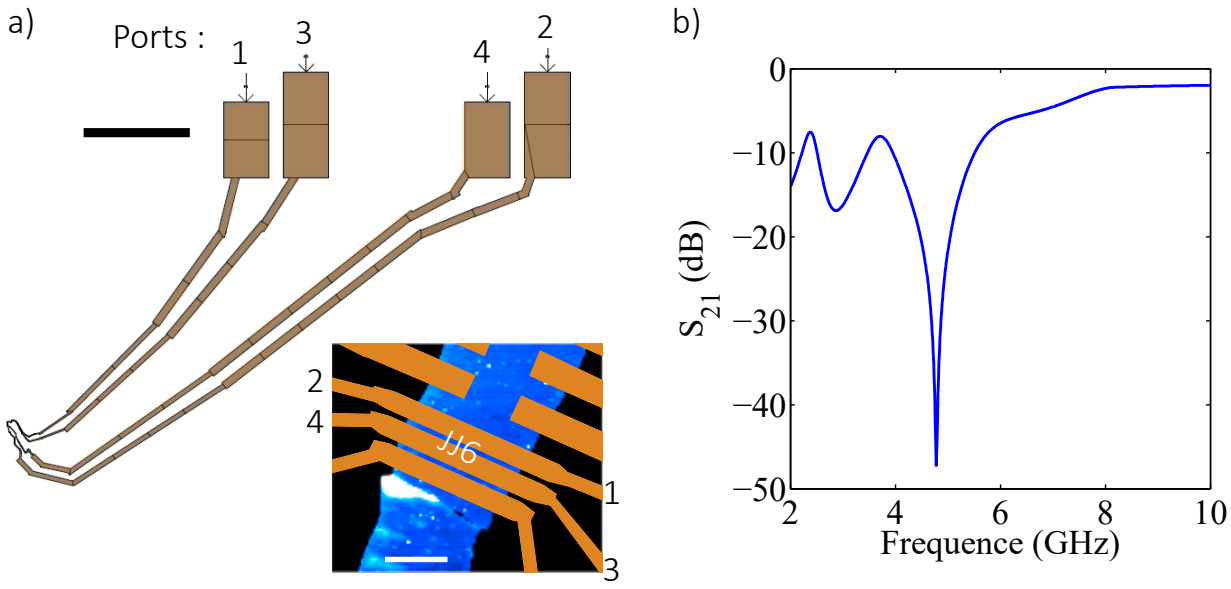

Figure 7.7. – a) Design of the electrodes patterned on the substrate that form the junction JJ6. The pads are labeled from 1 to 4. The black line is 250 µm for scale. (inset) False colors image of an atomic force microscopy. In blue is the flake of BSTS and in orange are the design of the superconducting electrodes. The Junction JJ6 is formed in-between the two leads that are connected to the four labeled pads. The white line is 1 µm for scale. b) Transmission matrix coefficient from line 1 to line 2 versus the frequency of the input signal. A dip in the coefficient means a poor transmission of the signal that stays located inside the sample.

to a voltage plateau.

As we can see from the transmission amplitude, there exists no resonance at multiple of 4.78 GHz. Therefore, the plateaus at multiple of 9.88 µeV in the VI characteristics cannot be explained by harmonics from the resonance cavity. They can however be explained by processes involving several photons at 4.78 GHz exciting multiple of the Josephson frequency $n \cdot f_J$ [48].

4.3 Impossible observation of the even-odd effect

Due to the presence of the self induced voltage steps, the Shapiro measurement is more difficult. Indeed, during this measurement, in addition to the presence of the resonant frequency f_{res}, we irradiate the junction with some external RF frequency f_{RF}. The response of a Josephson junction under two radio frequencies has already been observed by Grimes and Shapiro [72]. They observe and explain the appearance of additional voltage steps spaced by the difference frequency $|f_{res} - f_{RF}|$.

We could use the resistively shunted Josephson junction (RSJ) model, presented in chapter 5, to predict the behavior of a topological Josephson junction under two radio frequencies. However, we do not know the power at which the junction is irradiated at f_{res}. This study is possible but has not been done in this thesis due to a lack of time.

The results of the Shapiro measurements are presented in figure 7.8. The figure represent the colormaps of the differential resistance as a function of the irradiation power for two

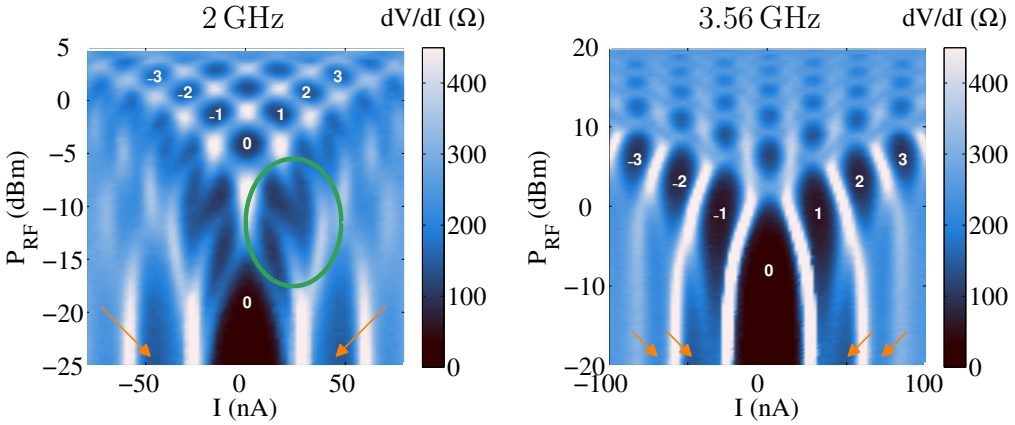

Figure 7.8. – Differential resistance of the junction JJ6 under RF irradiation at 2 and 3.56 GHz. The first Shapiro steps are labeled. The green circle delimits a region with features that unable the observation of any even-odd effect. It is further discussed in the main text. The orange arrows points at the voltage plateaus already present without any RF irradiation.

irradiation frequencies. The orange arrows points at the minima in the dV/dI that are already present without RF irradiation.

At frequency $f_{\mathrm{RF}} = 3.56\,\mathrm{GHz}$, the Shapiro plateaus are well defined as labeled by the indexes. The initial low power steps gradually disappear and are replaced by the Shapiro steps. At high RF power, we observe the usual oscillations of the currents for each step I_{n}. The appearance order of the Shapiro steps is regular: 0,1,2,3,...

At lower frequency ($f_{\mathrm{RF}} = 2\,\mathrm{GHz}$), the presence of the initial steps is forming complex structures in the colored map (green circle). Those structures correspond to the appearance of steps at the frequency difference $f_{\mathrm{RF}} - f_{\mathrm{res}}$ as predicted by [72]. This mixing of the two frequencies, hinders to identify the presence or absence of the even-odd effect.

Summary

THE previous chapter reported on the observation of the even-odd effect in long diffusive Josephson junctions fabricated on Bi_2Se_3. This topological insulator has a metallic bulk that reduces the visibility of the single 4π periodic topological Andreev Bound state (4π-tABS). To increase the visibility of the 4π-tABS, we fabricated Josephson junctions with bulk insulating topological insulator: $BiSbTeSe_2$ (BSTS).

In this chapter we have observed the superconducting proximity effect at the surface of such a BSTS crystal.

We present TJJs in the regime of long diffusive transport. The 2D nature of the superconducting proximity effect is proven by studying the thickness evolution of the critical current density and by performing Fraunhofer measurement. The latter presents a non regular Fraunhofer pattern with two periodicities that make the critical current to re-increase at a large perpendicular magnetic field. By applying a Fourier transform on the $I_c(B)$, we estimated the supercurrent profile inside the flake of BSTS. This profile shows a large intensity at the two edges of the flake. We explain this profile by the presence of a proximitized region on the bottom surface of the TI flake that causes as a SQUID-like behavior in the Fraunhofer measurement.

Shapiro measurement has been performed on these topological Josephson junctions but no conclusion could be drawn on the observation of the even-odd effect. Indeed, all junctions presented a current-voltage characteristic with voltage steps induced by the resonant circuit formed by the DC lines. To avoid this self irradiation, one must simply fabricate new samples with measurement lines that are non superconducting and deposit short superconducting lines only close to the topological insulator flake.

Conclusion & outlook

THE prospect of investigating the unconventional p-wave superconductivity that can host a Majorana bound state led us to investigate Josephson junctions on three dimensional topological insulators. We choose the compounds Bi_2Se_3 and $BiSbTeSe_2$ as materials to address the physics of topological Josephson junctions (TJJ).

With the resistively shunted junction (RSJ) model, we simulated the behavior of a TJJ containing both 2π and 4π periodic current-phase relations.

We confirmed the change of the appearance order of the Shapiro steps when increasing the irradiation power [49]. At high frequency the order is regular (0,1,2,3,4,...) whereas at an irradiation frequency smaller than the phase adjustment frequency of the 4π-tABS, the appearance order of the steps is subject to the even-odd effect (0,2,1,4,3,6,5,8,...). We also observed an anomaly on the critical current at all closing of the even Shapiro steps. This feature gives a second possibility to estimate the contribution of the 4π-tABS.

For the first time, we have introduced Joule heating in the RSJ model. Our heating model has been validated in conventional JJs by the publication [43]. As heating effects on the 4π-tABS cannot be handled in the same way as the conventional ABSs, we proposed a thermally assisted stochastic population of the 4π-tABS to describe quasiparticle poisoning leading to a gradual suppression of the supercurrent carried by this state. This thermally assisted poisoning can explain the absence of the even-odd effect on high order Shapiro steps observed in the literature.

The main experimental results of this thesis are the observation of possible signatures of Majorana bound states in Shapiro measurements on Bi_2Se_3 TJJ. We detected an even-odd effect in the Shapiro measurement at low RF frequency. In addition we observe the same anomaly at the closing of the Shapiro step $n = 0$ as in the simulation. These two features characteristic of the presence of the 4π-tABS provide convincing signature on the presence of a 4π periodic ABS. The fact that vanadium may induce magnetic momenta at the superconducting interface (contrary to usual aluminum or niobium electrodes) may be the explanation for this first observation of the fractional AC Josephson effect in bismuth based topological insulators Josephson junctions.

Yet, Bi_2Se_3 is a TI with a conducting bulk that hosts lots of conventional electronic

modes that disguise the signature of the 4π-tABS. To decrease their contribution we also worked with $BiSbTeSe_2$ that has an insulating bulk.

We observed surface superconductivity by proximity effect in Josephson junctions fabricated on $BiSbTeSe_2$. However, because of a new technique of sample fabrication, every junction embedded a resonant cavity formed by superconducting contacting lines that spoiled the Shapiro measurement. This work could be reproduced with a different fabrication technique.

In conclusion, we have observed the fractional AC Josephson effect in topological Josephson junctions fabricated on bismuth based topological insulators. We have included a Joule heating model in the simple and well known resistively shunted Josephson junction model. This new approach gives a quantitative explanation for the hysteresis observed in conventional Josephson junctions. In addition, we developed a thermally activated poisoning model to explain the observation of the even-odd effect on the $n = 1$ Shapiro step only. This phenomenon was observed in recent experiments of Shapiro measurement on 3D TI but no interpretation was given. Our model brings a possible explanation.

Despite a massive investment from the scientific community in bismuth based TI, up to now, signatures of the Majorana Bound states in transport measurement were only observed in InSb nanowires and Hg-based TI. Thanks to this work, the family of bismuth based 3D TI are brought back as serious candidates to be used in future topological quantum computing schemes.

Appendix A

Effect of perpendicular Magnetic field on a Josephson junction

APPLYING a perpendicular magnetic field on a JJ will dephase the electronic wave function of the quasi-particles and thus modify the critical current of the junction. The usual dependence of the critical current $I_c(B)$ is a Fraunhofer pattern ($x \rightarrowtail |\sin(x)/x|$ function) [16, 53]. For simplicity, we always refer to this dependence as the Fraunhofer pattern even if the shape is different from $x \rightarrowtail |\sin(x)/x|$. This pattern enables to reconstruct the profile of supercurrent J_c across a JJ.

In this chapter, we first derive the expected behaviour of the critical current vs magnetic field of a uniformly distributed superconducting proximity effect and then explain the approach to reconstruct an unknown profile of supercurrent according to [53].

1 Regular Fraunhofer pattern

FIGURE A.1 shows a typical geometry of a JJ under a perpendicular magnetic field. The length, width and thickness of the normal metal are defined by L, W and t respectively. The magnetic field will be non-zero on both inside the N region and also over a length scale of the magnetic field penetration depth λ_B inside both S electrodes.

The supercurrent flows in the y direction and can be considered as constant along this direction. The supercurrent density reads $J_y(x,z) = J_c(x,z)\sin(\phi(x,z))$ with $J_c(x,z)$ the maximum supercurrent density at the line between the two S electrodes at the coordinates (x,z) and $\phi(x,z)$ is the phase difference at (x,z) between the order parameters of the superconductors on either side of the junction.

Let us consider two points M_1 and M_2. The phase difference between the two points reads $\phi(x_2,z_2) - \phi(x_1,z_1) = 2\pi\varphi_B/\varphi_0$, with $\varphi_0 = h/2e$ is the flux quantum and φ_B is

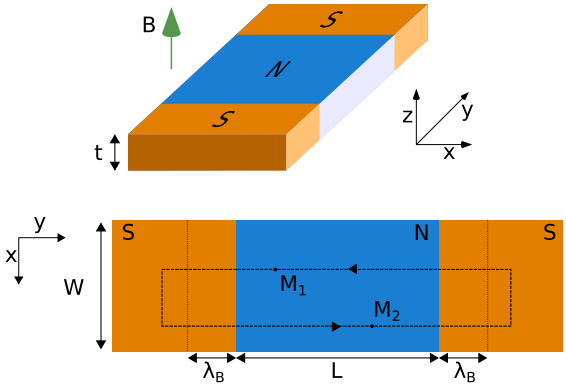

Figure A.1 – (upper part) 3D Schematic of a JJ with a perpendicular magnetic field applied. The magnetic field is in the z direction and the flow of electrons is in the y direction. (Lower part): top view of the upper part.

the amount of flux enclosed by a loop linking the two points (dashed loop in figure A.1). Hence, $\varphi_{\mathrm{B}} = B(2\lambda_B + L)(x_2 - x_1)$.

We define the origin of axes at the middle of the N region and fix the phase to be: $\phi(0,0) = \phi_0$. The total supercurrent from the left to the right electrode reads :

$$\begin{aligned} I_{\mathrm{S}}(B,\phi_0) &= \int_{-t/2}^{t/2} dz \int_{-W/2}^{W/2} dx \; J_{\mathrm{y}}(x,z) \\ &= \int_{-t/2}^{t/2} dz \int_{-W/2}^{W/2} dx \; J_{\mathrm{c}}(x,z) \sin\left(\frac{2\pi x B(2\lambda_B + L)}{\varphi_0} - \phi_0\right) \end{aligned} \tag{A.1}$$

We assume that the supercurrent is homogeneous along the z direction inside the normal metal and define the supercurrent profile to be : $\mathcal{J}(x) = \int_{-t/2}^{t/2} dz \; J_{\mathrm{c}}(x,z)$

From Eq. (A.1) we obtain :

$$I_{\mathrm{S}}(\beta,\phi_0) = \mathrm{Im}\left[e^{-i\phi_0} \int_{-W/2}^{W/2} dx \quad \mathcal{J}(x) e^{i\beta x}\right] \tag{A.2}$$

with $\beta = 2\pi B(2\lambda_B + L)/\varphi_0$ the normalized magnetic field and Im[] the imaginary part. The measured critical current $I_{\mathrm{c}}(B)$ is the maximum of $I_{\mathrm{S}}(B,\phi_0)$ (cf Eq. (4.8)). In the case of a uniformly distributed supercurrent ($\mathcal{J}(x) = \mathcal{J}_0$), the Fraunhofer pattern reads :

$$\begin{aligned} I_{\mathrm{c}}(\beta) &= |\mathcal{J}_0 \; \mathrm{Im}\left[\int_{-W/2}^{W/2} dx \quad e^{i\beta x}\right]| \\ &= |W\mathcal{J}_0 \; \mathrm{sinc}\,(\beta W/2)| \\ &= W\mathcal{J}_0 \; |\mathrm{sinc}\,(\pi B W(2\lambda_B + L)/\varphi_0)| \end{aligned} \tag{A.3}$$

The Fraunhofer pattern is therefore:

$$I_{\mathrm{c}}(B) = W\mathcal{J}_0 \; |\mathrm{sinc}\left(\frac{\pi\varphi_{\mathrm{B}}}{\varphi_0}\right)| \tag{A.4}$$

with $\varphi_{\mathrm{B}} = B \; W(2\lambda_B + L)$ the magnetic flux enclosed by the total area of the junction extended by the magnetic penetration depth.

2 Finding the current density profile

The profile $\mathcal{J}(x)$ depends on the exact geometry and characteristics of the N material. With the following method we can estimate this profile. It is used in this thesis to recover the profile of the Josephson junctions on Bi_2Se_3 and $BiSbTeSe_2$ flakes in chapters 6 & 7.

We can extend the integral of Eq. (A.3) and transform it into a Fourier transform. $\mathcal{J}(x)$ is now the supercurrent profile extended outside the physical limit of the normal region :

$$I_c(\beta) = \left| \mathrm{Im} \left[\int_{-\infty}^{\infty} dx \quad \mathcal{J}(x) e^{i\beta x} \right] \right| \tag{A.5}$$

Let us define the complex Fourier transform of $\mathcal{J}(x)$ by :

$$\mathcal{I}(\beta) = \int_{-\infty}^{\infty} dx \quad \mathcal{J}(x) e^{i\beta x} \tag{A.6}$$

The measured critical current profile is $I_c(\beta) = |\mathcal{I}(\beta)|$. Hence we can define the amplitude and the argument of the complex supercurrent by : $\mathcal{I}(\beta) = I_c(\beta) e^{i\theta(\beta)}$.

To reconstruct the current profile one needs to find $\theta(\beta)$. Two methods are possible [53]. The first one is based on a Hilbert transform procedure and the second simpler one uses the parity of $\mathcal{J}(x)$ and $I_c(\beta)$.

— Hilbert transform method

From [133], because $\mathcal{J}(x)$ has a "minimum-phase property", there is a relation between $I_c(\beta)$ and $\theta(\beta)$ by :

$$\theta(\beta) = \frac{\beta}{2\pi} \int_{-\infty}^{\infty} db \quad \frac{\ln(I_c(b)) - \ln(I_c(\beta))}{\beta^2 - b^2} \tag{A.7}$$

From this calculation, one can find the current profile by :

$$\mathcal{J}(x) = \frac{1}{2\pi} \int_{-\infty}^{\infty} d\beta \quad I_c(\beta) e^{i(\theta(\beta) - \beta x)} \tag{A.8}$$

Theoretically, the first method gives an exact solution. However, experimentally the measured $I_c(\beta)$ is noisy and this method does not give a convincing result of $\mathcal{J}(x)$ when $I_c(\beta)$ is not perfectly even.

— Parity method

The second approach is based on the fact that experimentally $I_c(\beta)$ and $\mathcal{J}(x)$ are almost even functions. Let us define $\mathcal{J}_e(x)$ and $\mathcal{J}_o(x)$ the even and odd parts of $\mathcal{J}(x)$. And their fourier transform :

$$\mathcal{E}(\beta) = \int_{-\infty}^{\infty} dx \mathcal{J}_e(x) \cos \beta x$$
$$\mathcal{O}(\beta) = \int_{-\infty}^{\infty} dx \mathcal{J}_o(x) \sin \beta x$$

Then $\mathcal{I} = \mathcal{E} + i\mathcal{O}$ and $I_c = |\mathcal{I}| = \sqrt{\mathcal{O}^2 + \mathcal{E}^2}$.

If $\mathcal{J}$ is an even function. Then $\mathcal{O} = 0$ and $\mathcal{I} = \mathcal{E}$ is real. If $\mathcal{J}(x)$ is constant, then it will result in a Fraunhofer pattern as seen in previous section with equidistant zeros. Now if $\mathcal{J}(x)$ is not constant, then $I_c(\beta)$ will oscillate and have the same zeros as $\mathcal{E}$.

If $\mathcal{J}$ is almost an even function. It means that away from the roots of $\mathcal{J}_e(x)$, we have $\mathcal{J}_o(x) \ll \mathcal{J}_e(x)$ and thus $\mathcal{J}(x) \simeq \mathcal{J}_e(x)$. And for all zeros of $\mathcal{J}_e(x)$, we have $\mathcal{J}(x) = \mathcal{J}_o(x)$. Hence, away from the minima of I_c, we have $|\mathcal{E}| = I_c$ as in the case of a purely even $\mathcal{J}$. At each minima of I_c, we have $|\mathcal{O}| = I_c$. At first approximation, we can linearly interpolate $|\mathcal{O}|$ between each zeros of $|\mathcal{E}|$. This method gives a semi-quantitative estimation of the odd part of $\mathcal{I}$ allowing us to recover the whole complex information of $\mathcal{I}$. From this estimation we can apply an inverse Fourier transform and have an estimation of the supercurrent profile $\mathcal{J}(x)$.

This last method is used in this thesis to recover the profile of the Josephson junctions on Bi_2Se_3 and $BiSbTeSe_2$ flakes in chapters 6 & 7.

Appendix B

Detailed calculations of chapter topological Josephson junction

1 Finding the eigenvalues of $\mathcal{H}$

We start with the compact form of the Hamiltonian describing superconducting proximity effect on the surface of a 3D topological insulator :

$$\mathcal{H} = \hbar v_{\mathrm{F}} \tau^z \otimes \boldsymbol{\sigma}.\boldsymbol{k} - \mu \tau^z \otimes \mathbb{1}_2 + \Delta_0 (\tau^x \cos\phi - \tau^y \sin\phi) \otimes \mathbb{1}_2 \tag{B.1}$$

To find the eigenvalues, it is easier to square the Hamiltonian. We use the properties of the Pauli matrices : $\sigma^i \sigma^j + \sigma^j \sigma^i = [\sigma^i, \sigma^j] = 2\delta_{\mathrm{i,j}}$.

$$
\begin{aligned}
\mathcal{H}^2 =&\hbar^2 v_{\mathrm{F}}^2(\tau^z * \tau^z) \otimes (\boldsymbol{\sigma}.\boldsymbol{k} * \boldsymbol{\sigma}.\boldsymbol{k}) + \mu^2(\tau^z * \tau^z) \otimes (\mathbb{1}_2 * \mathbb{1}_2) + \Delta_0^2(\tau^x \cos\phi - \tau^y \sin\phi)^2 \otimes (\mathbb{1}_2 * \mathbb{1}_2) \\
&-\hbar v_{\mathrm{F}}\mu \left[(\tau^z * \tau^z) \otimes (\boldsymbol{\sigma}.\boldsymbol{k} * \mathbb{1}_2) + (\tau^z * \tau^z) \otimes (\mathbb{1}_2 * \boldsymbol{\sigma}.\boldsymbol{k})\right] \\
&+\hbar v_{\mathrm{F}}\Delta_0 \left[(\tau^z * (\tau^x \cos\phi - \tau^y \sin\phi)) \otimes (\boldsymbol{\sigma}.\boldsymbol{k} * \mathbb{1}_2) + ((\tau^x \cos\phi - \tau^y \sin\phi) * \tau^z) \otimes (\mathbb{1}_2 * \boldsymbol{\sigma}.\boldsymbol{k})\right] \\
&-\mu\Delta_0 \left[(\tau^z * (\tau^x \cos\phi - \tau^y \sin\phi)) \otimes (\mathbb{1}_2 * \mathbb{1}_2) + ((\tau^x \cos\phi - \tau^y \sin\phi) * \tau^z) \otimes (\mathbb{1}_2 * \mathbb{1}_2)\right] \\
\\
=&\hbar^2 v_{\mathrm{F}}^2 \mathbb{1}_2 \otimes (k_{\mathrm{x}}^2 + k_{\mathrm{y}}^2)\mathbb{1}_2 + \mu^2 \mathbb{1}_4 + \Delta_0^2(\cos^2\phi + \sin^2\phi)\mathbb{1}_2 \otimes \mathbb{1}_2 \\
&-\hbar v_{\mathrm{F}}\mu(\mathbb{1}_2 \otimes \boldsymbol{\sigma}.\boldsymbol{k} + \mathbb{1}_2 \otimes \boldsymbol{\sigma}.\boldsymbol{k}) \\
&+\hbar v_{\mathrm{F}}\Delta_0 \left[(i\tau^y \cos\phi + i\tau^x \sin\phi) - (i\tau^y \cos\phi + i\tau^x \sin\phi)\right] \otimes \boldsymbol{\sigma}.\boldsymbol{k} \\
&-\mu\Delta_0 \left[(i\tau^y \cos\phi + i\tau^x \sin\phi) - (i\tau^y \cos\phi + i\tau^x \sin\phi)\right] \otimes \mathbb{1}_2 \\
\\
=&\hbar^2 v_{\mathrm{F}}^2 |\boldsymbol{k}|^2 \mathbb{1}_4 + \mu^2 \mathbb{1}_4 + \Delta_0^2 \mathbb{1}_4 - 2\hbar v_{\mathrm{F}}\mu \mathbb{1}_2 \otimes \boldsymbol{\sigma}.\boldsymbol{k}
\end{aligned}
\tag{B.2}
$$

From this expression we can square a second time the Hamiltonian :

$$
\begin{aligned}
\left(\mathcal{H}^2 - (\hbar^2 v_{\mathrm{F}}^2 |\boldsymbol{k}|^2 \mathbb{1}_4 + \mu^2 \mathbb{1}_4 + \Delta_0^2 \mathbb{1}_4)\right)^2 =&4\hbar^2 v_{\mathrm{F}}^2 \mu^2 \mathbb{1}_2^2 \otimes (\boldsymbol{\sigma}.\boldsymbol{k})^2 \\
=&4\hbar^2 v_{\mathrm{F}}^2 \mu^2 \mathbb{1}_2 \otimes \mathbb{1}_2 |\boldsymbol{k}|^2 \\
=&4\hbar^2 v_{\mathrm{F}}^2 \mu^2 \mathbb{1}_4 |\boldsymbol{k}|^2
\end{aligned}
\tag{B.3}
$$

This expression implies only unit matrices. Hence, applying a ket operator on the this equation gives directly access to the eigenvalues of the matrice $\mathcal{H}$:

$$
\begin{aligned}
\left(\mathcal{H}^2 - (\hbar^2 v_{\mathrm{F}}^2 |\boldsymbol{k}|^2 \mathbb{1}_4 + \mu^2 \mathbb{1}_4 + \Delta_0^2 \mathbb{1}_4)\right)^2 |\Psi\rangle =&4\hbar^2 v_{\mathrm{F}}^2 \mu^2 \mathbb{1}_4 |\boldsymbol{k}|^2 |\Psi\rangle \\
\left(E^2 - (\hbar^2 v_{\mathrm{F}}^2 |\boldsymbol{k}|^2 + \mu^2 + \Delta_0^2\right)^2 |\Psi\rangle =&4\hbar^2 v_{\mathrm{F}}^2 \mu^2 |\boldsymbol{k}|^2 |\Psi\rangle \\
\left(E^2 - (\hbar^2 v_{\mathrm{F}}^2 |\boldsymbol{k}|^2 + \mu^2 + \Delta_0^2\right)^2 =&4\hbar^2 v_{\mathrm{F}}^2 \mu^2 |\boldsymbol{k}|^2 \\
{E_{\uparrow,\downarrow}}^2 - (\hbar^2 v_{\mathrm{F}}^2 |\boldsymbol{k}|^2 + \mu^2 + \Delta_0^2)^2 =& \pm 2\hbar v_{\mathrm{F}}\mu |\boldsymbol{k}| \\
{E_{\uparrow,\downarrow}}^2 =& \pm 2\hbar v_{\mathrm{F}}\mu |\boldsymbol{k}| + \hbar^2 v_{\mathrm{F}}^2 |\boldsymbol{k}|^2 + \mu^2 + \Delta_0^2 \\
{E_{\uparrow,\downarrow}}^2 =&(\mu \pm \hbar v_{\mathrm{F}} |\boldsymbol{k}|)^2 + \Delta_0^2 \\
E_{\uparrow,\downarrow}^{\pm} =& \pm \sqrt{(\mu \pm \hbar v_{\mathrm{F}} |\boldsymbol{k}|)^2 + \Delta_0^2}
\end{aligned}
\tag{B.4}
$$

We find the energy dispersion of the four possible states available for a given $|\boldsymbol{k}|$. This energy dispersion is drawn in figure 4.12.

2 Diagonilization of $\mathcal{H}_{\rm TI}$

In order to diagonalise the normal part of the Hamiltonian $H_{\rm TI}$, one needs to use the following notations

$$\boldsymbol{k} = k_0(\cos\theta_{\rm k}, \sin\theta_{\rm k}) \tag{B.5}$$

Moreover, we can use the expressions :

$$\begin{aligned} e^{i\phi\sigma^j} &= \mathbb{1}_2 \cos\phi + i\sigma^j \sin\phi \\ e^{i\sigma^j\phi/2}\sigma^{j'}e^{-i\sigma^j\phi/2} &= \sigma^{j'}\cos\phi + i\sigma^j\sigma^{j'}\sin\phi \end{aligned} \tag{B.6}$$

With theses expressions, we have

$$\begin{aligned} \sigma^x &= e^{-i\sigma^y\pi/4}\sigma^z e^{i\sigma^y\pi/4} \\ \sigma^y &= e^{-i\sigma^z\pi/4}\sigma^x e^{i\sigma^z\pi/4} \\ \sigma^z &= e^{-i\sigma^x\pi/4}\sigma^y e^{i\sigma^x\pi/4} \end{aligned} \tag{B.7}$$

Hence the diagonalization of the normal part of the Hamiltonian gives:

$$\begin{aligned} \mathcal{H}_{\rm TI} &= \hbar v_{\rm F}\boldsymbol{\sigma}.\boldsymbol{k} - \mu \\ &= \hbar v_{\rm F}k_0(\cos\theta_{\rm k}\sigma^x + \sin\theta_{\rm k}\sigma^y) - \mu \\ &\overset{1}{=} \hbar v_{\rm F}k_0 e^{-i\sigma^z\theta_{\rm k}/2}\sigma^x e^{i\sigma^z\theta_{\rm k}/2} - \mu \\ &= \hbar v_{\rm F}k_0 e^{-i\sigma^z\theta_{\rm k}/2}e^{-i\sigma^y\pi/4}\sigma^z e^{i\sigma^y\pi/4}e^{i\sigma^z\theta_{\rm k}/2} - \mu \\ &= e^{-i\sigma^z\theta_{\rm k}/2}e^{-i\sigma^y\pi/4}\left(\hbar v_{\rm F}k_0\sigma^z - \mu\right)e^{i\sigma^y\pi/4}e^{i\sigma^z\theta_{\rm k}/2} \end{aligned} \tag{B.8}$$

The aim of this change of reference frame is to have a fixed direction for the momentum $\vec{k}$ in the new frame. For that we use the rotating frame (rotation around z by an angle $\theta_{\rm k}$ done in the calculation by the matrices $e^{i\sigma^z\theta_{\rm k}/2}$) drawn in figure B.1. The second rotation around the y axis enables to have $\vec{k}$ along the 3$^{\rm rd}$ direction of the final basis.

Therefore, in second quantification the Hamiltonian is given by:

$$\begin{aligned} H_{\rm TI} &= \sum_{\rm k}\psi^\dagger_{\rm k}(\hbar v_{\rm F}\boldsymbol{\sigma}.\boldsymbol{k} - \mu)\psi_{\rm k} \\ &= \sum_{\rm k} a^\dagger_{\rm k}(\hbar v_{\rm F}k_0\sigma^z - \mu)a_{\rm k} \end{aligned} \tag{B.9}$$

with

$$a_{\rm k} = e^{i\sigma^y\pi/4}e^{i\sigma^z\theta_{\rm k}/2}\psi_{\rm k} \tag{B.10}$$

1. $-i\sigma^z\sigma^x = i\sigma^x\sigma^z = i(i\epsilon_{\rm x,z,y}\sigma^y) = -(-1)\sigma^y = \sigma^y$

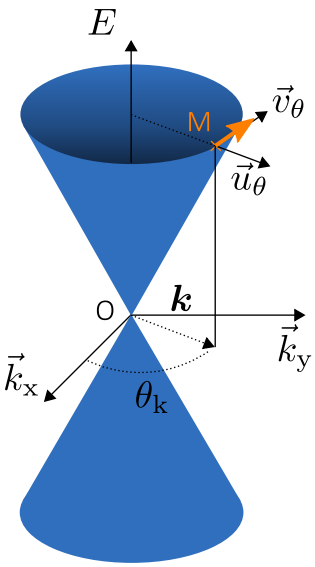

Figure B.1 – Schematic of the change of reference frame useful to diagonalize $\mathcal{H}_{\mathrm{TI}}$. The energy dispersion of the electron is linear. The spin (orange arrow) is in the $(M, \vec{k}_\mathrm{x}, \vec{k}_\mathrm{y})$ plane, perpendicular the momentum. After the first rotation used in the diagonalization, the frame changes from $(O, \vec{k}_\mathrm{x}, \vec{k}_\mathrm{y}, \vec{k}_\mathrm{z})$ to $(O, \vec{u_\theta}, \vec{v_\theta}, \vec{k}_\mathrm{z})$.

$$
\begin{aligned}
\left(a_{\mathrm{k},\uparrow}; a_{\mathrm{k},\downarrow}\right) &= \frac{1}{\sqrt{2}} \begin{pmatrix} 1 & 1 \\ -1 & 1 \end{pmatrix} \begin{pmatrix} e^{i\theta_\mathrm{k}/2} & 0 \\ 0 & e^{-i\theta_\mathrm{k}/2} \end{pmatrix} \left(\psi_{\mathrm{k},\uparrow}; \psi_{\mathrm{k},\downarrow}\right) \\
\left(a_{\mathrm{k},\uparrow}; a_{\mathrm{k},\downarrow}\right) &= \frac{1}{\sqrt{2}} \begin{pmatrix} e^{i\theta_\mathrm{k}/2} & e^{-i\theta_\mathrm{k}/2} \\ -e^{i\theta_\mathrm{k}/2} & e^{-i\theta_\mathrm{k}/2} \end{pmatrix} \left(\psi_{\mathrm{k},\uparrow}; \psi_{\mathrm{k},\downarrow}\right) \\
\left(a^\dagger_{\mathrm{k},\uparrow}; a^\dagger_{\mathrm{k},\downarrow}\right) &= \frac{1}{\sqrt{2}} \begin{pmatrix} e^{-i\theta_\mathrm{k}/2} & -e^{-i\theta_\mathrm{k}/2} \\ e^{i\theta_\mathrm{k}/2} & e^{i\theta_\mathrm{k}/2} \end{pmatrix} \left(\psi^\dagger_{\mathrm{k},\uparrow}; \psi^\dagger_{\mathrm{k},\downarrow}\right)
\end{aligned}
\tag{B.11}
$$

$$
\begin{aligned}
\left(\psi_{\mathrm{k},\uparrow}; \psi_{\mathrm{k},\downarrow}\right) &= \frac{1}{\sqrt{2}} \begin{pmatrix} e^{-i\theta_\mathrm{k}/2} & -e^{-i\theta_\mathrm{k}/2} \\ e^{i\theta_\mathrm{k}/2} & e^{i\theta_\mathrm{k}/2} \end{pmatrix} \left(a_{\mathrm{k},\uparrow}; a_{\mathrm{k},\downarrow}\right) \\
\left(\psi^\dagger_{\mathrm{k},\uparrow}; \psi^\dagger_{\mathrm{k},\downarrow}\right) &= \frac{1}{\sqrt{2}} \begin{pmatrix} e^{i\theta_\mathrm{k}/2} & e^{-i\theta_\mathrm{k}/2} \\ -e^{i\theta_\mathrm{k}/2} & e^{-i\theta_\mathrm{k}/2} \end{pmatrix} \left(a^\dagger_{\mathrm{k},\uparrow}; a^\dagger_{\mathrm{k},\downarrow}\right)
\end{aligned}
\tag{B.12}
$$

Hence the superconducting Hamiltonian in this new basis reads :

$$
\begin{aligned}
H_{\mathrm{S}} = \quad & \sum_k \Delta \psi^\dagger_{\mathrm{k},\uparrow} \psi^\dagger_{-\mathrm{k},\downarrow} \\
& + \Delta^* \psi_{-\mathrm{k},\downarrow} \psi_{\mathrm{k},\uparrow} \\
= \frac{1}{2} & \sum_k \Delta (e^{i\theta_{\mathrm{k}}/2} a^\dagger_{\mathrm{k},\uparrow} + e^{-i\theta_{\mathrm{k}}/2} a^\dagger_{\mathrm{k},\downarrow})(-e^{i\theta_{-\mathrm{k}}/2} a^\dagger_{-\mathrm{k},\uparrow} + e^{-i\theta_{-\mathrm{k}}/2} a^\dagger_{-\mathrm{k},\downarrow}) \\
& + \Delta^* (e^{i\theta_{-\mathrm{k}}/2} a_{-\mathrm{k},\uparrow} + e^{i\theta_{-\mathrm{k}}/2} a_{-\mathrm{k},\downarrow})(e^{-i\theta_{\mathrm{k}}/2} a_{\mathrm{k},\uparrow} - e^{-i\theta_{\mathrm{k}}/2} a_{\mathrm{k},\downarrow}) \\
\overset{2}{=} \frac{1}{2} & \sum_k \Delta \left[i e^{i\theta_{\mathrm{k}}} a^\dagger_{\mathrm{k},\uparrow} a^\dagger_{-\mathrm{k},\uparrow} - i a^\dagger_{\mathrm{k},\uparrow} a^\dagger_{-\mathrm{k},\downarrow} - i a^\dagger_{\mathrm{k},\downarrow} a^\dagger_{-\mathrm{k},\uparrow} - i e^{-i\theta_{\mathrm{k}}} a^\dagger_{\mathrm{k},\downarrow} a^\dagger_{-\mathrm{k},\downarrow} \right] \\
& + \mathrm{H.c.}\ ^3 \\
\overset{4}{=} \frac{1}{2} & \sum_k i\Delta \left[e^{i\theta_{\mathrm{k}}} a^\dagger_{\mathrm{k},\uparrow} a^\dagger_{-\mathrm{k},\uparrow} - e^{-i\theta_{\mathrm{k}}} a^\dagger_{\mathrm{k},\downarrow} a^\dagger_{-\mathrm{k},\downarrow} \right] \\
& - i\Delta^* \left[e^{-i\theta_{\mathrm{k}}} a_{-\mathrm{k},\uparrow} a_{\mathrm{k},\uparrow} - e^{i\theta_{\mathrm{k}}} a_{-\mathrm{k},\downarrow} a_{\mathrm{k},\downarrow} \right]
\end{aligned}
\tag{B.13}
$$

This Hamiltonian in the new basis couples fermions with same spin ($\uparrow\uparrow$ and $\downarrow\downarrow$) and depending on the direction of propagation (θ_{k}), the coupling changes its sign. It describes a so-called $p_x + ip_y$ superconducting pairing symmetry:

$$
H_{\mathrm{S}} = \frac{1}{2} \sum_k i\Delta \left[\frac{(k_x + ik_y)}{k_0} a^\dagger_{\mathrm{k},\uparrow} a^\dagger_{-\mathrm{k},\uparrow} - \frac{(k_x - ik_y)}{k_0} a^\dagger_{\mathrm{k},\downarrow} a^\dagger_{-\mathrm{k},\downarrow} + H.c. \right] \tag{B.14}
$$

2. $\theta_{-\mathrm{k}} = \theta_{\mathrm{k}} + \pi$
3. Hermitian conjugate of previous line.
4. $a^\dagger_{\mathrm{k},\uparrow} a^\dagger_{-\mathrm{k},\downarrow} = -a^\dagger_{-\mathrm{k},\downarrow} a^\dagger_{\mathrm{k},\uparrow}$

Appendix C

Influence of Landau-Zener transitions on the fractional AC Josephson effect

In the case of high transmission channels ($\mathcal{T}_i \approx 1$), when the system evolves in a non-adiabatic manner, some lower energy state can jump to an excited state thanks to Landau-Zener transition. In this section we introduce the Landau-Zener transition (inspired by Appendix D of ref [27]) and describe the influence of this process on the detection of the 4π periodic ABS.

1 Landau-Zener transition

Let us consider a system of two ABSs : $|-\rangle$ and $|+\rangle$. These states are eigenvectors of the time independent Hamiltonian Eq. (4.10). Therefore, during an adiabatic (infinitely slow) evolution of the phase ϕ, the final state of the system will be the same as the initial one [1].

However, if the voltage across the junction is not small (i.e. the system does not have the time to relax to its equilibrium), according to Eq. (4.3), the phase variation may lead to non adiabatic transition of the ABS from $|-\rangle$ to $|+\rangle$ (cf figure C.1). This so-called Landau-Zener transition has a probability given by [108, 186]:

$$p_{\mathrm{LZ}} = \exp\left(-\pi \frac{|2\epsilon_{12}|^2}{2\hbar\left|\frac{d}{dt}(\epsilon_1 - \epsilon_2)\right|}\right) \tag{C.1}$$

1. If the initial state is an eigenvector of the Hamiltonian, then the final state is the same eigenvector as the initial one.

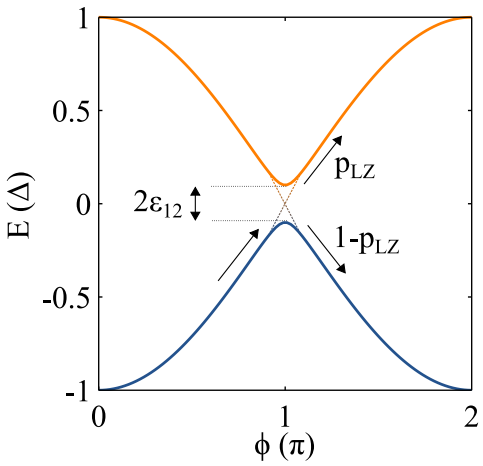

Figure C.1 – Schematic of a Landau-Zener transition in a short JJ with a transmission coefficient $T_1 = 0.97$. When the phase is close to π, the quasiparticle at energy E^- (blue) can transit to the upper branch (green) with a probability p_{LZ} or remain in the ground state with a probability $1-p_{\mathrm{LZ}}$. The coloured dashed lines represent the energy dispersion of the states without interaction.

where $2\epsilon_{12}$ is the energy gap between the two levels and $\epsilon_1 - \epsilon_2$ is the energy difference between the levels in the case of non interacting states [2].

In the case of ABS, we have:

$$\begin{aligned} 2\epsilon_{12} &= E^+(\mathcal{T}_\mathrm{i}, \pi) - E^-(\mathcal{T}_\mathrm{i}, \pi) = 2\Delta\sqrt{1-\mathcal{T}_\mathrm{i}} \\ \epsilon_1 - \epsilon_2 &= 2\left(E^+(1,\pi) + \phi \lim_{\phi\to\pi} \frac{\partial E^+}{\partial t}\right) = \phi\Delta \end{aligned} \tag{C.2}$$

where we have approximated the second term by a Taylor expansion.

Hence, at finite voltage V, we obtain

$$p_{\mathrm{LZ}} = \exp\left(-\pi \frac{\Delta(1-\mathcal{T}_\mathrm{i})}{eV}\right) \tag{C.3}$$

Consequently, the Landau-Zener transition has a high probability for highly transparent channels and high voltages (close to Δ/e). The LZ transition can hence transit a quasiparticle from $-\Delta$ to $+\Delta$ during a 2π winding of the phase. We will see in paragraph 3 that LZ transitions on a 2π periodic ABS can artificially produce the same signature as the 4π periodic ABS.

2 Effect of Landau-Zener transitions on the 4π periodic ABS

When two MBSs are located at a finite distance at the two extremity of a JJ, they interact and a small gap E_g is created in the ABS spectrum. A priori, this gap breaks the 4π periodicity of the zero energy Majorana mode. One could think that, from this interaction, the two MBSs are not protected anymore. However, because of possible LZ

2. Time evolution of a perfect transmitted channel ($\mathcal{T}_\mathrm{i} = 1$)

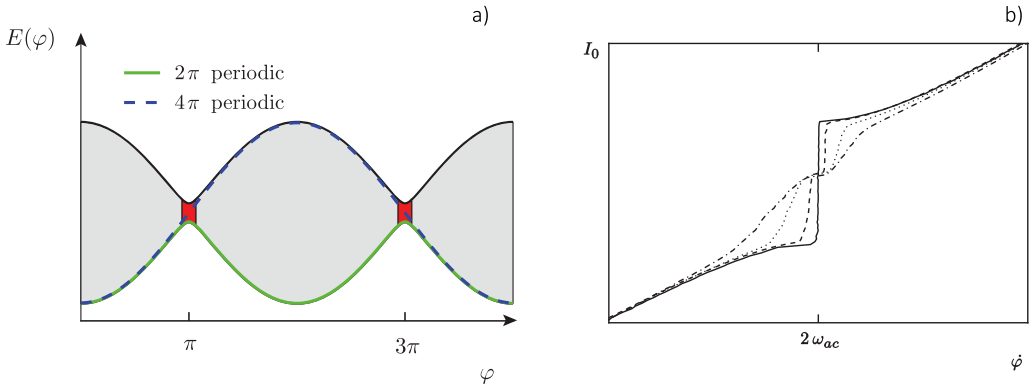

Figure C.2. – (a): Energy-phase relation of the 4π periodic ABS by taking into account LZ transitions. The grey and red regions corresponds to the adiabatic and non-adiabatic evolution of the system. In the adiabatic limit, the 4π periodic ABS is not subject to LZ transitions (dashed blue line), whereas in the non-adiabatic limit, the 4π periodic ABS losses its 4π periodicity. (b): Zoom on the second Shapiro step of the simulated current-voltage characteristic of a 1D topological Josephson junction hosting zero energy Majorana modes. The junction is current biased and irradiated with radio-frequencies. The curves are different simulations for an increasing gap E_g between the upper and lower energy states using the resistively shunted junction model with a $E_J/E_g = 500$ (solid), 100 (dashed), 50(dotted), 30(dotted-dashed). With $E_J = \hbar I_c/2e$ being the Josephson energy. Extracted from [49].

transitions between the lower and the upper part of the ABS spectrum, the 4π periodicity is restored and the fractional AC Josephson effect is still predicted to be measurable.

The only counterpart of the LZ transition in this case is that for large gap E_g, the Shapiro steps are less defined and split in two non universal steps. This effect has been simulated by [49, 178] and the result is shown in figure C.2. The zoom of the current-voltage characteristic on the Shapiro step $n = 2$ shows a splitting of the plateau when the gap E_g increases. Hence, the interaction of the two MBSs destroys the quantization of the Shapiro steps.

3 Effect of Landau-Zener transitions on high transmitted channels

In the case of non-topological JJ, high transmitted channels also have a small gap between the excited and ground states (cf Eq. (4.20)). When the junction is driven out of equilibrium, this small gap allows LZ transitions in between a ground and an excited 2π periodic ABS. These LZ transitions could hence transform a 2π ABS into an artificial 4π periodic state that produces a fractional AC Josephson effect. This effect has been measured in the photon emission of a Single Cooper-pair transistor [21]. Hence, a high transmitted channel produces a false positive signature that could be confused with the one from the 4π-tABS.

The difference between the 4π-tABS of previous paragraph and artificial 4π periodic ABS of this paragraph is that in 2, the *broken* 4π ABS are not degenerated in spin and are still associated with a spinless p-wave superconductivity. However, here, in the conventional

JJ, each ABS is spin degenerated. Hence this artificial 4π periodic signal is not associated with the coveted MBSs.

A major question stems from this observation: Experimentally, how do we distinguish between a fractional Josephson effect coming from a 4π-tABS from a false positive signal that originates from a high transmitted channel ?

This issue has been addressed by Sau et al [150, 152] who concluded that the best way to distinguish those two signals is to perform a Shapiro measurement at different frequency excitations. The non-topological 4π periodic signal is visible at high voltages and hence high frequency excitation. The signal stemming from the 4π-tABS will be instead more visible at low frequency when the system is in the adiabatic limit ($f_{\mathrm{RF}} \ll R_{\mathrm{N}} I_{\mathrm{c}}$).

In conclusion, a reliable signature of the 4π-tABS is the fractional Josephson effect measured by Shapiro measurement at low frequency excitation.

Bibliography

[1] Nicolas Agraït, Alfredo Levy Yeyati, and Jan M. van Ruitenbeek. "Quantum properties of atomic-sized conductors". In: *Phys. Rep.* 377.2-3 (2003), pp. 81–279 (cit. on p. 45).

[2] A. R. Akhmerov, Johan Nilsson, and Carlo W. J. Beenakker. "Electrically detected interferometry of Majorana fermions in a topological insulator". In: *Physical Review Letters* 102.21 (2009), pp. 1–4 (cit. on p. 62).

[3] Jason Alicea. "New directions in the pursuit of Majorana fermions in solid state systems". In: *Reports Prog. Phys.* 75.7 (2012), p. 076501 (cit. on pp. 12, 65).

[4] Monica T. Allen, Oles Shtanko, Ion Cosma Fulga, A. R. Akhmerov, Kenji Watanabi, Takashi Taniguchi, Pablo Jarillo-Herrero, Leonid S. Levitov, and Amir Yacoby. "Spatially resolved edge currents and guided-wave electronic states in graphene". In: *Nat. phys* 12 (2015), pp. 128–133 (cit. on p. 125).

[5] Alexander Altland and Martin R. Zirnbauer. "Nonstandard symmetry classes in mesoscopic normal-superconducting hybrid structures". In: *Phys. Rev. B - Condens. Matter Mater. Phys.* 55.2 (Jan. 1997), pp. 1142–1161 (cit. on p. 3).

[6] James G. Analytis, Ross D. McDonald, Scott C. Riggs, Jiun-Haw Chu, G. S. Boebinger, and Ian R. Fisher. "Two-dimensional surface state in the quantum limit of a topological insulator". In: *Nat. Phys.* 6.12 (2010), pp. 960–964 (cit. on p. 15).

[7] A. F. Andreev. "The thermal conductivity of the intermediate state in superconductors". In: *Sov Phys JETP* 19.5 (1964), pp. 1228–1231 (cit. on p. 45).

[8] A. F. Andreev. "Thermal Conductivity of the intermediate State of Superconductors. part 2". In: *Sov. Phys. - J. Exp. Theor. Phys.* 20.6 (1965), pp. 1490–1493 (cit. on pp. 42, 45).

[9] T. Arakane, T. Sato, S. Souma, K. Kosaka, K. Nakayama, M. Komatsu, T. Takahashi, Zhi Ren, Kouji Segawa, and Yoichi Ando. "Tunable Dirac cone in the topological insulator Bi2-xSbxTe3-ySey". In: *Nat. Comm.* 3 (2012), p. 636 (cit. on p. 15).

[10] Janos Asboth, Laszlo Oroszlany, and Andras Palyi. *Topological Insulators*. 2013 (cit. on p. 5).

[11] D. Averin and A Bardas. “Adiabatic dynamics of superconducting quantum point contacts.” In: *Phys. Rev. B. Condens. Matter* 53.4 (1996), R1705–R1708 (cit. on p. 72).

[12] D. Averin and H. Imam. “Supercurrent noise in quantum point contacts”. In: *Phys. Rev. Lett.* 76.20 (1996), p. 12 (cit. on p. 72).

[13] Philip F. Bagwell. “Suppression of the Josephson current through a narrow, mesoscopic, semiconductor channel by a single impurity”. In: *Physical Review B* 46.19 (1992), pp. 12573–12586 (cit. on pp. 47, 50, 51).

[14] Lihong Bao, Liang He, Nicholas Meyer, Xufeng Kou, Peng Zhang, Zhi-Gang Chen, Alexei V Fedorov, Jin Zou, Trevor M Riedemann, Thomas a Lograsso, Kang L Wang, Gary Tuttle, and Faxian Xiu. “Weak anti-localization and quantum oscillations of surface states in topological insulator Bi2Se2Te.” In: *Sci. Rep.* 2 (Jan. 2012), p. 726 (cit. on p. 15).

[15] John Bardeen and Jared L. Johnson. “Josephson current flow in pure superconducting-normal-superconducting junctions”. In: *Physical Review B* 5.1 (1972), pp. 72–78 (cit. on p. 50).

[16] Antonio Barone and Gianfranco Paterno. *Physics and applications of the Josephson Effect*. 1982 (cit. on pp. 45, 79, 80, 127, 135).

[17] R. Baskaran, A. V. Thanikai Arasu, E. P. Amaladass, and M. P. Janawadkar. “High upper critical field in disordered niobium nitride superconductor”. In: *J. Appl. Phys.* 116.163908 (2014) (cit. on p. 36).

[18] W. Belzig, Christoph Bruder, and Gerd Schön. “Local density of states in a dirty normal metal connected to a superconductor.” In: *Physical review. B, Condensed matter* 54.13 (Oct. 1996), pp. 9443–9448 (cit. on p. 105).

[19] S P Benz and C A Hamilton. “Application of the Josephson effect to voltage metrology”. In: *Proc. IEEE* 92.10 (Oct. 2004), pp. 1617–1629 (cit. on p. 42).

[20] Andrei B. Bernevig, Taylor L. Hughes, and Shou-cheng Zhang. “Quantum Spin Hall Effect and Topological Phase Transition in HgTe Quantum Wells”. In: *Science (80-.).* 314 (2006), pp. 1757–1762 (cit. on pp. 8, 9).

[21] P. M. Billangeon, F. Pierre, H. Bouchiat, and R. Deblock. “Ac Josephson effect and resonant cooper pair tunneling emission of a single cooper pair transistor”. In: *Phys. Rev. Lett.* 98.21 (2007), pp. 1–4 (cit. on p. 147).

[22] Ya. M. Blanter and M. Büttiker. “Shot noise in mesoscopic conductors”. In: *Phys. Rep.* 336 (2000), pp. 1–166 (cit. on pp. 43, 44).

[23] Felix Bloch. “Über die Quantenmechanik der Elektronen in Kristallgittern”. In: *Zeitschrift für Phys.* 52.7 (1929), pp. 555–600 (cit. on p. 1).

[24] G. E. Blonder, M. Tinkham, and Teun M. Klapwijk. "Transition from metallic to tunelling regimes in superconducting microconstrictions: Excess current, charge imbalance and supercurrent conversion". In: *Phys. Rev. B* 25.7 (1982), pp. 4515–4532 (cit. on pp. 42, 105, 106).

[25] Erwann Bocquillon, Russell S. Deacon, Jonas Wiedenmann, Philipp Leubner, Teun M. Klapwijk, Christoph Brüne, Koji Ishibashi, Hartmut Buhmann, and Laurens W. Molenkamp. "Gapless Andreev bound states in the quantum spin Hall insulator HgTe". In: *Nat. Nanotechnol.* August (2016), pp. 1–27 (cit. on pp. 70, 75, 93).

[26] Ivan V. Borzenets, F. Amet, C. T. Ke, K. Watanabe, T. Taniguchi, M. Yamamoto, S. Tarucha, and Gleb Finkelstein. "Supercurrent in long ballistic graphene Josephson junctions". In: *Condens. Matter - Mesoscale Nanoscale Phys.* (2016), pp. 1–6 (cit. on p. 50).

[27] Landry Bretheau. "Localized Excitations in Superconducting Atomic Contacts : Probing the Andreev Doublet". PhD thesis. 2013 (cit. on pp. 49, 145).

[28] Landry Bretheau, C. O. Girit, C. Urbina, D. Esteve, and H. Pothier. "Supercurrent spectroscopy of andreev states". In: *Phys. Rev. X* 3.4 (2014), pp. 1–7 (cit. on p. 72).

[29] Alexander Brinkman and A. A. Golubov. "Coherence effects in double-barrier Josephson junctions". In: *Physical Review B* 61.17 (2000), pp. 11297–11300 (cit. on p. 93).

[30] Christoph Brüne, C. X. Liu, E. G. Novik, E. M. Hankiewicz, H. Buhmann, Y. L. Chen, X. L. Qi, Z. X. Shen, S. C. Zhang, and L. W. Molenkamp. "Quantum Hall effect from the topological surface states of strained bulk HgTe". In: *Physical Review Letters* 106.12 (2011), pp. 1–4 (cit. on p. 10).

[31] Nicholas P. Butch, Kevin Kirshenbaum, P. Syers, a. B. Sushkov, G. S. Jenkins, H. D. Drew, and J. Paglione. "Strong surface scattering in ultrahigh-mobility Bi2Se3 topological insulator crystals". In: *Phys. Rev. B - Condens. Matter Mater. Phys.* 81.24 (June 2010), p. 241301 (cit. on p. 15).

[32] Cui-Zu Chang, Weiwei Zhao, Duk Y. Kim, Haijun Zhang, Badih A. Assaf, Don Heiman, Shou-cheng Zhang, Chaoxing Liu, Moses H. W. Chan, and Jagadeesh S. Moodera. "High-precision realization of robust quantum anomalous Hall state in a hard ferromagnetic topological insulator". In: *Nature Materials* 14.March (2015), pp. 1–16 (cit. on p. 118).

[33] J. T. Chen, T. F. Finnegan, and Donald N. Langenberg. "Anomalous dc current singularities in Josephson tunnel junctions". In: *Physica* 55.C (1971), pp. 413–420 (cit. on p. 127).

[34] Hang Chi, Wei Liu, Kai Sun, Xianli Su, Guoyu Wang, Petr Lošt'ák, Vladimír Kucek, Čestmír Drašar, and Ctirad Uher. "Low-temperature transport properties of Tl-doped Bi2Te3 single crystals". In: *Phys. Rev. B* 88.4 (2013), p. 045202 (cit. on p. 15).

[35] Yi-Jiunn Chien. "Transition Metal-Doped Sb2Te3 and Bi2Te3 Diluted Magnetic Semiconductors". PhD thesis. 2007 (cit. on p. 118).

[36] Sungjae Cho, Brian Dellabetta, Alina Yang, John Schneeloch, Zhijun Xu, Tonica Valla, Genda Gu, Matthew J Gilbert, and Nadya Mason. "Symmetry protected Josephson supercurrents in three-dimensional topological insulators." In: *Nat. Commun.* 4 (2013), p. 1689 (cit. on p. 32).

[37] John F. Cochran and D. E. Mapother. "Superconducting Transition in Aluminum". In: *Phys. Rev.* 111.1 (1958), pp. 132–142 (cit. on p. 36).

[38] Hervé Courtois, M. Meschke, J. T. Peltonen, and J. P. Pekola. "Origin of hysteresis in a proximity josephson junction". In: *Phys. Rev. Lett.* 101.6 (2008), pp. 1–4 (cit. on pp. 84, 87).

[39] Hung T. Dang and Andrew J. Millis. "Theory of ferromagnetism in vanadium-oxide based perovskites". In: *Phys. Rev. B - Condens. Matter Mater. Phys.* 87.15 (2013), pp. 1–11 (cit. on p. 118).

[40] Sankar Das Sarma, Amit Nag, and Jay Deep Sau. "How to infer non-Abelian statistics and topological invariants from tunneling conductance properties of realistic Majorana nanowires". In: 035143 (2016), pp. 31–33 (cit. on p. 64).

[41] Anindya Das, Yuval Ronen, Yonatan Most, Yuval Oreg, Moty Heiblum, and Hadas Shtrikman. "Zero-bias peaks and splitting in an Al-InAs nanowire topological superconductor as a signature of Majorana fermions". In: *Nat. Phys.* 8.12 (2012), pp. 887–895 (cit. on pp. 54, 64).

[42] Bastien Dassonneville. "Dynamics of Andreev states in a normal metal - superconductor ring : Supercurrent fluctuations and spectroscopy of the minigap". PhD thesis. Universite Paris Sud- Paris XI, 2014, p. 129 (cit. on pp. 40, 51, 65).

[43] Alessandro De Cecco, Kévin Le Calvez, Benjamin Sacépé, Clemens B. Winkelmann, and Hervé Courtois. "Interplay Between Electron Over-Heating and ac Josephson Effect". In: *Physical Review B* 180505 (2016), pp. 1–5 (cit. on pp. 87–89, 133).

[44] Pierre Gilles De Gennes. *Superconductivity of metals and alloys*. Ed. by New York W.A. Benjamin. 1966 (cit. on p. 45).

[45] Pierre Gilles De Gennes and D. Saint James. "Elementary Excitations in the civinity of a Normal Metal - Superconducting Metal Contact". In: *Phys. Lett.* 4.2 (1963), pp. 151–152 (cit. on p. 42).

[46] Russell S. Deacon, Jonas Wiedenmann, Erwann Bocquillon, Teun M. Klapwijk, Philipp Leubner, Christoph Brüne, Seigo Tarucha, Koji Ishibashi, Hartmut Buhmann, and Laurens W. Molenkamp. "Josephson radiation from gapless Andreev bound states in HgTe-based topological junctions". In: *Condens. Matter - Mesoscale Nanoscale Phys.* (2016), pp. 1–19 (cit. on p. 71).

[47] M. T. Deng, C. L. Yu, Guang-yao Huang, M. Larsson, and H. Q. Xu. "Anomalous Zero–Bias Conductance Peak in a Nb – InSb Nanowire – Nb Hybrid Device". In: *Nano Lett.* 12 (2012), pp. 6414–6419 (cit. on p. 54).

[48] R. C. Dinsmore, Myung Ho Bae, and A. Bezryadin. "Fractional order Shapiro steps in superconducting nanowires". In: *Applied Physics Letters* 93.19 (2008), pp. 128–130 (cit. on p. 129).

[49] Fernando Domínguez, Fabian Hassler, and Gloria Platero. "Dynamical detection of Majorana fermions in current-biased nanowires". In: *Physical Review B* 86.14 (Oct. 2012), pp. 1–16 (cit. on pp. 67, 99, 102, 133, 147).

[50] O. N. Dorokhov. "on the Coexistence of Localized and Extended Electronic States in the Metallic Phase". In: *Solid State Commun.* 51.6 (1984), pp. 381–384 (cit. on p. 50).

[51] P. Dubos, Herve Courtois, B. Pannetier, Frank Wilhelm, Andrei Zaikin, and Gerd Schon. "Josephson critical current in a long mesoscopic S-N-S junction". In: *Physical Review B* 63.6 (Jan. 2001), p. 064502 (cit. on pp. 45, 88, 106).

[52] Jeffrey S. Dyck, Pavel Hajek, Petr Lost'ak, and Ctirad Uher. "Diluted magnetic semiconductors based on Sb2-xVxTe3 (0.01<x<0.03)". In: *Phys. Rev. B* 65.115212 (2002) (cit. on p. 118).

[53] R. C. Dynes and T. a. Fulton. "Supercurrent density distribution in josephson junctions". In: *Phys. Rev. B* 3.9 (1971), pp. 3015–3023 (cit. on pp. 135, 137).

[54] P. M. Echternach, M. R. Thoman, C. M. Gould, and H. M. Bozler. "Electron-phonon scattering rates in disordered metallic films below 1K". In: *Phys. Rev. B - Condens. Matter Mater. Phys.* 46.16 (1992), pp. 10339–10344 (cit. on pp. 86, 110).

[55] Kazuma Eto, Zhi Ren, A. A. Taskin, Kouji Segawa, and Yoichi Ando. "Angular-dependent oscillations of the magnetoresistance in Bi2Se3 due to the three-dimensional bulk Fermi surface". In: *Phys. Rev. B - Condens. Matter Mater. Phys.* 81.19 (2010), pp. 2–6 (cit. on p. 15).

[56] Richard P. Feynman, Robert B. Leighton, and Matthew Sands. *The Feynman Lectures on Physics*. Ed. by Addison-Wesley. 1964 (cit. on p. 41).

[57] Lukasz Fidkowski, Jason Alicea, Netanel H. Lindner, Roman M. Lutchyn, and Matthew P A Fisher. "Universal transport signatures of Majorana fermions in superconductor- Luttinger liquid junctions". In: *Phys. Rev. B - Condens. Matter Mater. Phys.* 85.24 (2012), pp. 1–22 (cit. on p. 64).

[58] D. Milan Fiske. "Temperature and Magnetic Field dependences of the Josephson Tunneling current". In: *Rev. Mod. Phys.* (1964), pp. 221–222 (cit. on p. 127).

[59] E. Frantzeskakis, N. De Jong, B. Zwartsenberg, T. V. Bay, Y. K. Huang, S. V. Ramankutty, A. Tytarenko, D. Wu, Y. Pan, S. Hollanders, M. Radovic, N. C. Plumb, N. Xu, M. Shi, C. Lupulescu, T. Arion, R. Ovsyannikov, A. Varykhalov, W. Eberhardt, A. De Visser, E. Van Heumen, and M. S. Golden. "Dirac states with knobs on: Interplay of external parameters and the surface electronic properties of three-dimensional topological insulators". In: *Phys. Rev. B - Condens. Matter Mater. Phys.* 91.20 (2015), pp. 1–15 (cit. on p. 15).

[60] S. M. Frolov, D. J. Van Harlingen, V. A. Oboznov, V. V. Bolginov, and V. V. Ryazanov. "Measurement of the current-phase relation of superconductor/ferromagnet/ superconductor pi Josephson junctions". In: *Phys. Rev. B - Condens. Matter Mater. Phys.* 70.14 (2004), pp. 1–5 (cit. on p. 65).

[61] Liang Fu and C. L. Kane. "Probing neutral Majorana fermion edge modes with charge transport". In: *Phys. Rev. Lett.* 102.21 (2009), p. 216403 (cit. on p. 62).

[62] Liang Fu and Charles L. Kane. "Josephson current and noise at a superconductor/quantum-spin-Hall-insulator/superconductor junction". In: *Phys. Rev. B* 79.16 (Apr. 2009), p. 161408 (cit. on pp. 58, 73).

[63] Liang Fu and Charles L. Kane. "Superconducting Proximity Effect and Majorana Fermions at the Surface of a Topological Insulator". In: *Phys. Rev. Lett.* 100.9 (Mar. 2008), p. 096407 (cit. on pp. viii, 12, 40, 52, 56, 59, 62, 101).

[64] Liang Fu and Charles L. Kane. "Topological insulators with inversion symmetry". In: *Phys. Rev. B - Condens. Matter Mater. Phys.* 76.4 (July 2007), p. 045302 (cit. on pp. 10, 14).

[65] Liang Fu, Charles L. Kane, and E. J. Mele. "Topological Insulators in Three Dimensions". In: *Phys. Rev. Lett.* 98.10 (Mar. 2007), p. 106803 (cit. on pp. vii, 9, 14).

[66] L. Galletti, S Charpentier, M. Iavarone, P. Lucignano, D. Massarotti, R. Arpaia, Yusuke Suzuki, Kazuo Kadowaki, T. Bauch, A. Tagliacozzo, F. Tafuri, and F. Lombardi. "Influence of topological edge states on the properties of Al/Bi2Se3/Al hybrid Josephson devices". In: *Physical Review B - Condensed Matter and Materials Physics* 89.13 (2014), pp. 1–9 (cit. on pp. 32, 102).

[67] L. Galletti, S. Charpentier, P. Lucignano, D. Massarotti, R. Arpaia, F. Tafuri, T. Bauch, Yusuke Suzuki, A. Tagliacozzo, K. Kadowaki, and F. Lombardi. "Josephson effect in Al/Bi2Se3/Al coplanar hybrid devices". In: *Phys. C Supercond. its Appl.* 503 (2014), pp. 162–165 (cit. on p. 32).

[68] Francesco Giazotto, Tero T. Heikkilä, Arttu Luukanen, Alexander M. Savin, and Jukka P. Pekola. "Opportunities for mesoscopics in thermometry and refrigeration: Physics and applications". In: *Rev. Mod. Phys.* 78.1 (2006), pp. 217–274 (cit. on p. 86).

[69] Sébastien Giraud, Arijit Kundu, and Reinhold Egger. "Electron-phonon scattering in topological insulator thin films". In: *Phys. Rev. B* 85.3 (2012), pp. 1–10 (cit. on p. 111).

[70] Caglar Girit, Vincent Bouchiaty, Ofer Naamany, Yuanbo Zhang, M. F. Crommie, A. Zettl, and Irfan Siddiqi. "Current-phase relation in graphene and application to a superconducting quantum interference device". In: *Phys. Status Solidi Basic Res.* 246.11-12 (2009), pp. 2568–2571 (cit. on p. 65).

[71] A. A. Golubov, M. Yu Kupriyanov, and E. Ilichev. "The current-phase relation in Josephson junctions". In: *Rev. Mod. Phys.* 76.2 (2004), pp. 411–469 (cit. on pp. 42, 65).

[72] C. C. Grimes and Sidney Shapiro. "Millimeter-wave Mixing with Josephson Junctions". In: *Phys. Rev.* 169.2 (1968), pp. 397–406 (cit. on pp. 67, 129, 130).

[73] Mahdi Hajlaoui. "Entre métal et isolant: dynamique ultra-rapide dans l'isolant topologique Bi2Te3 et domaines microscopiques à la transition de Mott dans V2O3". PhD thesis. 2013 (cit. on pp. 1, 3).

[74] Sean Hart, Hechen Ren, Timo Wagner, Philipp Leubner, Mathias Mühlbauer, Christoph Brüne, Hartmut Buhmann, Laurens W. Molenkamp, and Amir Yacoby. "Induced superconductivity in the quantum spin Hall edge". In: *Nat. Phys.* 10.September (Aug. 2014) (cit. on p. 125).

[75] M. Zahid Hasan and Charles L. Kane. "Colloquium: Topological insulators". In: *Rev. Mod. Phys.* 82.4 (Nov. 2010), pp. 3045–3067 (cit. on p. 5).

[76] Hong-Tao He, Gan Wang, Tao Zhang, Iam Keong Sou, George K L Wong, Jian Nong Wang, Hai Zhou Lu, Shun Qing Shen, and Fu Chun Zhang. "Impurity effect on weak antilocalization in the topological insulator Bi2Te3". In: *Phys. Rev. Lett.* 106.16 (2011), pp. 1–4 (cit. on p. 15).

[77] Michel Héritier. *Physique de la matière condensée: Des atomes froids aux supraconducteurs à haute température critique*. Ed. by EDP Sciences. QuinteScie. 2013 (cit. on p. 54).

[78] Yew San Hor, A. Richardella, P. Roushan, Yuqi Xia, and Joseph G. Checkelsky. "p-type Bi2Se3 for topological insulator and low temperature thermoelectric applications". In: *Phys. Rev. B - Condens. Matter Mater. Phys.* 79.195208 (2009), pp. 1–20 (cit. on p. 14).

[79] Manuel Houzet, Julia S. Meyer, Driss M. Badiane, and Leonid I. Glazman. "Dynamics of Majorana States in a Topological Josephson Junction". In: *Phys. Rev. Lett.* 111.4 (July 2013), p. 046401 (cit. on pp. 73, 74, 102).

[80] D. Hsieh, Yuqi Xia, Dong Qian, Lewis Andrew Wray, F. Meier, J. Osterwalder, L. Patthey, Joseph G. Checkelsky, N. P. Ong, Alexei V. Fedorov, Hsin Lin, Arun Bansil, D. Grauer, Yew San Hor, Robert J. Cava, and M. Zahid Hasan. "A tunable topological insulator in the spin helical Dirac transport regime". In: *Nature* 460.7259 (2009), pp. 1101–1105 (cit. on p. 15).

[81] Masatoshi Imada, Atsushi Fujimori, and Yoshinori Tokura. "Metal-insulator transitions". In: *Rev. Mod. Phys.* 70.4 (1998), pp. 1039–1263 (cit. on p. 118).

[82] P. A. Ioselevich, P. M. Ostrovsky, and Mikhail V. Feigel'man. "Majorana state on the surface of a disordered three-dimensional topological insulator". In: *Phys. Rev. B - Condens. Matter Mater. Phys.* 86.3 (July 2012), p. 035441 (cit. on p. 56).

[83] Chikara Ishii. "Josephson Currents through Junctions with Normal Metal Barriers". In: *Progress of Theoretical Physics* 44.6 (1970), pp. 1525–1547 (cit. on p. 50).

[84] Dmitri Ivanov, Raphael von Roten, and Gianni Blatter. "Minigap in a long disordered SNS junction: Analytical results". In: *Physical Review B* 66.5 (2002), p. 052507 (cit. on pp. 51, 56).

[85] L. D. Jackel, R. A. Buhrman, and W. W. Webb. "Direct measurement of current-phase relations in superconducting weak links". In: *Phys. Rev. B* 10.7 (1974), pp. 2782–2785 (cit. on p. 65).

[86] Jaesung Jang, D. G. Ferguson, V. Vakaryuk, R. Budakian, S. B. Chung, P. M. Goldbart, and Y. Maeno. "Magnetization Steps in Sr2RuO4". In: *Science (80-.).* 331.January (2011), pp. 186–188 (cit. on p. 52).

[87] Shuang Jia, Huiwen Ji, E. Climent-Pascual, M. K. Fuccillo, M. E. Charles, Jun Xiong, N. P. Ong, and Robert J. Cava. "Low-carrier-concentration crystals of the topological insulator Bi2Te2Se". In: *Physical Review B - Condensed Matter and Materials Physics* 84.23 (Dec. 2011), p. 235206 (cit. on p. 26).

[88] Na Hyun Jo, Kyujoon Lee, Jinsu Kim, Jungwon Jang, Jinhee Kim, and Myung Hwa Jung. "Crossover between two-dimensional surface state and three-dimensional bulk phase in Fe-doped Bi2Te3". In: *Appl. Phys. Lett.* 104.25 (2014), pp. 2012–2016 (cit. on p. 15).

[89] Wayne Jon Johnson. "Nonlinear wave propagation on superconducting tunneling junctions". PhD thesis. University of Wisconsin–Madison, 1969, p. 196 (cit. on p. 78).

[90] Brian D. Josephson. "Coupled superconductors and beyond". In: *Rev. Mod. Phys.* 36 (1964), pp. 216–220 (cit. on p. 40).

[91] Brian D. Josephson. "Possible new effects in superconductive tunnelling". In: *Phys. Lett.* 1.7 (1962), pp. 251–253 (cit. on pp. 40, 41).

[92] P. Joyez, P. Lafarge, A. Filipe, D. Esteve, and M. H. Devoret. "Observation of parity-induced suppression of Josephson tunneling in the superconducting single electron transistor". In: *Phys. Rev. Lett.* 72.15 (1994), pp. 2458–2461 (cit. on p. 72).

[93] Charles L. Kane and E. J. Mele. "Quantum Spin Hall Effect in Graphene". In: *Phys. Rev. Lett.* 95.22 (Nov. 2005), p. 226801 (cit. on p. 7).

[94] Alexei Yu Kitaev. "Periodic table for topological insulators and superconductors". In: *AIP Conf. Proc.* 1134 (2009), pp. 22–30 (cit. on p. 3).

[95] Alexei Yu Kitaev. "Unpaired Majorana fermions in quantum wires". In: *Phys. Uspekhi* 44.131 (2001), pp. 1–16 (cit. on pp. 55, 56, 58).

[96] Charles Kittel and Donald F. Holcomb. "Introduction to Solid State Physics". In: *Am. J. Phys.* 35.6 (1967), p. 547 (cit. on p. 36).

[97] K. V. Klitzing, G. Dorda, and M. Pepper. "New method for high-accuracy determination of the fine-structure constant based on quantized hall resistance". In: *Phys. Rev. Lett.* 45.6 (1980), pp. 494–497 (cit. on pp. vii, 2).

[98] Markus König, Hartmut Buhmann, Laurens W. Molenkamp, Taylor L. Hughes, Chao Xing Liu, Xiao-Liang Qi, and Shou-Cheng Zhang. "The quantum spin Hall effect: Theory and experiment". In: *J. Phys. Soc. Japan* 77.3 (2008), pp. 1–14 (cit. on p. 9).

[99] Markus König, Steffen Wiedmann, Christoph Brüne, Andreas Roth, Hartmut Buhmann, Laurens W. Molenkamp, Xiao-Liang Qi, and Shou-Cheng Zhang. "Quantum spin hall insulator state in HgTe quantum wells." In: *Science (80-.).* 318.5851 (Nov. 2007), pp. 766–70 (cit. on p. 9).

[100] Nicholas C. Koshnick, Martin E. Huber, Julie A. Bert, Clifford W. Hicks, Jeff Large, Hal Edwards, and Kathryn A. Moler. "A terraced scanning supper conducting quantum interference device susceptometer with submicron pickup loops". In: *Appl. Phys. Lett.* 93.24 (2008) (cit. on p. 65).

[101] Yaacov E. Kraus, Assa Auerbach, H. a. Fertig, and Steven H. Simon. "Majorana fermions of a two-dimensional px + i py superconductor". In: *Phys. Rev. B* 79.13 (2009), p. 134515 (cit. on p. 56).

[102] I. O. Kulik. "Macroscopic Quantization and the Proximity Effect in S-N-S Junctions". In: *Sov. Phys. JETP* 30.5 (1970), p. 944 (cit. on pp. 45, 50).

[103] I. O. Kulik and A. N. Omel'yanchuk. "Properties of superconducting microbridges in the pure limit". In: *Sov. J. Low Temp. Phys.* 3.7 (1977), pp. 459–461 (cit. on p. 45).

[104] I. O. Kulik and An Omel'Yanchuk. "Contribution to the microscopic theory of the Josephson effect in superconducting bridges". In: 21.4 (1975), p. 96 (cit. on p. 45).

[105] C. Kurter, A. D. K. Finck, P. Ghaemi, Yew San Hor, and D. J. Van Harlingen. "Dynamical Gate Tunable Supercurrents in Topological Josephson Junctions". In: *Phys. Rev. B - Condens. Matter Mater. Phys.* 90.1 (Feb. 2014), pp. 3–7 (cit. on p. 32).

[106] C. Kurter, a. D. K. Finck, Yew San Hor, and D. J. Van Harlingen. "Evidence for an anomalous current-phase relation in topological insulator Josephson junctions". In: *Nat. Commun.* 6 (2013), p. 12 (cit. on pp. 32, 65).

[107] Hyok-jon Kwon, K. Sengupta, and Victor M. Yakovenko. "Fractionnal AC Josephson Effect in p- and d-wave superconductors". In: *Eur. Phys. J. B* 37 (2004), pp. 349–361 (cit. on pp. 40, 56).

[108] L. D. Landau. "A Theory of Energy Transfer. II". In: *Collect. Pap. L.D. Landau* 46.2 (1965), pp. 63–66 (cit. on pp. 49, 145).

[109] Rolf Landauer. "Electrical resistance of disordered one-dimensional lattices". In: *Philosophical Magazine* 21.172 (1970), pp. 863–867 (cit. on p. 48).

[110] K. T. Law, Patrick a. Lee, and T. K. Ng. "Majorana Fermion Induced Resonant Andreev Reflection". In: *Phys. Rev. Lett.* 103.23 (2009), pp. 2–5 (cit. on p. 64).

[111] Eduardo J H Lee, Xiaocheng Jiang, Ramón Aguado, Georgios Katsaros, Charles M. Lieber, and Silvano De Franceschi. "Zero-bias anomaly in a nanowire quantum dot coupled to superconductors". In: *Phys. Rev. Lett.* 109.18 (2012), pp. 1–5 (cit. on p. 64).

[112] Jae Hyeong Lee, Gil-Ho Lee, Joonbum Park, Janghee Lee, Seung-Geol Nam, Yun-Sok Shin, Jun Sung Kim, and Hu-Jong Lee. "Local and Nonlocal Fraunhofer-like Pattern from an Edge-Stepped Topological Surface Josephson Current Distribution." In: *Nano Lett.* 14.9 (Sept. 2014), pp. 5029–34 (cit. on pp. 32, 33, 122).

[113] Martin Leijnse and Karsten Flensberg. "Introduction to topological superconductivity and Majorana fermions". In: *Semicond. Sci. Technol.* 27.12 (Dec. 2012), p. 124003 (cit. on p. 55).

[114] Chuan Li. "Superconducting proximity effect in graphene and Bi nanowire based junctions". PhD thesis. Université Paris-Sud, 2014 (cit. on p. 40).

[115] H. Lin, Tanmoy Das, L. Andrew Wray, S. Y. Xu, M. Zahid Hasan, and Arun Bansil. "An isolated Dirac cone on the surface of ternary tetradymite-like topological insulators". In: *New J. Phys.* 13 (2011) (cit. on p. 32).

[116] Jacob Linder, Yukio Tanaka, Takehito Yokoyama, Asle Sudbø, and Naoto Nagaosa. "Unconventional superconductivity on a topological insulator". In: *Physical Review Letters* 104.6 (2010), pp. 1–4 (cit. on p. 62).

[117] Greg Lynn. *Animate Form: a book & interactive CD-ROP*. Press Arch. Princeton, 1999 (cit. on p. 4).

[118] Ettore Majorana. "A symmetric theory of electrons and positrons". In: *Sci. Pap.* 63.3 (1981), pp. 149–163 (cit. on pp. viii, 52).

[119] T. B. Massalski and H. Okamoto. *Binary alloy phase diagrams*. Ed. by Ohio : ASM International Materials Park. 1990 (cit. on p. 18).

[120] D. E. McCumber. "Tunneling and weak-link superconductor phenomena having potential device applications". In: *J. Appl. Phys.* 39.6 (1968), pp. 2503–2508 (cit. on p. 78).

[121] V. P. Mineev and K. Samokhin. *Introduction to Unconventional Superconductivity.* Taylor & Francis, 1999 (cit. on p. 54).

[122] Takeshi Mizushima, Masatoshi Sato, and Kazushige MacHida. "Symmetry protected topological order and spin susceptibility in superfluid He3-B". In: *Phys. Rev. Lett.* 109.16 (2012), pp. 1–5 (cit. on p. 52).

[123] C. G. Molenaar, D. P. Leusink, X. L. Wang, and Alexander Brinkman. "Geometric dependence of Nb-Bi 2 Te 3 -Nb topological Josephson junction transport parameters". In: *Superconductor Science and Technology* 27.10 (Oct. 2014), p. 104003 (cit. on p. 102).

[124] Joel E. Moore. "The birth of topological insulators." In: *Nature* 464.7286 (2010), pp. 194–198 (cit. on p. 4).

[125] V. Mourik, K. Zuo, Sergey Maksimovich Frolov, S. R. Plissard, Erik P. A. M. Bakkers, and Leo P. Kouwenhoven. "Signatures of Majorana fermions in hybrid superconductor-semiconductor nanowire devices." In: *Science* 336.6084 (May 2012), pp. 1003–7 (cit. on pp. 54, 64, 65).

[126] Shuichi Murakami. "Phase transition between the quantum spin Hall and insulator phases in 3D: Emergence of a topological gapless phase". In: *New J. Phys.* 9 (2007) (cit. on p. 8).

[127] Stevan Nadj-perge, Ilya K. Drozdov, Jian Li, Hua Chen, Sangjun Jeon, Jungpil Seo, Allan H. MacDonald, Andrei B. Bernevig, and Ali Yazdani. "Observation of Majorana fermions in ferromagnetic atomic chains on a superconductor". In: *Science (80-.).* 346.6209 (2014) (cit. on p. 66).

[128] J. Navrátil, J. Horák, T. Plecháček, S. Kamba, P. Lošt'ák, J.S. Dyck, W. Chen, and C. Uher. "Conduction band splitting and transport properties of Bi2Se3". In: *J. Solid State Chem.* 177.4-5 (2004), pp. 1704–1712 (cit. on p. 14).

[129] Chetan Nayak, Steven H. Simon, Ady Stern, Michael Freedman, and Sankar Das Sarma. "Non-Abelian anyons and topological quantum computation". In: *Rev. Mod. Phys.* 80.September (2008), pp. 1083–1159 (cit. on p. 52).

[130] Yuli V. Nazarov. "Limits of universality in disordered conductors". In: *Phys. Rev. Lett.* 73.1 (1994), pp. 134–137 (cit. on p. 50).

[131] Madhab Neupane, Su-Yang Xu, Lewis Andrew Wray, A. C. Petersen, R. Shankar, Nasser Alidoust, Chang Liu, Alexei V. Fedorov, Huiwen Ji, J. M. Allred, Yew San Hor, T.-R. Chang, H.-T. Jeng, Hsin Lin, Arun Bansil, Robert J. Cava, and M. Zahid Hasan. "Topological surface states and Dirac point tuning in ternary topological insulators". In: *Phys. Rev. B - Condens. Matter Mater. Phys.* 85.23 (June 2012), p. 235406 (cit. on pp. 15, 32).

[132] Y. Pan, D. Wu, J. R. Angevaare, H. Luigjes, E. Frantzeskakis, N. De Jong, E. Van Heumen, T. V. Bay, B. Zwartsenberg, Y. K. Huang, M. Snelder, A. Brinkman, M. S. Golden, and A. De Visser. "Low carrier concentration crystals of the topological insulator Bi2-xSbxTe3-ySey: A magnetotransport study". In: *New J. Phys.* 16 (2014) (cit. on p. 15).

[133] Athanasios Papoulis. *The Fourier Integral and Its Applications*. Ed. by McGraw-Hill Book Company. 1962 (cit. on p. 137).

[134] Yang Peng, Falko Pientka, Erez Berg, Yuval Oreg, and Felix von Oppen. "Signatures of topological Josephson junctions". In: *Condens. Matter - Mesoscale Nanoscale Phys.* (2016), p. 1604.04287 (cit. on p. 73).

[135] Falko Pientka, Leonid I. Glazman, and Felix Von Oppen. "Topological superconducting phase in helical Shiba chains". In: *Phys. Scr.* 164 (2015), p. 014008 (cit. on p. 64).

[136] Vlad S Pribiag, Arjan J a Beukman, Fanming Qu, Maja C Cassidy, Christophe Charpentier, Werner Wegscheider, and Leo P. Kouwenhoven. "Edge-mode Superconductivity in a Two Dimensional Topological Insulator: Supplementary info". In: *Nat. Nanotechnol.* 10.7 (2015), pp. 593–597 (cit. on p. 125).

[137] Dong-Xia Qu, Yew San Hor, Jun Xiong, Robert J. Cava, N. P. Ong, Qu Dong-Xia, Yew San Hor, Jun Xiong, Robert J. Cava, and N. P. Ong. "Quantum oscillations and hall anomaly of surface states in the topological insulator Bi2Te3." In: *Science* 329.5993 (Aug. 2010), pp. 821–4 (cit. on p. 15).

[138] Nicholas Read and Dmitry Green. "Paired states of fermions in two dimensions with breaking of parity and time-reversal symmetries and the fractional quantum Hall effect". In: *Phys. Rev. B* 61.15 (2000), p. 10267 (cit. on p. 51).

[139] Nicholas Read and Dmitry Green. "Paired states of fermions in two dimensions with breaking of parity and time-reversal symmetries and the fractional quantum Hall effect". In: *Phys. Rev. B* 61.15 (2000), p. 10267 (cit. on pp. 52, 56, 58).

[140] Zhi Ren, A. A. Taskin, Satochi Sasaki, Kouji Segawa, and Yoichi Ando. "Optimizing Bi2-xSbxTe3-ySey solid solutions to approach the intrinsic topological insulator regime". In: *Phys. Rev. B - Condens. Matter Phys* 84.16 (Oct. 2011), p. 165311 (cit. on p. 15).

[141] Zhi Ren, A. A. Taskin, Satoshi Sasaki, Kouji Segawa, and Yoichi Ando. "Large bulk resistivity and surface quantum oscillations in the topological insulator Bi2Te2Se". In: *Phys. Rev. B - Condens. Matter Mater. Phys.* 82.24 (Dec. 2010), p. 241306 (cit. on p. 15).

[142] Leonid P. Rokhinson, Xinyu Liu, and Jacek K. Furdyna. "The fractional a.c. Josephson effect in a semiconductor–superconductor nanowire as a signature of Majorana particles". In: *Nature Physics* 8.11 (Sept. 2012), pp. 795–799 (cit. on pp. 54, 67, 68, 102).

[143] Shinsei Ryu, Andreas P. Schnyder, Akira Furusaki, and Andreas W W Ludwig. "Topological insulators and superconductors: Tenfold way and dimensional hierarchy". In: *New J. Phys.* 12 (2010) (cit. on p. 3).

[144] B. Sacépé, J. Seidemann, M. Ovadia, I. Tamir, D. Shahar, C. Chapelier, C. Strunk, and B. A. Piot. "High-field termination of a Cooper-pair insulator". In: *Phys. Rev. B - Condens. Matter Mater. Phys.* 91.22 (2015), pp. 1–5 (cit. on p. 36).

[145] Benjamin Sacépé, Jeroen B. Oostinga, Jian Li, Alberto Ubaldini, Nuno J.G. Couto, Enrico Giannini, and Alberto F. Morpurgo. "Gate-tuned normal and superconducting transport at the surface of a topological insulator". In: *Nature Communications* 2 (2011), p. 575 (cit. on pp. 32, 102).

[146] D. Saint James. "Excitations elementaires au voisinage de la surface de separation d'un metal normal et d'un metal supraconducteur". In: *J. Phys.* 25.10 (), p. 899 (cit. on p. 42).

[147] J. Sánchez-Barriga, A. Varykhalov, J. Braun, S. Y. Xu, N. Alidoust, O. Kornilov, J. Minár, K. Hummer, G. Springholz, G. Bauer, R. Schumann, L. V. Yashina, H. Ebert, M. Z. Hasan, and O. Rader. "Photoemission of Bi2Se3 with circularly polarized light: Probe of spin polarization or means for spin manipulation?" In: *Phys. Rev. X* 4.1 (2014), pp. 1–10 (cit. on pp. 11, 14).

[148] Masatoshi Sato, Yoshiro Takahashi, and Satoshi Fujimoto. "Non-Abelian Topological Order in s-Wave Superfluids of Ultracold Fermionic Atoms". In: *Phys. Rev. Lett.* 103.2 (2009), pp. 1–4 (cit. on p. 52).

[149] C. B. Satterthwaite and R. W. Jr. Ure. "Electrical and thermal properties of Bi2Te3". In: *Phys. Rev.* 108.5 (1957), pp. 1164–1170 (cit. on p. 15).

[150] Jay Deep Sau, Erez Berg, and Bertrand I. Halperin. "On the possibility of the fractional ac Josephson effect in non-topological conventional superconductor-normal-superconductor junctions". In: 1 (June 2012), p. 5 (cit. on p. 148).

[151] Jay Deep Sau, Roman M. Lutchyn, Sumanta Tewari, and Sankar Das Sarma. "Generic New Platform for Topological Quantum Computation Using Semiconductor Heterostructures". In: *Phys. Rev. Lett.* 104.4 (2010), p. 040502 (cit. on p. 68).

[152] Jay Deep Sau and F. Setiawan. "Detecting topological superconductivity using the Shapiro steps". In: *Condens. Matter - Mesoscale Nanoscale Phys.* (2016), pp. 1–8 (cit. on pp. 72, 148).

[153] E. Scheer, P. Joyez, D. Esteve, C. Urbina, and M. Devoret. "Conduction Channel Transmissions of Atomic-Size Aluminum Contacts". In: *Phys. Rev. Lett.* 78.18 (1997), pp. 3535–3538 (cit. on p. 50).

[154] Andreas P. Schnyder, Shinsei Ryu, Akira Furusaki, and Andreas W W Ludwig. "Classification of topological insulators and superconductors". In: *AIP Conf. Proc.* 1134 (2009), pp. 10–21 (cit. on p. 3).

[155] Andreas P. Schnyder, Shinsei Ryu, Akira Furusaki, and Andreas W. W. Ludwig. "Classification of topological insulators and superconductors in three spatial dimensions". In: *Phys. Rev. B* 78.195125 (2008) (cit. on p. 3).

[156] S. T. Sekula and R. H. Kernohan. "Magnetic properties of superconducting vanadium". In: *Phys. Rev. B* 5.3 (1972), pp. 904–911 (cit. on p. 36).

[157] Sidney Shapiro. "Josephson Currents in superconducting Tunneling: The effect of microwaves and other observations". In: *Phys. Rev. Lett.* 11.2 (1963), pp. 80–82 (cit. on pp. 67, 81).

[158] Manfred Sigrist. *Introduction to Unconventional Superconductivity* (cit. on p. 54).

[159] M. Snelder, C. G. Molenaar, Y. Pan, D. Wu, Y. K. Huang, A. de Visser, A. A. Golubov, W. G. van der Wiel, H. Hilgenkamp, M. S. Golden, and Alexander Brinkman. "Josephson supercurrent in a topological insulator without a bulk shunt". In: *Supercond. Sci. Technol.* 27.10 (Oct. 2014), p. 104001 (cit. on pp. 33, 122).

[160] M. Snelder, M. Veldhorst, A. A. Golubov, and Alexander Brinkman. "Andreev bound states and current-phase relations in three-dimensional topological insulators". In: *Phys. Rev. B* 87.10 (Mar. 2013), p. 104507 (cit. on pp. 40, 62, 63).

[161] Ilya Sochnikov, Andrew J. Bestwick, James R. Williams, Thomas M. Lippman, Ian R. Fisher, David Goldhaber-Gordon, John R. Kirtley, and Kathryn a. Moler. "Direct Measurement of Current-Phase Relations in Superconductor/Topological Insulator/Superconductor Junctions." In: *Nano Lett.* (June 2013) (cit. on pp. 32, 65).

[162] Ilya Sochnikov, Luis Maier, Christopher a. Watson, John R. Kirtley, Charles Gould, Grigory Tkachov, Ewelina M. Hankiewicz, Christoph Brüne, Hartmut Buhmann, Laurens W. Molenkamp, and Kathryn a. Moler. "Nonsinusoidal Current-Phase Relationship in Josephson Junctions from the 3D Topological Insulator HgTe". In: *Phys. Rev. Lett.* 114.February (2015), pp. 1–6 (cit. on p. 65).

[163] W. C. Stewart. "Current-voltage characteristics of Josephson junctions". In: *Appl. Phys. Lett.* 12.8 (1968), pp. 277–280 (cit. on p. 78).

[164] W. P. Su, John Robert Schrieffer, and A. J. Heeger. "Solitons in polyacetylene". In: *Phys. Rev. Lett.* 42.25 (1979), pp. 1698–1701 (cit. on pp. viii, 5, 7, 10).

[165] Yusuke Suzuki, Kévin Le Calvez, Philippe Plaindoux, Frederic Gay, Takashi Mochiku, Shoji Yoshida, Yuka Hosomi, Zi-Han Wang, Fumiya Kimizuka, Akinori Hoshikawa, Toru Ishigaki, Ryozo Yoshizaki, Hervé Courtois, Benjamin Sacépé, Hidemi Shigekawa, Takanari Kashiwagi, and Kazuo Kadowaki. "Single crystal growth and the characterization of the crystal structure in BiSbTeSe2". In: () (cit. on p. 27).

[166] K Takanaka. "Zero-field steps in josephson junctions". In: *Solid State Commun.* 29.4 (1979), pp. 443–445 (cit. on p. 127).

[167] Yukio Tanaka, Takehito Yokoyama, and Naoto Nagaosa. "Manipulation of the majorana fermion, andreev reflection, and josephson current on topological insulators". In: *Physical Review Letters* 103.10 (2009), pp. 1–4 (cit. on p. 62).

[168] A. A. Taskin, Zhi Ren, Satoshi Sasaki, Kouji Segawa, and Yoichi Ando. "Observation of dirac holes and electrons in a topological insulator". In: *Phys. Rev. Lett.* 107.1 (2011), pp. 1–4 (cit. on pp. 15, 122).

[169] "Topological phase transitions and topological phases of matter". In: *R. Swedish Acad. Sci.* (2016) (cit. on p. 2).

[170] M. Veldhorst, M. Hoek, T. Gang, V. K. Guduru, X. L. Wang, U. Zeitler, W. G. van der Wiel, A. A. Golubov, H. Hilgenkamp, and Alexander Brinkman. "Josephson supercurrent through a topological insulator surface state." In: *Nature materials* 11.5 (May 2012), pp. 417–21 (cit. on p. 102).

[171] Louis Veyrat. "Quantum Transport Study in 3D Topological Insulators Nanostructures". PhD thesis. 2016 (cit. on pp. 1, 6, 7).

[172] Pauli Virtanen, F. Sebastián Bergeret, Juan Carlos Cuevas, and Tero T. Heikkilä. "Linear ac response of diffusive SNS junctions". In: *Phys. Rev. B - Condens. Matter Mater. Phys.* 83.14 (2011), pp. 2–6 (cit. on p. 50).

[173] Pauli Virtanen and Patrik Recher. "Microwave spectroscopy of Josephson junctions in topological superconductors". In: *Phys. Rev. B* 88.14 (Oct. 2013), p. 144507 (cit. on pp. 73, 102).

[174] Felix Von Oppen. "Magnetic adatoms on superconductors - a new venue for Majorana bound states?" In: *GDR - Phys. Mesoscopique.* 2015 (cit. on p. 64).

[175] Lin-lin Wang and Duane D. Johnson. "Ternary Tetradymite Compounds as Topological Insulators". In: *Physical Review B - Condensed Matter and Materials Physics* 83.111 (June 2011), pp. 1–12 (cit. on p. 32).

[176] Wei Wang, Li Li, Wenqin Zou, Liang He, Fengqi Song, Rong Zhang, Xiaoshan Wu, and Fengming Zhang. "Intrinsic Topological Insulator Bi1.5Sb0.5Te3-xSex Thin crystals". In: *Sci. Rep.* 5.003 (2015), pp. 1–5 (cit. on p. 15).

[177] F. C. Wellstood, C. Urbina, and John Clarke. "Hot-electron effects". In: *Phys. Rev. B - Condens. Matter Mater. Phys.* 49.9 (1994), p. 5942 (cit. on p. 86).

[178] Jonas Wiedenmann, Erwann Bocquillon, Russell S. Deacon, Simon Hartinger, T. Herrmann, Teun M. Klapwijk, Luis Maier, Christopher Ames, Christoph Brüne, Koji Ishibashi, Seigo Tarucha, Hartmut Buhmann, Laurens W. Molenkamp, Oliver Herrmann, Teun M. Klapwijk, Luis Maier, Christopher Ames, Christoph Brüne, Charles Gould, Akira Oiwa, Koji Ishibashi, Seigo Tarucha, Hartmut Buhmann, and Laurens W. Molenkamp. "4 π -periodic Josephson supercurrent in HgTe-based topological Josephson junctions". In: *Nat. Commun.* 7 (2016), p. 10303 (cit. on pp. 68, 93, 102, 109, 147).

[179] James R. Williams, Andrew J. Bestwick, P. Gallagher, Seung Sae Hong, Yi Cui, Andrew S. Bleich, James G. Analytis, and Ian R. Fisher. "Unconventional Josephson effect in Hybrid Superconductor-Topological Insulator Devices". In: *Phys. Rev. Lett.* 109.05 (2012), p. 056803 (cit. on pp. 32, 54).

[180] Bin Xia, Peng Ren, Azat Sulaev, Peng Liu, Shun Qing Shen, and Lan Wang. "Indications of surface-dominated transport in single crystalline nanoflake devices of topological insulator Bi1.5Sb0.5Te 1.8Se1.2". In: *Phys. Rev. B - Condens. Matter Mater. Phys.* 87.8 (2013), pp. 1–8 (cit. on p. 15).

[181] Y. Xia, D. Qian, D. Hsieh, Lewis Andrew Wray, A. Pal, H. Lin, Arun Bansil, D. Grauer, Yew San Hor, Robert J. Cava, and M. Zahid Hasan. "Observation of a large-gap topological-insulator class with a single Dirac cone on the surface". In: *Nature Physics* 5.6 (2009), p. 18 (cit. on pp. 10, 11, 14, 15).

[182] Yang Xu, Ireneusz Miotkowski, Chang Liu, Jifa Tian, and Hyoungdo Nam. "Observation of topological surface state quantum Hall effect in an intrinsic three - dimensional topological insulator". In: *Nat. Phys.* 10.12 (2014), pp. 956–963 (cit. on pp. 15, 26, 32, 33, 121–123).

[183] Fan Yang, Yue Ding, Fanming Qu, Jie Shen, Jun Chen, Zhongchao Wei, Zhongqing Ji, Guangtong Liu, Jie Fan, Changli Yang, Tao Xiang, and Li Lu. "Proximity effect at superconducting Sn Bi2Se3 interface". In: *Phys. Rev. B - Condens. Matter Mater. Phys.* 85.10 (Mar. 2012), p. 104508 (cit. on p. 32).

[184] Fan Yang, Fanming Qu, Jie Shen, Yue Ding, Jun Chen, Zhongqing Ji, Guangtong Liu, Jie Fan, Changli Yang, Liang Fu, and Li Lu. "Proximity effect induced superconducting phase in the topological insulator Bi2Se3". In: *Phys. Rev. B - Condens. Matter Mater. Phys.* 86.13 (Oct. 2012), p. 134504 (cit. on p. 32).

[185] Hongtao Yuan, Hongwen Liu, Hidekazu Shimotani, Hua Guo, Mingwei Chen, Qikun Xue, and Yoshihiro Iwasa. "Liquid-Gated Ambipolar Transport in Ultrathin Films of a Topological". In: *Nano Lett.* 11.7 (2011), pp. 2601–2605 (cit. on p. 15).

[186] Clarence Zener. "Non-adiabatic crossing of energy levels". In: *Proc. R. Soc. London. Ser. A* 137 (1932), pp. 696–702 (cit. on pp. 49, 145).

[187] M. Zgirski, Landry Bretheau, Q. Le Masne, H. Pothier, D. Esteve, and C. Urbina. "Evidence for long-lived quasiparticles trapped in superconducting point contacts". In: *Phys. Rev. Lett.* 106.25 (2011), pp. 1–4 (cit. on p. 72).

[188] Duming Zhang, Jian Wang, Ashley M. DaSilva, Joon Sue Lee, Humberto R. Gutierrez, Moses H. W. Chan, Jainendra Jain, and Nitin Samarth. "Superconducting proximity effect and possible evidence for Pearl vortices in a candidate topological insulator". In: *Phys. Rev. B - Condens. Matter Mater. Phys.* 84.16 (Oct. 2011), pp. 1–21 (cit. on p. 32).

[189] H. B. Zhang, H. L. Yu, D. H. Bao, S. W. Li, C. X. Wang, and G. W. Yang. "Weak localization bulk state in a topological insulator Bi 2Te 3 film". In: *Phys. Rev. B - Condens. Matter Mater. Phys.* 86.7 (2012), pp. 1–7 (cit. on p. 15).

[190] Haijun Zhang, Chao-Xing Liu, Xiao-Liang Qi, Xi Dai, Zhong Fang, and Shou-Cheng Zhang. "Topological insulators in Bi2Se3, Bi2Te3 and Sb2Te3 with a single Dirac cone on the surface". In: *Nat. Phys.* 5.6 (May 2009), pp. 438–442 (cit. on pp. 10, 11, 14, 15, 31, 122).

[191] Huihuo Zheng and Lucas K. Wagner. "Computation of the correlated metal-insulator transition in vanadium dioxide from first principles". In: *Phys. Rev. Lett.* 114.17 (2015), pp. 1–5 (cit. on p. 118).

[192] F. Zhou, P. Charlat, B. Spivak, and Bernard Pannetier. "Density of States in Superconductor-Normal Metal-Superconductor Junctions". In: *Journal of Low Temperature Physics* 110.3 (1998), pp. 841–850 (cit. on p. 51).

Résumé :

Les isolants topologiques 3D sont un nouvel état de la matière décrit par un volume isolant électriquement et recouvert par des états de surface métalliques. Une jonction Josephson topologique (TJJ) formée autour de ces états de surface peut théoriquement contenir un mode lié d'Andreev ayant une périodicité doublée par rapport aux modes liés d'Andreev conventionnels 2π périodiques. Le mode d'Andreev 4π périodique serait la brique élémentaire de l'ordinateur quantique topologique. Ainsi, nous étudions la dynamique de ce mode particulier lors de mesures de Shapiro sur des jonctions Josephson fabriquées sur des isolants topologiques à base de bismuth.

Afin d'identifier les effets d'un mode 4π-périodique dans une mesure de Shapiro, nous utilisons un model phénoménologique permettant de simuler la caractéristique courant-tension d'une TJJ lors de telles mesures. Nous prédisons deux signatures du mode 4π-périodique et estimons leur robustesse face aux effets de chauffage par effet Joule et face à un modèle d'empoisonnement thermiquement activé du mode 4π-périodique.

Par des mesures de Shapiro, nous étudions la dynamique des TJJ basées sur le matériau simple qu'est le Bi2Se3. L'observation des deux mêmes signatures précédemment anticipées par nos simulations, à savoir un ordre d'apparition non conventionnel des pas de Shapiro ainsi que la persistance d'un supercourant à la fermeture du plateau de Shapiro $n = 0$ prouve la présence d'un mode 4π-périodique.

Notre étude s'est également portée sur un autre isolant topologique le BiSbTeSe2. Nous avons effectué sa croissance par cristallisation liquide-solide et avons mis en évidence, par des mesures d'interférométrie supraconductrice une supraconductivité de surface sans transport électronique par le volume.

Abstract :

Three dimensional topological insulators (3D TI) are a new state of matter composed of an electrically insulating bulk covered by metallic surface states. Theoretically, a topological Josephson junction composed of these surface states can host an Andreev Bound state (ABS) that has twice the periodicity of the conventional 2π periodic ABSs. The 4π periodic ABS is expected to be the building block of topological quantum computing. Therefore, we study the dynamic of this particular ABS by performing Shapiro measurement on Josephson junctions built with bismuth based 3D TI.

To identify the effects of a 4π periodic ABS in a Shapiro measurement, we use a phenomenological model that simulates the voltage-current characteristics of a TJJ. We predict two signatures of the 4π periodic ABS and estimate their robustness against Joule heating and thermally activated quasiparticle poisoning of the 4π periodic mode.

We study the Josephson junctions dynamics by performing Shapiro measurements on junctions built on Bi2Se3. We observe the two previously anticipated signatures, which are the non-conventional appearance order of the Shapiro steps and the remaining of a supercurrent at the closing of the Shapiro step $n = 0$. They prove the presence of a 4π periodic ABS.

We also study the topological insulator BiSbTeSe2 that we have grown by using the melting growth method. By superconducting interferometric measurements, we show a superconducting surface transport without bulk electronic conduction.